PASSIVE TREATMENT OF LOW PH, FERRIC IRON-DOMINATED ACID ROCK DRAINAGE

by

ROBERT CARL THOMAS

(Under the Direction of Christopher S. Romanek)

ABSTRACT

An experimental system was constructed with a limestone-buffered organic substrate (LBOS) to study the effects of passive treatment of low pH (<3), ferric iron-dominated acid rock drainage (ARD). Low pH, ferric iron-dominated ARD was passed through the LBOS for two years and the mechanism of acidity neutralization and alkalinity generation studied. Influent ARD was completely neutralized at a limestone dissolution front within the LBOS. Consequently, the total alkalinity generated in the LBOS was more than double the total alkalinity previously realized in any other passive treatment system.

Three reaction zones surrounding the limestone dissolution front were identified: 1) an overlying oxide zone, characterized by iron oxyhydroxides and no limestone; 2) a transitional zone at the dissolution front, characterized by aluminum hydroxysulfate and partially dissolved limestone; and 3) an underlying sulfide zone, characterized by ubiquitous sulfide minerals and pristine limestone. The majority of the influent iron was removed in the oxide zone through hydrolysis and precipitation of ferric iron. The acidity generated through the precipitation of ferric oxyhydroxides was balanced by the dissolution of aluminum hydroxysulfate. Aluminum dissolved from the oxide zone was reprecipitated in the transitional zone in the presence of limestone. The acidity generated during the precipitation of aluminum hydroxysulfate was balanced by the dissolution of limestone. Ferrous iron generated in the oxide and transitional zones was removed in the sulfide zone, mainly as framboidal pyrite.

The sulfide zone formed ahead of the limestone dissolution front at pH >6.5. As the limestone was completely removed from the transitional zone, the dissolution front advanced deeper into the LBOS. As a consequence, the leading edge of transitional zone overprinted the sulfide zone, while the oxide zone overprinted the trailing edge of the transitional zone. Therefore, with complete migration of the limestone dissolution front through the substrate, the LBOS will evolve towards oxide zone material.

Several trace elements (As, Cr, Cu, U, Cd, Co, Ni, Zn) were also sequestered in LBOS. As the substrate evolved toward oxide zone material, uranium, chromium, copper, cadmium, cobalt, nickel, and zinc were remobilized and migrated with the limestone dissolution front. Arsenic was not remobilized once sequestered.

INDEX WORDS: Acid rock drainage, Constructed treatment wetlands, Acid neutralization, Passive treatment

PASSIVE TREATMENT OF LOW PH, FERRIC IRON-DOMINATED ACID ROCK DRAINAGE

by

ROBERT CARL THOMAS

B.S., The University of the South, 1992

M.S., Auburn University, 1996

A Dissertation Submitted to the Graduate Faculty of The University of Georgia in Partial Fulfillment of the Requirements for the Degree

DOCTOR OF PHILOSOPHY

ATHENS, GEORGIA

2002

PASSIVE TREATMENT OF LOW PH, FERRIC IRON-DOMINATED ACID ROCK DRAINAGE

by

ROBERT CARL THOMAS

Major Professor:	Christopher Romanek
Committee:	Douglas Crowe Valentine Nzengung Paul Schroeder John Seaman Juergen Wiegel

Electronic Version Approved:

Maureen Grasso
Dean of the Graduate School
The University of Georgia
December 2002

DEDICATION

Dedicated to my wife, Patty Jo, and my parents, Bobby and Carole, for their support and their patience. wroque!

ACKNOWLEDGEMENTS

This research was funded by Financial Assistance Award Number De-FC09-96SR18546 between the United States Department of Energy and The University of Georgia as a part of the US DOE National Water Research Center. I would like to thank the principle investigators of this grant, Dr. Rebbecca Sharitz, Dr. J Vaun McArthur, and Dr. Beverly Collins for their continued support and assistance. Additional funding for this research and travel assistance was provided by the Wheeler-Watts Awards, Levy Award, The Department of Geology and The Graduate School at The University of Georgia, and The Geological Society of America.

During the course of this project, two undergraduate students, Kris Paul and Catherine Brown, conducted preliminary research as a part of the Savannah River Ecology Lab's (SREL) Research Experience for Undergraduates (REU) program. Their preliminary findings greatly facilitated my research and I am grateful for their efforts. Support for these students was provided by the National Science Foundation Grant #DBI-0139572 and the Savannah River Ecology Laboratory under Financial Assistance Award DE-FC09-96SR18-546 between the University of Georgia and the U.S. Department of Energy.

I am especially appreciative of the direction and encouragement of Chris Romanek and Doug Crowe. They have been exemplary advisors. I am also thankful for the guidance provided by Juergen Wiegel. I came to The University of Georgia with very little background in microbiology and I am leaving with a wealth of information. John

Seaman, Valentine Nzengun, and Paul Schroeder have been more than accommodating with lab space, late night phone calls, last minute reviews, and lending general insights regarding my observations.

This research would not have been possible without the technical assistance of Linda Paddock, Daniel Coughlin, Matt Opdyke, Brian Jackson, Morris Jones, and numerous other researchers at SREL. Dan and I built the system; Lindy and I sampled the system; Lindy, Brian, Morris, and I analyzed the samples; and Matt, Lindy, and I took the system down. We had a lot of help at all stages and I am very appreciative to those that helped.

My understanding of passive treatment systems would not have been possible without the assistance and guidance from members of the American Society of Mining and Reclamation (ASMR). Especially, George Watzlaf and Bob Kleinmann of the Department of Energy's National Energy Technology Laboratory, Pittsburg; Art Rose, emeritus Penn. State University; Joe Galetovic, US Office of Surface Mining; Jim Gusek, Knight Píesold Co.; Paul Eger, Minnesota DNR; Norrie Robbins (retired) and Chuck Cravotta, USGS; Carl Kirby, Bucknell University; Margaret Dunn and Tim Daheny, Biomost, Inc.; Bob Nairn, University of Oklahoma; Jeff Skousen, UWV; and Bill Garrett, Alabama Power.

TABLE OF CONTENTS

CHAPTER 1

INTRODUCTION

Acid rock drainage (ARD) is a major source of water contamination in metal- and coal-mining areas worldwide (Powell, 1988; Herlihy et al., 1990). When ARD reaches a receiving stream, it is often toxic to aquatic life and can threaten domestic drinking water supplies (Eger, 1992). Dissolved metal concentrations and pH affect drainage toxicity (Earle and Callaghan, 1998). In their 2000 Toxics Release Inventory (TRI), the United States Environmental Protection Agency (U.S. EPA) reported that metal mining accounted for 47% (3.34 billion pounds) of total on- and off-site releases of toxic pollutants. Moreover, the U.S. EPA considers mine drainage to be one of the most significant non-point pollution problems in EPA Region 3 (Central Appalachian Region of the U.S.; Kleinmann et al., 2000); with the majority of ARD originating from abandoned coal mines.

Acid rock drainage forms when sulfide minerals are exposed to oxygen and water during and after mining and other large-scale land disturbances. Pyrite (FeS_2), associated with coal and metal-ore deposits is responsible for producing the majority of ARD in mining areas (e.g., Stumm and Morgan, 1981; Rose and Cravotta, 1998). Generation of ARD is initiated with the oxidation of pyrite in the presence of water and the consequent release of Fe^{2+}, SO_4^{2-}, and acidity. Trace metals such as As, Cu, Ni, Zn, Co, and Cr, associated with the pyrite may also be released to the environment at levels above the drinking water standards (Sobolewski, 1999).

In the U.S., mining companies commonly treat contaminated drainage using chemical methods. This conventional treatment of ARD involves the "active" addition of alkaline chemicals to raise pH and remove acidity through the precipitation of metal oxyhydroxides:

$$4\ NaOH + H^+ + Fe^{3+} \rightarrow FeOOH + 4\ Na^+ + 2H_2O \qquad (1).$$

For highly mineralized ARD, treatment is often a two-staged process involving the initial addition of alkalinity in excess of proton and mineral (i.e., hydrolyzable metal) acidity followed by aeration and settling to promote metal. Although effective, active chemical treatment is expensive when the cost of equipment, chemicals, and manpower is considered (Kleinmann, 1990; Phipps et al., 1991; Skousen et al., 1998) and responsibility for treatment may be a long-term liability. It is not unusual for water treatment costs to exceed $10,000 per year at sites that are otherwise successfully reclaimed (Watzlaf et al., 2002). The high costs of water treatment place a serious financial burden on active mining companies and have contributed to the bankruptcies of many others. In fact in 1990, Kleinmann estimated the United States coal industry spends over $1 million per day on active treatment of ARD.

The high costs of chemical systems limit water treatment efforts at abandoned sites. However, Kleinmann et al. (2000) estimate that, in the United States alone, over 19,300 km (12,000 miles) of rivers and streams and over 730 km^2 (180,000 acres) of lakes and reservoirs are impacted by ARD from sites that were mined and abandoned before enactment of strict effluent regulations. State and Federal reclamation agencies, local conservation organizations, and watershed associations all consider the treatment of contaminated mine discharges to be a high priority. However, insufficient funds are available for chemical water treatment except in a few watersheds of special value (Watzlaf et al., 2002).

One alternative to chemical treatment is passive treatment, which refers to any zero to low maintenance ARD treatment method that does not require continual chemical addition and monitoring. Passive treatment systems offer control of ARD at substantially lower operating costs than conventional treatment plants, are environmentally safe, and they can be installed in remote locations such as abandoned mine lands. During the past two decades, the possibility that ARD might be treated passively has developed from an experimental concept to full-scale field implementation at hundreds of sites around the world (Hedin et al., 1994; Watzlaf et al., 2002). Types of passive treatment systems range from aerobic and compost wetlands modeled after natural peat wetlands (e.g., Hedin et al., 1994; Skousen et al., 1998) to more engineered units such as anoxic limestone drains (ALD, e.g Turner and McCoy, 1990) and reducing and alkalinity producing systems (RAPS, e.g. Kepler and McCleary, 1994; Watzlaf, 1997). Selection of an appropriate passive system is based on ARD water chemistry, flow rate, local topography, and various other site characteristics (Hyman and Watzlaf, 1995); ARD chemistry places the greatest constraints.

Reducing and alkalinity producing systems (RAPS) are passive alkalinity generating systems of particular interest because RAPS are the only passive technology capable of treating highly acidic, oxygenated, ARD containing elevated concentrations of iron and aluminum (Watzlaf et al., 2000). A RAPS is a type of constructed treatment wetland with a layer of organic matter (generally compost; 0.1 – 0.5 m) that overlies a layer of limestone (0.5 – 1.0 m Kepler and McCleary, 1994; Watzlaf, 1997; Skousen et al., 1998; Zipper and Jage, 2001). A perforated pipe drainage system is placed at the bottom of the limestone layer to regulate water depth and insure that the organic and limestone layers remain submerged (Kepler and McCleary, 1994; Watzlaf, 1997; Zipper and Jage, 2001). The RAPS design directs water to flow downward through the organic matter and limestone layers, by gravity, for surface discharge at a lower relative elevation.

While in theory, RAPS can treat low pH, highly oxidized ARD, there are no known reports on RAPS receiving ARD that has a pH consistently < 3.0 and is dominated by ferric iron (i.e., $Fe^{3+} \gg Fe^{2+}$). The purpose of this research, therefore, was to simulate a RAPS-type passive treatment system receiving low pH, ferric iron-dominated ARD. In the first chapter, the mechanism of acidity neutralization and alkalinity generation is reported. In the second chapter, three distinctly colored reaction zones are identified and a model is presented for their development. In the third chapter, the behavior of eight trace elements (As, Cr, Cu, U, Cd, Co, Ni, Zn) within these three reaction zones is investigated.

CHAPTER 2

ALKALINITY GENERATION WITH A LIMESTONE-BUFFERED ORGANIC SUBSTRATE DURING PASSIVE TREATMENT OF LOW-PH, FERRIC IRON-DOMINATED ACID ROCK DRAINAGE [1]

---

[1] Thomas, R.C. and Romanek, C.S. 2002. To be submitted to *Applied Geochemistry*.

Abstract

Reducing and alkalinity producing systems (RAPS) are a limestone-based passive treatment option for the remediation of acid rock drainage (ARD) from coal and ore mines. They function to neutralize proton acidity and generate alkalinity. Reducing and alkalinity producing systems are not traditionally designed to remove mineral acidity *in situ*; this process typically occurs in a downstream aerobic wetland. In coal-related ARD, mineral acidity comprises >85% of the total acidity. Therefore, by design, RAPS neutralize only a small portion of total acidity in ARD internally.

In this study, acidity neutralization and alkalinity generation reactions were studied using an experimental mesocosm system modeled after RAPS, but containing limestone-buffered organic substrate (LBOS). Highly acidic (1304 $mg \cdot L^{-1}$ $CaCO_3$ equivalents), low pH (2.4), ferric iron-dominated (95 – 100 % ferric iron; 92 – 237 $mg \cdot L^{-1}$ total iron) ARD was passed through the system for two years. Effluent pH was consistently near-neutral (6.4) and alkaline (619 $mg \cdot L^{-1}$ $CaCO_3$ equivalents) with >97% of the influent acidity removed (15 $mg \cdot L^{-1}$ iron). Total alkalinity generated in the system (1832 $mg \cdot L^{-1}$ $CaCO_3$ equivalents) was more than four times greater than traditional RAPS systems, because mineral acidity, as ferric iron and aluminum, was neutralized at relatively low pH (<4.5) simultaneously with proton acidity. Although ferric iron oxyhydroxide and aluminum hydroxysulfate precipitated in the presence of limestone, armoring and passivation of the limestone was not observed, nor was there any reduction in permeability. Therefore, LBOS-amended treatment systems may be able to effectively treat low pH (<3.0), ferric iron-dominated ARD over long periods of time.

1. Introduction

Acid rock drainage (ARD) from coal and ore mines is a significant problem worldwide (Herlihy et al., 1990). It forms when sulfide minerals are exposed to oxygen and water during and after mining operations and during other large-scale land disturbances involving sulfide minerals. Pyrite (FeS_2) is responsible for the majority of ARD in mining areas (e.g., Stumm and Morgan, 1981; Rose and Cravotta, 1998). Generation of ARD is initiated with the oxidation of pyrite in the presence of water:

$$FeS_2 + 3.5\ O_2 + H_2O \Leftrightarrow Fe^{+2} + 2SO_4^{2-} + 2\ H^+ \qquad (1)$$

The resulting drainage can be highly acidic and low in pH, and contain elevated concentrations of dissolved sulfate, iron, manganese, and other acid soluble metals (e.g., aluminum; Hedin et al., 1994a). When ARD reaches a receiving stream, it is often toxic to aquatic life and can threaten domestic drinking water supplies (Eger, 1992). Kleinmann et al. (2000) estimated that in the United States alone over 19,300 km of rivers and streams and over 730 km^2 of lakes and reservoirs are impacted by ARD from abandoned mines.

Active chemical treatment of ARD is well understood and effective; however this is an expensive and long-term commitment, particularly since drainage problems can persist for over a hundred years (Kleinmann, 1990; Phipps et al., 1991; Skousen et al., 1998). During the past two decades, the possibility that ARD might be treated passively using constructed treatment wetlands (CTW) has developed from an experimental concept to full-scale field implementation at hundreds of sites (Hedin et al., 1994a). Types of passive treatment systems range from aerobic and compost wetlands modeled after natural peat wetlands (e.g., Hedin et al., 1994a; Skousen et al., 1998) to more engineered units such as anoxic limestone drains (ALD, e.g Turner and McCoy, 1990) and reducing and alkalinity producing systems (RAPS, e.g. Kepler and McCleary, 1994; Watzlaf, 1997; Zipper and Jage, 2001). Selection of an appropriate passive system is based on ARD water chemistry, flow rate, local topography, and various other site characteristics (Hyman and Watzlaf, 1995).

Acidity and alkalinity are probably the two most important water quality parameters of ARD that dictate the type of passive technology to be employed. The two major sources of acidity in ARD are proton acidity (pH) and mineral acidity associated with dissolved metals (Hem, 1992). In ARD related to coal mining, mineral acidity arises primarily through the hydrolysis and precipitation of dissolved iron, aluminum, and manganese:

$$Fe^{2+} + 0.25\ O_2 + 1.5\ H_2O \Leftrightarrow FeOOH + 2H^+ \qquad (2)$$

$$Fe^{3+} + 2\ H_2O \Leftrightarrow FeOOH + 3H^+ \qquad (3)$$

$$Al^{3+} + 3\ H_2O \Leftrightarrow Al(OH)_3 + 3H^+ \qquad (4)$$

$$Mn^{2+} + 0.25\ O_2 + 1.5\ H_2O \Leftrightarrow MnOOH + 2H^+ \qquad (5)$$

Mineral acidity typically accounts for greater than 85% of the total acidity in coal-related ARD (Hedin et al., 1994a); therefore, metal removal is an integral part of acidity neutralization in treatment systems.

Alkalinity is generated through acid neutralization reactions that occur along the ARD flow path. When proton acidity (Eqs. 1 –5) contacts carbonate-, hydroxide-, or other base-containing solids, a sequence of pH-buffering reactions occurs (Morin et al., 1988; Blowes and Ptacek, 1994), with carbonate reactions having the greatest impact:

$$CaCO_3 + 2H^+ \Leftrightarrow Ca^{2+} + H_2CO_3^* \qquad (6)$$

$$CaCO_3 + H_2CO_3^* \Leftrightarrow Ca^{2+} + 2\ HCO_3^- \qquad (7)$$

where $[H_2CO_3^*] = [CO_2\ (aq)] + [H_2CO_3]$ (Plummer et al., 1979; Stumm and Morgan, 1981). Such acid neutralization reactions can increase pH (>6.0), generate alkalinity (Eqs. 6-7), and remove ferric iron (Eq. 3). Compilation of coal-related ARD data shows that pH values commonly have a bimodal frequency distribution; most ARD waters are either distinctly low pH (2.5 to 4.0) or near-neutral (pH 6.0 to 7.0), with few having pH values between 4.0 and 6.0 (Rose and Cravotta, 1998). Low pH ARD is commonly found near the surface, contains > 1 $mg \cdot L^{-1}$ ferric iron, aluminum, or oxygen, and no alkalinity. Near-neutral ARD is commonly found in oxygen-limited systems (e.g. anoxic groundwater), where mineral acidity (Fe^{2+}, Mn^{2+}) may coexist with alkalinity. Consequently, in carbonate-bearing areas (e.g. Appalachian coal fields, USA), near-neutral (pH 6 – 7), ferrous iron-dominated ARD is common (Rose and Cravotta, 1998).

If alkalinity is greater than the acidity, then the drainage is considered “net alkaline”, whereas the opposite is true in “net acidic” ARD. Net alkaline drainage contains sufficient neutralizing potential, generally as bicarbonate ion (HCO_3^-), to effectively buffer pH during proton acidity generation as mineral acidity is realized through the oxidation and/or hydrolysis of dissolved constituents (Eqs. 2-5). Net acidic drainage lacks adequate buffering capacity to neutralize the entire complement of protons produced by the oxidation and hydrolysis of dissolved metals.

Passive treatment of net alkaline drainage requires only oxygen and time for redox and precipitation reactions to produce metal-oxyhydroxides, and a quiescent pool or pond to settle and collect the fine product (e.g., Hedin et al., 1994a; Watzlaf et al., 2000). Traditionally, these requirements have been successfully met using aerobic wetlands. Aerobic wetlands are constructed as shallow depressions containing composted organic-rich substrates and emergent vegetation (Skousen et al., 1998). These systems are designed to aerate mine waters flowing among the vegetation, thereby promoting metal removal via Eqs. 2-5.

Net alkaline ARD generally has sufficiently low metal loads to make small CTWs an economically feasible remediation technology. Net acidic ARD, however, has inherently higher metal loads and lacks adequate buffering capacity, so enormous tracts of land and long residence times are required for these aerobic systems to be effective. To reduce the residence time and size of CTW systems for net acidic ARD, a mechanism for passive alkalinity generation must be incorporated into CTW design. Passive alkalinity addition generally requires an anaerobic environment and is commonly accomplished by directing ARD through an alkalinity-generating material. Calcitic limestone ($CaCO_3$) is by far the most common alkalinity-generating material used in passive treatment[2]; however when it comes in contact with oxidized ARD (i.e., Fe^{3+} > 1mg·L^{-1}), metal oxyhydroxides tend to precipitate on the limestone surface, effectively reducing the neutralization capacity of the limestone (e.g., Wentzler and Aplan, 1972; Hedin et al., 1994a; Watzlaf and Hyman, 1995). Commonly referred to as "armoring", this process limits the diffusion of Ca^{2+} from and H^+ to the limestone surface (Rose, 1999). In addition to iron oxyhydroxide coatings, calcium sulfate (i.e., gypsum) and aluminum oxyhydroxide films have also been observed armoring limestone (Barton and Vatanatham, 1976; Booth et al., 1997; Rose, 1999). Therefore, limestone alone is not economically effective for treatment of ARD containing ferric iron, aluminum, and/or oxygen (Hedin et al., 1994a; Ziemkiewicz et al., 1997; Sterner et al., 1998). As a result, net acidic ARD is commonly divided into two categories based on the presence or absence of these constituents for the purpose of selecting the appropriate passive treatment system. Type I net acidic ARD has little or no alkalinity (pH<4.0), contains > 1 mg·L^{-1} of ferric iron, aluminum, or oxygen, and therefore cannot be treated directly with limestone in traditional passive systems (Skousen et al., 1998). Type II net acidic ARD contains some alkalinity (pH>6.0) and < 1 mg·L^{-1} of ferric iron, aluminum, or oxygen and can be treated directly with limestone. However, without treatment, upon oxidation, the pH of this water drops dramatically and becomes Type I ARD (Skousen et al., 1998) through conversion of mineral acidity to proton acidity (Eqs. 2-5)

---

[2] There is sufficient evidence that biological reactions alone can neutralize ARD and passive treatment systems have been designed solely around biological alkalinity generation using organic matter as the "alkalinity-generating material" (Wildeman et al., 1993; Gusek, 1998). However, biological alkalinity generation is beyond the scope of this paper and will be discussed only as it affects limestone dissolution.

Turner and McCoy (1990) first described the use of buried limestone beds to intercept and treat Type II net acidic ARD in the subsurface. Since then thousands of "anoxic limestone drains" (ALD) have been constructed to add alkalinity to Type II ARD, potentially converting it to net alkaline drainage. Anoxic limestone drains function by raising the pH and adding bicarbonate alkalinity through limestone dissolution (Eqs. 6-7) under conditions where armoring cannot occur. Anoxia limits the oxidation and hydrolysis of metals (e.g., Fe^{2+}, Mn^{2+}), allowing them to pass through ALDs unchanged. However, Hedin et al. (1994b) demonstrated that proton acidity (i.e., pH) contributes < 1 $mg \cdot L^{-1}$ $CaCO_3$ equivalents to the total acidity in Type II ARD. Therefore, by allowing the mineral acidity to pass completely through the ALD, very little acid neutralization actually occurs within the drain. The neutralization of mineral acidity, and hence the removal of metals, is achieved downstream in an aerobic wetland system through *ex situ* mineral precipitation buffered by alkalinity generated in the ALD. Moreover, if the mineral acidity component of the ARD is greater than the alkalinity generated in the ALD, then upon oxidation the effluent will be converted to Type I net acidic ARD.

The generation of alkalinity in an ALD is limited by the solubility of calcite (Hedin and Watzlaf, 1994; Hedin et al., 1994b). Because the influent pH is relatively high, the principle bicarbonate-producing process in ALDs is the reaction of calcite with $H_2CO_3^*$ (Eq. 7; Hedin et al., 1994b). Hence, the presence of high P_{CO2} in the influent ARD will enhance alkalinity generating potential by increasing the equilibrium concentrations of dissolved carbonate ($[HCO_3^-] + 2[CO_3^{2-}]$; Hem, 1992) and by increasing the rate of calcite dissolution (Plummer et al., 1979). Although high P_{CO2} increases the equilibrium concentration of carbonate, even under very high P_{CO2}, the amount of alkalinity that develop in ALDs rarely exceeds 350 mg·L^{-1} $CaCO_3$ equivalents (Hedin et al., 1994b; Watzlaf and Hyman, 1995; Watzlaf et al., 2000). Measured effluent alkalinities generally range between 150 and 300 mg·L^{-1} $CaCO_3$ equivalents depending on ARD P_{CO2} (Hedin et al., 1994b; Watzlaf et al., 2000). Therefore, in instances where ARD mineral acidity exceeds effluent alkalinity, additional treatment will be required.

In an effort to overcome the constraints imposed by oxygen, ferric iron, and aluminum on direct treatment of Type I ARD with limestone, reducing and alkalinity producing systems (RAPS) were developed over the past ten years (e.g., Wildeman et al., 1993; Kepler and McCleary, 1994; Watzlaf, 1997; Watzlaf et al., 2000). Rooted in ALD technology, RAPS are designed with an organic layer (usually compost) overlying a limestone drain. These systems are designed so that both layers remain submerged and anoxic, while ARD flows vertically through the organic layer and out the limestone drain (Kepler and McCleary, 1994; Watzlaf, 1997; Skousen et al., 1998; Zipper and Jage, 2001). The principle behind the RAPS design is to convert Type I ARD to Type II by pretreatment in the organic layer before the ARD reaches the limestone drain (Kepler and McCleary, 1994; Watzlaf et al., 2000). This pretreatment is accomplished by the high biological oxygen demand (BOD) and low reduction potential (Eh) of the organic layer, which removes dissolved oxygen and promotes the reduction of ferric iron to ferrous iron (Watzlaf and Hyman, 1995); ideally alkalinity is then added through limestone dissolution in the drain (Eqs. 6-7). However, by converting Type I to Type II ARD, mineral acidity is allowed to pass through the RAPS unreacted. As with an ALD, RAPS are not designed for metal retention; metal removal is dependent on *ex situ* mineral precipitation in an aerobic wetland. Consequently, the same limitations of alkalinity generation observed in ALDs apply to RAPS. Watzlaf et al. (2000) found that RAPS can generate from approximately 100 $mg \cdot L^{-1}$ up to almost 450 $mg \cdot L^{-1}$ $CaCO_3$ equivalents total alkalinity, where total alkalinity includes the influent (mainly proton) acidity neutralized and the measured effluent alkalinity. The slightly higher amount of alkalinity generated in RAPS compared to ALDs can be attributed to the slightly larger proportion of proton acidity in Type I ARD and internal removal of minor mineral acidity (e.g., Rose, 1999).

Although in theory RAPS remove dissolved oxygen and reduce ferric iron, a survey of the literature indicates that, for most RAPS studied, the amount of ferric iron in the influent is apparently minor compared to the ferrous component. Several RAPS studies have documented that when minor influent ferric iron is present, it is precipitated as iron oxyhydroxide in the organic layer rather than being converted to ferrous iron and passing unreacted. Moreover, the precipitation of iron oxyhydroxide in the organic layer did not have a discernible negative effect on alkalinity production (Dietz and Stidinger, 1996; Watzlaf, 1997; Nairn et al., 2000). The benefit of ferric iron (and aluminum) precipitation in the organic substrate is that mineral acidity is converted to proton acidity (Eq. 3 - 4), which can be neutralized directly with limestone. If the ARD is highly mineralized, this precipitation can buffer the pH at acidic conditions (i.e. < 4.0). Because limestone dissolution rate and pH are closely related (Plummer et al., 1978), converting mineral acidity to proton acidity will not only increase the amount of total alkalinity generated but it may also increase the rate at which it is generated (i.e., by keeping the pH low; Sterner et al., 1998). However, there are few studies of RAPS receiving low pH, ferric iron-dominated ARD.

Watzlaf (1997) reported the results of a column experiment designed to simulate RAPS receiving low pH, ferric iron-dominated ARD, but the ARD was not highly mineralized, containing only 10 mg·L^{-1} ferric iron and 18 mg·L^{-1} aluminum. He showed that complete neutralization of the influent ARD occurred above a sharp, dynamic reaction front in the organic layer with the bulk of the alkalinity generation occurring at or below the reaction front. The pH increased (3.1 to 7.0) and the dissolved iron and aluminum decreased (to < 1 mg·L^{-1}) sharply across the reaction front (Watzlaf, 1997). Aluminum precipitates were found concentrated in a narrow zone demarcating the reaction front (Watzlaf, 1997). Over time, the reaction boundary migrated through the organic material in the direction of flow as the neutralizing capacity of the organic layer was consumed. The aluminum-rich zone moved with the reaction front, successively precipitating and dissolving with the changing pH conditions. While Watzlaf (1997) found that mineral acidity was converted to proton acidity in the organic substrate, he also noted that the limestone drain did not contribute significant alkalinity, rather all of the influent acidity was neutralized by the buffering capacity of the organic substrate.

In RAPS construction, spent mushroom compost, which contains horse manure (56% by weight), hay (22%), straw (10%), chicken manure (10%), and gypsum (2%), is the organic material of choice (Watzlaf et al., 2000), but it possesses <10 % $CaCO_3$ equivalents by weight neutralizing potential (NP; Watzlaf, 1997). Several researchers (Dvorak et al., 1992; Hedin et al., 1994a; Hellier, 1996; Watzlaf, 1997) suggest the incorporation of additional limestone in the organic layer may bolster the NP of the organic substrate in RAPS, while others (e.g., Skousen et al., 1998; Zipper and Jage, 2001) recommend against mixing organic-layer materials with limestone, due to the potential for metal oxyhydroxide floc precipitation within the small pores of the compost layer. However, the addition of limestone to the organic layer of RAPS has never been fully tested.

One of the main objectives of this paper, therefore, is to investigate alkalinity generation in a RAPS-type passive system containing a limestone amended organic substrate and receiving low-pH (<3.0) ARD that is ferric iron-dominated ($Fe^{3+} \gg Fe^{2+}$) and highly mineralized. By amending the organic substrate with limestone, the pH in the organic substrate can be quickly raised to circumneutral values (> 6.0). At circumneutral pH, dissolved ferric iron (and aluminum) is highly insoluble ($<1\ mg \cdot L^{-1}$) and will precipitate as hydroxy-minerals (Eq. 3 - 4), converting mineral acidity to proton acidity. Therefore, we hypothesize that by converting mineral acidity to proton acidity in a limestone buffered organic substrate (LBOS), the total alkalinity generated may grossly exceed previously reported maximum values for limestone-based passive systems.

Traditionally, passive systems are not designed so that ferric iron and aluminum precipitate in the presence of limestone due to the potential for armoring of the limestone. Therefore, a second goal of this study is to determine the degree of limestone armoring within the LBOS and to determine whether armoring presents any long-term limitations to treating ferric iron-dominated ARD.

2. Materials and Methods

2.1. Experimental system

Eight plastic tanks (92 cm diameter by 122 cm tall) were used to simulate replicate RAPS-type passive treatment systems. Each tank was filled with 92 cm of organic material (described below) overlying 15 cm of coarse (i.e. ~1.3 cm) calcitic limestone (Fig. 2.1a).

2.2. Limestone buffered organic substrate (LBOS)

The organic material used in the experimental system was a mixture of composted stable waste (96%), spent brewing grains (4%), and Kriket Krap® (composted cricket manure, <1%) (Table 2.1). The stable waste was composed mainly of wood shavings with minor amounts of straw and horse manure; it was collected from a refuse pile that was 3 to 5 years old. Components of the organic material were mixed with fine-grained limestone “screenings” at a ratio of 1 to 3 (organic material to limestone) by volume. The limestone screenings were 91.5% by weight $CaCO_3$ (as reported by the quarry) with a nominal grain size of 1.2 mm; greater than 80% of the screenings were between 0.6 and 4.8 mm (Table 2.1). The screenings were Santee Limestone, quarried from the Martin Marietta Berkeley pit in the Coastal Plain of South Carolina (79°41’21” W, 33°11’34” N). This middle Eocene-aged unit is a soft limestone deposit consisting of alternating beds of friable and more indurated layers (Banks, 1977). Most of the screenings material was taken from the more friable sections (Frank Manos, Martin Marietta, pers. comm., 2002); this material was composed mainly of poorly-cemented bioclastic material.

The organic material and limestone were combined in small batches with a cement mixer. The cement mixer provided thorough mixing and homogenization of the limestone throughout the substrate. The mixture is referred to as a limestone-buffered organic substrate (LBOS; Table 2.1).

2.3. Influent ARD

The ARD used in this experiment was drawn from a coal pile retention basin (CPRB) that collects runoff from a nearby coal storage pile at the Department of Energy (DOE) Savannah River Site (SRS), near Aiken, S.C., USA. Published data from the CPRB show that the ARD source was consistently oxic (i.e., near oxygen saturation; Millings, 1999), ferric iron-dominated (>95% ferric iron; Anderson et al., 1991), and low pH (<3.0; Anderson, 1990) over time. Moreover, data collected weekly for nine months prior to the initiation of the experiment (March 1998 – December, 1998) showed that the ARD source had a consistently low pH (2.1 – 2.8) and was highly mineralized (40 $mg \cdot L^{-1}$ aluminum and 72 $mg \cdot L^{-1}$ iron, average; Thomas, unpublished data).

The ARD was delivered continuously to the top of each tank from December 1998 to December 2000 using a single pump and a distribution manifold under constant positive pressure (20 psi). Influent flow rate on each individual tank was controlled manually with a precision needle valve attached to the distribution manifold. A flow rate of ~50 $mL \cdot min^{-1}$ was targeted for each tank. Once the ARD was delivered to the top of the tanks, flow through the LBOS was driven by gravity. The effluent drained from the bottom of the tanks through standpipes such that a 15-cm column of ARD was maintained over the LBOS at all times. To minimize the effects of evaporation and dilution by rain, a cover was placed on the top of each tank.

2.4. Water Sampling

Although ARD flow was initiated in December 1998, the effluent sampling was not started until April 1999 for logistical reasons. Tank influent and effluent were sampled weekly from April 1999 to December 2000. A single ARD sample was taken directly from the distribution manifold for the measurement of influent water chemistry. Tank effluent was sampled from a valve installed on the effluent pipe of each tank at ground level (Fig. 2.1a). A second valve downflow from the effluent sampling port was closed prior to sampling to avoid back-flow and contamination from oxygenated water in the standpipe. Influent and effluent samples were analyzed for temperature, pH, and major dissolved metal (Al, Fe, Ca) and sulfate content. Acidity and ferrous iron content were also measured on influent samples, whereas alkalinity and dissolved sulfide content were measured on the effluent samples.

Pore water samples were collected using a vacuum-operated pore-water extractor (i.e. swamper; Winger and Lasier, 1991). Swampers were constructed from 6.4 mm diameter stainless steel (SS) pipe fitted with a metal fritt (30 or 60 µm pore size) welded at one end (see Fig. 2.2). Teflon tubing, inserted inside the SS pipe, extended from the fritt to the open end and was locked into place with a compression fitting. The Teflon tubing was connected to a vacuum flask through a rubber stopper. To collect a pore water sample, the fritt-end of the swamper was inserted into the LBOS to a specified depth, measured from the end of the fritt, and fluid was withdrawn by applying a vacuum to the flask. Swamper samples were taken June 2000 from two tanks (30A and 36A). Three different areas, approximately 120° apart, were sampled in each tank (e.g., tank 30A-1, 30A-2, and 30A-3). Pore water was drawn at three different depth horizons below the substrate-water interface (2-, 11-, and 19-cm deep; Fig. 2.1b). Approximately 100 mL of pore water was recovered at each horizon. In addition, a single sample of the ARD water column overlying the LBOS was taken with a syringe. The pore water was analyzed for temperature, pH, alkalinity, dissolved metal content (Al, Fe, Ca), and sulfide.

2.5. Water flow and analysis

Flow through each tank was measured at the effluent standpipe using a graduated cylinder and a stopwatch. Temperature and pH were measured in the field using a portable meter with a combination temperature-pH electrode (Orion model 250A meter, Orion Corporation) calibrated with pH 2 and 7 standard buffer solutions. Water samples for dissolved sulfate, sulfide, and metal analyses were filtered (0.45 μm). Samples for dissolved metal analysis were preserved with ultrapure concentrated nitric acid to a final concentration of 1% HNO_3. Preserved samples for dissolved metals were analyzed within three months of collection by inductively coupled plasma mass spectrometry (ICP-MS, Elan 6000, Perkin-Elmer Corporation, Norwalk, CT) using the QA/QC protocols outlined in EPA method 200.8. During analysis, the ICP-MS collected three readings for each sample to determine instrument precision. The internal relative standard deviation of these readings was generally < 3%. Samples were diluted appropriately and calibrated to certified standards at various concentrations (EPA 200.8). In addition, certified standards from a different source were inserted between blocks of 10 samples as calibration checks. If both bounding checks were within 10% of the known value, samples values were accepted as accurate.

Unfiltered samples were collected for acidity (≥60 mL) and alkalinity (30 mL) in polyethylene bottles that were filled to the top and sealed with minimal headspace. Acidity (APHA method 2310, hot peroxide, pH = 8.3 endpoint) and alkalinity (APHA method 2320, pH = 4.3 endpoint) were measured by titration using standardized reagents (APHA, 1998). Alkalinity was measured within six hours of sample collection. Over the course of the study, replicates were within 1.5% of one another on average. Acidity was generally measured within three months of sampling, however values were reproducible within 10% up to a year after sample collection. Replicates were within 5%. No difference was noted between acidity and alkalinity measurements made on filtered and unfiltered samples.

Acidity measurements were not conducted on the effluent or swamper water samples. Instead, acidity was calculated based on the theoretical contribution of cation concentrations in the ARD. Using pH, the concentration of ferric iron, ferrous iron, aluminum, manganese, and zinc in mgL^{-1}, and previously published conversion factors (Hyman and Watzlaf, 1995), acidity was calculated as follows:

$$10^{-pH}\cdot 50{,}045 + [Fe^{3+}]\cdot 2.69 + [Fe^{2+}]\cdot 1.79 + [Al^{3+}]\cdot 5.56 + [Mn^{2+}]\cdot 1.82 + [Zn^{2+}]\cdot 1.54$$

To validate the calculations, measured values of influent acidity were compared to calculated values and found to be within 10%.

Samples collected for ferrous iron determination were filtered (0.1 μm), acidified with 6 N trace metal grade hydrochloric acid to a final concentration of 1% HCl, and stored in brown amber bottles at 4°C (To et al., 1999). Analysis was conducted within three months of sampling. Ferrous and total iron concentrations were measured using a colorimetric FerroZine technique (To et al., 1999). Ferric iron was determined by difference. Further details are presented in chapter 3.

Samples for dissolved sulfide were filtered (0.45 μm) and analyzed in the field using a CHEMetrics™ sulfide test kit. The sulfide test kit employed a self-filling reaction ampoule and methylene blue indicator, where sulfide reacts with dimethyl-p-phenylenediamine in the presence of ferric chloride to produce methylene blue. The blue color of the ampoule was compared to standards. Accuracy was estimated as one-half of the range between two bracketing standards.

Samples for dissolved sulfate were filtered (0.22 μm) into a glass vial containing silver phosphate (~50 mg) such that no headspace remained. This prevented the exsolution and oxidation of dissolved sulfide, while dissolved silver phosphate reacted to remove the sulfide as silver sulfide. Dissolved sulfate was determined by filtering the silver phosphate and sulfide solids and then analyzing the filtrate by a standard gravimetric method using a BaCl reagent (APHA, 1998).

2.6. Substrate Sampling and Analysis

Samples of the initial substrate were collected, one from each tank, at different depths as the tanks were initially filled with LBOS (n=8). Each sample was air-dried, homogenized, and stored for later analysis. Samples of the initial LOBS were treated according to the methodologies outlined below for core samples to provide baseline data on the initial solid phase.

Substrate cores (5 cm diameter) were taken from the upper 20 – 25 cm of the LBOS from two tanks (30A and 36A) in June 2000 and November 2000, just prior to the end of the project. In each tank, three areas, 120° apart, were sampled in duplicate, followed by a similar sampling strategy approximately 60° away from the first event approximately six months later. For the June 2000 sampling, the core tubes were inserted into the LBOS and swamper samples were extracted from the area around the core tube before the cores were removed from the substrate.

Cores were extruded in an anaerobic glove bag (96:4 N_2:H_2), cut in half lengthwise, and divided into three sections based on distinct color zonations (see Chapter 3). Representative sections from one half of the core were oriented in plastic cups and dried in the anaerobic glove bag, while representative samples from the other half of the core were sealed separately in air-tight polyethylene bottles under nitrogen, and frozen for later analysis. Once the oriented samples were dried, they were impregnated with epoxy for electron microprobe analysis following methods described elsewhere (see Chapter 3). Dried initial substrate was also impregnated and prepared for electron microprobe to establish textures and elemental associations specific to the starting material. Epoxy-impregnated samples were examined with an electron microprobe using back-scatter electron (BSE) imaging (JOEL, Nortrace Corporation) as described in Chapter 3. Frozen samples from the other half of the core were thawed under nitrogen and homogenized with a small rubber policeman. Splits of each color zone were air-dried for several days and then ground to a fine powder with a cryogenic grinder. Samples of the initial substrate were also cryogenically ground. The dried, ground samples were digested for total calcium content using a block digestor according to EPA method 3050B for the acid digestion of sediments, sludges, and soils (for details, see Chapter 4). Total calcium was analyzed by inductively coupled plasma optical emission spectrometry (ICP-OES, Elan 4300DV, Perkin-Elmer Corporation, Norwalk, CT) following the methodology presented in Chapter 4. Instrument precision was generally < 2% and accuracy was within 10% based on second source calibration checks.

At the completion of the experiment, five 2.5-cm diameter cores were taken from the top 15 cm of the LBOS from each tank for neutralization potential (NP) analysis (40 cores total). In addition, splits from the glass cores taken in November 2000 (n=6), plus splits from an additional five glass cores taken for another study (Thomas, unpublished) were also analyzed for NP. The cores were divided into three sections based on color as described above. Each section was lyophilized and ground with a cryogenic grinder to a fine powder. Fifty-one samples of the uppermost color zonation were analyzed, while 13 samples were selected randomly from each of the other two color sections for NP determination.

The NP method of Sobek et al. (1978) was used in this study. Dried samples (1 – 2 g) were digested in 50 mL of 0.5 N hydrochloric acid. The solution was then titrated with 0.5 N NaOH to pH 7.0 using a calibrated combination temperature-pH electrode and meter to determine the neutralizing content (NP) of the sample. Substrate NP was reported as calcium carbonate equivalents as follows:

$$\% \ \mathrm{CaCO_3} = \left\{ \frac{(\text{meq HCl added} - \text{meq NaOH used in titration}) * 0.05 \ \mathrm{g \cdot meq^{-1}} \ \mathrm{CaCO_3}}{\text{dry sample weight (grams)}} \right\} *100 \qquad (8)$$

3. Results

3.1. Flow

Maintaining the targeted 50 $\mathrm{mL \cdot min^{-1}}$ flow rate of the ARD with the manifold-needle valve delivery system proved to be difficult. Occasional pump failure and ruptured pipe in the manifold (mainly due to freezing temperatures in January 2000) temporarily interrupted flow to the tanks, while sedimentation in the manifold reduced ARD delivery in some instances. Initial attempts to adjust the valves often resulted in ephemeral spikes or sharp decreases in flow. Consequently, from September 1999 until the end of the project, weekly adjustments were made only when the measured flow of the respective effluent was above 100 $\mathrm{mL \cdot min^{-1}}$ or below 5 $\mathrm{mL \cdot min^{-1}}$. Flows of over 100 $\mathrm{mL \cdot min^{-1}}$ were rarely encountered. The flow of all eight tanks is plotted as a weekly average in Fig. 2.3.

Average flow rate over the two years of the study for all eight tanks was 20 $\mathrm{mL \cdot min^{-1}}$ and ranged between 16 and 28 $\mathrm{mL \cdot min^{-1}}$ for any individual tank average. Zero flows were recorded at least once for every tank due to ARD delivery failure. Small, random flow peaks occurred in all tanks from week to week, but the fluctuations were not synchronous among tanks indicating they were due to changes in flow paths within the LBOS of individual tanks. Additionally, the height of the ARD water column overlying the substrate remained fairly constant over time, indicating the permeability of the LBOS was not noticeably comprised over the course of the experiment. Maximum recorded flow rate for an individual tank ranged from 72 to 380 $mL\cdot min^{-1}$.

3.2. Influent Water Chemistry

A single sample of the ARD, taken from the distribution manifold, was used as the influent for all eight tanks. Influent ARD was low pH (<3.0) and dominated by sulfate and ferric iron. Between April 1999 and December 2000, the influent ARD ranged from a pH of 1.6 to 3.0 (average = 2.4), acidity from 738 to 2320 (average = 1304) $mg\cdot L^{-1}$ as $CaCO_3$ equivalents, total iron from 92 to 237 (average = 142) $mg\cdot L^{-1}$, aluminum from 39 to 274 (average = 84) $mg\cdot L^{-1}$, and sulfate from 926 to 3385 (average = 1521) $mg\cdot L^{-1}$ as primary constituents (Fig. 2.4). Influent calcium was also relatively low (range 23 - 114; average = 52 $mg\cdot L^{-1}$). Ferric iron comprised from 95 to 100% of the total iron (99% average), after removing two ephemeral spikes of ferrous iron (up to 40% ferrous iron) that were observed following rain events, one lasting less than a week, while the other lasted two weeks.

3.3. Effluent Water Chemistry

The LBOS consistently produced circumneutral pH water (average = 6.4; range 5.5 – 7.1; Fig. 2.4), and the effluent was always alkaline (alkalinity average = 619; range observed in all eight tanks = 280 – 1575 mg·L^{-1} as $CaCO_3$ equivalents). The average effluent alkalinity varied sporadically during the first year of the study with a wide range of values measured between tanks (Fig. 2.4). The average stabilized in February 2000 with much less variation between tanks and some indication of seasonal variation during the second year as concentration peaked in the beginning of August 2000 and gradually declined thereafter. The average calculated effluent acidity concentration was approximately 35 mg·L^{-1} as $CaCO_3$ equivalents with a total range of average values from 4 – 100 mg·L^{-1}. Thus, on average, greater than 97% of the influent acidity was neutralized in the LBOS.

Dissolved iron in the effluent averaged 15 mg·L^{-1} (range = 0 – 123 mg·L^{-1}) and showed an approximate ten-fold decrease from the average influent concentration, while the effluent aluminum concentration averaged 0.05 mg·L^{-1} (range = 0 – 9.3 mg·L^{-1}). The drop in dissolved aluminum concentration between the influent and effluent was three orders of magnitude. However, for the majority of the effluent samples, aluminum concentration was below the detection limit (BDL) of the ICP-MS (approximately 0.03 mg·L^{-1} for aluminum). In the case where aluminum concentrations were below the ICP-MS detection limits, an operationally-defined value, equal to the lower detection limit, was entered for the purpose of calculating effluent averages.

Effluent calcium averaged 600 $mg\cdot L^{-1}$ and exhibited an order of magnitude increase from influent concentrations (range = 268 – 1003 $mg\cdot L^{-1}$). Sulfate in effluent averaged 1201 $mg\cdot L^{-1}$ (range = 263 – 2732 $mg\cdot L^{-1}$) and removal was 320 $mg\cdot L^{-1}$ or about 20% of the ARD influent. However, removal was seasonal with most of the sulfate removed in the months following April 2000. Dividing the data seasonally around April showed that only 10% of the influent sulfate was removed prior to April (i.e., in the winter), while 30% of the influent sulfate was reduced in the summer months (i.e., post April 2000). Average sulfide concentrations in the effluent ranged from 0.7 to 16 $mg\cdot L^{-1}$. Dissolved sulfide displayed a seasonal variation with near zero values during the winter and up to 50 $mg\cdot L^{-1}$ measured during the summer.

3.4. Swamper Data

3.4.1. pH. The pH of the ARD water column overlying the LBOS was similar to the influent measured at the manifold within tanks 30A and 36A (Fig. 2.5a). Pore water extracted at 2 cm had a narrow range in pH (2.8 – 3.3) that was slightly higher than the influent. In contrast, pore water extracted at 11 and 19 cm yielded a broader range in pH (6.8 – 7.6) that was higher than the effluent.

3.4.2. Alkalinity. Swamper pore water samples showed that the influent and pore water at 2 cm did not contain any alkalinity, while at 11 and 19 cm depth, values were relatively high (556 – 1100 $mg\cdot L^{-1}$ $CaCO_3$ equivalents; Fig. 2.5b). Effluent values were slightly lower (690 – 740 $mg\cdot L^{-1}$ $CaCO_3$ equivalents). Although acidity was not measured in the swamper samples, values were calculated. Calculated acidity values were used to determine the net alkalinity at each depth (Fig. 2.5c). Because the alkalinity was zero at 2 cm depth and a large amount of acidity was calculated, net alkalinity is negative (i.e., acidic). At the 2 cm sampling depth, net alkalinity decreased with increasing pH (-963 mg·L^{-1} $CaCO_3$ equivalents at pH 2.8 and -1810 mg·L^{-1} $CaCO_3$ equivalents at pH 3.3), indicating the mineral acidity component was increasing with increasing pH at 2 cm depth. There was only minor acidity calculated for samples below 11 cm and therefore the net alkalinity values are indistinguishable from the measured values.

3.4.3. Iron and aluminum. While the influent ARD was dominantly ferric iron, there was a minor ferrous iron component; however, it was lower than the effluent ferrous iron concentration, indicating that at least some ferrous iron was generated in the LBOS. Therefore, pore water data for iron are presented as the ferrous and ferric components and not as total iron (Fig. 2.5d,e).

The ferric iron concentration in the influent ARD, measured at the manifold, was 224 mg·L^{-1} the day before swamper sampling (Fig. 2.5d). Analysis of the ARD water column overlying the LBOS showed that ~50 – 60% of the influent dissolved ferric iron (114 and 127 mg·L^{-1}, tanks 30A and 36A, respectively) was removed either in the distribution manifold or within the ARD water column. Pore water extracted at 2 cm with the swamper exhibited changes in the dissolved ferric iron concentrations that were strongly pH dependent. Pore water extracted at 2 cm at a pH of 2.8 contained 57 mg·L^{-1} ferric iron, which represented a 50% decrease relative to overlying ARD water column. In contrast, pore water from the same depth at a pH 3.3, contained 27 mg·L^{-1} ferric iron, which represented a 79% decrease relative to overlying ARD water column. Pore water extracted at 11 and 19 cm with the swamper showed that ferric iron was completely removed at pH ≥ 6.8, consistent with the effluent data.

There was no ferrous iron detected in the influent ARD, measured at the manifold, the day before swamper sampling (Fig. 2.5e). Analysis of the ARD water column overlying the LBOS showed small amounts of ferrous iron in both tanks. Similar to ferric iron, pore water extracted at 2 cm exhibited changes in dissolved ferrous iron concentrations that were strongly pH dependent. Pore water extracted at 2 cm at a pH of 2.8 contained 38 $mg \cdot L^{-1}$ ferrous iron. In contrast, pore water from the same depth at a pH 3.3, contained 291 $mg \cdot L^{-1}$ ferrous iron. At 11 cm, most of the pore water samples contained ferrous iron concentrations lower (≤ 6.5 $mg \cdot L^{-1}$) than the final effluent concentration (i.e., 38 – 41 $mg \cdot L^{-1}$) with the exception of a single outlier. At 19 cm, the measured pore water ferrous iron concentrations were all lower than the final effluent (i.e., < 29 $mg \cdot L^{-1}$).

The dissolved aluminum concentration in the influent ARD, measured at the manifold, was slightly lower (72 $mg \cdot L^{-1}$) than the ARD water column overlying the LBOS (100 and 140 $mg \cdot L^{-1}$ for tanks 30A and 36A, respectively; Fig. 2.5f). Swamper pore water samples, extracted at 2 cm depth, exhibited an increase in dissolved aluminum relative to the overlying ARD that was pH dependent. At pH 2.8, the aluminum concentration was only slightly higher than the overlying ARD water column (i.e., 116 $mg \cdot L^{-1}$), but it increased with increasing pH and was approximately 1.5 times greater than the overlying ARD at pH 3.3 (i.e., 211 $mg \cdot L^{-1}$). Similar to the final effluent, the swamper pore water collected at 11 cm and 19 cm (pH > 6.8) contained aluminum concentrations below the ICP-MS detection limit.

3.4.4. Calcium. The dissolved calcium concentration in the influent ARD, measured at the manifold (50 mg·L^{-1}), was similar to slightly lower than water overlying the LBOS (62 – 90 mg·L^{-1}; Fig. 2.5g). Swamper pore water samples, extracted at 2 cm depth, exhibited an increase in dissolved calcium concentration, but with a wide range of values (222 – 405 mg·L^{-1}) that was pH dependent. Calcium concentration was lower in samples at a pH of 2.8 and higher in samples at a pH of 3.3. Swamper samples extracted at 11 and 19 cm contained a wide range of calcium concentrations that were more than 10 times higher than the influent concentration, but generally less than the final effluent concentration (~830 mg·L^{-1}).

3.5. Substrate cores

Cores taken from the LBOS showed three distinct color zones (Fig. 2.6). While Chapter 3 characterized these three zones based on the mineralogy of secondary precipitates, this chapter focuses on the limestone content of the zones. The first 7 to 10-cm of the LBOS, which contained orange iron oxyhydroxides, was termed the oxide zone. Below the oxide zone was a thin (2 – 5 cm) friable hardpan of white secondary aluminum and calcium hydroxysulfate with minor iron oxyhydroxide in the upper portions and iron sulfide in the lower half. Based on the presence of both iron oxyhydroxides and sulfides, this zone was called the transitional zone. Underlying the transitional zone was a black sulfide zone, characterized by ubiquitous iron sulfides and the general lack of aluminum hydroxysulfate.

3.6. Electron Microprobe Analysis

Back-scatter electron (BSE) imaging and semi-quantitative energy dispersive spectroscopy (EDS) analyses were conducted on core and initial substrate material to determine the character of LBOS over the course of the experiment. The photomicrographs presented are limited to textures related to limestone dissolution. A more detailed analysis of the secondary precipitates may be found elsewhere (Chapter 3).

3.6.1. Initial substrate. The LBOS contained a soft, friable fossiliferous-limestone with lesser amounts of more indurated, micritic-limestone and organic matter composed largely of wood chips with lesser amounts of straw, manure, and quartz-rich detritus (Fig. 2.7a-c). Back-scatter electron imaging showed that the organic fragments were commonly associated with fine-grained limestone (Fig. 2.7a). Pyrite was found associated with both the limestone (Fig. 2.7b) and the organic matter, but, in general, it was rare (see Chapter 3).

3.6.2. Oxide zone. No limestone or other calcium-bearing minerals, were detected in any of the samples from the oxide zone. The upper half of the oxide zone contained only three components: organic fragments (largely wood), iron precipitates (mainly goethite and ferrihydrite), and quartz (Fig. 2.7d; see Chapter 3). The iron oxyhydroxides displayed textures indicative of rapid precipitation (for details see Chapter 3) and were commonly found nucleating from surfaces in the LBOS (e.g. organic matter). In several instances, bands of iron oxyhydroxide were found surrounding open space (e.g. dotted lines Fig. 2.7d,e), indicating a former nucleation surface had been removed. These iron oxyhydroxide replacement textures were restricted to the upper half of the oxide zone.

While absent from the very upper portions of the oxide layer, aluminum precipitates (amorphous hydroxysulfate) occurred with increasingly greater frequency towards the bottom of the oxide layer. The aluminum precipitates were frequently found outlining the shape of relict grains dissolved from the LBOS (Fig. 2.7f; see Chapter 3).

3.6.3. Transitional zone. In handsample, the transitional zone appeared as white, friable hardpan cementing organic fragments together. Back-scatter electron images coupled with EDS analysis indicated that the boundary between the oxide and transitional zones was characterized by a rapid shift from iron- to aluminum-dominated coatings and textures. Electron microprobe analyses showed that the transitional zone was not mineralogically complex, containing only calcite (i.e., limestone), quartz, gypsum, pyrite, and aluminum hydroxysulfate, in addition to the organic material. The mineralogy was confirmed by x-ray diffraction (XRD) analysis (Chapter 3). Back-scatter electron imaging showed there was no limestone present in the upper half of the transitional zone. Abundant relict grains outlined by aluminum hydroxysulfate were typical in the upper portions of the transitional zone (Fig. 2.7g). With depth, gypsum (Fig. 2.7h) and remnant limestone (Fig. 2.7i) occupied the outlined grains with increasing abundance. Midway through the transitional zone, remnant limestone was universal in the relict grains. Overall, the limestone content of the transitional zone gradually increased with depth. In addition to forming coatings around limestone, aluminum hydroxysulfate precipitated within intergranular primary porosity and occasionally cemented organic fragments.

Gypsum was generally not found in the lower half of the transitional zone and the abundance of aluminum-sulfate precipitates decreased with depth.

3.6.4. Sulfide zone. The sulfide zone was characterized by a lack of gypsum, a sharp decrease in the amount of aluminum-sulfate precipitates, pristine limestone, and an abundance of iron sulfides (Fig. 2.7j-k). Limestone in the sulfide zone was pristine and indistinguishable from the limestone in the original substrate (Fig. 2.7j-k).

3.7. Geochemical analysis of the three reaction zones

One of the main goals of this study was to test the effect of adding limestone to the organic layer of a RAPS passive treatment unit. There are two geochemical approaches to determining the amount of limestone utilization in the LBOS: comparing the calcium concentration in the three reaction zones to the initial concentration and comparing the neutralization potential of the three zones to the initial value. Both methods can be used to independently determine the amount of calcium carbonate remaining in the three reaction zones, assuming that most of the calcium and the neutralization potential in the three reaction zones is attributed to limestone.

3.7.1. Total calcium. Total digests of the initial substrate showed that the starting calcium concentrations averaged 217 $g{\cdot}kg^{-1}$ with a fairly narrow range (202 – 233 $g{\cdot}kg^{-1}$; Fig. 2.8). Digests of the oxide zone samples collected in June 2000 indicated that the average calcium concentration was 20 $g{\cdot}kg^{-1}$ (range = 1.5 – 59 $g{\cdot}kg^{-1}$) and all but two samples were <6.5 $g{\cdot}kg^{-1}$; these values were approximately an order of magnitude lower than the average initial substrate. The average total calcium concentration was lower in

November 2000 at 4.5 $g \cdot kg^{-1}$ (range = 0.8 – 15 $g \cdot kg^{-1}$), with only one sample having a value >4 $g \cdot kg^{-1}$ (Fig. 2.8).

Calcium in samples of the transitional zone from June 2000 cores averaged 201 $g \cdot kg^{-1}$ (range = 150 – 250 $g \cdot kg^{-1}$) and this was similar to the calcium concentration of the initial substrate (Fig. 2.8). Samples collected in November 2000 averaged 122 $g \cdot kg^{-1}$ (range = 76 – 155 $g \cdot kg^{-1}$) and showed an approximate 40% reduction concentration over time. All samples were below the initial substrate concentration range.

Total calcium concentration in digests of sulfide zone samples collected in June 2000 averaged 232 $g \cdot kg^{-1}$ (range = 214 – 248 $g \cdot kg^{-1}$), which was slightly higher than the initial LBOS (Fig. 2.8). The digests of November 2000 samples were even higher having an average value of 238 $g \cdot kg^{-1}$ (range = 232 – 244 $g \cdot kg^{-1}$), with the entire range being greater than the highest initial calcium concentration.

3.7.2. Neutralization potential. The average neutralization potential of the initial substrate was 54.3% (48 – 60% range) as $CaCO_3$. Assuming that all of the neutralization potential comes from limestone, the NP can be converted to an equivalent calcium concentration ($g \cdot kg^{-1}$) using a conversion factor (4.004) based on the molar ratio of calcium in calcium carbonate. Thus, based on the initial NP, the starting calcium concentration was identical to the values derived from the total digest (217 $g \cdot kg^{-1}$). On average, samples from the oxide zone exhibited a greater than 85% reduction in NP (7.4 % as $CaCO_3$ or 30 $g \cdot kg^{-1}$ as calcium) compared to the initial average NP; however, the range in oxide zone NP values was fairly wide (0 – 44% as $CaCO_3$). Samples from the transitional zone also showed a slight reduction in the average NP value relative to the initial substrate (35.1% as $CaCO_3$ or 140 $g \cdot kg^{-1}$ as calcium) with a range that fell between the oxide zone and initial NP values (11 – 58% as $CaCO_3$). The sulfide zone NP values were fairly similar to the initial substrate (49% as $CaCO_3$ average or 196 $g \cdot kg^{-1}$ as calcium) with a little more than half of the values equivalent to the initial NP (37 – 62% as $CaCO_3$ range).

4. Discussion

The limestone-buffered organic substrate (LBOS) was capable of generating effluent alkalinity (619 $mg \cdot L^{-1}$ $CaCO_3$ equivalents average) that was almost double the highest alkalinity concentrations reported for ALDs (350 $mg \cdot L^{-1}$ $CaCO_3$ equivalents; Watzlaf et al., 2000). In fact, alkalinity concentrations of less than 300 $mg \cdot L^{-1}$ $CaCO_3$ equivalents were rarely recorded and single measurements > 1500 $mg \cdot L^{-1}$ $CaCO_3$ equivalents were recorded several times from individual tanks. Furthermore, on top of the average 619 $mg \cdot L^{-1}$ $CaCO_3$ equivalents alkalinity measured in the effluent, an additional amount of alkalinity was generated to neutralize >97% of the influent acidity (i.e., ~1300 $mg \cdot L^{-1}$ $CaCO_3$ equivalents). Accordingly, the total net alkalinity generated in the LBOS, which equals the amount of acidity neutralized plus the measured effluent alkalinity, averaged 1832 $mg \cdot L^{-1}$ $CaCO_3$ equivalents with values greater than ~3000 $mg \cdot L^{-1}$ $CaCO_3$ equivalents being recorded in single sampling events. Moreover, the minimum net alkalinity generated in a single sampling event was >1000 $mg \cdot L^{-1}$ $CaCO_3$ equivalents, which is more than twice the maximum net alkalinity afforded by a RAPS (i.e., 450 $mg \cdot L^{-1}$ $CaCO_3$ equivalents; Watzlaf et al., 2000).

4.1. Source of Alkalinity

Although RAPS-type passive systems are designed to generate alkalinity via limestone dissolution (LSD), numerous studies have demonstrated that a significant portion of the effluent alkalinity may be generated through the biological oxidation of organic matter (BOOM) by microorganisms living in the RAPS organic layer (Wildemann et al., 1993; Watzlaf et al., 2000). Of the microbial processes that could contribute to alkalinity, bacterial sulfate reduction is by far the most significant within RAPS (Wildeman et al., 1993; Gusek, 1998).

Several researchers have attempted to quantify the source of alkalinity (LSD or BOOM) based on the removal of sulfate from the influent ARD and the increase in calcium in the effluent (e.g., Watzlaf, 1997, Nairn et al., 2000). Assuming all of the sulfate removal is due to bacterial sulfate reduction, a 1 mg·L^{-1} decrease in sulfate stoichiometrically yields 1.042 mg·L^{-1} of alkalinity as $CaCO_3$ (Watzlaf, 1997). Likewise, assuming all of the increase in calcium is due to limestone dissolution, a 1 mg·L^{-1} increase in calcium stoichiometrically yields 2.497 mg·L^{-1} of alkalinity as $CaCO_3$ (Watzlaf, 1997). Adding these two calculated values should, in theory, equal the total net alkalinity generated in LBOS.

In Fig. 2.9, the calculated net alkalinity due to limestone dissolution (LSD) and sulfate reduction (BOOM) is compared to the measured net alkalinity (-acidity + alkalinity) over time. The actual values and the calculated sum are similar (within 10%) and therefore, the calculations should give a fair representation of the source of alkalinity generated in the LBOS, assuming significant amounts of calcium and sulfate are not lost by other mechanisms. Overall, calculations indicated approximately 77% of the alkalinity generated in the LBOS was attributed to limestone dissolution, but the range in values was wide (50 – 100%). Considering the data seasonally, approximately 90% of the alkalinity can be attributed to limestone dissolution in the colder months with a fairly narrow range (76 – 100%), whereas the amount of limestone attributed alkalinity dropped to 70% in the summer months with a much wider range (50 – 98%). Even in the summer months, when the calculated alkalinity due to limestone dissolution was lowest, the amount of alkalinity attributed to increases in calcium was rarely <1000 $mg \cdot L^{-1}$ CaCO3 equivalents on any individual tank, which is more than twice the amount found in typical limestone-based passive treatment systems.

4.2. Location of limestone dissolution

Swamper pore water data showed that the bulk of acidity neutralization occurred within a fairly narrow depth range between 2 and 11 cm; pH increased from <3.3 to 7.4 and mineral acidity (ferric iron, ferrous iron, and aluminum) dropped from influent to effluent concentrations. The substrate cores extracted from the upper 30 cm of the LBOS captured the transition from the orange color of the oxide zone to the black color of the sulfide zone. The lack of limestone in the oxide zone and the pristine nature of the limestone in the sulfide zone indicated that limestone dissolution occurred along the contact between the two zones. Thus, the transitional zone, which contained partially dissolved limestone, was the site of most of the limestone dissolution within the substrate.

Total calcium content of the three reaction zones further demonstrates that limestone dissolution occurred in the fairly thin transitional zone. The transitional zone was depleted in total calcium over time. Moreover, total digests of the oxide zone showed that limestone dissolution was complete by the end of the experiment. Although electron microprobe analysis shows that limestone below the dissolution front was similar in appearance to the initial LBOS, total calcium from the sulfide zone shows a slight accumulation of secondary calcium over time. Neither gypsum nor secondary calcium carbonate was observed in the sulfide zone, and therefore, the nature of calcium increase remains unresolved.

Using a computer program developed by Romanek (1991) and water chemistry from the LBOS, the calcite saturation index ($SI_{calcite}$) and P_{CO2} were calculated. Influent ARD was highly undersaturated with respect to calcite averaging log $SI_{calcite} = -5.8 \pm 0.3$ (Fig. 2.10a). Likewise, the calculated $SI_{calcite}$ from swamper data of the oxide zone indicated the pore water remained highly undersaturated (log $SI_{calcite} = -4.9$; Fig. 2.10b). Below the limestone dissolution front at 11 cm, pore water was supersaturated (log $SI_{calcite} > 0.9$), such that precipitation of calcite was possible (Fig. 2.10b). Moreover, pH and alkalinity at this depth were higher than final effluent values. However, by the effluent, $SI_{calcite}$ was no longer supersaturated (log $SI_{calcite} = -0.2$) and dissolved calcium concentrations had increased indicating further limestone dissolution between 11 cm and the effluent. In fact, the effluent was consistently close to calcite saturation but only periodically supersaturated (log $SI_{calcite} = -0.1 \pm 0.4$; Fig. 2.10a).

The higher-than-effluent pH and alkalinity coupled with the calculated calcite supersaturation observed below the dissolution front was most likely attributed to the degassing of undissociated dissolved CO_2. During swamper sampling, a profusion of bubbles was often observed emanating from the top of the LBOS upon insertion of the swamper probe. Similarly, if the tank was disturbed by kicking the side, abundant gas bubbled from the LBOS. Analysis of trapped gas from the LBOS by gas chromatography indicates that it was largely CO_2 (Thomas, unpublished data). Furthermore, calculations indicated the final effluent had a higher P_{CO2} (log P_{CO2} = -0.06) compared the swamper pore water collected below 11 cm (log P_{CO2} = -1.3), further supporting the idea that undissociated CO_2 was escaping from the substrate at shallow depths (Fig. 2.10c). The lower pH and alkalinity observed in the effluent data was likely due to the fact that CO_2 could not escape the LBOS at depth and was trapped. The trapped CO_2 (i.e., increase in P_{CO2}) led to further limestone dissolution, the net result of which lowered alkalinity and pH, while increasing the effluent calcium concentration.

4.3. Rate of limestone dissolution in LBOS compared to other limestone-based systems

While the calculations indicate that limestone dissolution occurred between 11 cm and the effluent, this dissolution can be considered more of an adjustment, than a factor in acidity neutralization and alkalinity generation; the bulk of the limestone dissolution occurred along the reaction boundary and was driven by the neutralization of mineral acidity. In fact, calculations indicate the rate of limestone dissolution at the reaction front must have been relatively rapid to achieve supersaturation over only a few centimeters. This is in contrast to traditional limestone-based passive treatment systems.

Several researchers (Hedin et al., 1994b; Cravotta and Trahan, 1999) have observed that the calcite saturation index ($SI_{calcite}$) of fluids in limestone-based systems (i.e., ALDs and RAPS) increases asymptotically with residence time (i.e., the distance ARD has traveled through an ALD), but never reaches saturation. Although influent ARD is generally highly undersaturated with respect to calcite (Log [$SI_{calcite}$] ~ -3.0 for ALDs, Hedin et al., 1994b), the effluent remains undersaturated with respect to calcite (Log [$SI_{calcite}$] ~ -1.0; Hedin et al., 1994b; Cravotta and Trahan, 1999) even after prolonged periods of contact between ARD and limestone (Watzlaf and Hedin, 1993).

The main difference between LBOS and traditional systems is the chemistry of the ARD treated by the LBOS. Traditional systems permit mineral acidity to pass unreacted and therefore rely largely on the P_{CO2} of pore water to drive limestone dissolution at near-neutral pH (>6.0), whereas LBOS is designed to neutralize mineral acidity in the presence of limestone. The conversion of mineral acidity to proton acidity through hydrolysis and precipitation buffers the pH < 4.5 until the entire complement of acidity has been neutralized. Plummer et al. (1978) showed that for pH lower than about 5, the calcite dissolution rate is proportional to concentration of H^+, and the rate is transport controlled (i.e., the rate of H^+ diffusion to the limestone surface). The rate at pH 3 is therefore 100 times the rate at pH 5. Above pH 5, the rate is dominated by surface reaction kinetics (Chou et al., 1989). Therefore, the rate of dissolution in traditional limestone-based systems, in which limestone dissolution largely occurs at pH > 5, is slow and these systems can never reach calcite saturation within a practical time frame.

Another major difference between traditional limestone-based systems and the LBOS is the size of the limestone employed. Most limestone-based systems are constructed with limestone ranging in size from 3.2 to 7.6 cm (or bigger) in an effort to optimize dissolution without compromising permeability (Rose, 1999; Watzlaf et al., 2000; Skousen pers. comm., 2001). In contrast, the LBOS was constructed with sand-size limestone screenings (1.2 mm). Although it is well understood that grain size affects the dissolution rate (e.g., Barton and Vatanatham, 1976), no systematic studies have been conducted on the effect of the different limestone sizes used in limestone drains. In addition to the small size, the fossiliferous (i.e., porous) nature of the Santee Limestone may predispose it to a faster rate of dissolution compared to limestone obtained from more indurated limestone quarries (e.g., Paleozoic-aged limestone of the central Appalachian region); however this remains to be tested.

4.4. Armoring and plugging concerns.

The trade-off in having mineral acidity neutralized within the LBOS is that the precipitates may inhibit the long-term effectiveness of the system. Two of the biggest concerns are armoring with subsequent passivation of limestone surfaces and reduced permeability due to plugging. Dissolved ferric iron and aluminum are traditionally the main limitation to using limestone for passive ARD treatment. Armoring by ferric iron may rapidly passivate the limestone surface, rendering it ineffective. However, electron microprobe data coupled with total calcium analyses indicated that the limestone was completely removed from the oxide zone above the limestone dissolution front.

Moreover, the relict grains outlined by iron oxyhydroxide in the upper oxide zone and by aluminum hydroxysulfate in the lower oxide zone and upper transitional zone were most likely limestone grains that were completely dissolved. These relict limestone grains demonstrate that armoring by ferric iron and aluminum does occur, but that they do not result in passivation. This may be due to the fine-grain size (1.2 mm) and porous nature of the limestone screenings; however, the effectiveness of a comparable LBOS with coarser grained or more indurated limestone has yet to be tested.

The only major limitation regarding plugging is that a calcium sulfate and aluminum hydroxysulfate hardpan develops at the transitional zone (see also Chapter 3). However, over the two years of the study, LBOS did not show any signs of plugging or decrease in hydraulic connectivity, such as ponding of ARD over the LBOS. Pulses in measured flow rate did occur and may be attributed to short-term changes in the permeability of the substrate caused by dissolution and precipitation reactions that occur in the LBOS. One advantage to having fine-grained limestone evenly distributed throughout the LBOS is that, while aluminum hydroxysulfate precipitates occluded primary porosity, the reaction rims of aluminum hydroxysulfate around relict limestone grains maintained secondary porosity created by the dissolution of limestone. Furthermore, (Demchak et al., 2001) noted that wood chips, which comprise the majority of the composted stable waste used in manufacturing the LBOS, might decrease compaction and increase permeability by encouraging particle separation.

If a LBOS system is designed to last 20 years, as is the rule of thumb for ALD sizing (e.g., Skousen et al., 1998; Watzlaf et al., 2000), then plugging and hydrologic short-circuiting constitute a major concern and warrant further investigation. If the hardpan presents a long-term plugging problem, periodic maintenance will be required to disrupt the layer. Flushing has been suggested for removal of iron and aluminum oxyhydroxide floc (e.g., Zipper and Jage, 2001). However, in the LBOS, the aluminum forms hydroxysulfates that are attached to surfaces and, thus, not amenable to flushing. The iron oxyhydroxides are also not likely to flush because they form above the transitional zone. Small garden tillers have been used to mix fresh organic material into the upper portion of passive treatment bioreactors (Gusek, pers. comm., 1998) and may be used in conjunction with flushing to help maintain hydraulic conductivity within the upper portion of LBOS if this becomes a concern.

5. Conclusions

One of the main limitations to passive treatment of net acidic ARD is the ability of treatment systems (i.e., ALD, RAPS) to generate sufficient alkalinity to completely neutralize the influent acidity. While influent proton acidity is commonly neutralized within a typical limestone-based passive system, the system is generally designed to permit mineral acidity to pass through unaffected. Because <15% of the total acidity in ARD related to coal mining is attributed to proton acidity (Hedin et al., 1994a), by design, the majority of the influent acidity must be neutralized *ex situ* through oxidation and hydrolysis of ferrous iron in an aerobic wetland. Moreover, dissolution of limestone in ALDs and RAPS is slow and generally driven by pore water P_{CO2} (Hedin et al., 1994b). Thus, the total alkalinity generation of these systems is relatively low. Consequently, if influent mineral acidity is greater than the alkalinity generating capacity of the system (i.e. ~150 – 350 mg·L^{-1} $CaCO_3$ equivalents for ALDs; ~450 mg·L^{-1} $CaCO_3$ equivalents for RAPS), ARD neutralization will not be complete and further treatment is required.

Results from this study show that by treating fully oxidized (i.e. ferric » ferrous iron) ARD in a RAPS-type system amended with a limestone-buffered organic substrate (LBOS), >97% of the influent acidity can be neutralized *in situ* and an alkaline effluent maintained. Swamper pore water data and electron microprobe results demonstrated that dissolved ferric iron and aluminum were removed above the limestone dissolution front. The precipitation of iron and aluminum concomitant with limestone dissolution buffers the pore water pH (<4.5) at a level conducive for rapid limestone dissolution and subsequent alkalinity generation. Thus, the ferric iron – aluminum hydrolysis and precipitation process is one of the key mechanisms of acid neutralization in the upper LBOS, because it essentially converts all of the mineral acidity to proton acidity (e.g., Eq 3 – 4) above the reaction boundary. If the ferrous iron component of the ARD used in this study had been larger, then the level of alkalinity attained could not have been realized.

Acknowledgements

This research was funded by Financial Assistance Award Number De-FC09-96SR18546 between the United States Department of Energy and the University of Georgia as a part of the US DOE National Water Research Center. The authors would like to thank the principle investigators of this grant, Dr. Rebbecca Sharitz, Dr. J Vaun

McArthur, and Dr. Beverly Collins for their continued support and assistance. The authors would also like to acknowledge Linda Paddock, Daniel Coughlin, Matt Opdyke, and Morris Jones for their technical assistance in sample processing.

Literature Cited

American Public Health Association. (1998) *Standard Methods for the Examination of Water and Wastewater*. APHA.

Anderson M. A. (1990) A Hydrogeochemical Investigation of Metalliferous Coal Pile Runoff and Its Interaction with Soil and Groundwater. Ph.D., Virginia Polytechnic Institute and State University.

Anderson M. A., Bertsch P. M., Feldman S. B., and Zelazny L. W. (1991) Interactions of acidic metal-rich coal pile runoff with a subsoil. *Environ. Sci. Technol.* **25**(12), 2038-2046.

Banks R. S. (1977) Stratigraphy of the Eocene Santee Limestone in three quarries of the Coastal Plain of South Carolina. *South Carolina Geological Survey Geological Notes* **21**(3), 88 - 149.

Barton P. and Vatanatham T. (1976) Kinetics of limestone neutralization of acid waters. *Environ. Sci. Technol.* **10**(3), 262-266.

Blowes D. W. and Ptacek C. J. (1994) Acid-neutralization mechanisms in inactive mine tailings. In *The Environmental Geochemistry of Sulfide Mine-Wastes, Short Course Handbook*, Vol. 22 (ed. J. L. Jambor and D. W. Blowes), pp. 271 - 292. Mineralogical Association of Canada.

Booth J., Hong Q., Compton R. G., Prout K., and Payne R. M. (1997) Gypsum overgrowths passivate calcite to acid attack. *Journal of Colloid and Interface Science* **192**, 207 - 214.

Chou L., Garrels R. M., and Wollast R. (1989) Comparative study of the kinetics and mechanisms of dissolution of carbonate minerals. *Chemical Geology* **78**, 269-282.

Cravotta III C. A. and Trahan M. K. (1999) Limestone drains to increase pH and remove dissolved metals from acidic mine drainage. *Applied Geochemistry* **14**, 581 - 606.

Demchak J., Morrow T., and Skousen J. (2001) Treatment of acid mine drainage by vertical flow wetlands in Pennsylvania. *Geochemistry: Exploration, Environment, and Analysis* **1**, 71-80.

Dietz J. M. and Stidinger D. M. (1996) Acidic mine drainage abatement in an anaerobic sub-surface flow wetland environment - case history of the treatment system at Corsica, PA. *Proceedings of the 13th Annual National Meeting of the American Society of Surface Mining and Reclamation*, 531-540.

Dvorak D. H., Hedin R. S., Edenborn H. M., and McIntire P. E. (1992) Treatment of metal-contaminated water using bacterial sulfate reduction: results from pilot-scale reactors. *Biotechnol. Bioeng.* **40**, 609-616.

Eger P. (1992) The use of sulfate reduction to remove metals from acid mine drainage. *Proceedings of the 9th Annual National Meeting of the American Society of Surface Mining and Reclamation*, 563-578.

Gusek J. (1998) Three case histories of passive treatment of metal mine drainage. *Proceedings of the 19th Annual West Virginia Surface Mine Drainage Task Force Symposium*.

Hedin R. S., Nairn R. W., and Kleinmann R. L. P. (1994a) Passive treatment of coal mine drainage, pp. 35. US Dept. of Interior, Bureau of Mines.

Hedin R. S. and Watzlaf G. R. (1994) The effects of anoxic limestone drains on mine water chemistry. *Proc. Int. Land Reclamation and Mine Drainage Conference and Third Int. Conference on the Abatement of Acidic Drainage*, 185-194.

Hedin R. S., Watzlaf G. R., and Nairn R. W. (1994b) Passive treatment of acid mine drainage with limestone. *J. Environ. Qual.* **23**, 1338-1345.

Hellier W. W. (1996) The Bark Camp Run constructed wetlands: Findings and recommendations for future design criteria. *Proceedings of the 13th Annual National Meeting of the American Society of Surface Mining and Reclamation.*, 550-559.

Hem J. D. (1992) *Study and interpretation of the chemical characteristics of natural water*. U.S. Geol. Surv. Water Supply Paper 2254.

Herlihy A. T., Kaufmann P. R., Mitch M. E., and Brown D. D. (1990) Regional estimates of acid mine drainage impact on streams in the mid-Atlantic and southeastern United States. *Water Air Soil Pollution* **50**, 91 - 107.

Hyman D. M. and Watzlaf G. R. (1995) Mine Drainage Characterization for the Successful Implementation of Passive Treatment Systems. *17th Annual National Association of Abandoned Mine Lands Conference*, 170 - 185.

Kepler D. A. and McCleary E. C. (1994) Successive alkalinity-producing systems (SAPS) for the treatment of acidic mine drainage. *Proc. Int. Land Reclamation and Mine Drainage Conference and Third Int. Conference on the Abatement of Acidic Drainage*, 195-204.

Kleinmann R. L. P. (1990) Acid mine drainage in the United States. *Proceedings of the First Midwestern Region Reclamation Conference*.

Kleinmann R. L. P., Hornberger R., Leavitt B., and Hyman D. (2000) Introduction and recommendations. In *Prediction of Water Quality at Surface Coal Mines* (ed. R. L. P. Kleinmann), pp. 1-7. National Mine Land Reclamation Center.

Millings V. E. (1999) Stable isotopes as groundwater tracers at the D-Area Coal Pile Runoff Basin of the Savannah River Site, Aiken, SC. MS, University of Georgia.

Morin K. A., Cherry J. A., Dave N. K., Lim T. P., and Vivyurka A. J. (1988) Migration of acidic groundwater seepage from uranium-tailings impoundments, 1. Field study and conceptual hydrogeochemical model. *Journal of Contaminant Hydrology* **2**, 271 - 303.

Nairn R. W., Mercer M. N., and Lipe S. A. (2000) Alkalinity generation and metals retention in vertical-flow treatment wetlands. *Proceedings of the 17th Annual National Meeting of the American Society of Surface Mining and Reclamation.*, 412-420.

Phipps T. T., Fletcher J. J., Fiske W., and Skousen J. G. (1991) A methodology for evaluating the costs of alternative AMD treatment systems. *Proceedings of the 12th Annual West Virginia Surface Mine Drainage Task Force Symposium*.

Plummer L. N., Wigley T. M. L., and Parkhurst D. L. (1978) The kinetics of calcite dissolution in CO_2-water systems at 5° to 60°C and 0.0 to 1.0 ATM CO_2. *American Jounral of Science* **278**, 179-216.

Plummer L. N., Wigley T. M. L., and Parkhurst D. L. (1979) Critical review of the kinetics of calcite dissolution and precipitation. In *Chemical Modeling in Aqueous*

Systems - Speciation, Sorption, Solubility, and Kinetics, Vol. 93 (ed. E. A. Jenne), pp. 537-573. Am. Chem. Soc. Symp. Ser. 93.

Romanek C. S. (1991) Carbon isotope fractionation and precipitation kinetics of synthetic aragonite and calcite grown in dilute solutions. Dissertation, Texas A&M University.

Rose A. W. (1999) Chemistry and kinetics of calcite dissolution in passive treatment systems. *Proceedings of the 16th Annual National Meeting of the American Society of Surface Mining and Reclamation.*, 599-608.

Rose A. W. and Cravotta III C. A. (1998) Geochemistry of Coal Mine Drainage. In *Coal Mine Drainage Prediction and Pollution Prevention in Pennsylvania* (ed. K. B. C. Brady, M. W. Smith, and J. Schueck), pp. 1-1 to 1-22. The Pennsylvania Department of Environmental Protection.

Skousen J., Rose A., Geidel G., Foreman J., Evans R., and Hellier W. (1998) *A Handbook of Technologies for the Avoidance and Remediation of Acid Mine Drainage*. Acid Drainage Technology Initiative (ADTI).

Sobek A. A., Schuller W. A., Freeman J. R., and Smith R. M. (1978) Field and laboratory methods applicable to overburdens and minesoils, pp. 203. U.S. Gov. Print. Office.

Sterner P., Skousen J., and Donovan J. (1998) Geochemistry of laboratory anoxic limestone drains. *Proceedings of the 15th Annual National Meeting of the American Society of Surface Mining and Reclamation*, 214-234.

Stumm W. and Morgan J. J. (1981) *Aquatic Chemistry*. John Wiley & Sons.

Thomas R. C., Romanek C. S., Coughlin D. P., and Crow D. E. (1999) Treatment of acid mine drainage using anaerobic constructed treatment wetlands: predicting longevity with substrate neutralization potential. *Proceedings Sudbury '99 - Mining and the Environment II*, 449-458.

To T. B., Nordstrom D. K., Cunningham K. M., Ball J. W., and McCleskey R. B. (1999) New method for the direct determination of dissolved Fe(III) concentration in acid mine waters. *Environ. Sci. Technol.* **33**(5), 807-813.

Turner D. and McCoy D. (1990) Anoxic alkaline drain treatment system, a low cost acid mine drainage treatment alternative. *Proc. 1990 Nat. Symp. on Mining*, 73-75.

Watzlaf G. R. (1997) Passive treatment of acid mine drainage in down-flow limestone systems. *Proceedings of the 14th Annual National Meeting of the American Society of Surface Mining and Reclamation.*, 611-622.

Watzlaf G. R. and Hedin R. S. (1993) A method for predicting the alkalinity generated by anoxic limestone drainage. *Proceedings of the 14th Annual West Virginia Surface Mine Drainage Task Force Symposium*.

Watzlaf G. R. and Hyman D. M. (1995) Limitations of Passive Systems for the Treatment of Mine Drainage. *17th Annual Association of Abandoned Mine Lands Conference*, 186-199.

Watzlaf G. R., Schroeder K. T., and Kairies C. (2000) Long-term performance of alkalinity-producing passive systems for the treatment of mine drainage. *Proceedings of the 17th Annual National Meeting of the American Society of Surface Mining and Reclamation.*, 262 - 274.

Wentzler T. H. and Aplan F. F. (1972) Kinetics of limestone dissolution by acid waters. In *Environmental Control* (ed. C. Rampacek), pp. 513 - 523. AIME.

Wildeman T., Brodie G., and Gusek J. (1993) *Wetland Design for Mining Operations*. BiTech Publishers Ltd.

Winger P. V. and Lasier P. J. (1991) A vacuum-operated pore-water extractor for estuarine and freshwater sediments. *Arch. Environ. Contam. Toxicol.* **21**, 321-324.

Ziemkiewicz P. F., Skousen J. G., Brant D. L., Sterner P. L., and Lovett R. J. (1997) Acid mine drainage treatment with armored limestone in open limestone channels. *Journal of Environmental Quality* **26**, 1017 - 1024.

Zipper C. E. and Jage C. R. (2001) Passive treatment of acid-mine drainage with vertical-flow systems, pp. 1-16. Powell River Project/Virginia Cooperative Extension.

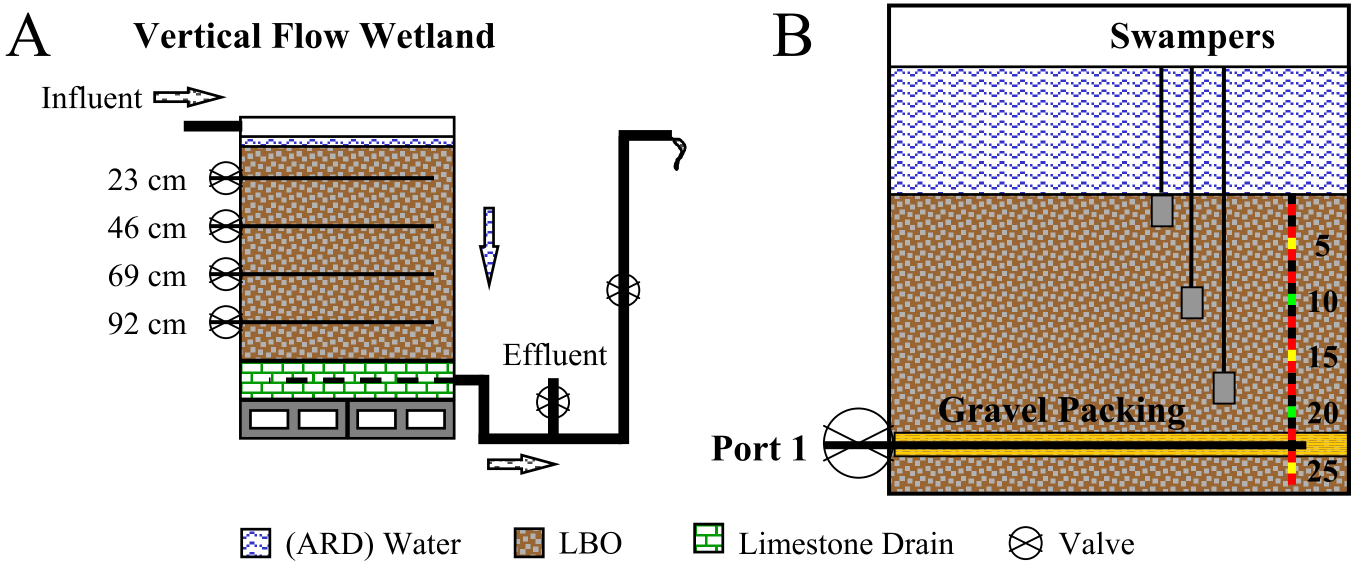

Figure 2.1. Cross section of the vertical flow wetland tank. A. Overview of the tank set up. B. Close-up of substrate above 23 cm showing the sampling depths of the swamper, the position of port one, and the gravel packing around port one. The scale to the right is in centimeters.

Table 2.1. Composition and physicochemical attributes of the limestone buffered organic substrate (LBOS).

LBOS Composition (by volume)	**Physicochemical Attributes**[†]	
	• CEC: 83.29 meq·100 gm^{-1} soil **• NP: 529 g $CaCO_3$·Kg^{-1} soil**	
• 25% Limestone Screenings • 72% Composted Stable Waste • 3% Spent Brewing Grains • <1% Kricket Krap ®	**• Paste pH 7.61** **• Density: 0.741 g·cm^{-3}**	**• Carbon 36 %** **• C:N 28.8**

all values in mg·kg^{-1}	**Fe**	**Al**	**Ca**	**Mn**	**As**	**Cr**	**Cu**	**U**	**Cd**	**Co**	**Ni**	**Zn**
LBOS Total	2805	1611	217048	135	2.5	6.7	4.5	23	0.9	0.9	93	35
Limestone Total	546	543	694339	143	6.0	7.1	1.2	2.5	0.6	2.3	18	4
Limestone Contribution [a]	289	287	367305	76	3.2	3.8	0.6	1.3	0.3	1.2	10	2
Org. Matter Contribution [b]	2516	1324	-	59	-	3.0	3.8	22	0.6	-	84	33

Limestone Screenings - Grain Size Distribution

(mm)	**9.5 - 4.8**	**4.8 - 2.4**	**2.4 - 1.2**	**1.2 - 0.6**	**0.6 - 0.3**	**0.3 - 0.15**	**0.15 - 0.07**	**< 0.07**
Percent	**2.50%**	**22.2%**	**31.5%**	**27.0%**	**13.4%**	**3.12%**	**0.32%**	**0.03%**

[†] Physicochemical attributes are from Thomas et al. (1999)

[a] Limestone contribution was determined by multiplying the limestone total metal concentration by the proportion of limestone in the LBOS (i.e., 0.529)

[b] Organic matter contribution was determined by difference. Values are not given where the metal concentration measured in the limestone was greater than the concentration measured in the final LBOS.

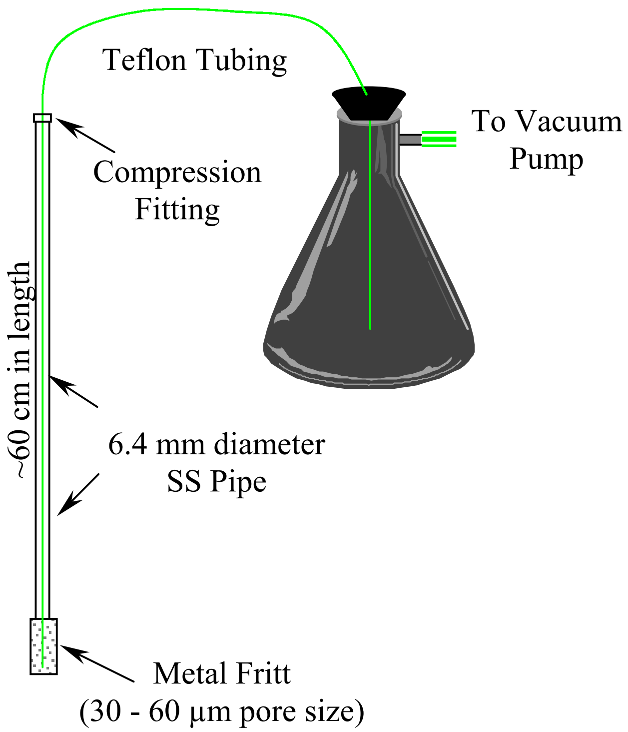

Figure 2.2. Schematic detailing the components of the swamper pore water sampler used in this study. Construction of the swamper was based on designs previously reported in the literature (e.g., Winger and Lasier, 1991). See text for details on construction and implementation.

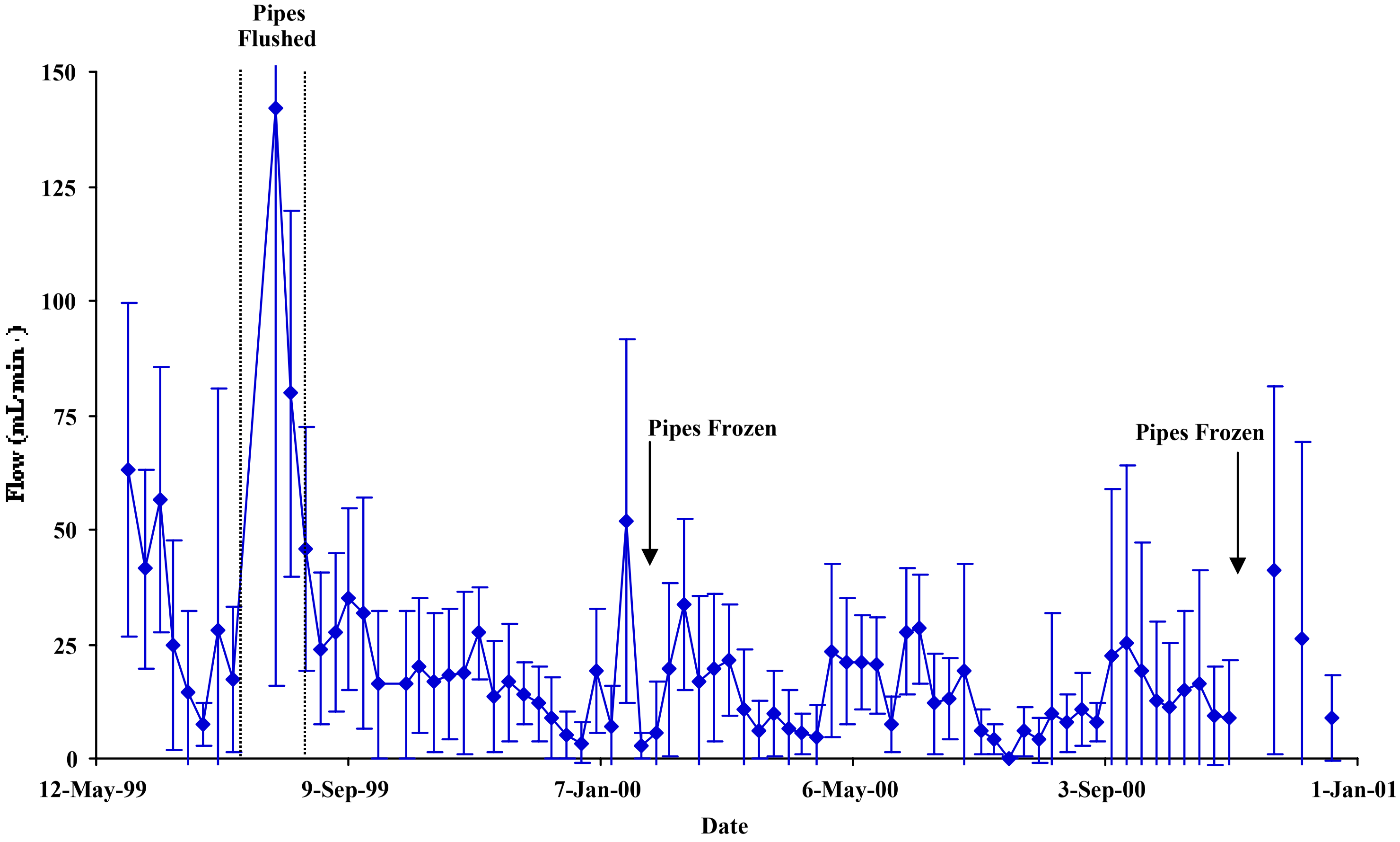

Figure 2.3. Average flow rate through the eight VFW tanks. Error bars show the standard deviation (1 σ) of the weekly tank average. In August 1999, sedimentation of the distribution manifold required the influent pipes to be flushed to maintain flow, resulting in flows >100 $mL \cdot min^{-1}$ in some tanks. Frozen pipes in January and late November 2000 resulted in zero flow for several tanks.

Figure 2.4. Influent and average effluent (n=8) water chemistry of the LBOS over the two years of the tank study. Influent values are from a single sample taken weekly from the distribution manifold. Effluent values are the average effluent concentration calculated from the eight replicate tanks. Error bars show the standard deviation (1 σ) of the weekly average. A) Acidity, alkalinity, and pH; B) influent ARD concentrations of iron, aluminum, and calcium; C) influent and effluent sulfate, and effluent sulfide; D) effluent concentrations of iron, aluminum, and calcium.

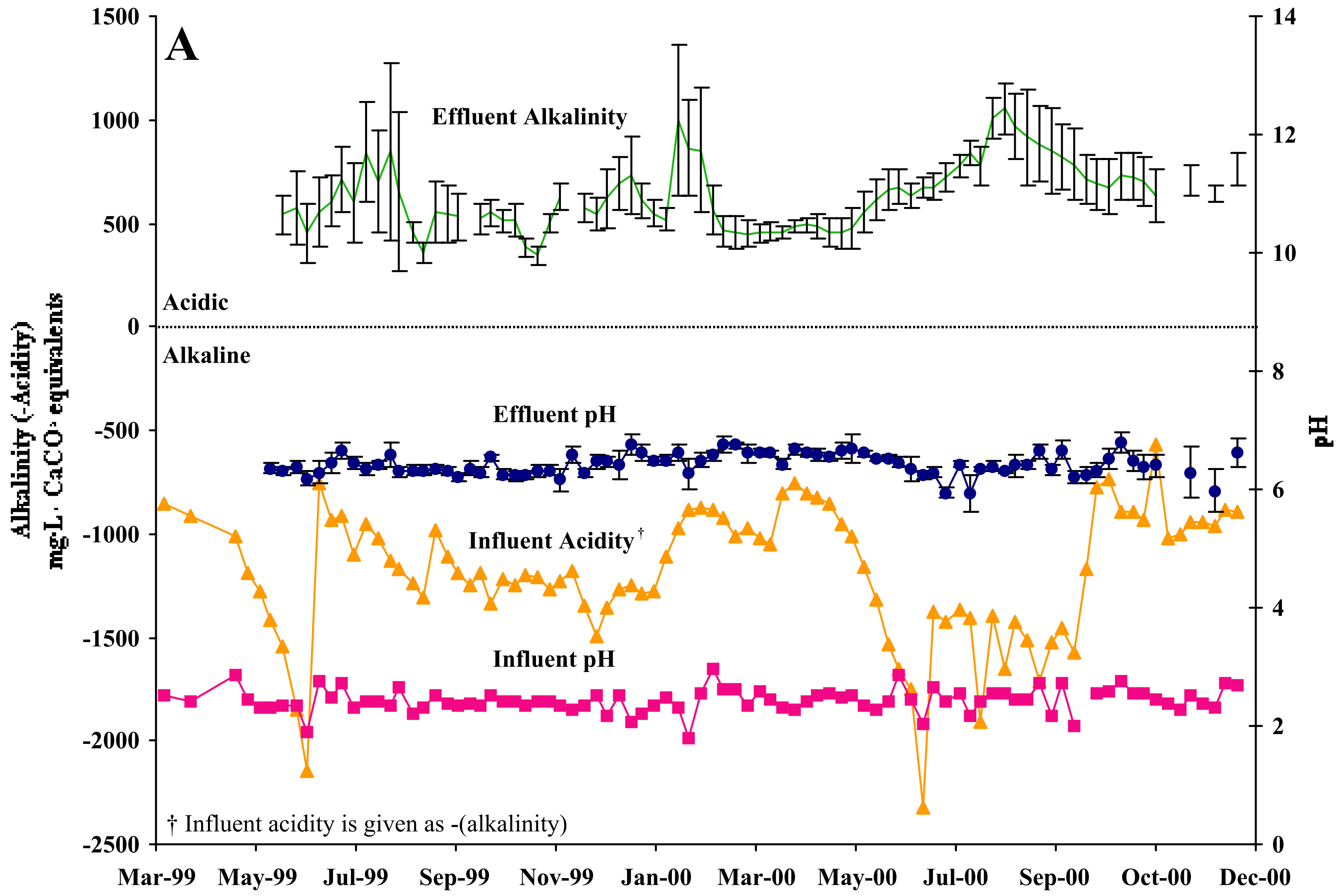

† Influent acidity is given as -(alkalinity)

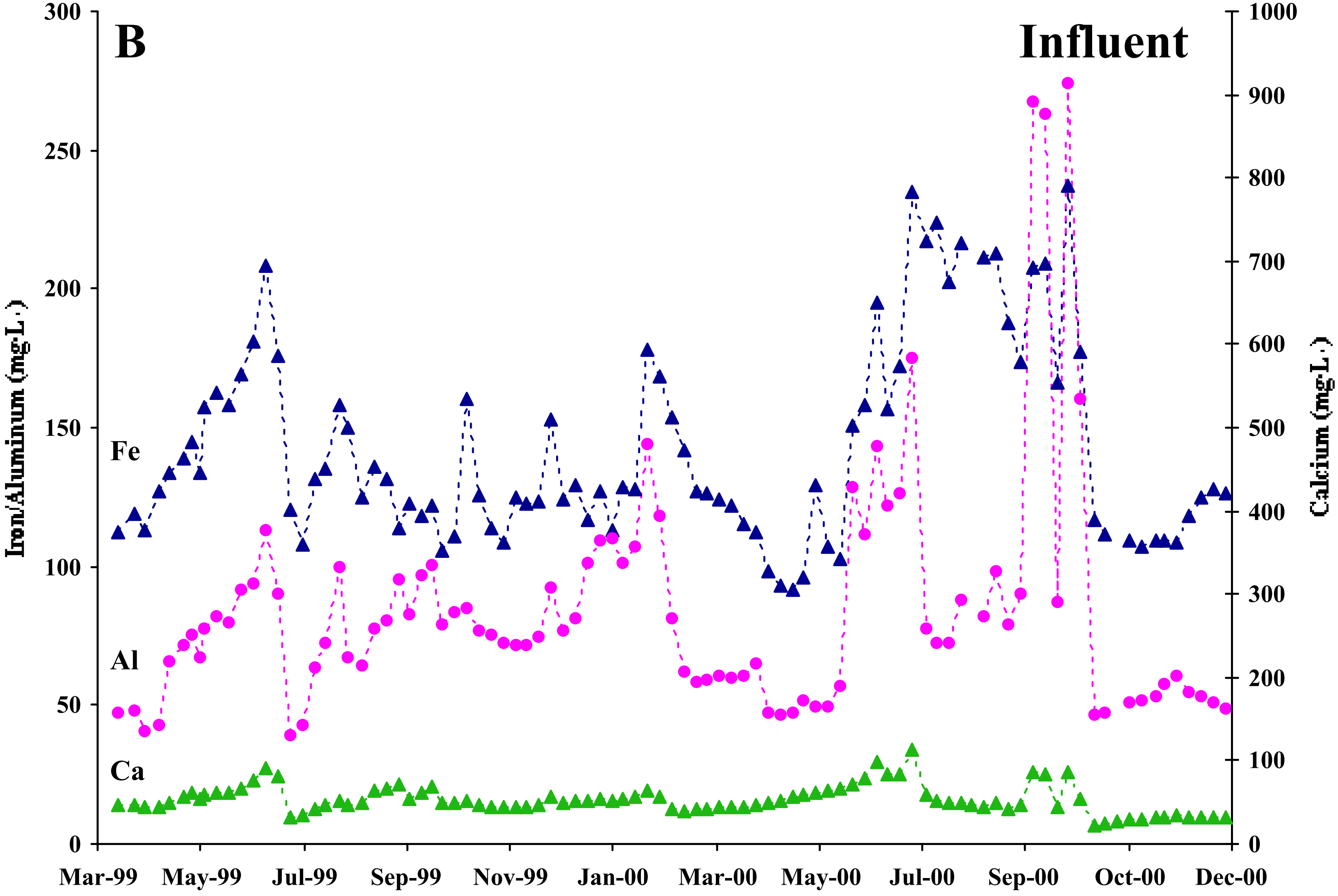
B
Influent
Fe
Al
Ca
Iron/Aluminum (mg·L·)
Calcium (mg·L·)
0
50
100
150
200
250
300
0
100
200
300
400
500
600
700
800
900
1000
Mar-99
May-99
Jul-99
Sep-99
Nov-99
Jan-00
Mar-00
May-00
Jul-00
Sep-00
Oct-00
Dec-00

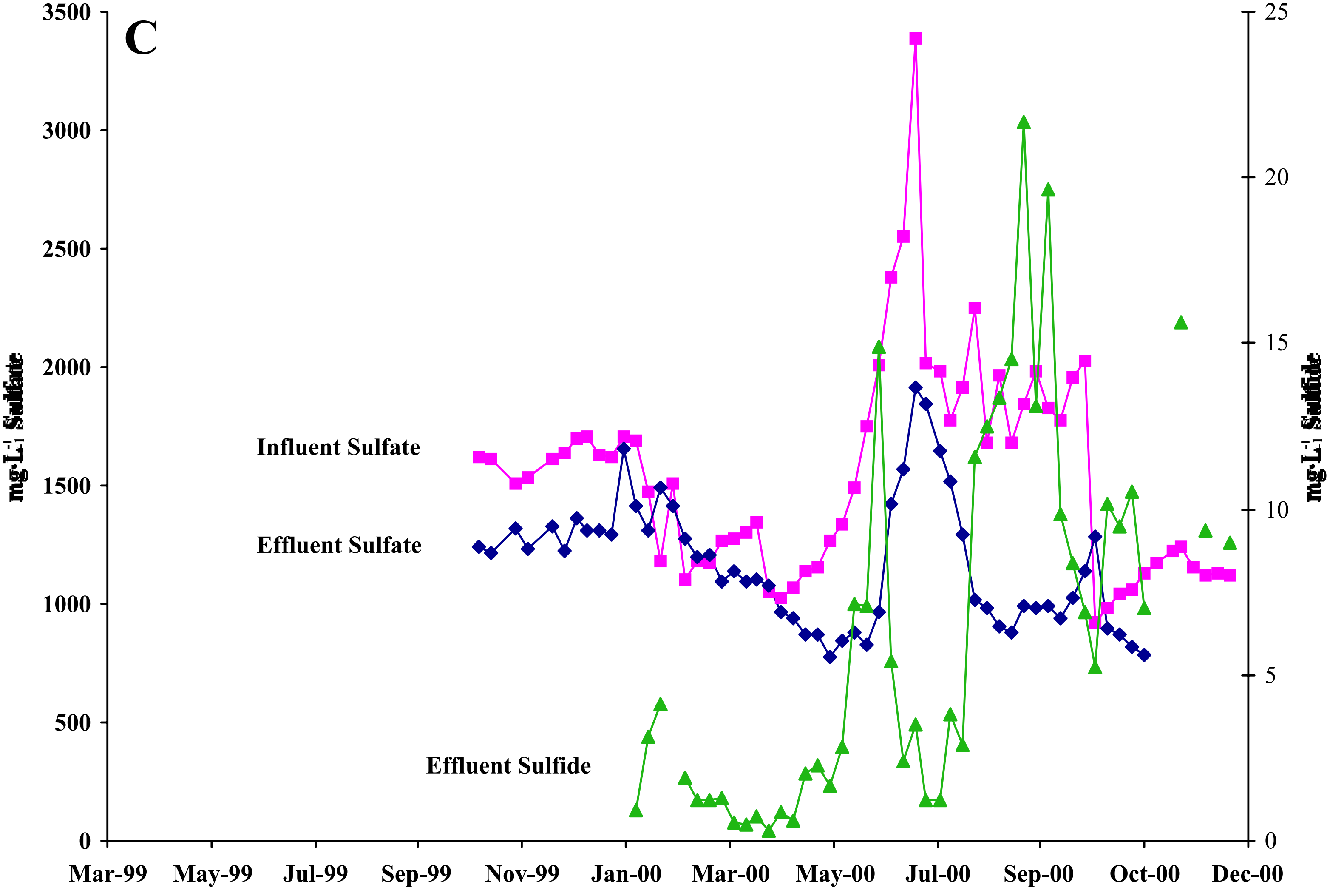C
mg·L⁻¹ Sulfate
mg·L⁻¹ Sulfide
3500
3000
2500
2000
1500
1000
500
0
25
20
15
10
5
0
Mar-99
May-99
Jul-99
Sep-99
Nov-99
Jan-00
Mar-00
May-00
Jul-00
Sep-00
Oct-00
Dec-00
Influent Sulfate
Effluent Sulfate
Effluent Sulfide

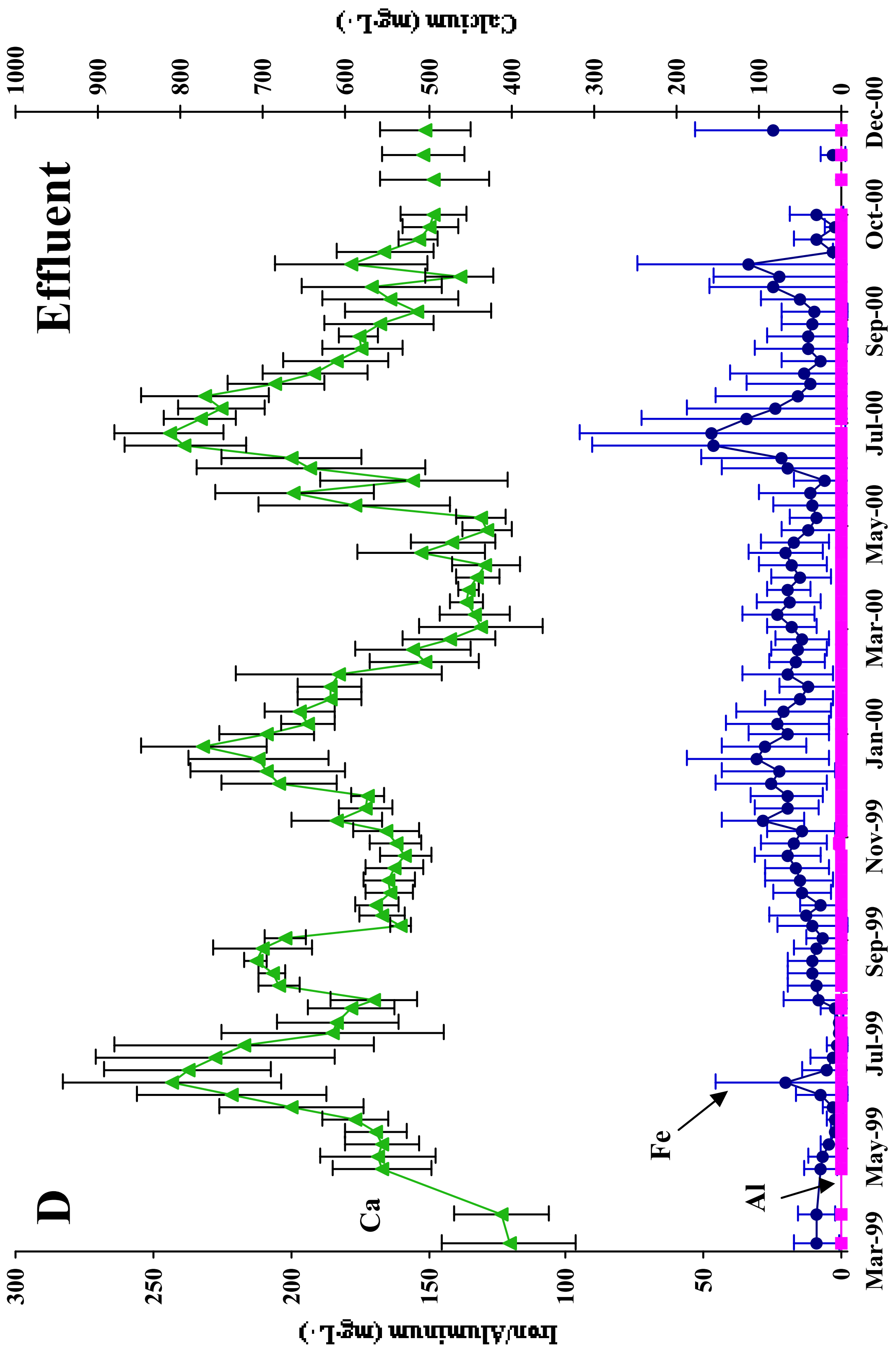
D
Effluent
Ca
Fe
Al
Iron/Aluminum (mg·L⁻¹)
0
50
100
150
200
250
300
Calcium (mg·L⁻¹)
0
100
200
300
400
500
600
700
800
900
1000
Mar-99
May-99
Jul-99
Sep-99
Nov-99
Jan-00
Mar-00
May-00
Jul-00
Sep-00
Oct-00
Dec-00

Figure 2.5. Pore water chemistry collected with the swamper sampler. The vertical axes represent sampling depth; negative values indicate the samples were collected from the ARD overlying the substrate. Values for the influent ARD collected one day prior to sampling from the distribution manifold are also given. Effluent samples from each tank, taken the day before swamper sampling are shown as well. Swamper pore water was analyzed for: A) pH, B) alkalinity ($mg \cdot L^{-1}$ $CaCO_3$ equivalents), C) net alkalinity, where net alkalinity = total alkalinity – calculated acidity, dissolved D) ferric iron, E) ferrous iron, F) aluminum, and G) calcium.

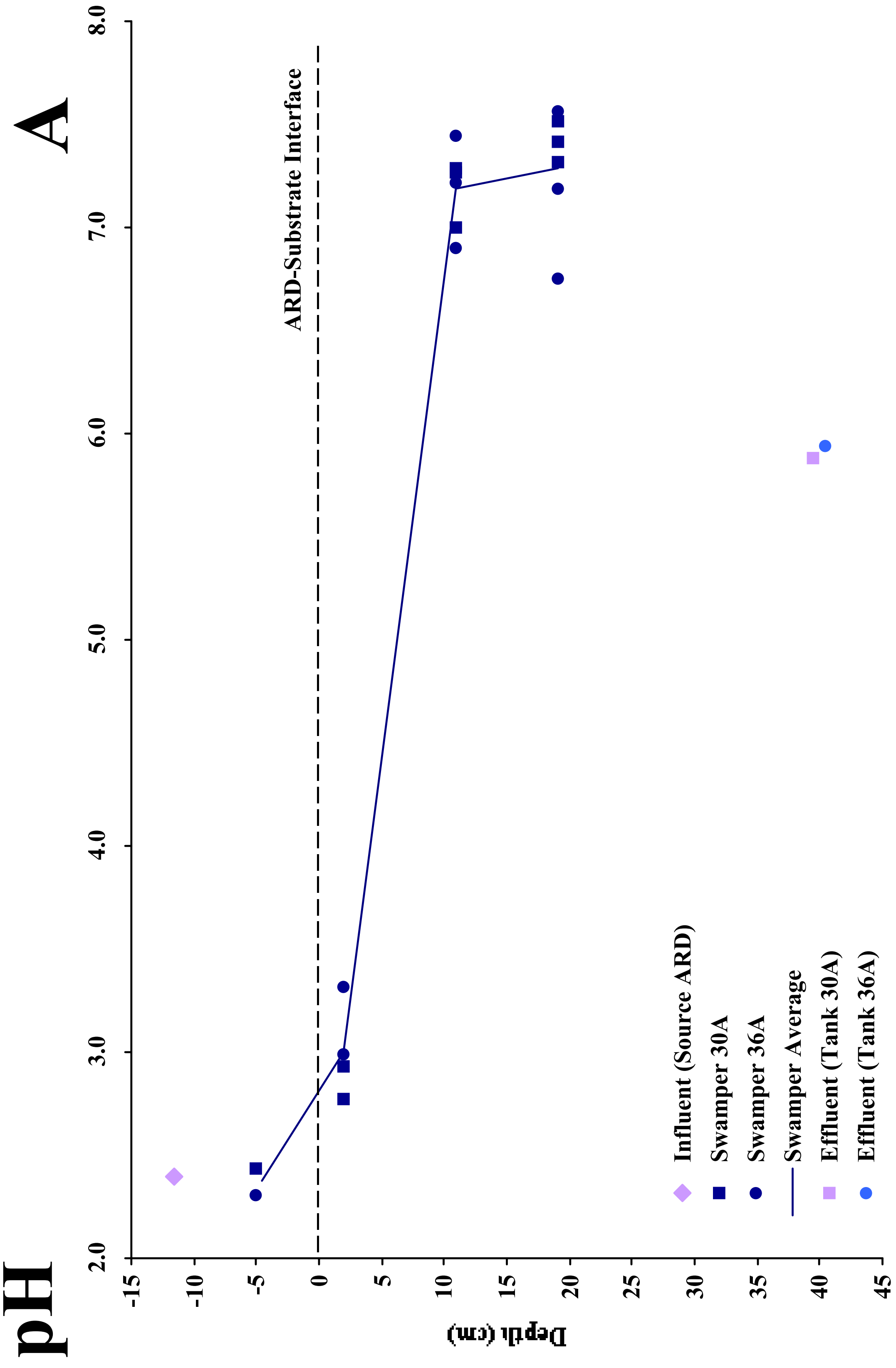
pH
A
ARD-Substrate Interface
Depth (cm)
-15
-10
-5
0
5
10
15
20
25
30
35
40
45
2.0
3.0
4.0
5.0
6.0
7.0
8.0
◆ Influent (Source ARD)
■ Swamper 30A
● Swamper 36A
Swamper Average
■ Effluent (Tank 30A)
● Effluent (Tank 36A)

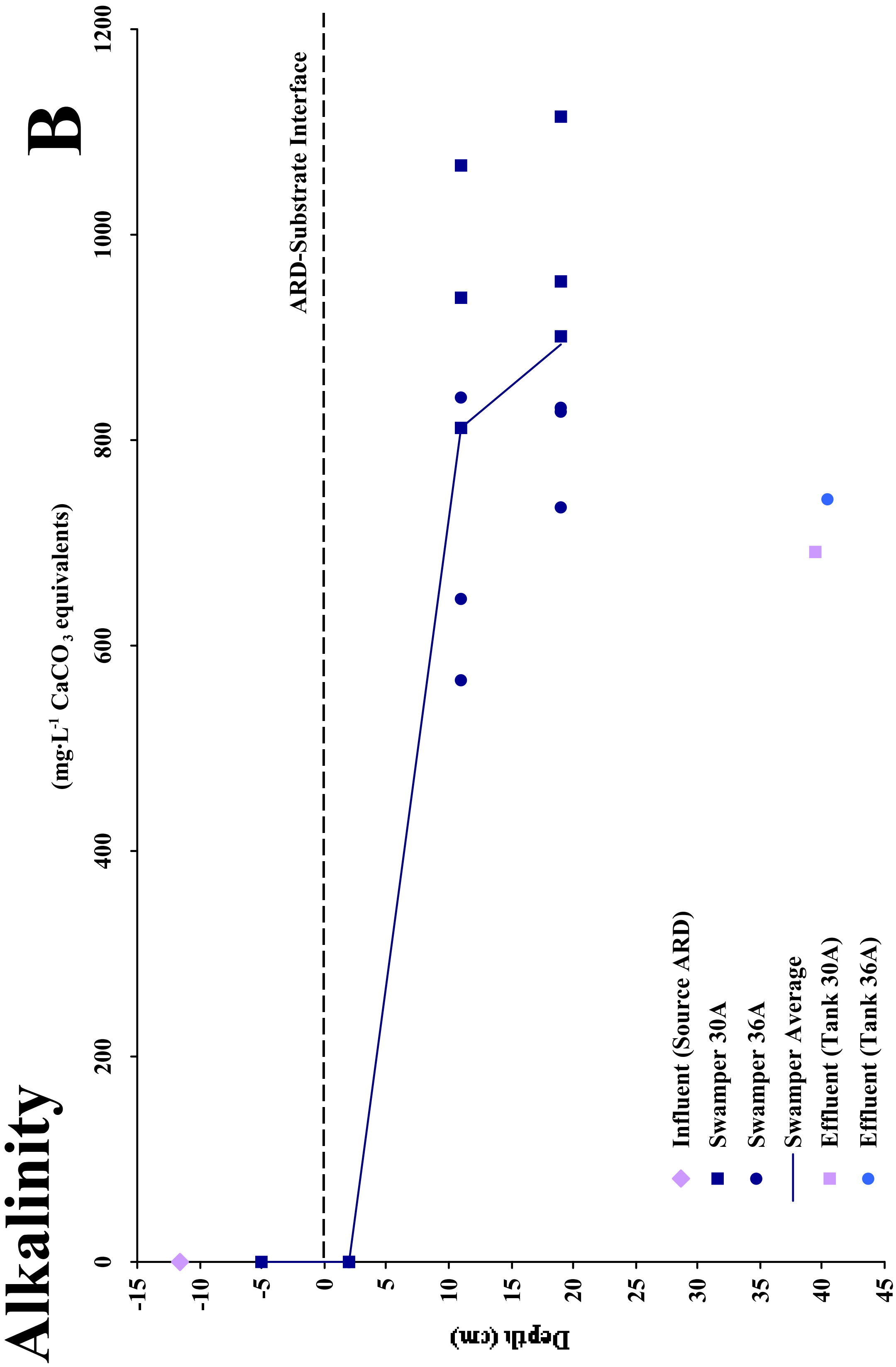
Alkalinity
B
$(mg{\cdot}L^{-1}\ CaCO_3$ equivalents)
0
200
400
600
800
1000
1200
Depth (cm)
-15
-10
-5
0
5
10
15
20
25
30
35
40
45
ARD-Substrate Interface
Influent (Source ARD)
Swamper 30A
Swamper 36A
Swamper Average
Effluent (Tank 30A)
Effluent (Tank 36A)

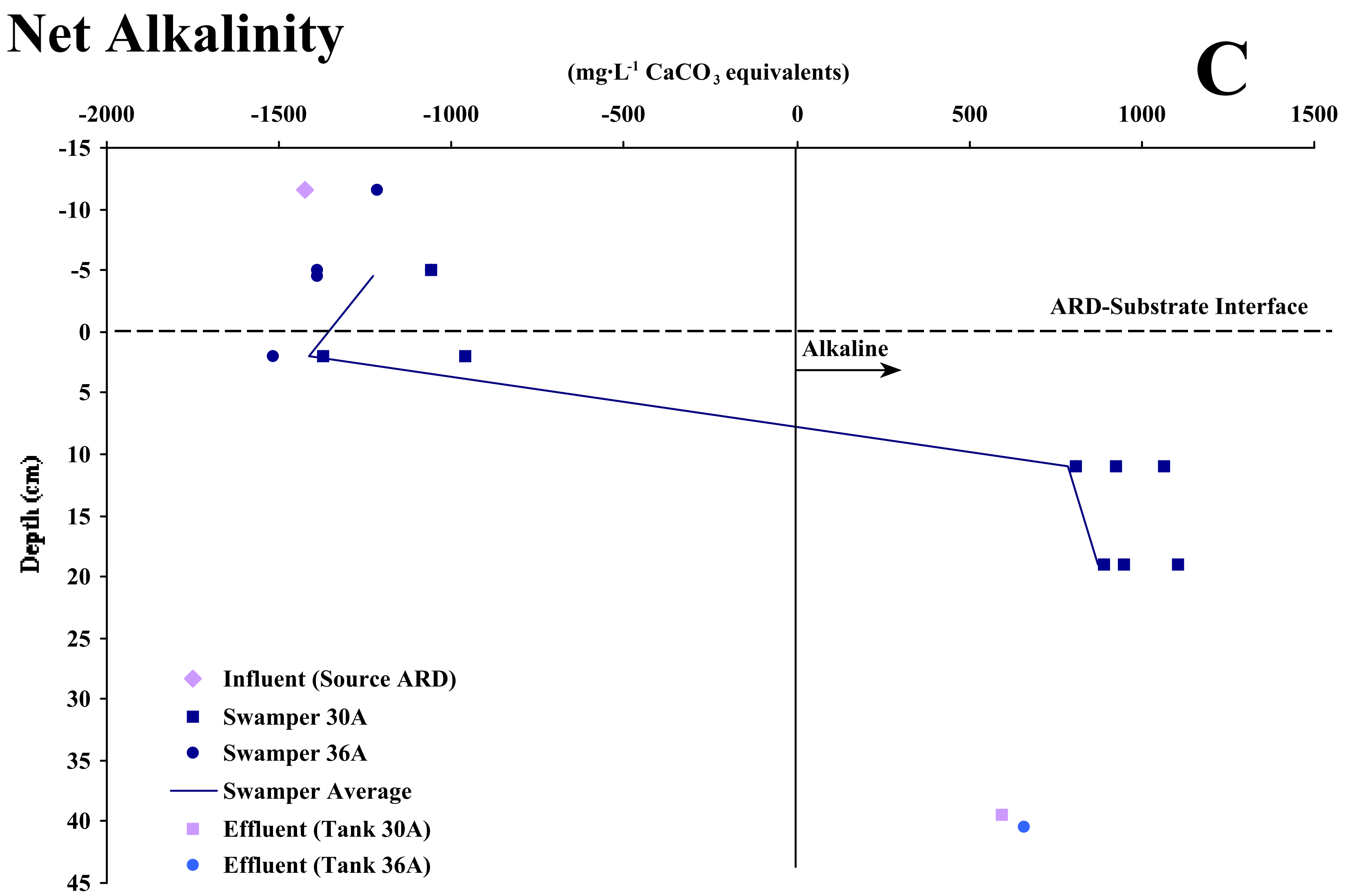
Net Alkalinity
C
(mg·L-1 CaCO3 equivalents)
-2000
-1500
-1000
-500
0
500
1000
1500
Depth (cm)
-15
-10
-5
0
5
10
15
20
25
30
35
40
45
ARD-Substrate Interface
Alkaline
Influent (Source ARD)
Swamper 30A
Swamper 36A
Swamper Average
Effluent (Tank 30A)
Effluent (Tank 36A)

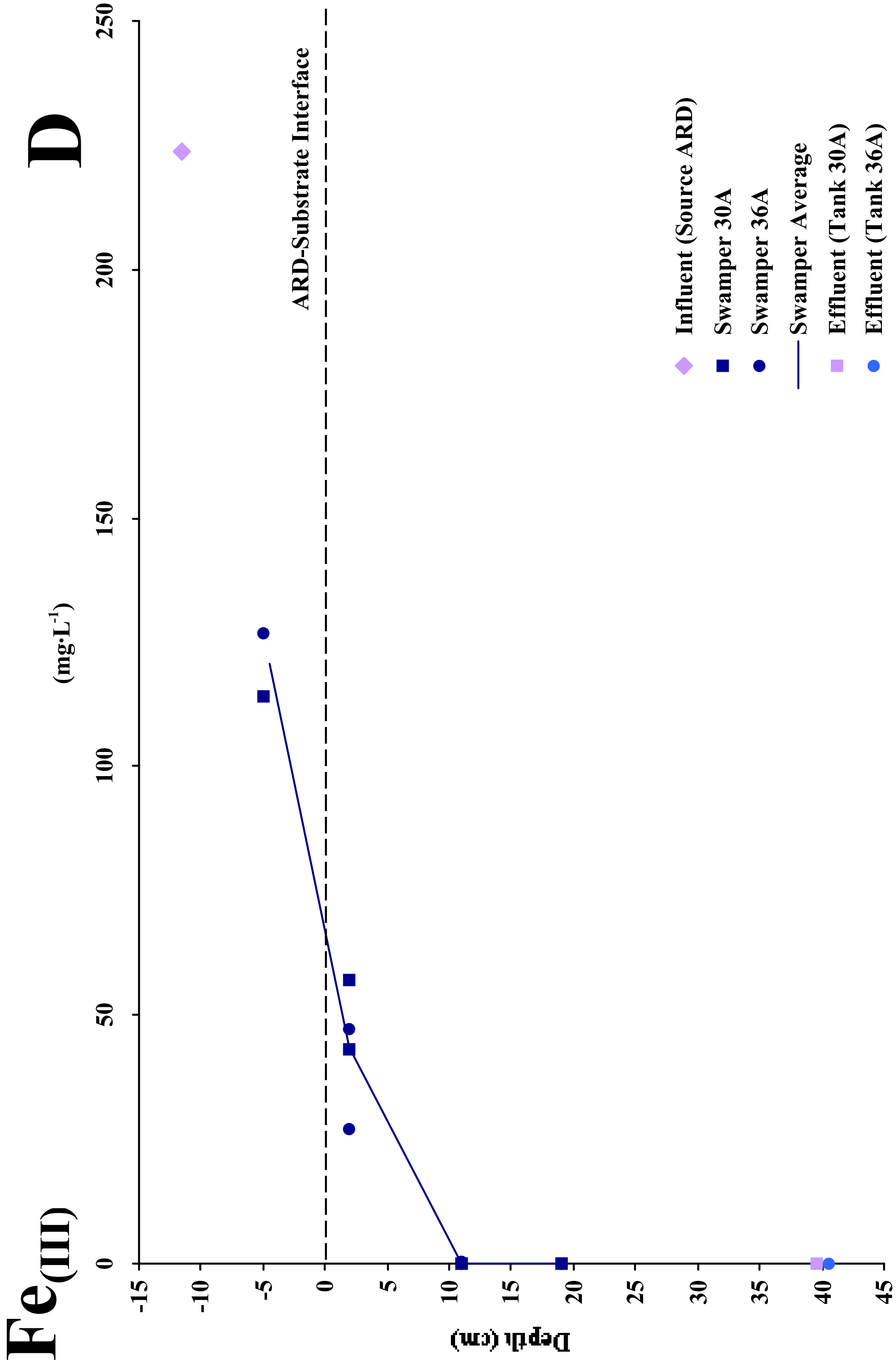
Fe(III)
D
(mg·L-1)
0
50
100
150
200
250
Depth (cm)
-15
-10
-5
0
5
10
15
20
25
30
35
40
45
ARD-Substrate Interface
Influent (Source ARD)
Swamper 30A
Swamper 36A
Swamper Average
Effluent (Tank 30A)
Effluent (Tank 36A)

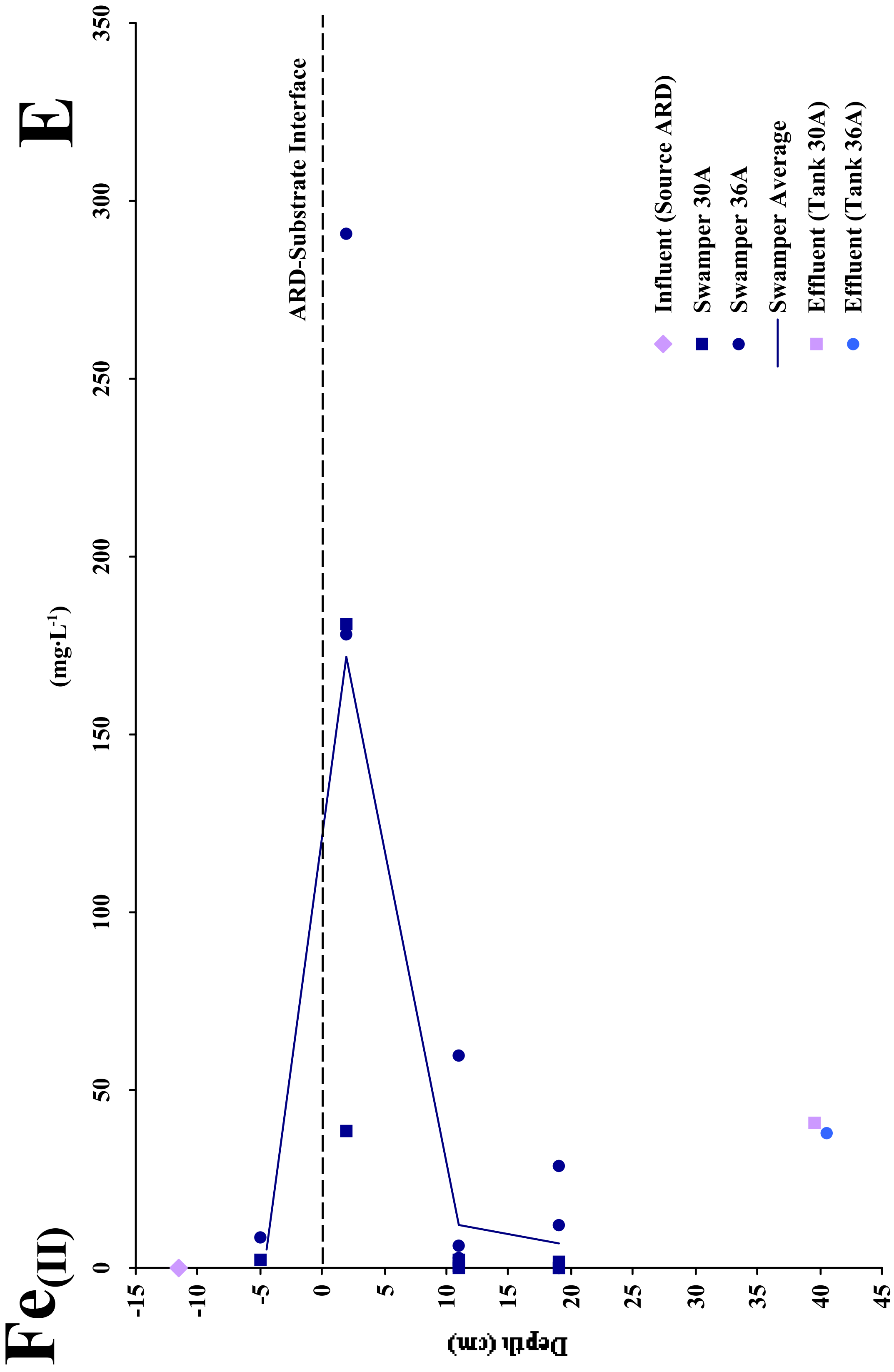
Fe(II)
E
(mg·L-1)
0
50
100
150
200
250
300
350
ARD-Substrate Interface
Influent (Source ARD)
Swamper 30A
Swamper 36A
Swamper Average
Effluent (Tank 30A)
Effluent (Tank 36A)
-15
-10
-5
0
5
10
15
20
25
30
35
40
45
Depth (cm)

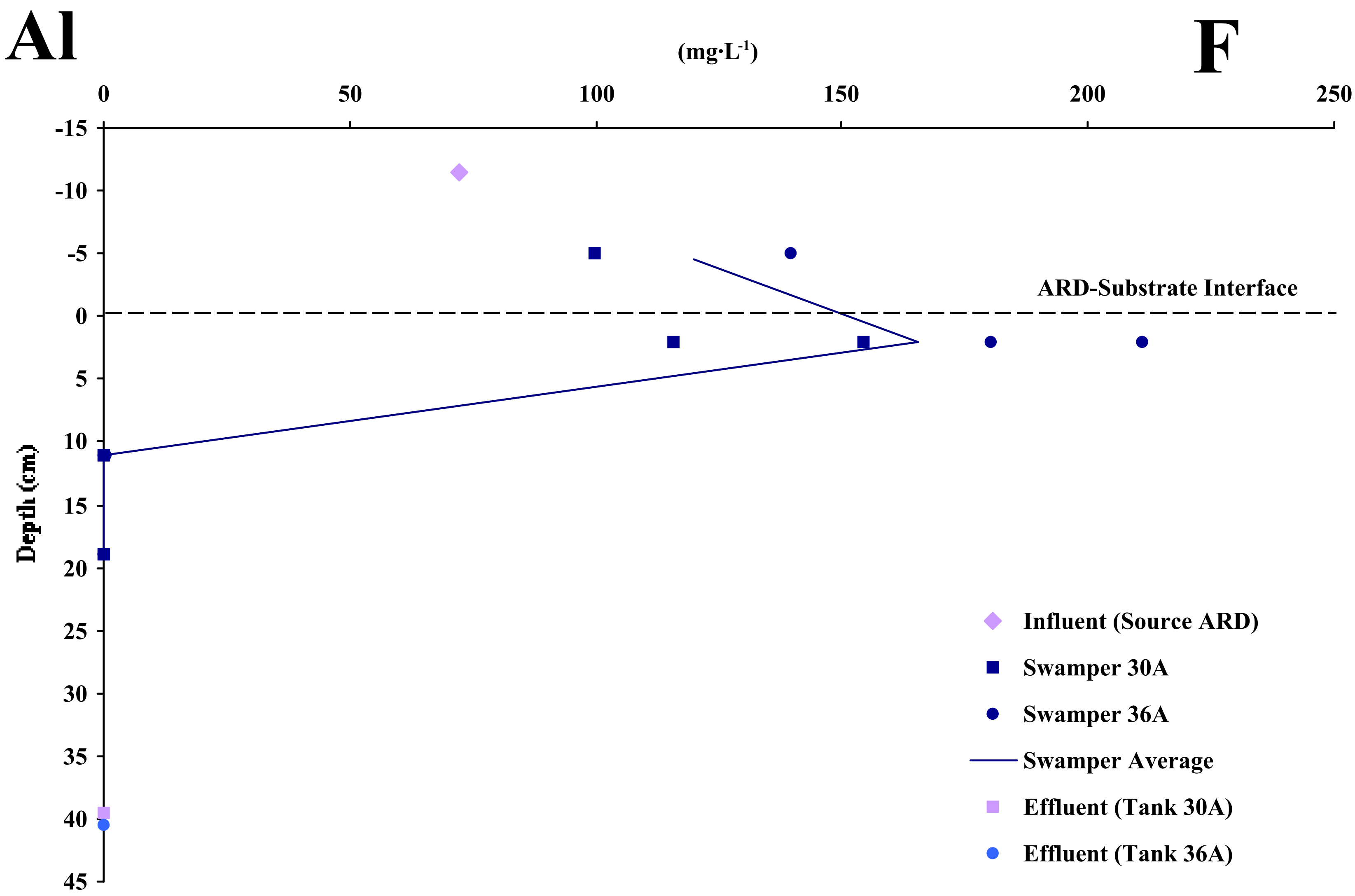
Al
F
(mg·L-1)
0
50
100
150
200
250
-15
-10
-5
0
5
10
15
20
25
30
35
40
45
Depth (cm)
ARD-Substrate Interface
Influent (Source ARD)
Swamper 30A
Swamper 36A
Swamper Average
Effluent (Tank 30A)
Effluent (Tank 36A)

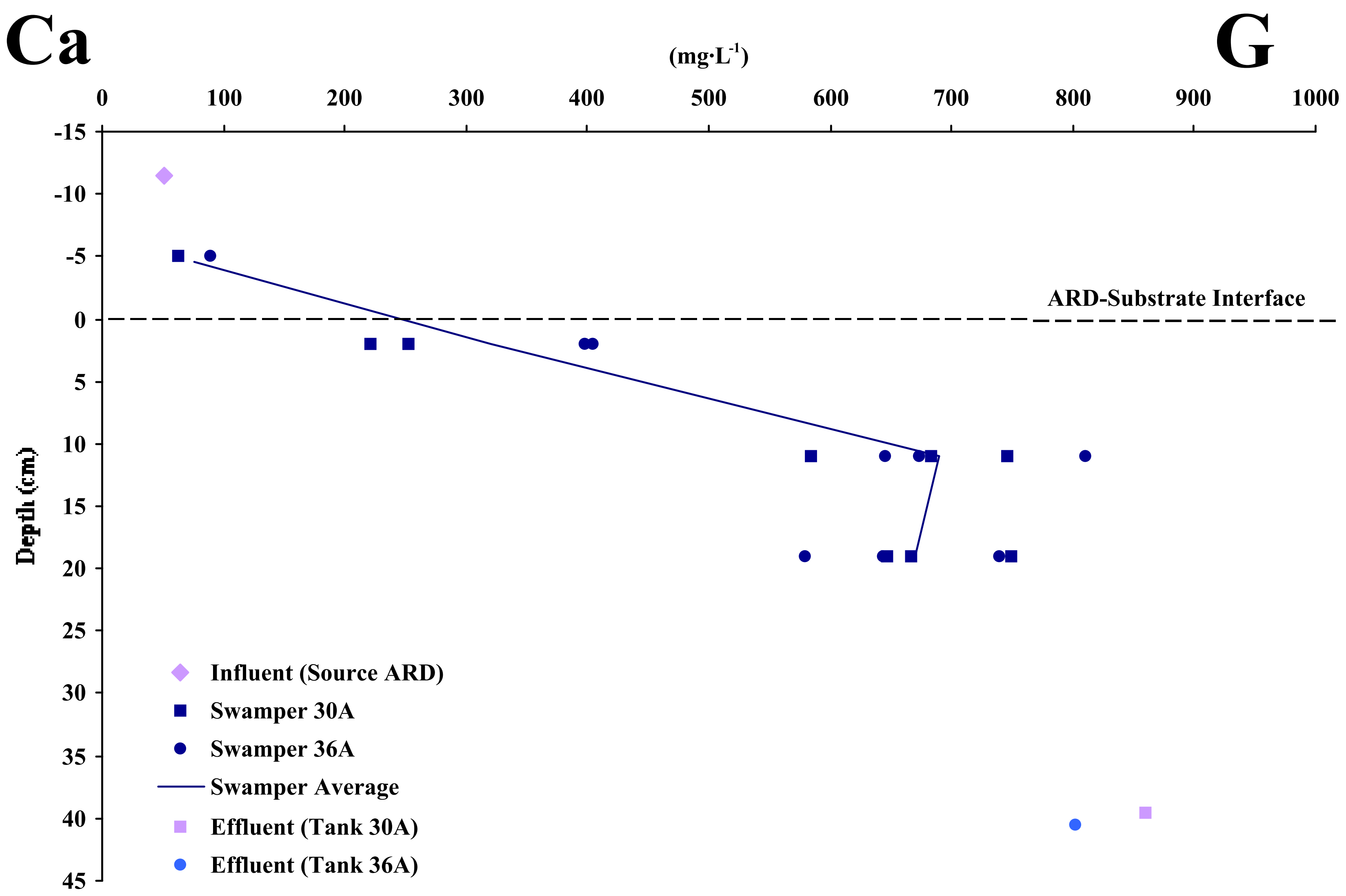
Ca
G
(mg·L-1)
0
100
200
300
400
500
600
700
800
900
1000
Depth (cm)
-15
-10
-5
0
5
10
15
20
25
30
35
40
45
ARD-Substrate Interface
◆ Influent (Source ARD)
■ Swamper 30A
● Swamper 36A
— Swamper Average
■ Effluent (Tank 30A)
● Effluent (Tank 36A)

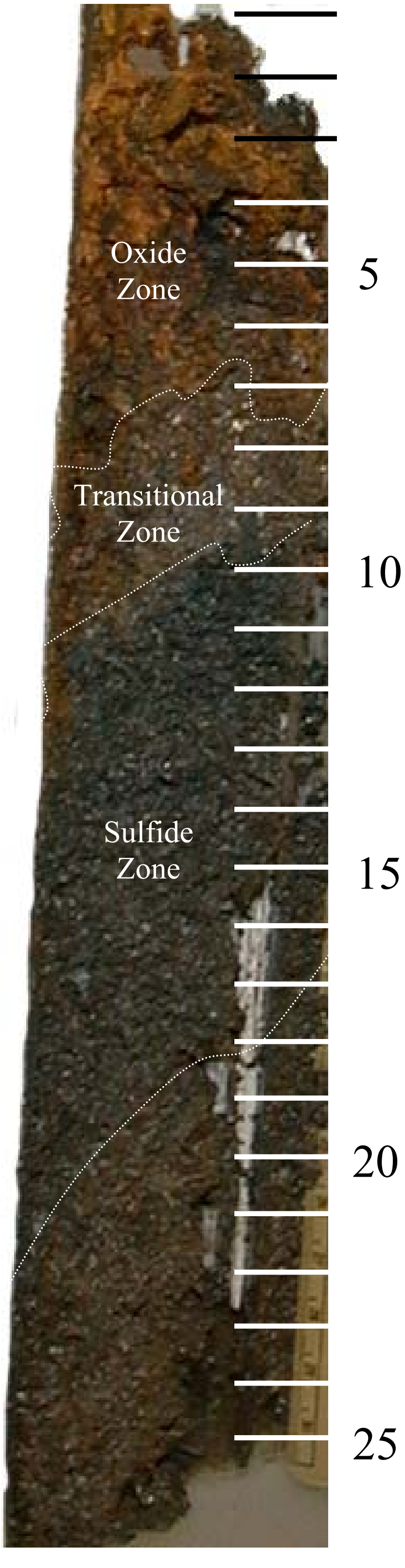

Figure 2.6. Photograph core extracted from the upper 30 cm of the LBOS showing the color reaction zones. Scale bar to the right is in centimeters.

Figure 2.7. Back-scatter electron images of the LBOS showing organic fragments, limestone (LS), pyrite (FeS_2), quartz grains (Qtz), aluminum hydroxysulfate (Al-S), and gypsum (Gy). A, B, C). The initial substrate contained only organic fragments, fossiliferous limestone, and rare pyrite grains. D, E). The upper oxide zone contained only organic fragments and quartz from the initial substrate and iron oxyhydroxide precipitates; no limestone was detected. Dotted lines (D, E) outline the existence of former (relict) grains. F). In the lower oxide zone, aluminum hydroxysulfate was also present and commonly found outlining and surrounding former grains. G). In the upper transitional zone, there was no limestone present. Aluminum hydroxysulfate was commonly found outlining relict grains. H, I). In the middle to lower transitional zone, gypsum and then limestone were found with increasing abundance within aluminum hydroxysulfate rims. The rims surround relict limestone grains. J, K, L). By the bottom of the transitional zone, limestone was pristine and indistinguishable from the initial substrate. The sulfide zone was very similar in appearance with the initial substrate. Notable differences included an abundance of pyrite framboids.

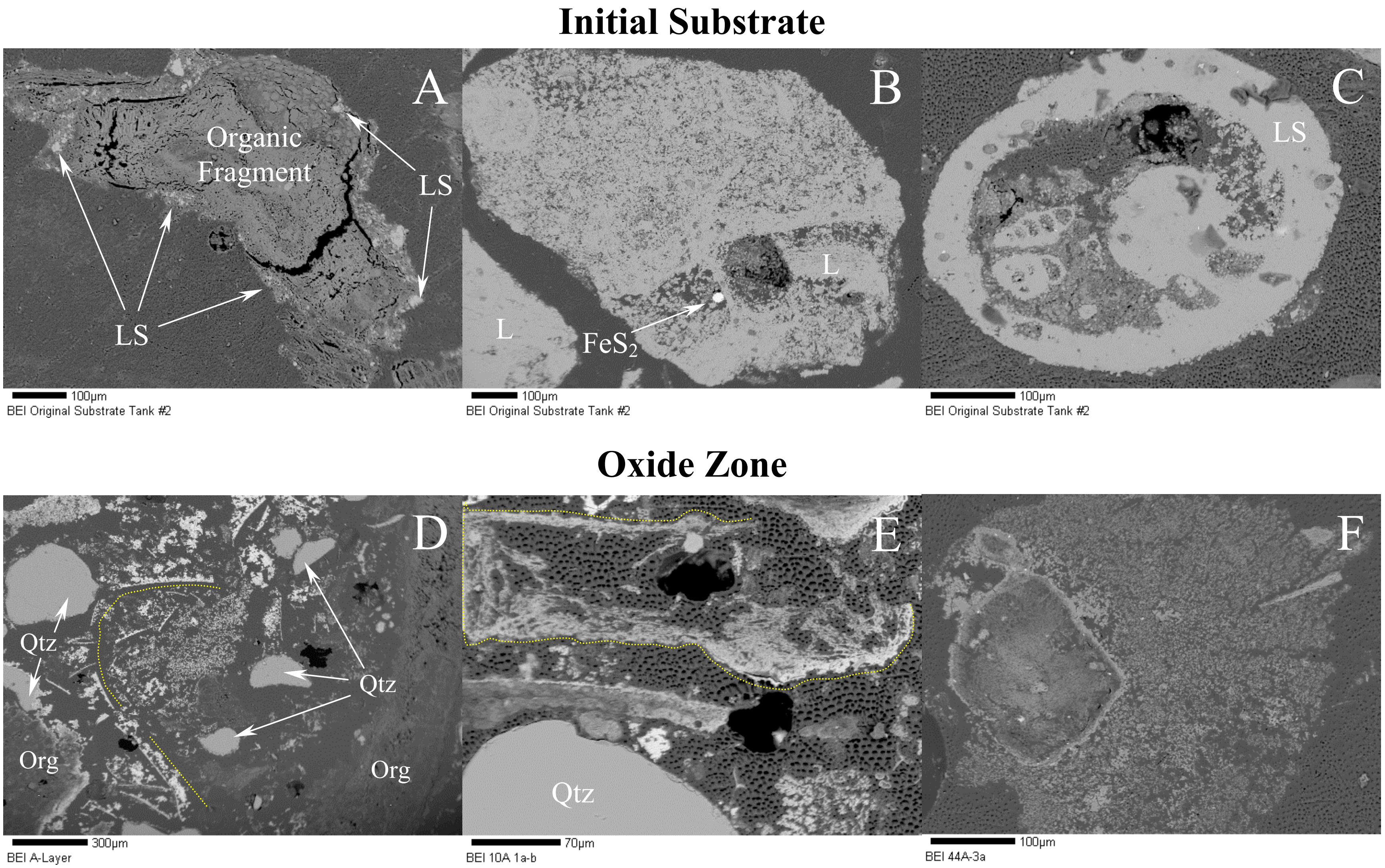
Initial Substrate
A
Organic
Fragment
LS
LS
100µm
BEI Original Substrate Tank #2
B
L
L
FeS2
100µm
BEI Original Substrate Tank #2
C
LS
100µm
BEI Original Substrate Tank #2
Oxide Zone
D
Qtz
Qtz
Qtz
Org
Org
300µm
BEI A-Layer
E
Qtz
70µm
BEI 10A 1a-b
F
100µm
BEI 44A-3a

Figure 2.7

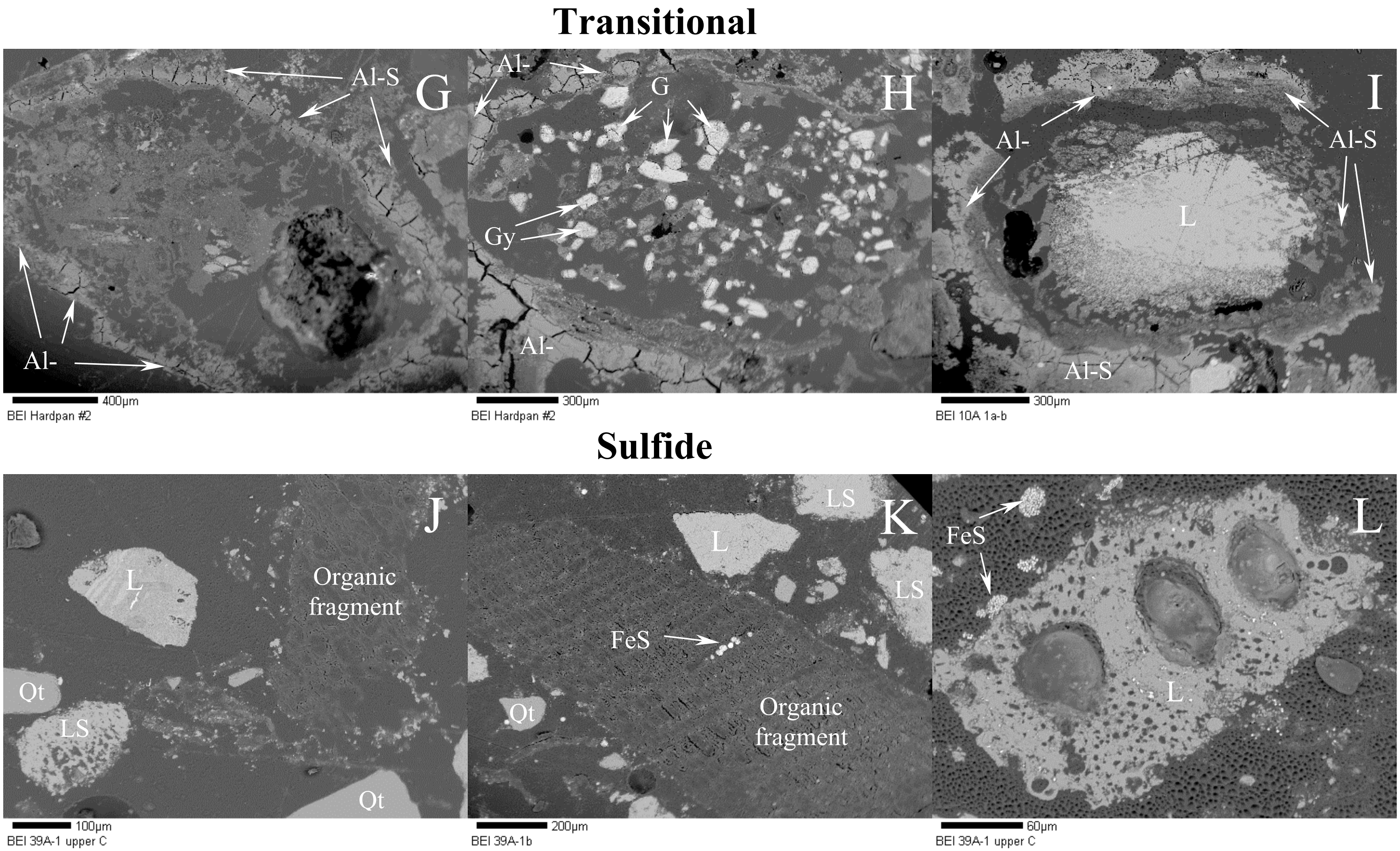
Transitional
G
Al-S
Al-
400µm
BEI Hardpan #2
H
Al-
G
Gy
Al-
300µm
BEI Hardpan #2
I
Al-
Al-S
L
Al-S
300µm
BEI 10A 1a-b
Sulfide
J
L
Organic fragment
Qt
LS
Qt
100µm
BEI 39A-1 upper C
K
LS
L
LS
FeS
Qt
Organic fragment
200µm
BEI 39A-1b
L
FeS
L
60µm
BEI 39A-1 upper C

Figure 2.7

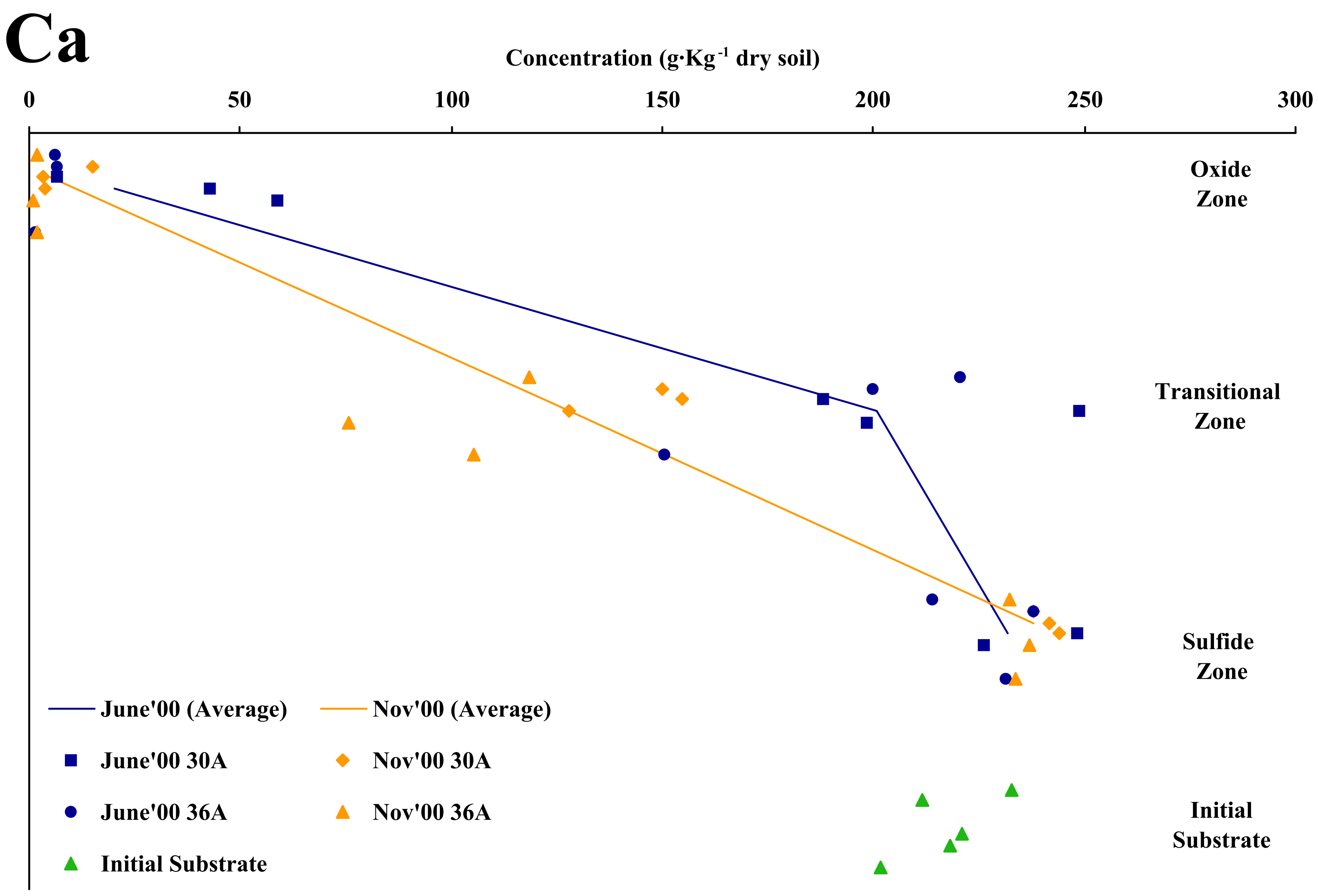

Figure 2.8. Total calcium concentration of the three reaction zones compared to the composition of the initial substrate

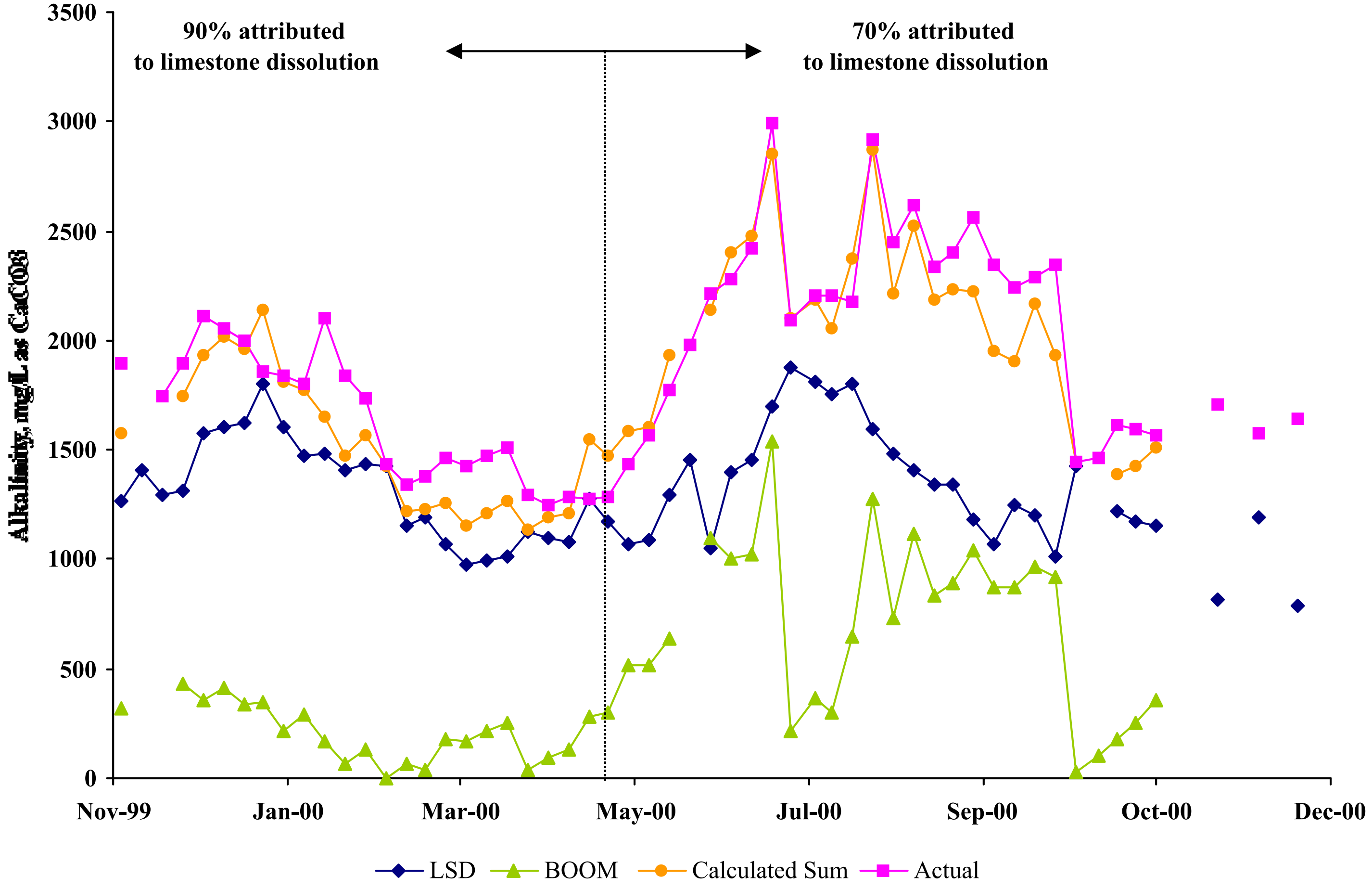

Figure 2.9. Average calculated total alkalinity production (calculated sum), based on the increase in dissolved calcium (through limestone dissolution, LSD) and decrease in dissolved sulfate (through biological oxidation of organic matter, BOOM), is compared to the actual total net alkalinity (-acidity + alkalinity) generated (actual).

Figure 2.10. Calculated calcite saturation index for A) the influent and effluent of tank 36A over time and B) the swamper pore water data. C) Calculated P_{CO2} of swamper data. Saturation indices and P_{CO2} were calculated using a computer program developed by Romanek (1991).

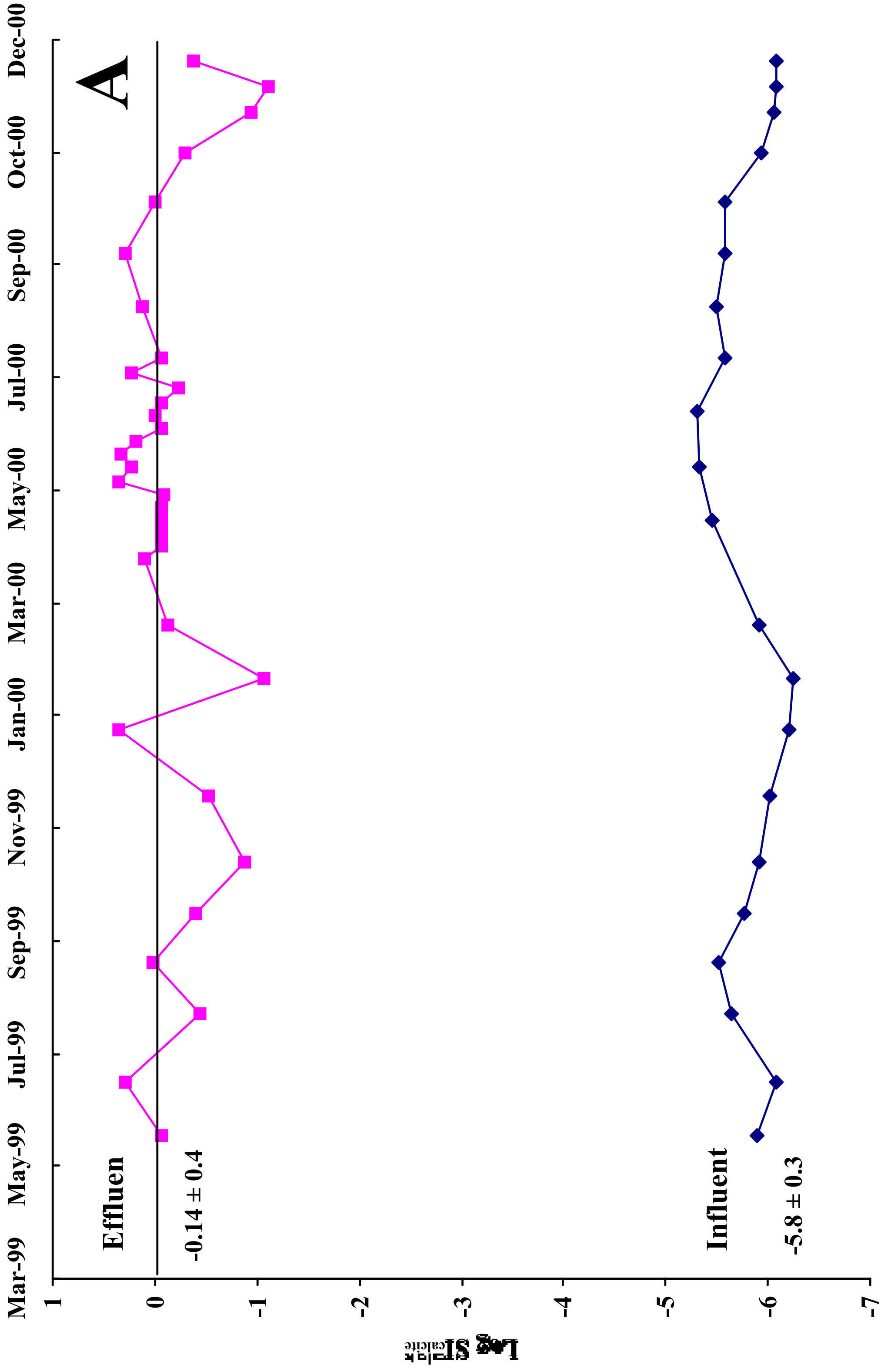
A
Effluen
-0.14 ± 0.4
Influent
-5.8 ± 0.3
Mar-99
May-99
Jul-99
Sep-99
Nov-99
Jan-00
Mar-00
May-00
Jul-00
Sep-00
Oct-00
Dec-00
1
0
-1
-2
-3
-4
-5
-6
-7
Log SI calcite

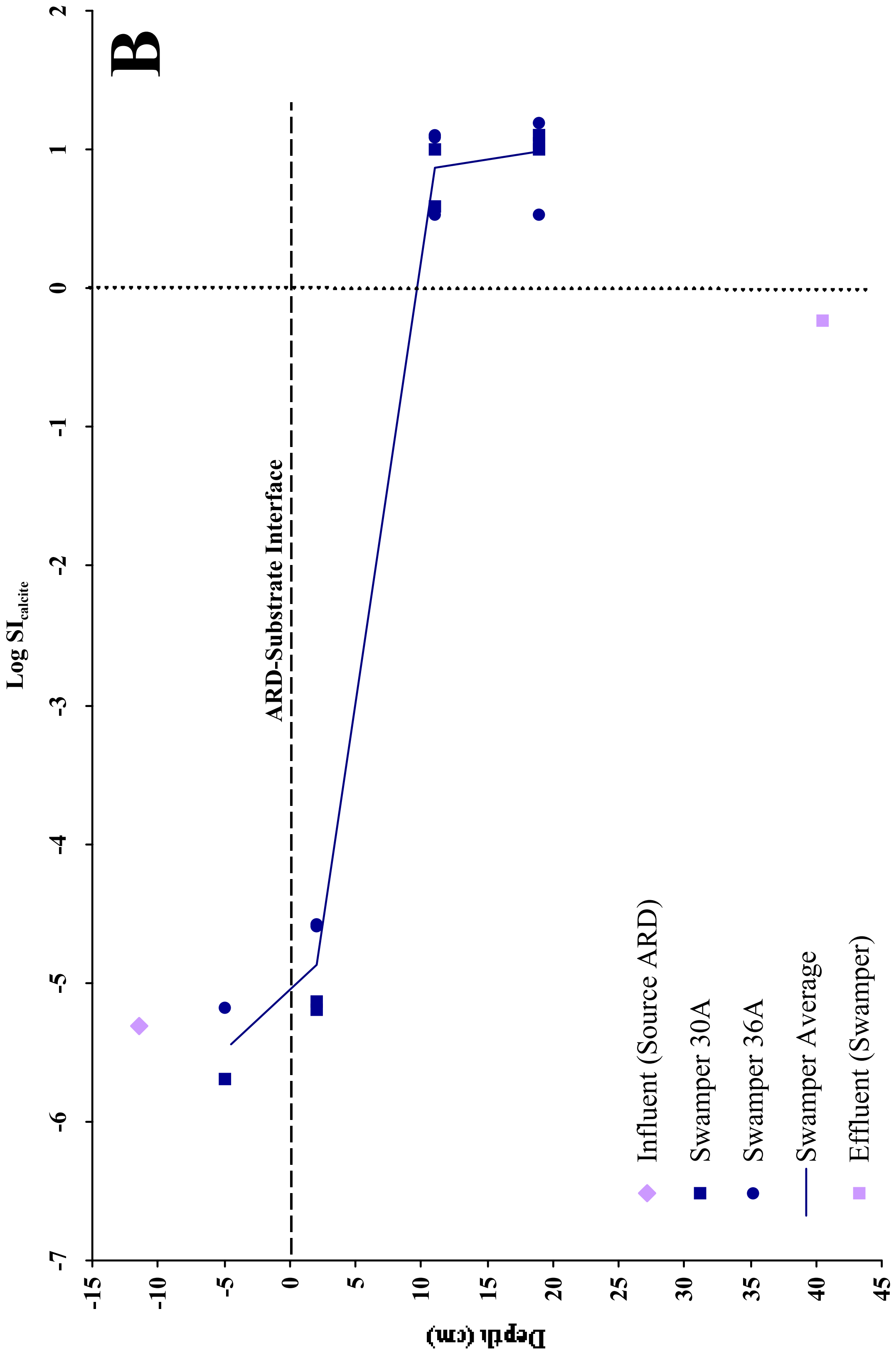
B
Log SI calcite
2
1
0
-1
-2
-3
-4
-5
-6
-7
ARD-Substrate Interface
Depth (cm)
-15
-10
-5
0
5
10
15
20
25
30
35
40
45
◆ Influent (Source ARD)
■ Swamper 30A
● Swamper 36A
Swamper Average
■ Effluent (Swamper)

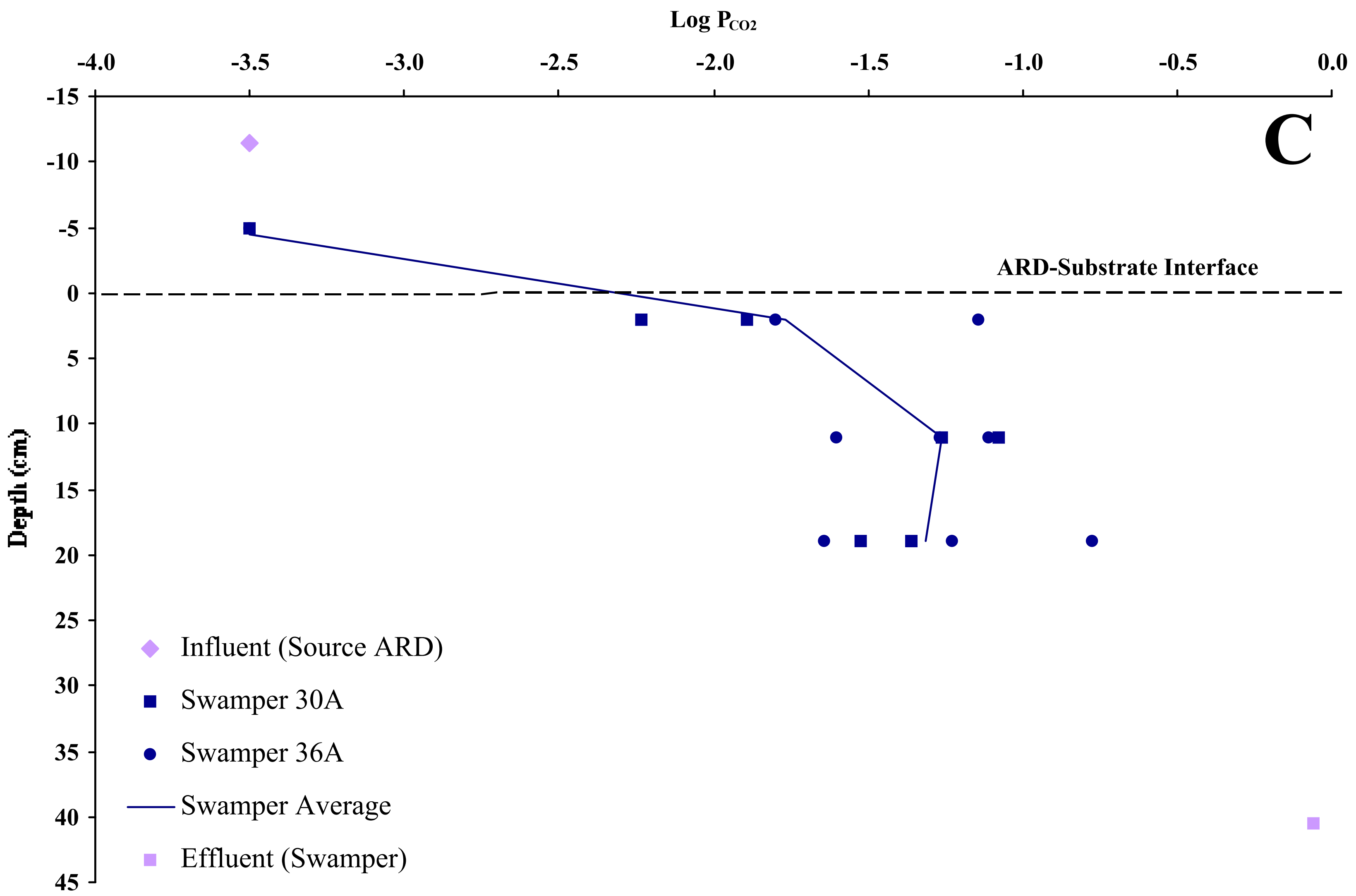
Log P_{CO2}
-4.0
-3.5
-3.0
-2.5
-2.0
-1.5
-1.0
-0.5
0.0
Depth (cm)
-15
-10
-5
0
5
10
15
20
25
30
35
40
45
C
ARD-Substrate Interface
◆ Influent (Source ARD)
■ Swamper 30A
● Swamper 36A
Swamper Average
■ Effluent (Swamper)

CHAPTER 3

DEVELOPMENT AND EVOLUTION OF REACTION ZONES IN CONSTRUCTED TREATMENT WETLANDS RECEIVING LOW-PH, FERRIC IRON-DOMINATED ACID ROCK DRAINAGE[3]

---

[3] Thomas, R.C. and Romanek, C.S. 2002. To be submitted to *Chemical Geology*.

Abstract

Passive alkalinity generation is a current option being used in the remediation of acid rock drainage (ARD). One particular design, the reducing and alkalinity producing system (RAPS), has gained popularity because it is the only system capable of long-term treatment of low pH ARD containing > 1 mg·L^{-1} ferric iron, aluminum, or oxygen. Although RAPS are not designed for metal retention, when they receive low pH (<3), ferric iron-dominated ARD, both ferric iron and aluminum are precipitated in distinct reaction zones.

In this study, a RAPS was simulated and the mechanism of iron and aluminum removal was investigated. Three distinct reaction zones were identified: 1) an orange "oxide zone" that is devoid of limestone and contains mainly goethite and ferrihydrite; 2) a white "transitional zone" which contains partially dissolved limestone, gypsum, and amorphous aluminum hydroxysulfates; and 3) a black "sulfide zone" that contains ubiquitous framboidal pyrite and acid volatile monosulfides (AVS).

The three reaction zones developed through a series of mineral dissolution-precipitation reactions that controlled pH and metal mobility. The oxide zone pH was maintained between 2.3 and 3.8 by the precipitation of iron oxyhydroxide balanced by the dissolution of aluminum hydroxysulfate. The transitional zone pH was maintained between 3.8 and 4.6 by a balance between aluminum hydroxysulfate precipitation and limestone dissolution. The pH of the sulfide zone was >6.5 due to carbonate buffering.

As the limestone content of the substrate was consumed at a limestone dissolution front, the boundaries between the three reaction zones migrated deeper into the substrate.

The sulfide zone formed downstream of the limestone dissolution front. Over time, the transitional zone migrated with the limestone dissolution front and overprinted the sulfide zone. As limestone was completely removed from the trailing edge of the transitional zone, the dissolution of aluminum hydroxysulfate was favored, resulting in overprinting of the transitional zone by the oxide zone. Over time, an increasingly greater amount of the substrate will evolve into oxide zone material. If the limestone dissolution front is allowed to pass completely through the substrate, then ferrous iron and aluminum may be released.

Additional Key Words: acid rock drainage, constructed treatment wetlands, acid neutralization

1. Introduction

Acid rock drainage (ARD) is a major source of water contamination in metal- and coal-mining areas worldwide (Powell, 1988). The iron disulfide, pyrite (FeS_2), associated with coal and metal-ore deposits, is responsible for producing the majority of ARD in mining areas (Stumm and Morgan, 1981; Rose, 1999). Generation of ARD is initiated with the oxidation of pyrite in the presence of water and oxygen with the consequent release of dissolved ferrous iron, sulfate, protons (H^+), and trace elements that commonly coprecipitate in sulfide-bearing minerals (e.g., As, Cd, Co, Cu, Ni, Zn). Secondary reactions that occur between ARD and aquifer materials along flow paths act to further modify the chemistry (Blowes and Ptacek, 1994). Contact with clays releases aluminum and sodium, while contact with carbonate minerals releases calcium, magnesium, and manganese (Watzlaf et al., 2002). The secondary reactions can produce a fairly innocuous drainage that has relatively high dissolved sulfate, but low dissolved metals and circumneutral pH. Alternatively, the resulting drainage can be highly acidic and low in pH, and contain elevated concentrations of dissolved sulfate, iron, manganese, and other acid soluble metals (e.g., aluminum; Hedin et al., 1994).

Conventional treatment of ARD involves the “active” addition of alkaline chemicals to raise pH and remove mineral acidity through the hydrolysis and precipitation of dissolved metals. Although effective, active chemical treatment is expensive when the cost of equipment, chemicals, and manpower is considered (Kleinmann, 1990; Phipps et al., 1991; Skousen et al., 1998), and the responsibility for treatment may be a long term liability. The United States coal industry spends over $1 million per day on active treatment of ARD (Kleinmann, 1990). One alternative to active chemical additions is passive treatment, which refers to any zero or low maintenance ARD treatment method that does not require continual chemical addition and monitoring. Passive treatment systems offer control of ARD at substantially lower operating costs than conventional treatment systems, they are environmentally safe, and they can be installed in remote locations such as abandoned mine lands.

Passive alkalinity generation is achieved by placing an alkalinity-generating material in the flow path of ARD. Calcitic limestone is by far the most common alkalinity-generating material used in passive treatment[4]. However, limestone utilization

---

[4] There is sufficient evidence that biological reactions alone can neutralize ARD and passive treatment systems have been designed solely around biological acidic neutralization through metal precipitation and alkalinity generation using organic matter as the “alkalinity-generating material” (Wildeman et al., 1993; Gusek, 1998). However, biological processes are beyond the scope of this paper.

is limited by the oxidation state of the ARD. When limestone comes in contact with oxic (i.e., ferric iron- and/or O_2-bearing) ARD, ochreous solids tend to armor limestone surfaces, which effectively reduces the buffering capacity of the limestone. Initially these systems work well, but once limestone is armored the performance of the passive system drops sharply (Ziemkiewicz et al., 1997; Sterner et al., 1998). Anoxia limits the oxidation and hydrolysis of ferrous iron, thereby minimizing the armoring of limestone and maximizing the neutralizing capacity of the system. Treatment by direct contact with limestone is typically limited to ferrous iron-dominated ARD having a pH ~ 6.0 (< 1 $mg \cdot L^{-1}$ ferric iron and/or oxygen; Hedin et al., 1994; Watzlaf and Hyman, 1995; Skousen et al., 1998). Consequently, oxygenated ferric iron-dominated ARD (e.g., ARD contained in surface ponds) requires pretreatment to remove dissolved oxygen and ferric iron for production of alkalinity.

Reducing and alkalinity producing systems (RAPS) are passive alkalinity generating systems of particular interest because they are the only passive technology capable of treating highly acidic, oxygenated, ARD containing elevated concentrations of iron and aluminum (Watzlaf et al., 2000). A RAPS is a type of constructed treatment wetland with a layer of organic matter (generally compost; 0.1 – 0.5 m thick) that overlies a layer of limestone (0.5 – 1.0 m thick; Kepler and McCleary, 1994; Watzlaf, 1997; Skousen et al., 1998; Zipper and Jage, 2001). A perforated pipe drainage system is placed at the bottom of the limestone layer to regulate water depth and insure that the organic and limestone layers remain submerged (Kepler and McCleary, 1994; Watzlaf, 1997; Zipper and Jage, 2001). The RAPS design allows ARD to flow downward through the organic matter and limestone layers by gravity for surface discharge at a lower relative elevation.

In theory, the high biologic oxygen demand (BOD) and low reduction potential (Eh) of the compost layer removes dissolved oxygen and promotes the reduction of ferric iron to ferrous iron before ARD reaches the limestone drain (Kepler and McCleary, 1994; Watzlaf et al., 2000). Thus, the original idea behind the RAPS was to have metals pass through the system in a reduced state producing a neutral pH, alkaline effluent for treatment in an aerobic settling wetland before discharge back to the environment. Both column and field studies have shown however, that metals are removed to a varying degree within RAPS, with most of the removal occurring when the influent ARD has a low pH and is ferric iron-dominated (Dietz and Stidinger, 1996; Watzlaf, 1997; Thomas et al., 1999; Jage et al., 2000; Nairn et al., 2000; Demchak et al., 2001; Garrett et al., 2001).

Metal removal is commonly documented in RAPS by measuring the difference in water chemistry of inflow and outflow ARD. However, the geochemical nature of metal removal has not been investigated to any great extent (Dietz and Stidinger, 1996; Watzlaf, 1997; Nairn et al., 2000). Based solely on changes in pore water chemistry, Watzlaf (1997) hypothesized that iron removal was due to a combination of adsorption and precipitation reactions that produce hydroxides and sulfides within the compost layer. Other studies noted that aluminum removal was directly related to the pH-dependent solubility of aluminum (Dietz and Stidinger, 1996; Watzlaf, 1997). In fact, most RAPS studies suggest metal removal occurs at a sharp pH boundary that develops in the compost layer. Across the boundary, pH shifts from an influent value above to an effluent value below (Dietz and Stidinger, 1996; Watzlaf, 1997; Thomas et al., 1999; Nairn et al., 2000). Moreover, as the neutralization potential of the organic material is consumed at the pH boundary over time, the boundary migrates deeper into the organic layer.

In chapter 2, three distinct color “reaction” zones were identified that developed at or near the pH boundary in the compost layer of a simulated RAPS. Above the pH boundary, the substrate was typically orange from secondary ochreous precipitates, while below the boundary the substrate was black. In between these two zones, a thin (2 – 5 cm) band of gray material was visible that was mottled in orange and black colors. At the start of the experiment, limestone was uniformly distributed through the compost layer; however results presented in chapter 2 showed that after two years the orange layer contained no limestone, the gray layer showed corroded limestone textures, while the black zone contained pristine limestone. Chapter 2 concluded that the gray zone represented a limestone dissolution front that developed in the compost layer and that most of the iron and aluminum removal occurred above the dissolution front within color reaction zones; however, they did not identify the specific iron and aluminum phases responsible for such removal nor did they delineate why the color reaction zones develop.

One of the main goals of this study was to identify and quantify the major phases of iron and aluminum removal in a RAPS-type alkalinity generating system treating oxygenated, low pH (<3.0), ferric iron-dominated ARD and correlate these phases to the three reaction zones previously identified (see Chapter 2). A second goal of this study was to develop a model to explain why these reaction zones develop. The third and final goal of this study was to predict the long-term fate of metals sequestered in a RAPS based on spatial and temporal trends in metal removal and relate this to changes in pore water chemistry.

2. Materials and Methods

2.1. Experimental System

Eight plastic tanks (92 cm diameter by 122 cm tall) were used to simulate RAPS-type passive systems. Each tank was filled with 92 cm of limestone-buffered organic substrate (LBOS; see Chapter 2) overlying 15 cm of coarse (#57; i.e. ~1.27 cm) limestone (Fig. 3.1a). The ARD used in this experiment was drawn from a coal pile retention basin (CPRB) that collects runoff from a nearby coal storage pile at the Department of Energy (DOE) Savannah River Site (SRS), near Aiken, S.C., USA. Using a single pump and a distribution manifold, ARD from the CPRB was delivered continuously to the top of each tank from December 1998 to December 2000. Once the ARD was delivered to the top of the tanks, flow through the LBOS was driven by gravity. Effluent drained from the bottom of the tanks through standpipes such that a 15-cm column of ARD was maintained over the LBOS at all times. To minimize the effects of evaporation and dilution by rain, a cover was placed on the top of each tank.

2.2. Limestone-Buffered Organic-Substrate (LBOS)

Limestone buffered organic substrate (LBOS) was made by mixing 25% limestone screenings with 75% organic material by volume (Table 3.1). Mixing limestone screenings into the LBOS increased the neutralization potential from ~10% $CaCO_3$ equivalents (commonly cited for typical RAPS compost layers; Watzlaf, 1997; Watzlaf et al., 2000), to ~54% $CaCO_3$ equivalents (see chapter 2). The limestone screenings were 91.5% by weight $CaCO_3$ with a nominal grain size of 1.2 mm; greater than 80% of the screenings were between 0.6 and 4.8 mm in diameter (Table 3.1). The organic material was composed of a mixture of composted stable waste (96%), spent brewing grains (4%), and Kriket Krap® (composted cricket manure, <1%). The stable waste contained mainly wood shavings with minor amounts of straw and horse manure; it was collected from a refuse pile that was 3 to 5 years old. Details on the preparation of the LBOS are presented elsewhere (see chapter 2).

2.3. Changes between influent and effluent water chemistry

Based on weekly samples collected from the distribution manifold (see chapter 2), influent ARD consistently had a low pH (<3.0), was ferric iron-dominated (99% Fe^{3+}), and highly mineralized (mainly iron and aluminum). Average effluent water chemistry was consistently circumneutral (6.4) with ~90% of the influent iron and >99% influent aluminum removed within the tanks (see chapter 2). Average influent and effluent water chemistry and the range in values over the two year study are given in Table 3.2.

2.4. Pore water sampling

Pore water samples were collected using an acrylic pore-water diffusion sampler (i.e. peeper; Hesslein, 1976; Carignan, 1984; Carignan et al., 1985). The peeper was constructed using two clear 15 x 36 x 1.9 cm acrylic (Plexiglas) plates and nylon screws (Fig. 3.1b). Wells, approximately 3 cm in diameter, were drilled through a thinner (0.6 cm) top plate and into the thicker (1.3 cm) bottom plate so that each well in the bottom plate had an approximate 3 mL volume. Seven well horizons were drilled with each horizon containing three wells. Wells were spaced about 5 cm on center.

To prepare the peeper for sampling, the plates were unscrewed and separated. Each well was filled with milli-Q water so that a meniscus formed above the well. A sheet of polycarbonate dialysis membrane with a 10 nm pore size, was carefully laid over the lower plate and air bubbles were removed. The top plate was then placed over the dialysis membrane and the plates were screwed together. The peeper was then placed in a moist plastic bag (to prevent evaporation) and left upright overnight to assure the wells were sealed. The peeper was kept in the plastic bag until insertion in the substrate.

The peeper was inserted into the center of tank 44A and allowed to equilibrate between May 21 and June 6, 2000. Influent and effluent samples from tank 44A were collected the day the peeper was installed, once in the middle of equilibration, and the day the peeper was removed. The peeper was inserted in the LBOS such that the first two well horizons were in the water column above the LBOS with the bottom edge of the second well horizon positioned at the sediment-water interface (Fig. 3.1b). The remaining five well horizons provided a pore water profile of the LBOS at 2.5, 7.5, 12.5, 17.5, and 22.5 cm depth.

Once pulled from the LBOS, the peeper was gently rinsed with milli-Q water to remove any sediment from the dialysis membrane surface and sampled immediately using a syringe and needle to penetrate the dialysis membrane. Approximately 3 mL of pore water was collected from each of the three wells in a horizon. Pore water from the first well was used to measure pH and temperature, water from the second well was used for metal analysis and the third well was used for determining ferrous and total iron concentrations.

2.5. Pore water analysis

Temperature and pH data were collected from peeper pore water samples as previously described (chapter 2). Because the dialysis membrane used in the peeper had a 10 nm pore size, peeper samples for dissolved metal analysis were not filtered before being preserved. Samples for dissolved metal analysis were preserved (1% HNO_3) and analyzed by inductively coupled plasma mass spectrometry (ICP-MS; described in chapter 2). Instrument precision was generally < 3%, while analyses were accurate to ±10%. Only the major elements iron, aluminum, and calcium are reported in this study; trace metal chemistry is reported in chapter 4.

Samples collected for ferrous iron determination were filtered (0.1 μm), acidified with 6 N trace metal grade hydrochloric acid to a final concentration of 1% HCl, and stored in brown amber bottles at 4°C (To et al., 1999). Although it has been shown that samples stored this way can be preserved for up to six months (To et al., 1999), analysis was conducted within three months of sampling. Ferrous iron was determined following a colorimetric FerroZine technique (To et al., 1999). Absorbance was measured at 562 nm using an ultraviolet-visible-near infrared (UV-VIS-NIR) spectrophotometer (Cary 500 Scan, Varian Corporation). Splits were analyzed for total iron by adding a reducing agent (hydroxylamine hydrochloride) to convert all ferric iron to ferrous iron. Ferric iron was determined by difference. Instrument precision was generally <0.5% and accuracy was better than 10% (determined by comparison to analyses performed by atomic adsorption spectroscopy).

2.6. Substrate Sampling and Analysis

Eight samples of the initial substrate were collected as the tanks were initially filled with LBOS. Each sample was air-dried, homogenized, and stored for later analysis. Dried substrate was impregnated with epoxy and examined by electron microprobe (as described below) to establish textures and elemental associations specific to the starting material. All samples of the initial LOBS were treated according to the methodologies outlined below for core samples to provide baseline data on the solid phase.

Substrate cores were extracted from two tanks (30A and 36A) in June 2000. In each tank, three areas, 120° apart, were sampled for a total of three cores per tank. An additional six cores were extracted from the same two tanks six months later (three from each tank in November 2000). Cores extracted in November 2000 followed by a sampling strategy similar to the June 2000 sampling event, but approximately 60° away from the June 2000 sampling areas. The cores were taken with 5 cm diameter glass tubes to prevent oxidation. The tubes were inserted ~20 – 25 cm in the LBOS and the tops were plugged with a rubber stopper before extraction. Rubber stoppers were placed in the bottom of the glass tubes immediately after they were removed from the LBOS. The tubes were placed on ice in a cooler and taken directly to the laboratory for processing.

Cores were extruded in an anaerobic glove bag (96:4 N_2:H_2), cut in half lengthwise, and divided into three sections based on distinct color zonations (see chapter 2). Representative, intact sections from one half of the core were oriented in plastic cups and dried in the anaerobic glove bag, while representative samples from the other half of the core were sealed separately in air-tight polyethylene bottles under nitrogen, and frozen for later analysis.

2.6.1. Electron microprobe analysis. Once the oriented samples were dried, they were taken from the glove bag and immediately vacuum impregnated with low viscosity epoxy resin. Samples of the initial LBOS were prepared by scooping loose material into a plastic cup and vacuum impregnating it. Cured billets were cut perpendicular to the original orientation of the core with a low speed diamond saw. The cut chips (~0.5 cm thick) were ground sequentially with 320 and 600 silicon carbide grit, followed by a 3 μm diamond paste, and finished with 0.05 μm colloidal silica polishing suspension. Polished chips were examined with a JOEL 8600 electron microprobe using back-scatter electron (BSE) imaging and Geller imaging software at an accelerating voltage of 15 KeV and beam current of 5 nA. Elemental composition of precipitates was identified and relative abundance qualified with an energy dispersive spectrometer (EDS; ~ 1μm spot size). Sodium is the lightest element routinely detectable by the EDS system used and the minimum detectable concentration of an element is between 0.5 and 1weight percent.

2.6.2. Total digests. Samples from the frozen half of the core were thawed under nitrogen and homogenized with a small rubber policeman within six months of collection. Representative splits of each homogenized color zone were weighed, air-dried, reweighed to determine water content, and ground to a fine powder with a cryogenic grinder. Samples of the initial LBOS from each tank were also cryogenically ground. The ground, dried samples were used for total metal (iron and aluminum) and x-ray diffraction (XRD) analyses (see below). Samples for total metal analysis were digested and analyzed by ICP-OES, according to methods presented in chapter 4

2.6.3. Sequential extractions. Initial LBOS and core samples were subjected to a sequential extraction scheme described in Fig. 3.2 (for details see chapter 4). Briefly, samples were subjected to extractions using four successively more aggressive dissolution techniques with a further subdivision of the fourth step into three additional sequential sub-steps for some samples. The four basic steps targeted iron and aluminum that were: (1) neutral-salt exchangeable (NSE), (2) acid soluble (AS), (3) pyrophosphate extractable (PYRO), or (4) recalcitrant. The recalcitrant fraction subdivided into three sequential steps: (1) oxalate-extractable iron (R_{ox}), (2) citrate-dithionite extractable iron (R_{cd}), and (3) residual material (R_{res}). The R_{res} step was the final step conducted on all samples, while the R_{ox} and R_{cd} steps were only conducted on samples from the orange and select samples of the gray reaction zones.

Five of eight initial substrate samples were subjected to the four basic extraction procedures, while the remaining three samples were subjected to all six extraction steps.

Extraction of the initial substrate was conducted on the dry unground material. Sequential extractions were performed on damp, unground splits of the thawed, homogenized core material. Neutral-salt exchangeable (NSE) and acid soluble (AS) extraction steps were conducted in an oxygen-free environment (including using oxygen-free solutions) to prevent oxidation of any acid volatile sulfides. Samples were analyzed for iron and aluminum by ICP-OES as described in chapter 4. To allow comparison between the initial dry substrate and the damp core material, ICP-OES analyses of the core material were back calculated to dry weight by subtracting the water content of the damp sample.

2.6.4. X-ray diffraction. Samples of the initial LBOS and representative splits of each color zonation were analyzed by XRD. These splits were sieved (200 mesh) to yield a < 74 μm size fraction. X-ray diffraction was performed with a Scintag XDS-2000 diffractometer operated at 40 kv and 35 mA using CoK$_\alpha$ radiation. Random powder mounts were prepared on low-background, single-crystal quartz plates and were step-scanned over the range of 10 to 75° 2θ with a step size of 0.01° and a count time of 10 sec·step^{-1}. Results were compared to the JCPDF database for mineralogical determinations.

2.6.5. Qualitative test for acid volatile sulfide. To qualitatively determine if the LBOS contained iron monosulfide (i.e., acid volatile sulfide, AVS), samples were subjected to acid dissolution following the methods of Kennedy et al. (1998). Briefly, a sample and a silver nitrate trap were placed in a tube sealed under nitrogen. A slight vacuum was created followed by injection of 6N de-oxygenated HCl. The 6N HCl dissolved AVS and eluted H_2S, which was subsequently trapped in the silver nitrate solution as a black Ag_2S precipitate (Kennedy et al., 1998). Samples that generated Ag_2S contained AVS.

3. Results

3.1. Pore Water

3.1.1. pH. During peeper pore water equilibration, the pH of the influent ARD, measured at the manifold, fluctuated between 2.4 and 2.8 (Fig. 3.3). Peeper samples collected from the two well horizons equilibrated with the ARD water column overlying the LBOS were identical in pH (2.2) and were lower than the influent delivered to the tank over the peeper equilibration period. Pore water pH at 2.5 cm depth was similar to the overlying ARD water column. The peeper pore water profile at 7.5 cm showed an increase in pH to a value of 3.8, while by 12.5 cm pH increased to a value of 4.6. The two lowermost peeper well horizons, at 17.5 and 22.5 cm, yielded pH values of 7.2 and 7.4, while effluent over this time period was lower at pH of 6.4 to 6.5.

3.1.2. Iron. While the influent ARD contained dominantly ferric iron, there was a minor ferrous iron component; however, it was lower than the effluent ferrous iron concentration, indicating that at least some ferrous iron was generated in the LBOS. Therefore, pore water data for iron is presented as the ferrous and ferric components and not as total iron.

Influent ferric iron concentration, measured at the manifold, varied between 154 and 192 $mg{\cdot}L^{-1}$ over the time the peeper was in the LBOS. Ferric iron concentrations measured from the two peeper well horizons equilibrated with the ARD water column overlying the LBOS (135 and 168 mg·L^{-1}) were similar to the range in influent ferric iron values experienced during equilibration. The ferric iron concentration (124 mg·L^{-1}) of pore water collected at 2.5 cm was slightly lower than the overlying water column, while ferric iron was completely removed from the pore water by 7.5 cm. Ferric iron was not detected at deeper horizons (i.e., 12.5, 17.5 or 22.5 cm) or in the final effluent.

Influent ferrous iron concentration was fairly consistent (3 – 5 mg·L^{-1}) during the peeper equilibration period. The two peeper well horizons from the ARD water column exhibited a slight increase in dissolved ferrous iron concentration (7 – 16 mg·L^{-1}) compared to influent values. The ferrous iron concentration increased to 57 mg·L^{-1} by 2.5 cm and to 123 mg·L^{-1} by 7.5 cm. At 12.5 cm, the ferrous iron concentration peaked at a value slightly higher (197 mg·L^{-1}) than the influent total iron concentration. Pore water from the last two peeper well horizons (17.5 and 22.5 cm) exhibited a decrease (129 and 41 mg·L^{-1}, respectively) toward the effluent levels (6 – 19 mg·L^{-1}).

3.1.3. Aluminum. Influent aluminum concentration, measured at the manifold, ranged from 122 to 143 mg·L^{-1} over the equilibration period. In the ARD water column overlying the LBOS, peeper analysis of dissolved aluminum followed trends identical to ferric iron. The two well horizons equilibrated with the ARD water column had aluminum concentrations similar to measured influent aluminum concentrations. Dissolved aluminum exhibited trends opposite to ferric iron in the upper portion of the LBOS. At 2.5 cm, where ferric iron displayed a slight decrease in concentration relative to ARD overlying the LBOS, dissolved aluminum showed a slight increase in concentration (197 mg·L^{-1}). At 7.5 cm, where ferric iron was completely removed, aluminum peaked at a concentration nearly three times greater than the influent concentration (365 mg·L^{-1}). Analysis of the pore water collected at 12.5 cm showed that dissolved aluminum was completely removed. Aluminum was not detected at deeper horizons (i.e., 17.5 or 22.5 cm) or in the final effluent.

3.2. Substrate cores – visual observations

Cores taken from the LBOS show three distinct color reaction zones (Fig. 3.4). Additionally, there was a thin (1-cm), green and orange layer on top of the LBOS in most cores. Beneath this layer of biomass, the orange color of ochreous sediment characterized the uppermost orange zone, which occupied the first 7 to 10-cm of actual LBOS material (Fig. 3.4). At approximately 7 to 10 cm, the color of the substrate changed fairly abruptly with the appearance of small irregular patches of buff-colored precipitates, which characterized the gray zone. The color of the gray zone was commonly a reddish-brown with discrete zones of black, but colors ranged from orange-brown to dark gray. In general, this zone faded from a more orange color above to a more gray color below. Moreover, the buff-colored precipitates formed a friable hardpan that loosely cemented between 2 – 5 cm of the LBOS. In sharp contact with the gray zone was a black zone entirely lacking buff-colored precipitates. The black zone extended a total of 5 – 10 cm and then gradually faded into the brownish color of the original LBOS material below (Fig. 3.4). Fresh samples of the black zone exposed to air for a prolonged period of time turned a brownish-orange color. Additionally, the black zone produced a strong smell of sulfide that was not readily detected in the other layers.

3.3. Substrate analysis – total and sequential extraction data

Total digests and sequential extractions were conducted on samples of the initial LBOS and the three color reaction zones to determine the relative contribution of each zone to metal removal in the LBOS. A summary of the data is presented in Table 3.3 and Figs. 2.6 and 2.7 for iron and aluminum, respectively. Total and sequential extraction data are presented for iron and aluminum in a sequence that begins with the initial substrate and moves from the bottom of core upward through the black, gray, and orange zones.

3.3.1. Iron. Total digests of the initial substrate averaged 2.8 $g \cdot kg^{-1}$ and ranged from 1.9 to 4.1 $g \cdot kg^{-1}$ (Fig. 3.5a). Sequential extraction data showed iron was predominantly distributed within the recalcitrant fraction (75 – 90%); the remaining balance was extracted in the AS and PYRO fractions (Fig. 3.5b). Subdivision of the recalcitrant fraction indicated that the R_{res} fraction accounted for almost all of the iron in this phase.

Total digest data from cores extracted in June 2000 showed that the average iron concentration in the black zone was 5.9 $g \cdot kg^{-1}$ (range: 4.3 – 8.0 $g \cdot kg^{-1}$) and this was more than double the initial substrate concentration (Fig. 3.5a). Digests of cores extracted in November 2000 showed there was no temporal change in the total iron (average: 5.8 $g \cdot kg^{-1}$; range: 3.7 – 7.9 $g \cdot kg^{-1}$). Likewise, the sequential extraction data did not display a change in the phases iron was partitioned to over time (Fig. 3.5b). Most of the increase in iron in the black zone relative to the initial substrate was attributed to the recalcitrant fraction (70 – 85%), although increases were also noted in the AS and PYRO fractions.

Total digests of samples from the gray zone taken in June 2000 averaged 9.9 g·kg^{-1}, which was over 3.5 times greater than the initial substrate and more than 1.5 times greater than the black zone (range: 4.7 – 20.7 g·kg^{-1}; Fig. 3.5a). Similar to the black zone, sequential extractions indicated that most of the increase was attributed to an increase in recalcitrant iron (50 – 80%); minor increases were also observed in the AS and PYRO fractions (Fig. 3.5b). Digests of the November 2000 samples exhibited a continued increase in total iron with an average value of 14.2 g·kg^{-1} (range: 10.9 – 17.4 g·kg^{-1}). As with the June 2000 samples, the increase occurred largely in the recalcitrant fraction (65 – 90%).

The average total iron concentration in the orange zone samples from June 2000 was 101.3 g·kg^{-1} (range: 56.4 – 162.2 g·kg^{-1}); this was almost two orders of magnitude higher than the initial substrate and an order of magnitude greater than the gray zone totals (Fig. 3.5a). Sequential extractions demonstrated the increase occurred overwhelmingly in the recalcitrant fraction (Fig. 3.5b). Subdivision of the recalcitrant fraction showed that the R_{res} step accounted for very little (<5%) of the total iron, whereas the R_{ox} and R_{cd} fractions combined accounted for 80 – 90% of the total iron. The distribution of iron between the R_{ox} and R_{cd} fractions was variable, although the R_{cd} fraction was generally the dominant phase (3:2 for R_{cd}:R_{ox}). There was also a notable increase in the PYRO fraction and compared to the gray zone, the AS fraction was often lower. Digests of the November 2000 oxide zone samples showed a continued increase in iron over time with an average value of 116.4 g·kg^{-1} (range: 82.4 – 158.1 g·kg^{-1}), although there was overlap with June 2000 values. Sequential extractions showed that iron distribution did not change in any predictable way over time.

3.3.2. Aluminum. Total digests of the initial substrate showed that the starting aluminum concentration averaged 1.6 $g \cdot kg^{-1}$ (range: 1.1 – 2.1 $g \cdot kg^{-1}$; Fig. 3.6a). Sequential extractions indicated that approximately 90% of the initial aluminum was partitioned in the recalcitrant phase (Fig. 3.6b). Within the recalcitrant fraction, the R_{res} fraction accounted for the majority of the extracted aluminum (>80%). There was no aluminum detected in R_{ox} extracts. The remaining aluminum was largely bound in the PYRO phase.

Total digests of the black zone collected in June 2000 averaged 2.6 $g \cdot kg^{-1}$ (range: 1.2 – 6.9 $g \cdot kg^{-1}$); they were only slightly higher than the initial substrate. Where increases relatively higher than the initial substrate were noted, they occurred in the AS and PYRO fractions. The average total aluminum concentration from the November 2000 digests was 2.1 $g \cdot kg^{-1}$ (range: 0.7 – 4.4 $g \cdot kg^{-1}$) and these values were indistinguishable from those measured in June 2000. Likewise, sequential extraction of November 2000 samples exhibited similar distribution patterns relative to June 2000 samples. Increases mainly occurred in the AS and PYRO steps with minor increases in the recalcitrant fraction.

The average total aluminum concentration from the June 2000 gray zone samples was 9.7 $g \cdot kg^{-1}$, which was more than six times higher than the initial substrate concentration; however, the range in values was wide (1.4 – 25.6 $g \cdot kg^{-1}$). Sequential extractions showed increases occurred in the AS (40 – 70%), PYRO (15 – 25%), and recalcitrant (10 – 40%) fractions. Upon further subdivision of the recalcitrant phase, 95% of the aluminum was extracted in the R_{res} step. Digests of November 2000 gray zone samples indicated that aluminum accumulation increased over time; the average total aluminum concentration, 38.6 $g \cdot kg^{-1}$ (range: 20.9 – 50.9 $g \cdot kg^{-1}$), was almost four times higher than the June 2000 samples. By the end of the project, total aluminum concentrations were 10 – 30 times greater in the gray zone compared to the initial substrate. As with the June samples, increases in aluminum were observed in all extraction steps in proportions similar to the increases observed in the June samples; the greatest increases were measured in the AS, PYRO, and recalcitrant steps.

Aluminum concentration from total digests of June 2000 core samples collected from the orange zone averaged 22.0 $g \cdot kg^{-1}$, which was nearly 15 times greater than the initial substrate and more than double the concentration measured in the gray zone. However, the range of values was wide (7.6 – 31.9 $g \cdot kg^{-1}$). It is noteworthy that, within a single core, samples taken in June 2000 from the orange zone were generally higher in aluminum than the underlying gray zone. Sequential extraction indicated that for samples with high total concentrations (i.e., > 25 $g \cdot kg^{-1}$), aluminum distribution was similar to gray zone samples with similar total aluminum values; most of the aluminum was extracted in the AS, PYRO, and recalcitrant fractions. Within the recalcitrant fraction, the distribution shifted relative to the initial substrate with an increase in the R_{ox} phase (50 – 75% of the recalcitrant fraction; Table 3.3). Total digests of the November 2000 samples showed that the average aluminum concentration (11.7 $g \cdot kg^{-1}$) decreased during the six months between sampling, although the range of values was still relatively wide (4.6 – 25.0 $g \cdot kg^{-1}$). In contrast to June 2000 samples, the November 2000 orange zone aluminum totals from a single core were generally lower than the underlying gray zone samples. Sequential extractions indicated the largest decreases in aluminum occurred in the AS and PYRO phases, although decreases were observed in most other fractions.

3.4. Substrate analysis – qualitative test for AVS

A faint smell of hydrogen sulfide was observed in black zone samples collected in the field. Further hydrogen sulfide was detected by smell when opening the Oakridge tubes after acid soluble extraction of samples from the gray and black zones, suggesting some of the acid soluble iron was associated with acid volatile iron monosulfides. The hydrogen sulfide smell was not noted for any other extraction step. Every sample from the gray and black zones produced measurable quantities of black Ag_2S precipitate during the qualitative test for the presence of AVS. Thus, qualitatively, the data supported the contention that iron monosulfides were generated in the LBOS below the orange layer.

3.5. Substrate analysis – XRD and EM data

3.5.1. Initial substrate. The LBOS was composed of a 1:4 mixture by volume of limestone and organic matter. The major solid components of polished chips observed by electron microprobe were: limestone, organic matter (mainly woodchips), and quartz (Fig. 3.7). Based on electron photomicrographs, limestone and organic matter were by far the most abundant solids. Fine-grained (<10 μm) limestone fragments rimmed individual particles of organic matter and larger pieces of limestone (> 100μm), and occurred within cavities of the larger limestone fragments (Fig. 3.7a,b,c). The organic material contributed a small mineral component to the LBOS from detrital material associated with the composted stable waste. The bulk of this detritus was quartz (i.e., “free quartz”; Fig. 3.7d), although minor amounts of ilmenite, rutile, and zircon were also noted. Minor quartz was also observed associated with the limestone (Fig. 3.7c). Rare pyrite grains were observed associated with the limestone; they were anhedral and larger than 50 μm (Fig. 3.7b). Pyrite framboids (10 – 20 μm diameter; not shown) were observed rarely and they were always associated with limestone.

3.5.2. Orange zone. The orange layer was fairly nondescript; organic fragments and orange ochreous precipitates were the only discernible components in hand sample. Qualitative EDS analysis indicated that some of the iron-bearing solids contained minor amounts of sulfur and aluminum (Fig. 3.8a). X-ray diffraction analysis of orange zone material displayed sharp and distinct peaks indicative of fairly well-crystallized goethite as well as broader peaks of poorly crystalline material attributable to poorly-crystalline goethite, schwertmannite, and/or ferrihydrite (Fig. 3.9). The only other mineral identified in the orange zone by XRD was quartz.

Back-scatter imaging coupled with EDS analysis showed that the orange zone was comprised of chemically and/or texturally unique layers (Fig. 3.10). The uppermost portions of the orange zone contained only three components: organic fragments (largely wood), iron precipitates, and quartz (Fig. 3.10a). Limestone was not observed and calcite was not detected by XRD (see Fig. 3.9). The iron precipitates displayed colloidal textures indicative of rapid precipitation (Ramdohr, 1980; Ineson, 1989), including spherical or “bubbly” textures (blue arrows, Fig. 3.10a), dendritic textures (orange arrows, Fig. 3.10a; also Fig. 3.10b), and botryoidal textures (green arrows, Fig. 3.10a,d).

Spherical textures were observed in open voids between grains, while dendritic and botryoidal growth habits nucleated from preexisting surfaces (i.e., wood fragments, quartz grains). In addition to the dendritic coatings, iron was found rimming almost all organic fragments, often permineralizing the outer edges of the fragments (Fig. 3.10c). Dendritic and botryoidal forms were also found nucleating from the convex side of arcs that partially enclosed empty space indicating iron oxyhydroxides enveloped grains that were subsequently dissolved away (Fig. 3.10a). Irregular and kidney-form patches of dendritic iron oxyhydroxide typically occurred within the boundary of former grains (Fig. 3.10a). Apparent skeletal replacement also occurred; former grains were outlined by botryoidal-textured iron coatings and completely replaced by sinuous skeletal-iron oxyhydroxide (Fig. 3.10d). Iron oxyhydroxide replacement textures were restricted to the upper half of the orange zone.

Aluminum precipitates occurred with greater frequency towards the bottom of the orange layer. Aluminum precipitates initially occurred intergrown with bands of dendritic iron precipitates, but with depth they occurred more frequently as very small (<500 µm), isolated patches and curved bands. The patches often contained subrounded voids (Fig. 3.10e) and the bands were usually arranged in a circular manner around an open space with aluminum precipitates thinly dispersed in the interior (Fig. 3.10f). Based on evidence presented in the gray zone (see below), the cavities outlined by the aluminum precipitates were probably relict limestone grains. Rare pyrite grains occurred in the lower portions of the orange zone and they were commonly associated with relict limestone grains (Fig. 3.10e).

3.5.3.Gray zone. In handsample, the gray zone appeared as white, friable hardpan that cemented organic fragments. Qualitative EDS analysis indicated that the gray zone was not mineralogically complex, containing only calcite (i.e., limestone), quartz, gypsum, pyrite, and an aluminum-bearing phase, in addition to the organic material. This mineralogy was confirmed by XRD analysis, which disclosed sharp distinct peaks for calcite, quartz, gypsum, and pyrite (Fig. 3.11). Although the powdered sample used for XRD analysis had an Al:Ca ratio of ~0.6, there were no minerals identified that could account for the aluminum-bearing phase. Qualitative EDS analysis of the aluminum precipitates indicated they were composed mainly of aluminum and sulfur (see Fig. 3.8b).

Back-scatter imaging coupled with EDS analysis indicated that the boundary between the orange and gray zones was characterized by a rapid shift from iron- to aluminum-dominated coatings and textures. Iron precipitates were still present in the upper portions of the gray zone, but they occurred as isolated patches and intergrowths within bands of the aluminum-sulfate precipitates. Abundant relict limestone grains outlined by aluminum-sulfate crusts were typical in the upper portions of the gray zone (Fig. 3.12a), although they were largely devoid of limestone. Gypsum, identified by EDS (not shown) and confirmed with XRD (Fig. 3.11), was occasionally observed within the boundary of the relict limestone grains (Fig. 3.12b,c) in the upper portions of the gray zone. Partially dissolved, the gypsum occurred as subrounded grains sparsely scattered within the bounds of former limestone fragments. Occasionally, aluminum-sulfate precipitates within the largely dissolved limestone relicts preserved the original euhedral, blocky shape of the gypsum (Fig. 3.12c). These aluminum-sulfate precipitates outlined relict gypsum grains within remnant limestone grains in the lower portions of the orange zone (e.g., see Fig. 3.10f).

With depth, gypsum (Fig. 3.12c) and minor amounts of remnant limestone increasingly occupied the interior of aluminum crusts, which outlined the former limestone grain boundary. Midway through the gray zone, the abundance of aluminum- and calcium-sulfate precipitates peaked and remnant limestone was ubiquitous within the aluminum crusts. In addition to forming coatings around limestone, aluminum-sulfate precipitated within intergranular primary porosity and occasionally cemented organic fragments together. While primary porosity was occluded by aluminum-sulfate precipitates, secondary porosity created by the dissolution of limestone was maintained by the aluminum-sulfate precipitate reaction rims around relict limestone grains. Gypsum was typically found within the boundaries of former limestone grains, although organic fragments were occasionally found permineralized by calcium sulfate. Small (<10 μm) remnant fragments of limestone were found enveloped by gypsum (Fig. 3.12d); however, the gypsum-limestone intergrowth was only found along former limestone grain boundaries (Fig. 3.12e). Most gypsum that precipitated within the relict limestone grains was devoid of trapped limestone and it was commonly coated by aluminum-sulfate precipitates. Gypsum was generally not found in the lower half of the gray zone and the abundance of aluminum-sulfate precipitates decreased with depth.

Pyrite framboids (yellow arrows, Fig. 3.12), identified by EDS (not shown) and confirmed in bulk samples by XRD (Fig. 3.11), were scarce in the upper portions of the gray zone. However, framboids exhibited a trend of increasing abundance with depth, concomitant with the appearance of partially-dissolved limestone and the disappearance of iron precipitates. Pyrite framboids were small (10 – 30 μm diameter), well-crystallized based on XRD analysis, and largely associated with surfaces (i.e., found closely associated with wood fragments, quartz grains, and limestone). In the middle of the gray zone where aluminum-sulfate precipitates and pyrite framboids were both common, framboids were typically engulfed by aluminum-sulfate precipitate reaction rims surrounding an associated surface (e.g., Fig. 3.12f). This textural relationship was commonly observed down into the upper reaches of the underlying black zone. At the contact between the gray and black zones, limestone was pristine, exhibiting few signs of dissolution, aluminum-sulfate precipitate coatings were sparse, and pyrite framboids were ubiquitous. Iron sulfides were the only metal sulfide found in the gray zone.

3.5.4. Black zone. The black zone was characterized by a sharp decrease in the amount of aluminum-sulfate precipitates, the occurrence of pristine limestone, ubiquitous iron sulfides, and a lack of gypsum (Fig. 3.13). In the upper portions of the black zone, aluminum-sulfate precipitate textures were indistinguishable from the overlying gray zone, largely occurring as reaction rims with dendritic overgrowths around quartz, organic fragments, and partially dissolved limestone (Fig. 3.13a). Additionally, organic fragments were often found permineralized by aluminum sulfate (Fig. 3.13b). As the amount of aluminum-sulfate precipitate diminished with depth, the predominant habit shifted from reaction rims associated with limestone to permineralized organic fragments.

Pyrite framboids were ubiquitous in the black zone; however they were largely concentrated in clusters and proximal to grain surfaces (i.e., limestone, quartz, or wood; yellow arrows, Fig. 3.13b,c,d) or former grain surfaces (yellow arrows, Fig. 3.13a). Framboids were found intimately associated with aluminum-sulfate precipitate in the upper reaches of the black zone. Pyrite was commonly encapsulated by aluminum-sulfate precipitate (Fig. 3.13a,d). Sulfide content was greatest at the top of the black zone and gradually decreased with depth. In the lower reaches of the black zone, framboids were found in close proximity to limestone grains (Fig. 3.13e,f) and organic fragments, or within wood vesicles. Although framboids were the dominant crystal habit, loose collections of very small (<1μm) pyrite spheres were also occasionally noted (green arrows, Fig. 3.13c,d). The tiny spheres were identical in size and shape to the individual pyrite crystallites that comprised the framboids. Large (>50μm) anhedral pyrite grains were rarely encountered (Fig. 3.13c). This large, non-framboidal iron sulfide was likely inherited from the limestone in the original substrate. Rare trace metal sulfides (e.g., cobalt, nickel, and zinc) were also identified in this zone (see chapter 4). Although in hand sample the black color that distinguished this zone was likely attributable to iron monosulfides (i.e., amorphous FeS, mackinawite, greigite) and acid volatile sulfides, they were only qualitatively identified (as described earlier). Upon exposure to air, the samples from the black zone turned a brownish color, suggesting the iron monosulfides were oxidized. Therefore, due to the oxygen sensitive nature of iron monosulfide compounds, detection by XRD or electron microprobe was probably not possible with the techniques employed; iron monosulfides were likely lost during sample preparation.

4. Discussion

One of the main goals of this study is to define the three reaction zones based on their key physicochemical characteristics. The orange reaction zone, which occupied the upper 7 to 10 cm of the LBOS, was characterized by ferric iron oxyhydroxides. While results from chapter 2 showed that the gray zone was the site of active limestone dissolution, results from this study indicate that it was also the site of aluminum precipitation (discussed below) and the transition from iron oxyhydroxides to iron sulfides. Finally, the black zone was the site of iron sulfide precipitation. Because most of the color change between the orange, gray, and black zones can be attributed to changes in iron chemistry, the three reaction zones are hereafter referred to as the oxide, transitional, and sulfide zones, respectively.

In addition to the peeper pore water samples presented in this chapter, pH and dissolved iron and aluminum concentrations in pore water collected with a swamper pore water sampler were presented in chapter 2. Swamper samples were extracted in three different locations from two different tanks (30A and 36A) for a total of six pore water profiles. The average and standard deviation of the six swamper profiles are also plotted in Fig. 3.3 for comparison to the single pore water profile generated with the peeper data. Although the swamper samples were collected from three specific sampling depths (2, 11, 19 cm; see chapter 2), four centimeters were added to each swamper sampling depth (i.e. 6, 15, 23 cm) in order to match the data with the peeper analysis. The offset between the two data sets may be due to differences in sampling technique or from differences between the tanks sampled; the swamper data were collected two weeks after the peeper and from different tanks. The swamper also employed a strong vacuum to extract the sample and therefore may have pulled pore water from slightly deeper than was originally targeted.

Based on visual observations of several cores (e.g., Fig. 3.4), the swamper and peeper pore water data can be spatially correlated to the three reaction zones (Fig. 3.14). The average thickness of the orange zone was approximately 10 cm and therefore, the first two peeper well horizons below the substrate-ARD interface (2.5 and 7.5 cm) and the 6 cm swamper sampling depth are representative of the oxide zone. Pore water data shows that over this interval all of the dissolved ferric iron is precipitated, which is in agreement with the ferric iron precipitates observed in the oxide zone. Based on the shift from maximum dissolved aluminum concentration at 7.5 cm to complete removal of dissolved aluminum by 12.5 cm, changes in the pore water chemistry of the transitional zone were most likely recorded by changes in the peeper data collected between the second and third peeper well horizon (7.5 and 12.5 cm). Likewise, changes in the ferrous iron content of the pore water indicated that the 17.5 and 22.5 cm peeper well horizons and the 15 and 23 cm swamper sampling depths are representative of the sulfide zone.

4.1. Mineralogy of Iron and Aluminum hydroxy-precipitates.

4.1.1. Iron. The ochreous precipitates found in the oxide zone resulted from the neutralization of a low-pH, ferric iron dominated ARD during limestone dissolution followed by the hydrolysis and precipitation of dissolved ferric iron. Of the common ochreous precipitates, only goethite, schwertmannite or ferrihydrite are possibilities for the precipitates analyzed in the oxide zone. The presence of goethite was unambiguous in the XRD data. However, peak broadening could not rule out the presence of poorly crystalline ferrihydrite and/or schwertmannite (Fig. 3.9). Goethite was distinguished from ferrihydrite and/or schwertmannite chemically. Because goethite is essentially insoluble in oxalate irrespective of crystal size and both ferrihydrite and schwertmannite are soluble (Schwertmann and Cornell, 2000), the ratio of oxalate soluble iron (Fe_o) to total iron "oxide" (Fe_t, where Fe_t = oxalate-extractable (R_{ox}) iron + dithionite-extractable (R_{cd}) iron) yields the combined proportion of ferrihydrite and schwertmannite in the sample (Schwertmann and Cornell, 2000). For the oxide zone, approximately 40 to 50% of the total iron oxide (i.e., $R_{ox} + R_{cd}$) was extracted in the R_{ox} fraction. Therefore, the Fe_o/Fe_t was approximately 0.4 to 0.5, indicating about 50 to 60% of the ochreous precipitates were goethite with the remaining iron being bound in ferrihydrite and/or schwertmannite. Because sulfur was only occasionally detected with iron in EDS analyses (Fig. 3.8a), the amount of schwertmannite in the ochreous precipitates, if at all present, was fairly minor. Goethite is known to adsorb sulfate (Schwertmann and Cornell, 2000) and, therefore, the presence of low sulfur quantities in the EDS analysis does not require that any schwertmannite exist in the oxide zone. Broadening of the goethite XRD peaks (Fig. 3.9), the abundance of an oxalate-extractable iron oxide, and the low amount of sulfur in the EDS analysis does imply that a significant amount of ferrihydrite precipitated in the oxide zone.

4.1.2. Aluminum. May and Nordstrom (1991) showed that when aluminum-bearing ARD is rapidly neutralized, an aluminum-hydroxysulfate compound precipitates immediately. This precipitate is usually white, and is most commonly amorphous. Back-scatter electron images of this study indicated distinct aluminum precipitates were ubiquitous in the transitional zone and EDS analysis demonstrated the aluminum precipitates were aluminum-sulfate compounds (Fig. 3.8b).

Given the large distinct peaks for calcite and gypsum in XRD diffractograms (Fig. 3.11), and the ~0.6 Al:Ca ratio in the powdered sample used for XRD analysis, it was anticipated that, if a crystalline aluminum compound was present, there was enough of it in the sample for detection. However, all peaks were accounted for by only four minerals (calcite, gypsum, pyrite, and quartz). Thus, it seems that the aluminum precipitates found in the LBOS were similar to the white, amorphous aluminum-hydroxysulfate compounds previously described (May and Nordstrom, 1991; Robbins et al., 1996; Nordstrom and Alpers, 1999).

4.2. Development of the three reaction zones

4.3.1. Initial conditions of the LBOS. The LBOS was mixed to promote carbonate-buffering reactions. Effluent pH from the LBOS was generally > 6.5 and depleted of iron and aluminum due to the precipitation of oxyhydroxides and sulfate minerals, respectively. Moreover, results from chapter 2 showed that the effluent was close to saturation with respect to calcite. At the beginning of the experiment, the LBOS surface would have been the site of an initial “zone of active limestone dissolution”. Dissolved ferric iron and aluminum would have rapidly precipitated at relatively high pH in this initial dissolution zone. Textural evidence from the upper oxide zone (0 – 2 cm) shows that ferric oxyhydroxide (Fig. 3.10a,d) initially precipitated in the presence of limestone during the formation of this initial dissolution zone. The bands of ferric iron (Fig. 3.10a) solids enclosing open cavities were most likely outlining relict limestone grains from the initial substrate that were completely dissolved away. In addition to outlining the shape of former limestone grains, ferric iron solids were also found replacing limestone grains (Fig. 3.10d).

Below the initial dissolution zone, after the complete removal of ferric iron, pore water conditions (i.e., waters were sulfate-rich, organic material was available, and pH > 6.5) would have been conducive to biological sulfate reduction (Widdel, 1988) and sulfide precipitates probably formed. It is conceivable that an initial sulfide zone would have developed just below the initial dissolution zone. Thus initially, the LBOS would have consisted of two main zones, a zone of active limestone dissolution containing mixed ferric oxyhydroxides and aluminum hydroxysulfates and a zone of unreacted limestone containing sulfide.

Continued precipitation of aluminum and iron in the initial dissolution zone eventually resulted in the complete removal of limestone. As limestone was depleted from the initial dissolution zone, pore-water pH would have declined abruptly until the dissolution of aluminum hydroxysulfate was favored (Morin et al., 1988; Blowes and Ptacek, 1994). Aluminum removed from the initial dissolution zone was reprecipitated deeper in the substrate (i.e., transitional zone), resulting in the segregation of iron and aluminum precipitates and development of the three distinct reaction zones observed.

4.3.2. Development of the oxide zone. Peeper data indicated a steady increase in dissolved aluminum above influent concentrations in the oxide zone (to 7.5 cm depth; Fig. 3.3), supporting the mobilization of previously precipitated aluminum from the oxide zone. Swamper data showed similar results (chapter 2). The total digest data further support the dissolution of secondary aluminum precipitates from the oxide zone. Total digests of the June 2000 cores indicated that the oxide zone accounted for the majority of the aluminum sequestered in the LBOS. Sixty-nine percent of total aluminum retained from the influent was captured in the oxide zone. However, by November 2000, the oxide zone accounted for only 25% of the total aluminum retained in the system (Fig. 3.6). Back-scatter electron imaging of the oxide zone from the November 2000 cores showed only occasional distinct aluminum hydroxysulfate precipitates and all were isolated in the bottom of the oxide zone near the contact with the transitional zone (Fig. 3.10e,f).

Due to the amphoteric nature of aluminum, the aluminum hydroxysulfate was likely extracted in the AS (pH ~2) and PYRO (pH ~10) sequential extraction steps, which accounted for the bulk of aluminum extracted from the oxide zone. Aluminum bound to labile organic matter may have also contributed to the PYRO fraction; however, distinction between organically bound aluminum and aluminum hydroxysulfate was not possible. Aluminum as measured by EDS was also occasionally found in association with iron oxyhydroxide precipitates (i.e., as a coprecipitate and not a distinct aluminum-bearing compound at the resolution of sampling). Even though aluminum may theoretically coprecipitate (Schwertmann and Cornell, 2000), sequential extractions indicated that only 10 – 20% of the total aluminum in the oxide zone was associated with iron oxides (i.e., R_{ox} and R_{cd} extraction steps; Fig. 3.6).

Despite the drop in pH and dissolution of aluminum hydroxysulfate, conditions in the oxide zone below 2.5 cm were appropriate for the precipitation of ferric iron (Fig. 3.3). While the dissolution of aluminum hydroxy-minerals typically buffers pH between 4.0 and 4.3 (Blowes and Ptacek, 1994), the precipitation of ferric oxyhydroxides will quickly depress the pH to <3.5. Thus, if there was sufficient aluminum hydroxysulfate present, then the pore water pH would be held at >4.0, but if the precipitation of ferric iron overwhelmed the buffering capacity generated by the dissolution of aluminum hydroxysulfate, then the pH will drop. The direct relationship between ferric iron precipitation and aluminum dissolution is evident in the peeper pore water data from the upper 7.5 cm of the LBOS (Fig. 3.3). It is notable that ferric iron precipitation and aluminum dissolution occurred at pH of 2.3 to 3.8 over this depth interval, indicating that the rate of ferric iron precipitation overwhelmed the rate of aluminum hydroxysulfate dissolution. However, these conditions are not usually conducive to the rapid precipitation of ferric hydroxy-compounds (Stumm and Morgan, 1981). In fact, decreases in ferric iron mirrored by increases in dissolved aluminum occurred in the LBOS at near influent pH levels (see Fig. 3.3). Thus, it appears that the dissolution of aluminum hydroxysulfate may be directly related to the precipitation of iron hydroxy-compounds as follows (using aluminite, $Al_2SO_4(OH)_4 \cdot 7\ H_2O$, as an example aluminum hydroxysulfate):

$$4\ Fe^{+3} + 3\ Al_2SO_4(OH)_4 \cdot 7\ H_2O \Leftrightarrow 4\ Fe(OH)_3 + 6\ Al^{+3} + 3\ SO_4^{2-} + 21\ H_2O \qquad (1).$$

Of the total dissolved iron removed from the influent ARD, >90% of it was retained in the oxide zone. The percentage of the influent iron removed remained constant between June and November 2000. The only way the oxide zone could consistently retain >90% of the influent iron without increasing the total concentration of sequestered iron was through steady growth of the oxide zone with advancement of the limestone dissolution front.

Sequential extractions indicate that ~15% of the iron retained in the oxide zone was associated with organic matter (Fig. 3.5). Iron rims around most organic fragments (e.g., Fig. 3.10a) coupled with the permineralization of a wood fragment (Fig. 3.10c) strongly supports organic complexation as a removal process of influent iron. However, the major metal removal process in the oxide zone was the precipitation of ferrihydrite and goethite (R_{ox} and R_{cd} fractions, respectively), accounting for 70 – 85% of the total iron (Fig. 3.5).

In addition to ferric iron precipitation, peeper data also indicated that there was dissolved ferrous iron generated in the oxide zone. Possible mechanisms for the generation of ferrous iron in the oxide zone include abiotic reduction of ferric iron hydrogen sulfide or the dissolution of pyrite; the low pH (<3.8) of the oxide zone was considered prohibitive to significant microbial reduction of ferric iron (Ehrlich, 1990). Results presented in chapter 2 showed that dissolved hydrogen sulfide was detected below the limestone dissolution front. Results from chapter 2 also demonstrated that there was a flux of carbon dioxide escaping from below the limestone dissolution front. Therefore, hydrogen sulfide generated at depth (i.e., sulfide zone) could have bubbled up through the oxide zone potentially reducing aqueous ferric iron or precipitated ferric solids (Rickard, 1974; Stanton and Goldhaber, 1991; Canfield et al., 1992).

Another potential pathway for the abiotic reduction of ferric iron involves the oxidative dissolution of pyrite, where dissolved ferric iron is reduced and the sulfur moiety is oxidized (Stumm and Morgan, 1981):

$$FeS_2 + 14\ Fe^{3+} + 8\ H_2O \Leftrightarrow 15\ Fe^{2+} + 2\ SO_4^{2-} + 16\ H^+ \qquad (2)$$

This reaction not only reduces influent ferric iron, but also dissolves pyrite, releasing additional ferrous iron. Ferric iron is a strong oxidant (Evangelou, 1995) and, therefore, any pyrite present in the oxide zone would have been subjected to oxidative dissolution by influent ferric iron. At the beginning of the experiment, minor amounts of pyrite were noted in the limestone fraction of the LBOS. By the end of the study, pyrite was rarely observed in the oxide zone and always found in the lower portions suggesting that pyrite was dissolved from the upper portions of the oxide zone. However, it is questionable whether there was enough initial pyrite in the oxide zone to solely account for the increases in ferrous iron observed in the pore water samples.

4.3.3. Development of the transitional zone. Once mobilized from the evolving oxide zone, aluminum was transported and reprecipitated in the developing, carbonate-buffered transitional zone. The rapid decrease in dissolved aluminum concentration between 7.5 and 12.5 cm following the concentration spike observed in the oxide zone (Fig. 3.3), supports the contention that aluminum is reprecipitated in the transitional zone. Total digests of the transitional zone over time further support the dissolution of aluminum from the oxide zone and reprecipitation in the transitional zone (Fig. 3.6). In June 2000, the transitional zone accounted for only 28% of the total aluminum sequestered in the LBOS, but, by November 2000, 74% of the total aluminum was sequestered in the transitional zone. Sequential extractions indicated that, similar to the oxide zone, aluminum hydroxysulfate (AS and PYRO steps) accounted for the majority of aluminum sequestered in the transitional zone (Fig. 3.6). However, rims rich in aluminum and sulfur were occasionally noted around organic fragments during electron microprobe analysis, indicating that binding to organic matter contributed at least a minor amount to the aluminum extracted in the PYRO step.

Back-scatter electron imaging of the transitional zone indicated the amount of aluminum hydroxysulfate increased with depth until approximately midway through the zone, after which the amount decreased sharply to the bottom of the transitional zone (Fig. 3.12). The increase paralleled the increase in the amount of limestone observed in chapter 2, until below the midway point in the transitional zone, where limestone appeared largely unreacted. Moreover, aluminum hydroxysulfate commonly precipitated in reaction rims surrounding limestone grains. This close spatial relation indicates that the precipitation of aluminum hydroxysulfate (using aluminite as an example):

$$2\ Al^{+3} + SO_4^{2-} + 11\ H_2O \Leftrightarrow Al_2SO_4(OH)_4 \cdot 7\ H_2O + 4\ H^+ \qquad (3)$$

was likely generating protons that were driving limestone dissolution (for details see chapter 2). In fact, the presence of limestone at peak aluminum hydroxysulfate precipitation (Fig. 3.12) suggests that aluminum precipitation should have occurred under carbonate-buffered conditions (pH >6.5; Blowes and Ptacek, 1994). However, peeper pore water data indicated that aluminum sulfate precipitated at pH 3.8 – 4.6. Thus, even though limestone was still present at peak aluminum precipitation (Fig. 3.12), the precipitation rate of aluminum hydroxysulfate overwhelmed the buffering capacity generated through limestone dissolution.

In addition to aluminum hydroxysulfate precipitation driving limestone dissolution in the transitional zone, the precipitation of aluminum hydroxysulfate reaction rims around limestone grains may have induced gypsum formation. Electron microprobe analysis showed that most of the aluminum precipitated in close association with limestone formed mainly as enveloping reaction rims. Localization of aluminum hydroxysulfate proximal to limestone demonstrates that precipitation may have been a surface-mediated reaction occurring at locally higher pH immediately adjacent to the limestone grain. Over time the aluminum hydroxysulfate reaction rim around limestone grew as precipitation of aluminum and concurrent dissolution of limestone continued. Eventually, the reaction rim was thick enough to limit the diffusion of calcium ions away from the dissolving limestone surface. This led to a localized build up of calcium with subsequent precipitation of gypsum and can explain why gypsum was only found in the interior of relict limestone grains outlined by aluminum hydroxysulfate. Over time, limestone was completely removed from the gypsum-bearing horizons within the transitional zone and consequently, the pore water pH dropped and the concentration of dissolved calcium decreased. Following the complete removal of limestone, the buffering capacity of the substrate shifted to the dissolution of aluminum hydroxysulfate, which held the pH between 2.3 and 3.8. The drop in calcium concentration led to the dissolution of gypsum. Consequently, in the oxide zone, only relict textures (Fig. 3.10f) indicated the former presence of gypsum originally formed in the transitional zone.

In addition to being the site of active limestone dissolution in the LBOS, the transitional zone also represented the transition between oxidized and reduced forms of iron. However, the transitional zone accounted for only 7 to 8% of the total iron removed in the three reaction zones. Back-scatter electron imaging showed that, although iron oxyhydroxide precipitates were present in the upper portions of the transitional zone, their abundance was lower than the overlying oxide zone and they diminished rapidly with depth. The sequential extractions confirmed the minor abundance of iron oxides in the transitional zone, with the iron oxide fractions accounting for <25% of the total iron retained (Fig. 3.5). Based on XRD (Fig. 3.11) and electron microprobe (Fig. 3.12) analyses, the remaining 80% of the recalcitrant iron fraction (i.e., the R_{res} phase) was most likely pyrite.

Although the majority of the transitional zone iron was extracted in the recalcitrant fraction (Fig. 3.5), up to 30% was extracted in the pyrophosphate and acid soluble steps. Iron extracted in the PYRO step was most likely partitioned to labile organic matter. The most likely acid soluble, potentially iron-bearing compounds identified (indirectly) in the LBOS was iron monosulfide. The presence of acid volatile sulfides in the LBOS was confirmed through several lines of reasoning: 1) rapid oxidation of the substrate from black to brown upon exposure to air (see chapter 2); 2) smell of hydrogen sulfide at the end of the acid soluble extractions; and 3) by the qualitative 6 N HCl extractions with precipitation of Ag_2S.

While ferrous iron solids (i.e., pyrite and AVS) were identified in the transitional zone, they were likely inherited from the sulfide zone (discussed below), as peeper pore water indicated ferrous iron was liberated from the substrate based on the increase in dissolved ferrous iron with depth (Fig. 3.3). Moreover, because there was only a minor amount of solid ferric iron and no dissolved ferric iron in the transitional zone, the increase in dissolved ferrous iron observed in the transitional zone was attributed to the dissolution of ferrous iron-bearing AVS. Pore water pH in the transitional zone (<4.6) was low enough to induce the dissolution of most acid volatile sulfides (e.g., Kennedy et al., 1998); however, pyrite is stable at this pH (e.g., Cornwell and Morse, 1987; Raiswell et al., 1994).

4.3.5. Development of the sulfide zone. The sulfide zone, which was characterized by ubiquitous iron sulfides, developed in front of the advancing limestone dissolution front. Based on pH constraints, the sulfide zone was the only reaction zone conducive to sulfate reduction (i.e., pH > 4.6; Widdel, 1988) and consequently, sulfide precipitation. Moreover, as the limestone dissolution front migrated deeper into the substrate over time, the sulfide zone was overprinted by the advancing transitional zone. Therefore, all authigenic iron sulfides found in the LBOS were most likely precipitated in sulfide zone. This is further substantiated by the peeper data, which indicated that the ferrous iron liberated from above the limestone dissolution front (i.e., oxide and transitional zones) was removed in the sulfide zone.

The paragenetic position of framboidal pyrite lends further credence to a sulfide zone origin for the pyrite observed in electron microprobe photomicrographs (Fig. 3.13). Early in the development of the reaction zones, a transitional zone would have developed near the substrate-ARD interface and overprinted the sulfide zone underlying the initial dissolution zone. Pyrite framboids and AVS found in the transitional zone were likely inherited from this initial sulfide zone. Back-scatter electron imaging of the sulfide (Fig. 3.13) and transitional (Fig. 3.12) zones showed that when framboidal pyrite was associated with aluminum sulfate, most of the pyrite was engulfed by and, hence, paragenetically older than the aluminum sulfate.

Despite the dark black appearance (Fig 2.4) and ubiquitous presence of framboidal pyrite (Fig. 3.13), the sulfide zone accounted for only 2 – 3% of the total iron removed in the three reaction zones (Fig. 3.5). Pyrite was the only iron-bearing phase observed in the sulfide zone during electron microprobe analysis. As with the transitional zone, the majority of the iron extracted from the sulfide zone resided in the recalcitrant fraction with the balance recovered in the acid soluble and pyrophosphate steps (Fig. 3.5). However, because there were no iron oxyhydroxides identified in the sulfide zone, all of the recalcitrant iron can be attributed to pyrite. Likewise, the acid soluble and pyrophosphate fractions are attributed to iron monosulfide and organically-bound iron, respectively.

Aluminum precipitation in the sulfide zone was insignificant, accounting for <1% of the total aluminum sequestered in the LBOS. Total digest and sequential extraction analyses indicated that most of the aluminum extracted from the sulfide zone may have been inherited from the initial substrate (Fig. 3.6). Sequential extractions showed that initial LBOS aluminum was largely removed during the residual extraction step. Although not observed in back-scatter electron imaging, it is reasonable to assume aluminosilicates (i.e., clays) containing recalcitrant, yet strong-acid extractable (i.e., HNO_3) aluminum likely contributed most of the total aluminum extracted. In addition, sequential extraction of the sulfide zone also yielded acid soluble (~10 – 25%) and organically-bound (~10 – 30%) aluminum. The acid soluble aluminum was probably due to the sparse aluminum sulfates observed in the upper portions of the sulfide zone, while the organically-bound aluminum can be attributed to the increased appearance in the sulfide zone of organic fragments permineralized by aluminum and sulfate (Fig. 3.13b).

4.5. Long-term fate of iron and aluminum precipitates.

In order to discuss the long-term retention of iron and aluminum in RAPS-type alkalinity generating systems, it is necessary to predict the long-term fate of the reaction zones wherein these metals reside. This paper and others (chapter 2 and 4) have demonstrated that three reaction zones were dynamically positioned around a limestone dissolution front such that progressive reaction resulted in the migration of the three zones sequentially through the LBOS. This study showed that the sulfide zone grew downflow of the limestone dissolution front in carbonate-buffered substrate through a sulfide precipitation reaction with ferrous iron released from the oxide and transitional zones. The transitional zone advanced as the carbonate buffering capacity of the LBOS was consumed, consequently overprinting the sulfide zone. Likewise, the oxide zone advanced and overprinted the transitional zone as aluminum hydroxysulfate buffering capacity was depleted. Therefore, the metal retention capacity of the oxide zone and the degree to which the oxide zone overprints and removes previously precipitated iron and aluminum in the transitional and sulfide zones will determine the long-term fate of these metals.

Based on pore water data, total digests, sequential extractions, and back-scatter electron imaging of the oxide zone (Figs. 2.6 – 2.8, 2.12), prediction of long-term aluminum retention is straightforward and similar to previous findings (Watzlaf, 1997). Previous studies (Watzlaf, 1997; Thomas et al., 1999) have shown that aluminum will migrate through a compost layer as the carbonate buffering capacity is consumed when the ARD influent is low in pH (<3.5) and dominated by ferric iron. This is due to the fact that, in these systems, dissolution of secondary aluminum precipitates usually provides substrate buffering once the carbonate has been completely consumed; as soon as enough limestone has been dissolved to limit carbonate buffering, the pH will drop and aluminum precipitates will start to dissolve. Therefore, in addition to being the site of active limestone dissolution, the transitional zone represents a rolling aluminum front. The upper portion of the transitional zone and the lower portion of the oxide zone are zones of active aluminum dissolution, while the middle transitional zone down into the upper sulfide zone is a zone of aluminum precipitation. Eventually, this rolling aluminum front will reach the bottom of the LBOS and result in the release of a large dissolved aluminum spike in the effluent, if flow to the system is continued.

In contrast to aluminum, the fate of sequestered iron is not as simple, due to the multiple phases of iron removal (i.e., sulfides and oxyhydroxides). However, as aforementioned, pyrite was largely absent from the oxide zone indicating it either did not form or was removed. Pyrite removal may be achieved through two possible mechanisms: physical transport or dissolution. Pyrite occurred as small (<1μm) spheres that were predominantly clustered into framboid structures. The framboids were intimately associated with limestone or other larger fragments coated with limestone (e.g., quartz, wood fragments) and, in most instances, appeared to precede the formation of any armoring aluminum precipitates. Consequently, pyrite, originally precipitated on and around limestone fragments, was commonly found engulfed and matrix-supported by aluminum hydroxysulfates (Fig. 3.13a,d). With complete limestone removal, the framboids will be left suspended in the disintegrating remains of the aluminum reaction rim. Dissolution of the aluminum matrix could result in the disaggregation of the framboid into individual pyrite crystallites that could be flushed from the oxide zone. Pyrite that was not physically removed could also be subject to attack by influent ferric iron (Eq. 2). Therefore, iron sulfide removal is considered temporary and it is not anticipated to play a major role in long-term iron retention.

The temporary nature of sulfide removal is, however, trivial considering the percentage of total iron removed as oxyhydroxide in the oxide zone. Thus, it is the long-term stability of the iron oxyhydroxides that will determine the long-term retention of iron. Theoretically, iron oxyhydroxides should have dissolved once enough aluminum hydroxysulfate was removed from the oxide zone to permit pore water pH to fall below 3.5 (Blowes and Ptacek, 1994), but results from this study indicate that ferric iron precipitation continued down to pH 2.3 through ferric iron "replacement" of aluminum precipitates. Thus, even though the pH was conducive for dissolution, iron oxyhydroxide precipitation would be expected to have continued until all aluminum was removed from the oxide zone. Once aluminum was completely removed, it is expected iron oxyhydroxide could eventually dissolve from the upper oxide zone. However, any ferric iron dissolved from the upper oxide zone would be reprecipitated in the lower oxide zone through further aluminum "replacement". Thus, buffering in the upper oxide zone through ferric iron dissolution could ultimately lead to ferric iron enrichment in the lower oxide zone.

One main concern for the long-term retention of iron in the oxide zone is the generation of dissolved ferrous iron. Once ferrous iron was generated in the LBOS, it was either released from the system (effluent average = 15 $mg \cdot L^{-1}$) or it precipitated as a ferrous iron solid (e.g., framboidal pyrite; Fig. 3.12 – 2.13); conditions were not conducive for oxidation to ferric iron. However, acid-volatile iron monosulfides and pyrite precipitated in the sulfide zone were dissolved with the encroachment of the transitional and oxide zones, respectively. Once released from the oxide and transitional zones, ferrous iron was reprecipitated in the sulfide zone. Since ferrous iron removal was cycled through continued precipitation, dissolution, and reprecipitation without significant release, it is expected that eventually a substantial pool of ferrous iron may develop in the transitional and sulfide zones of a RAPS-type system. As observed in the study by Dietz and Stidinger (1996), the organic layer of RAPS-type passive systems is not well suited for removal of large quantities of ferrous iron. Thus, the concentration of ferrous iron in the effluent may increase over time as the recycled ferrous iron pool accumulates and if the sulfide production capacity of the sulfide zone can not keep up with the increased concentration of ferrous iron. This is of particular concern in the winter when sulfide production is seasonally lowest (Watzlaf et al., 2000; see chapter 2). Alternatively the ferrous iron pool may be released as the limestone dissolution front approaches the bottom of the LBOS and there is no longer sufficient substrate available to support continued sulfate reduction.

Thus, as the limestone dissolution front approaches the bottom of the LBOS, the ferrous iron content in the effluent can be expected to increase. Moreover, with continued loading the aluminum concentration will also increase, signaling that the buffering capacity of the limestone is no longer capable of neutralizing the influent ARD. The increase in ferrous iron and aluminum, therefore, can be used as signals that the LBOS is almost spent and requires renovation. A steady, consistent increase in ferrous iron concentration would serve as an early warning indicating that the system should be closely monitored. A steady and consistent increase in aluminum is a signal that ARD should no longer be passed through the system without renovation.

5. Conclusions

The substrate used in this study, a mixture of organic matter and fine-grained limestone, allows for the near permanent removal of iron and aluminum from low pH ferric iron-dominated ARD if the system is properly monitored and decommissioned in a timely manner. Iron was removed as both oxyhydroxides and sulfides; fine-grained iron sulfides were likely ephemeral while oxyhydroxides are possibly a permanent removal phase. The circumneutral pH below a limestone dissolution front assured that aluminum removal was complete. However, when the limestone dissolution front moves completely through the substrate, a pulse of aluminum is expected, after which aluminum will no longer be retained. We propose that the formation of an oxide zone characterized by iron oxyhydroxides, very low neutralizing potential, and minimal amounts of aluminum; a transitional zone dominated by aluminum precipitates; and a zone of active sulfate reduction (sulfide zone) are attributes common to RAPS-type passive systems treating low pH (<3), ferric iron-dominated ($Fe^{3+} \gg Fe^{2+}$) ARD.

It was determined in chapter 2 that the conversion of mineral acidity to proton acidity in the presence of limestone was the key to completely treating low pH ferric iron-dominated ARD and maintaining an alkaline effluent. In this study, we find that it is specifically the aluminum component of mineral acidity (i.e., aluminum hydroxysulfate precipitation) that drives limestone dissolution.

Acknowledgements

This research was funded by Financial Assistance Award Number De-FC09-96SR18546 between the United States Department of Energy and the University of Georgia as a part of the US DOE National Water Research Center. The authors would like to thank the principle investigators of this grant, Dr. Rebbecca Sharitz, Dr. J Vaun McArthur, and Dr. Beverly Collins for their continued support and assistance. The authors would also like to acknowledge Linda Paddock, Daniel Coughlin, Matt Opdyke, and Morris Jones for their technical assistance in sample processing.

Literature Cited

Blowes D. W. and Ptacek C. J. (1994) Acid-neutralization mechanisms in inactive mine tailings. In *The Environmental Geochemistry of Sulfide Mine-Wastes, Short Course Handbook*, Vol. 22 (ed. J. L. Jambor and D. W. Blowes), pp. 271 - 292. Mineralogical Association of Canada.

Canfield D. E., Raiswell R., and Bottrell S. (1992) The reactivity of sedimentary iron minerals toward sulfide. *American Jounral of Science* **292**, 659-683.

Cornwell J. C. and Morse J. W. (1987) The characterization of iron sulfide minerals in anoxic marine sediments. *Marine Chemistry* **22**, 193 - 206.

Ehrlich H. L. (1990) *Geomicrobiology*. Marcel Dekker.

Evangelou V. P. (1995) *Pyrite Oxidation and Its Control*. CRC Press.

Ineson P. R. (1989) *Introduction to Practical Ore Microscopy*. Wiley & Sons.

Kennedy L. G., Everett J. W., Ware K. J., Parsons R., and Green V. (1998) Iron and sulfur mineral analysis methods for natural attenuation assessments. *Bioremediation Journal* **2**, 259-276.

Kleinmann R. L. P. (1990) Acid mine drainage in the United States. *Proceedings of the First Midwestern Region Reclamation Conference*.

May H. M. and Nordstrom D. K. (1991) Assessing the solubilities and reaction kinetics of aluminous minerals in soils. In *Soil Acidity* (ed. B. Ulrich and M. E. Sumner), pp. 125 - 148. Springer-Verlag.

Morin K. A., Cherry J. A., Dave N. K., Lim T. P., and Vivyurka A. J. (1988) Migration of acidic groundwater seepage from uranium-tailings impoundments, 1. Field study and conceptual hydrogeochemical model. *Journal of Contaminant Hydrology* **2**, 271 - 303.

Nordstrom D. K. and Alpers C. N. (1999) Geochemistry of acid mine waters. In *The Environmental Geochemistry of Mineral Deposits, Part A: Processes, Techniques, and Health Issues*, Vol. 6A, pp. 133 - 160. Society of Economic Geologists.

Phipps T. T., Fletcher J. J., Fiske W., and Skousen J. G. (1991) A methodology for evaluating the costs of alternative AMD treatment systems. *Proceedings of the 12th Annual West Virginia Surface Mine Drainage Task Force Symposium*.

Powell J. D. (1988) Origin and influence of coal mine drainage on streams of the United States. *Environ. Geol. Water Sci.* **11**, 141 - 152.

Raiswell R., Canfield D. E., and Berner R. A. (1994) A comparison of iron extraction methods for the determination of degree of pyritisation and the recognition of iron-limited pyrite formation. *Chemical Geology* **111**, 101 - 110.

Ramdohr P. (1980) *The Ore Minerals and their Intergrowths*. Pergamon Press.

Rickard D. T. (1974) Kinetics and mechanism of the sulfidation of goethite. *American Jounral of Science* **274**, 941-952.

Robbins E. I., G.L. Nord J., Savela C. E., Eddy J. I., Livi K. J. T., Gullett C. D., Nordstrom D. K., Chou I.-M., and Briggs K. M. (1996) Microbial and mineralogical analysis of aluminum-rich precipitates that occlude porosity in a failed anoxic limestone drain, Monongalia County, West Virginia. *Thirteenth Annual International Pittsburgh Coal Conference*, 761-767.

Schwertmann U. and Cornell R. M. (2000) *Iron Oxides in the Laboratory*. Wiley-VCH.

Skousen J., Rose A., Geidel G., Foreman J., Evans R., and Hellier W. (1998) *A Handbook of Technologies for the Avoidance and Remediation of Acid Mine Drainage*. Acid Drainage Technology Initiative (ADTI).

Stanton M. R. and Goldhaber M. B. (1991) An experimental study of goethite sulfidation - Relationships to the diagnesis of iron and sulfur. In *Geochemical, Biogeochemical, and Sedimentological Studies of the Green River Formation, Wyoming, Utah, and Colorado* (ed. M. L. Tuttle). U.S. Geological Survey Bulletin 1973E.

Sterner P., Skousen J., and Donovan J. (1998) Geochemistry of laboratory anoxic limestone drains. *Proceedings of the 15th Annual National Meeting of the American Society of Surface Mining and Reclamation*, 214-234.

Stumm W. and Morgan J. J. (1981) *Aquatic Chemistry*. John Wiley & Sons.

Thomas R. C., Romanek C. S., Coughlin D. P., and Crow D. E. (1999) Treatment of acid mine drainage using anaerobic constructed treatment wetlands: predicting longevity with substrate neutralization potential. *Proceedings Sudbury '99 - Mining and the Environment II*, 449-458.

To T. B., Nordstrom D. K., Cunningham K. M., Ball J. W., and McCleskey R. B. (1999) New method for the direct determination of dissolved Fe(III) concentration in acid mine waters. *Environ. Sci. Technol.* **33**(5), 807-813.

Watzlaf G. R., Schroeder K. T., and Kairies C. (2000) Long-term performance of alkalinity-producing passive systems for the treatment of mine drainage. *Proceedings of the 17th Annual National Meeting of the American Society of Surface Mining and Reclamation.*, 262 - 274.

Watzlaf G. R., Schroeder K. T., Kleinmann R. L. P., Kairies C. L., and Nairn R. W. (2002) The passive treatment of coal mine drainage. *Workshop presented at the 2002 Annual National Meeting of the American Society of Mining and Reclamation.*

Widdel F. (1988) Microbiology and Ecology of Sulfate- and Sulfur-Reducing Bacteria. In *Biology of Anaerobic Microorganisms* (ed. A. J. B. Zehnder), pp. 469-585. Wiley Interscience.

Ziemkiewicz P. F., Skousen J. G., Brant D. L., Sterner P. L., and Lovett R. J. (1997) Acid mine drainage treatment with armored limestone in open limestone channels. *Journal of Environmental Quality* **26**, 1017 - 1024.

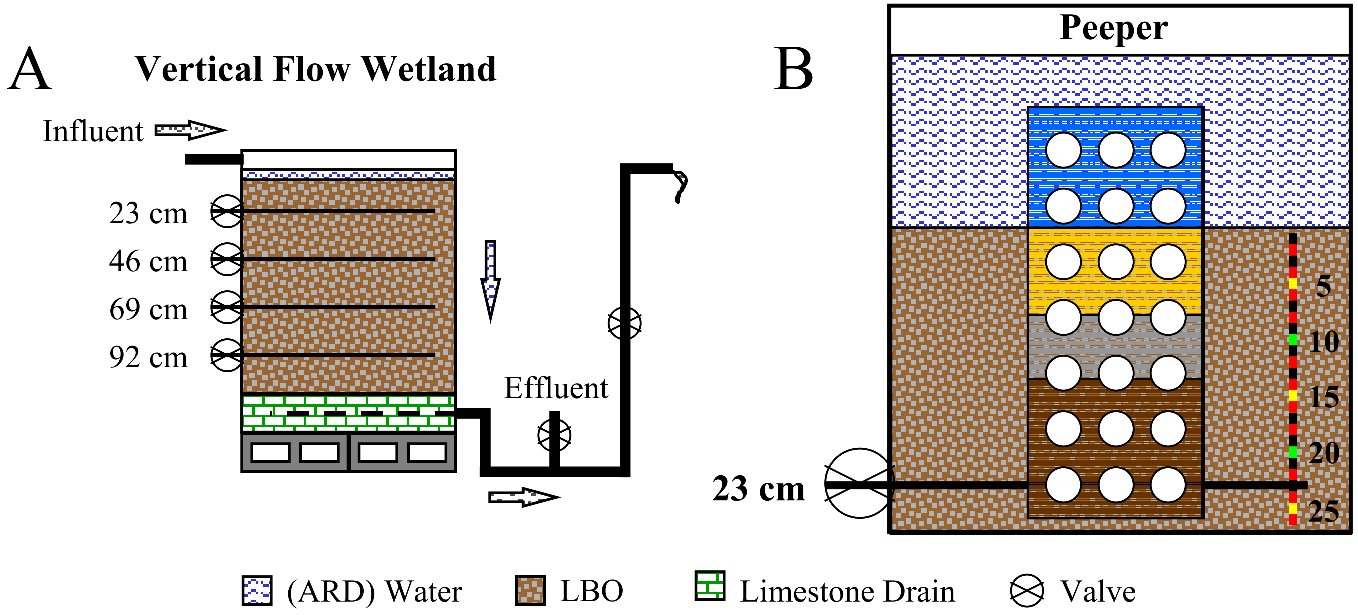

Figure 3.1. Cross section of the vertical flow wetland tank. A. Overview of the tank set up. B. Close-up of substrate above 23 cm showing the placement of the peeper (Hesslein, 1976). The scale to the right is in centimeters.

Table 3.1. Composition and physicochemical attributes of the limestone buffered organic substrate (LBOS).

LBOS Composition (by volume)	**Physicochemical Attributes**[†]	
	• CEC: 83.29 meq·100 gm^{-1} soil **• NP: 529 g CaCO$_3$·Kg^{-1} soil**	
• 25% Limestone Screenings • 72% Composted Stable Waste • 3% Spent Brewing Grains • <1% Kricket Krap ®	**• Paste pH 7.61** **• Density: 0.741 g·cm^{-3}**	**• Carbon 36 %** **• C:N 28.8**

all values in mg·kg^{-1}	**Fe**	**Al**	**Ca**	**Mn**	**As**	**Cr**	**Cu**	**U**	**Cd**	**Co**	**Ni**	**Zn**
LBOS Total	2805	1611	217048	135	2.5	6.7	4.5	23	0.9	0.9	93	35
Limestone Total	546	543	694339	143	6.0	7.1	1.2	2.5	0.6	2.3	18	4
Limestone Contribution [a]	289	287	367305	76	3.2	3.8	0.6	1.3	0.3	1.2	10	2
Org. Matter Contribution [b]	2516	1324	-	59	-	3.0	3.8	22	0.6	-	84	33

Limestone Screenings - Grain Size Distribution								
(mm)	**9.5 - 4.8**	**4.8 - 2.4**	**2.4 - 1.2**	**1.2 - 0.6**	**0.6 - 0.3**	**0.3 - 0.15**	**0.15 - 0.07**	**< 0.07**
Percent	**2.50%**	**22.2%**	**31.5%**	**27.0%**	**13.4%**	**3.12%**	**0.32%**	**0.03%**

[†] Physicochemical attributes are from Thomas et al. (1999)

[a] Limestone contribution was determined by multiplying the limestone total metal concentration by the proportion of limestone in the LBOS (i.e., 0.529)

[b] Organic matter contribution was determined by difference. Values are not given where the metal concentration measured in the limestone was greater than the concentration measured in the final LBOS.

Table 3.2. Influent and effluent water chemistry data for the individual tanks from chapter 2.

	pH Std Units	Fe ($mg \cdot L^{-1}$)	Al ($mg \cdot L^{-1}$)	Ca ($mg \cdot L^{-1}$)	Sulfate ($mg \cdot L^{-1}$)	Sulfide ($mg \cdot L^{-1}$)
L.D.L[a]		0.00139	0.0026	0.023	0.5	0.05
Influent ARD	2.4 (1.6 to 3.0)	142 (92 to 237)	84 (39 to 274)	52 (23 to 114)	1521 (926 to 3385)	n/a n/a
Tank 2A	6.48 (5.9 to 6.9)	12.9 (40)	0.17 (9.3)	570 (268 to 807)	1248 (696 to 1817)	1.2 (15)
Tank 10A	6.42 (5.9 to 6.9)	11.6 (0.1 to 90)	0.02 (0.2)	611 (371 to 1003)	1275 (495 to 2732)	3.2 (20)
Tank 13A	6.34 (5.5 to 6.9)	32.8 (0.6 to 123)	0.07 (4.2)	610 (392 to 921)	1277 (876 to 1938)	0.7 (15)
Tank 24A	6.40 (6.0 to 6.9)	16.7 (120)	0.03 (0.4)	619 (373 to 888)	1273 (541 to 2257)	4.0 (40)
Tank 30A	6.42 (5.9 to 6.8)	14.1 (0.01 to 76)	0.02 (0.3)	616 (380 to 943)	1302 (678 to 2323)	1.6 (15)
Tank 36A	6.33 (5.5 to 6.8)	19.2 (58)	0.02 (0.3)	604 (372 to 853)	1186 (627 to 2098)	2.8 (20)
Tank 39A	6.5 (6.0 to 7.0)	2.3 (11)	0.02 (0.2)	609 (398 to 915)	1113 (263 to 1585)	9.4 (1 to 30)
Tank 44A	6.50 (5.2 to 7.1)	6.8 (48)	0.05 (2.2)	558 (362 to 907)	936 (427 to 1569)	15.6 (0.1 to 50)
Average[b]	6.42	14.5	0.05	600	1201	4.8
Min	6.33	2.3	0.02	558	936	0.7
Max	6.50	32.8	0.17	619	1302	15.6

Values in parenthesis are the range over the 2 year study; where only one value is given, the lower value is below detection limits of the ICP-MS.

[a] L.D.L = lower detection limits of the ICP-MS, n/a = not analyzed

[b] Average, minimum, and maximum were calculated from the individual tank averages

Figure 3.2. Flow diagram for total digest and sequential extraction of the LBOS samples. Damp samples from the VFW substrate were used in sequential extractions, while samples from the initial substrate were extracted dry. All total digest samples were conducted on dried, cryogenicaly ground material. Total digests were conducted using a block digestor (105°C) instead of shaking in a water bath. From chapter 4.

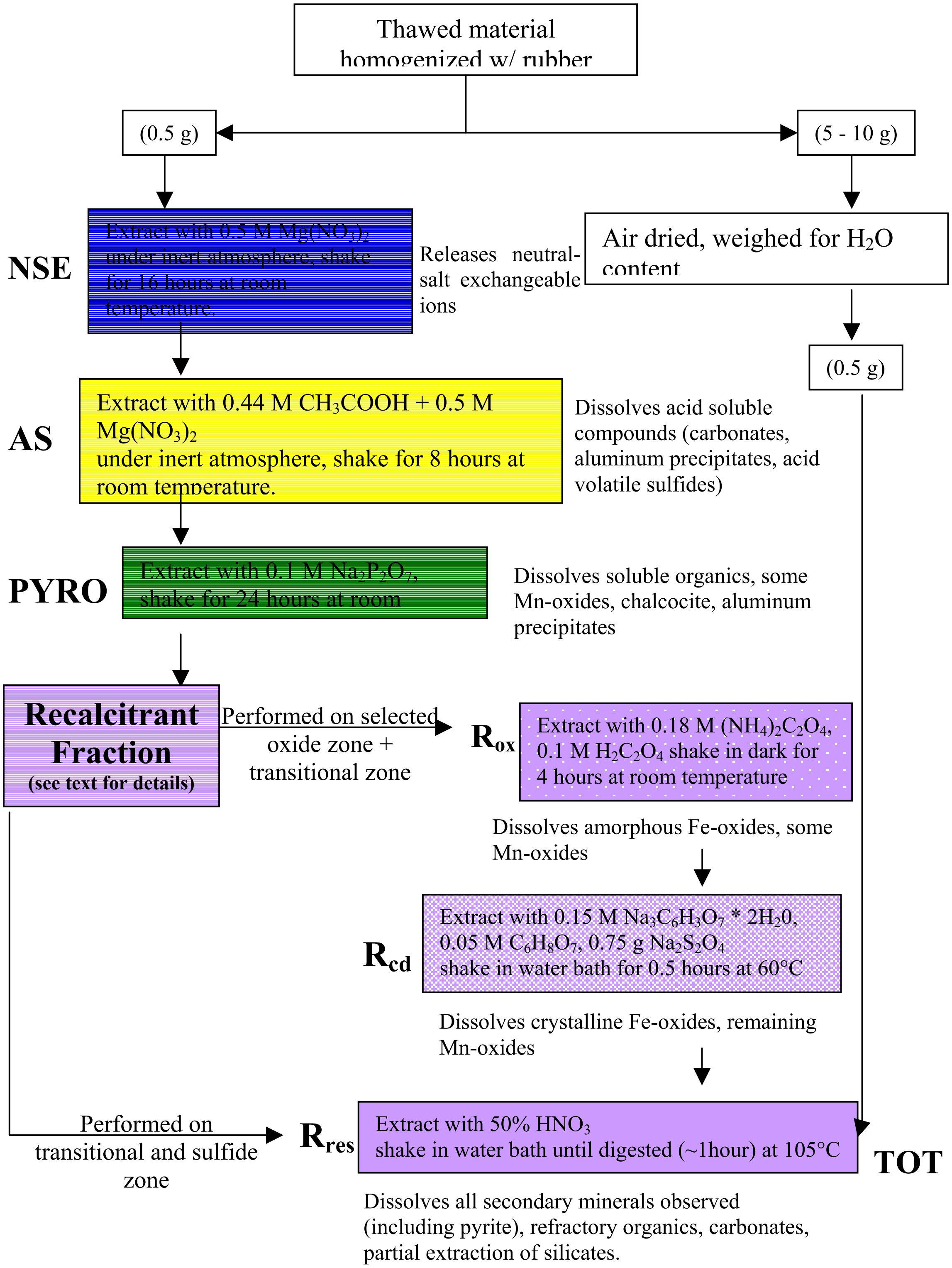
Thawed material homogenized w/ rubber
(0.5 g)
(5 - 10 g)
NSE
Extract with 0.5 M $Mg(NO_3)_2$ under inert atmosphere, shake for 16 hours at room temperature.
Releases neutral-salt exchangeable ions
Air dried, weighed for H_2O content
(0.5 g)
AS
Extract with 0.44 M CH_3COOH + 0.5 M $Mg(NO_3)_2$ under inert atmosphere, shake for 8 hours at room temperature.
Dissolves acid soluble compounds (carbonates, aluminum precipitates, acid volatile sulfides)
PYRO
Extract with 0.1 M $Na_2P_2O_7$, shake for 24 hours at room
Dissolves soluble organics, some Mn-oxides, chalcocite, aluminum precipitates
Recalcitrant Fraction
(see text for details)
Performed on selected oxide zone + transitional zone
R_{ox}
Extract with 0.18 M $(NH_4)_2C_2O_4$, 0.1 M $H_2C_2O_4$ shake in dark for 4 hours at room temperature
Dissolves amorphous Fe-oxides, some Mn-oxides
R_{cd}
Extract with 0.15 M $Na_3C_6H_3O_7 * 2H_20$, 0.05 M $C_6H_8O_7$, 0.75 g $Na_2S_2O_4$ shake in water bath for 0.5 hours at 60°C
Dissolves crystalline Fe-oxides, remaining Mn-oxides
Performed on transitional and sulfide zone
R_{res}
Extract with 50% HNO_3 shake in water bath until digested (~1hour) at 105°C
TOT
Dissolves all secondary minerals observed (including pyrite), refractory organics, carbonates, partial extraction of silicates.

Figure 3.3. Average substrate pore water chemistry collected with the peeper sampler. The vertical axes represent sampling depth; negative values indicate the samples were collected from the ARD overlying the substrate. Three samples of the influent ARD and tank effluent collected over the peeper equilibration period are shown for comparison. Pore water (swamper) analyses and accompanying influent and effluent data reported in chapter 2 are shown for comparison. Error bars on swamper data represent 1σ standard deviation from the average.

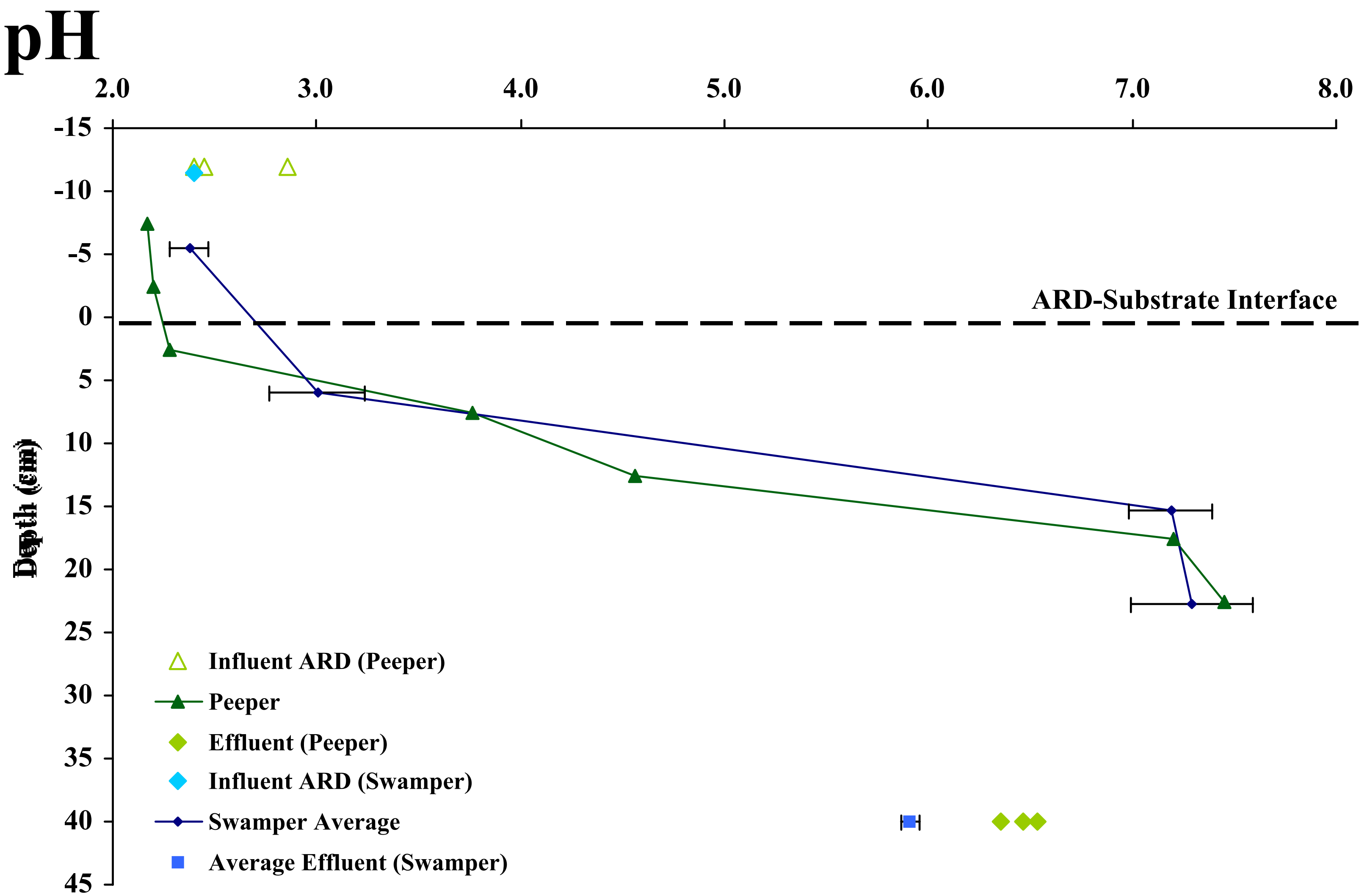
pH
2.0
3.0
4.0
5.0
6.0
7.0
8.0
Depth (cm)
-15
-10
-5
0
5
10
15
20
25
30
35
40
45
ARD-Substrate Interface
Influent ARD (Peeper)
Peeper
Effluent (Peeper)
Influent ARD (Swamper)
Swamper Average
Average Effluent (Swamper)

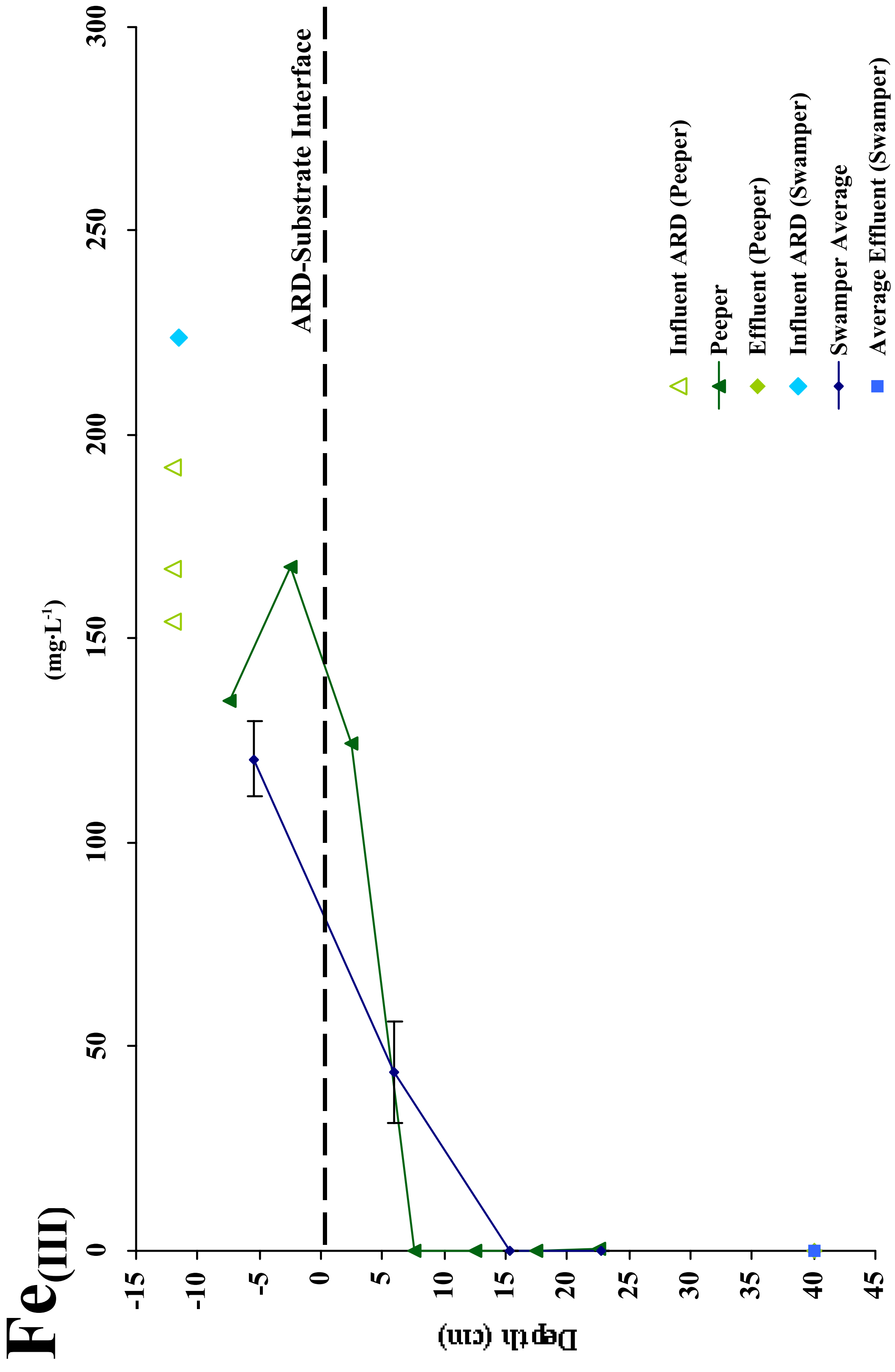

Fe(III)
Depth (cm)
(mg·L-1)
ARD-Substrate Interface
-15
-10
-5
0
5
10
15
20
25
30
35
40
45
0
50
100
150
200
250
300
Influent ARD (Peeper)
Peeper
Effluent (Peeper)
Influent ARD (Swamper)
Swamper Average
Average Effluent (Swamper)

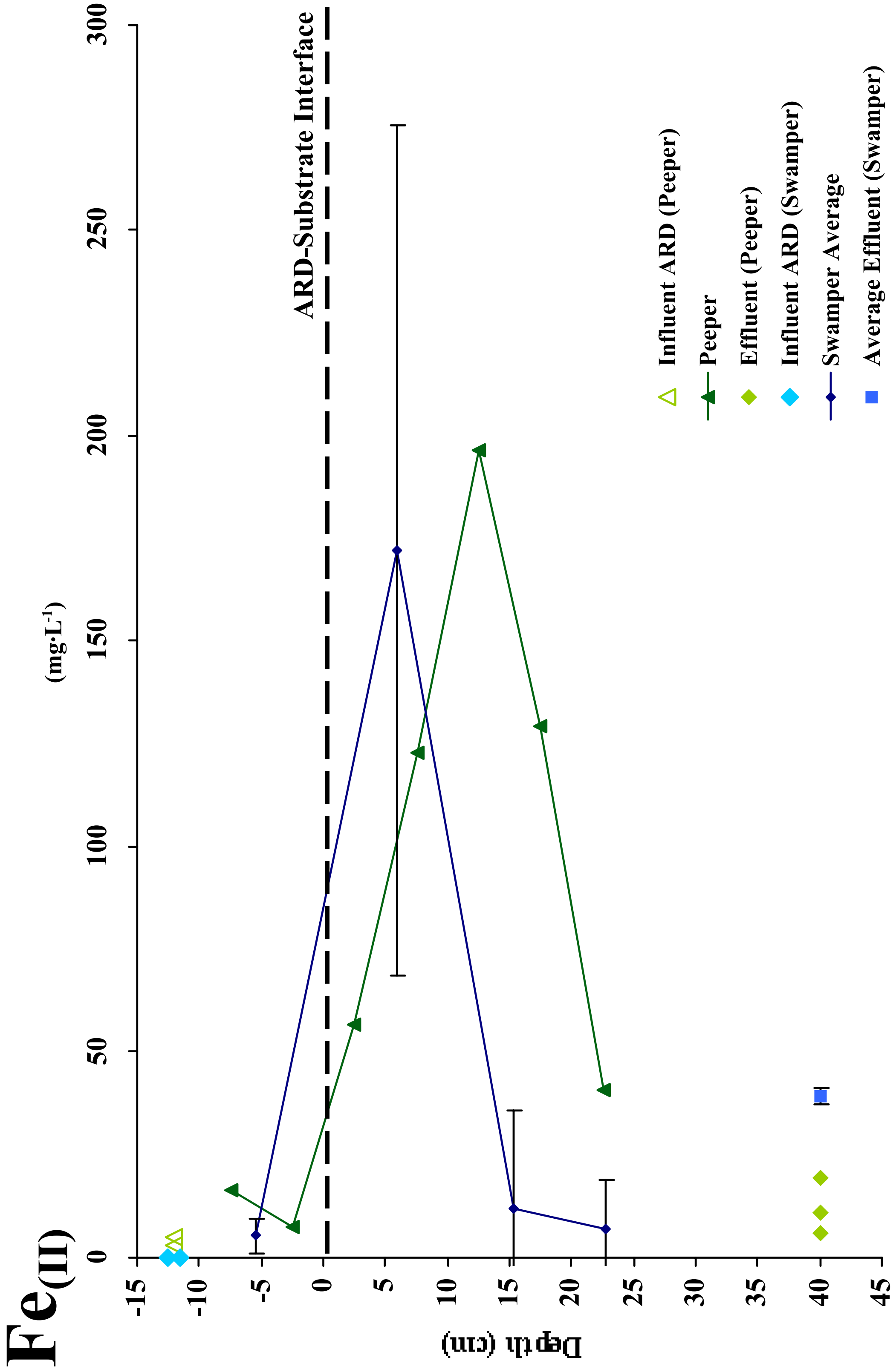
Fe(II)
(mg·L-1)
0
50
100
150
200
250
300
ARD-Substrate Interface
Depth (cm)
-15
-10
-5
0
5
10
15
20
25
30
35
40
45
Influent ARD (Peeper)
Peeper
Effluent (Peeper)
Influent ARD (Swamper)
Swamper Average
Average Effluent (Swamper)

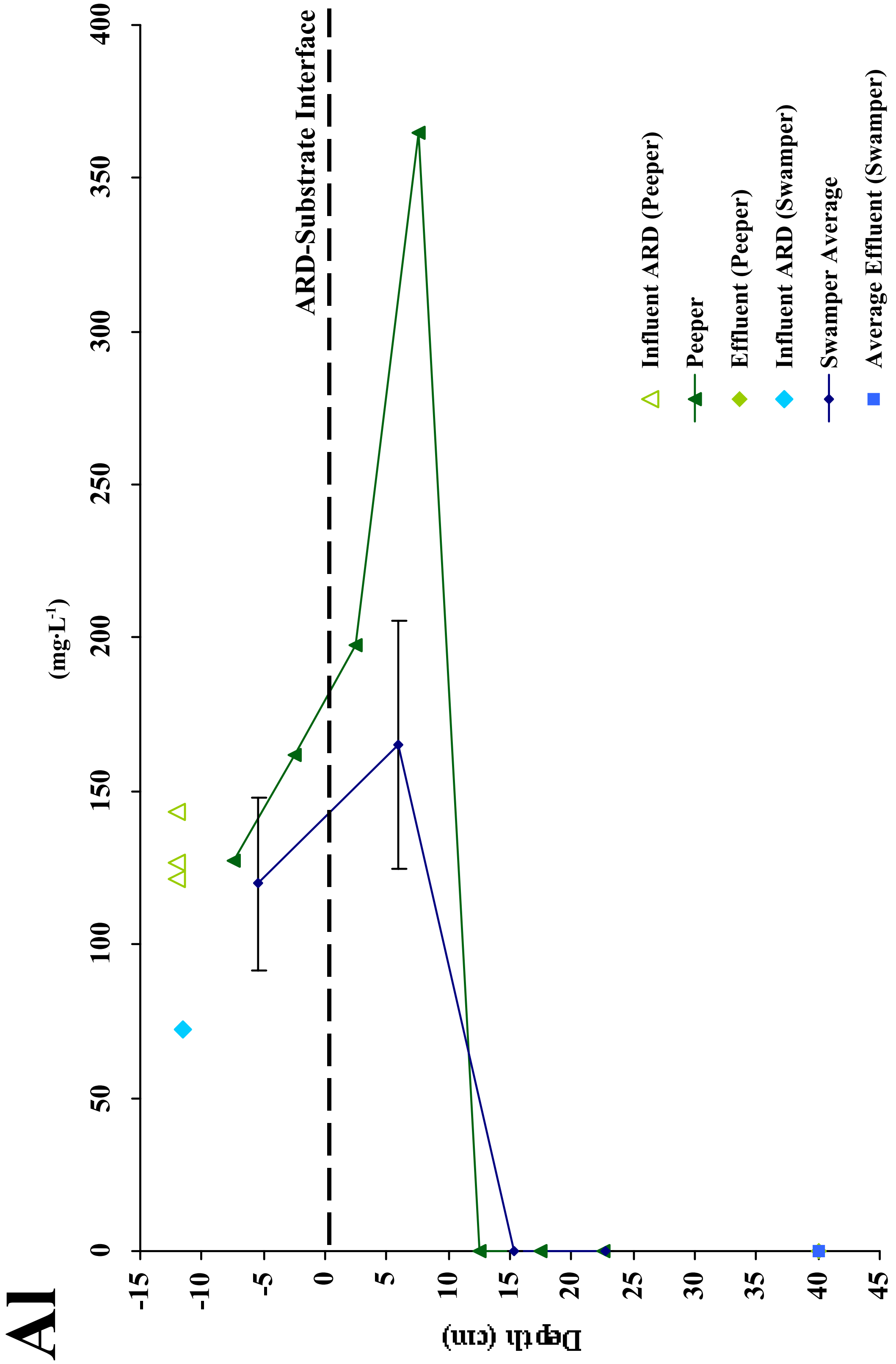
Al
(mg·L-1)
Depth (cm)
ARD-Substrate Interface
0
50
100
150
200
250
300
350
400
-15
-10
-5
0
5
10
15
20
25
30
35
40
45
Influent ARD (Peeper)
Peeper
Effluent (Peeper)
Influent ARD (Swamper)
Swamper Average
Average Effluent (Swamper)

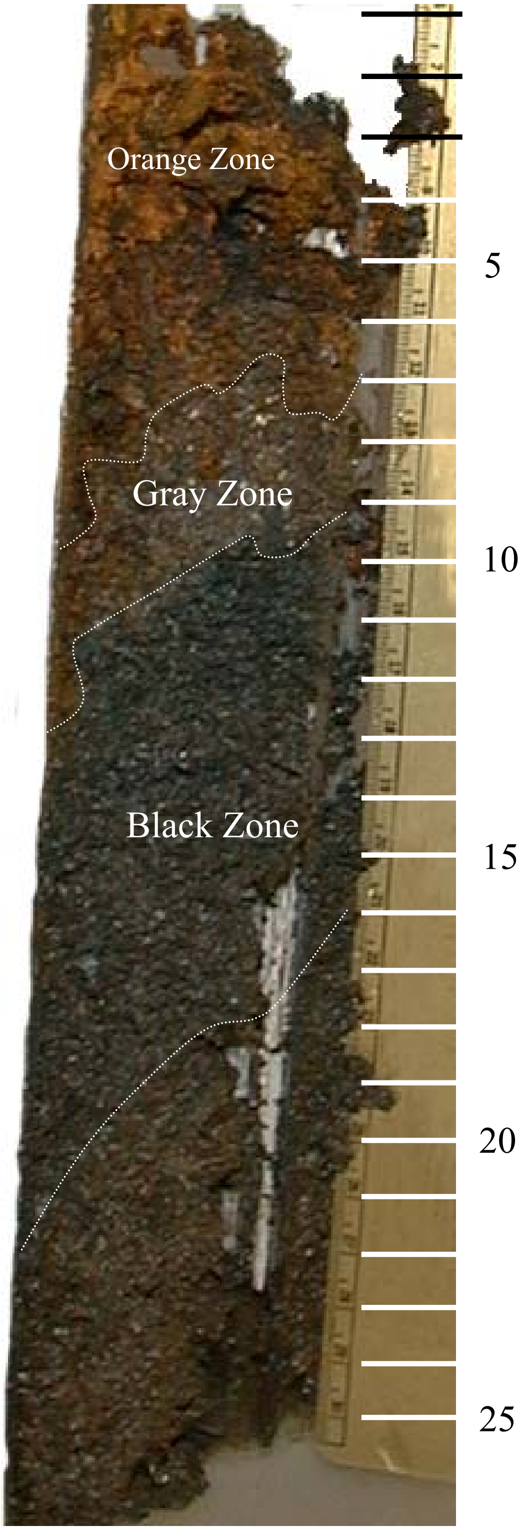

Figure 3.4. Photograph of a core taken from the LBOS showing the three reaction zones. Scale to the right is in centimeters.

Table 3.3. Sequential extraction results from the LBOS. All values are given as mg·kg^{-1}

Tank 30A		Iron								
Season	Zone	Core	NSE	AS	PYRO	Rox	Rcd	Rres	Cum Tot	Total Digest
Initial		#1	BDL	151	507	n/a	n/a	3062	3720	4074
Initial		#2	2.7	148	530	429	304	1977	3390	3010
Initial		#3	2.5	152	513	n/a	n/a	3040	3708	2564
Initial		#4	1.6	128	278	328	249	1256	2241	2564
Summer	Sulfide	#1	BDL	425	461	n/a	n/a	3596	4482	4329
		#2	BDL	971	634	n/a	n/a	3342	4947	5402
		#3	BDL	1587	827	n/a	n/a	4924	7338	n/a
Fall	Sulfide	#1	BDL	556	976	n/a	n/a	3530	5062	4833
		#2	13	803	927	n/a	n/a	6293	8036	5834
		#3	26	760	929	n/a	n/a	3950	5664	3733
Summer	Trans	#1	0.01	613	879	n/a	n/a	5117	6609	4662
		#2	BDL	3883	773	n/a	n/a	4864	9520	4883
		#3	BDL	1049	1417	n/a	n/a	11537	14003	13626
Fall	Trans	#1	46	3365	2871	n/a	n/a	19627	25908	14575
		#2	17	2641	1964	n/a	n/a	8670	13292	10869
		#3	111	4032	2335	n/a	n/a	7266	13743	12591
Summer	Oxide	#1	58	969	5126	24360	9508	2377	42398	56427
		#2	4.7	1527	9615	22289	30736	2985	67157	67195
		#3	103	2474	17110	37907	62274	3112	122980	117268
Fall	Oxide	#1	BDL	3684	9841	17328	74832	6199	111884	102950
		#2	1361	10362	21006	31885	27927	1576	94116	82350
		#3	980	7668	19062	30040	27838	3338	88927	118941

Tank 36A		Iron								
Season	Zone	Core	NSE	AS	PYRO	Rox	Rcd	Rres	Cum Tot	Total Digest
Initial		#5	3.5	187	518	n/a	n/a	2678	3387	2835
Initial		#6	0.4	201	565	n/a	n/a	2485	3251	2849
Initial		#7	3.9	168	426	n/a	n/a	2931	3529	1890
Initial		#8	1.7	96	288	756	494	1402	3037	2653
Summer	Sulfide	#1	BDL	903	687	n/a	n/a	4229	5819	7989
		#2	3.1	961	671	n/a	n/a	4026	5662	5085
		#3	5.0	1563	716	n/a	n/a	12948	15231	6844
Fall	Sulfide	#1	0.5	1440	973	n/a	n/a	5128	7542	6699
		#2	6.3	1095	672	n/a	n/a	4583	6355	5654
		#3	BDL	756	1396	n/a	n/a	5331	7483	7920
Summer	Trans	#1	0.04	656	978	n/a	n/a	7265	8900	7194
		#2	0.8	901	1292	2484	1722	2612	9012	8547
		#3	6.5	4221	1751	n/a	n/a	19789	25768	20659
Fall	Trans	#1	66	5447	2464	n/a	n/a	16763	24740	17403
		#2	31	3025	1349	n/a	n/a	10998	15402	16469
		#3	BDL	1363	1701	n/a	n/a	11404	14468	13519
Summer	Oxide	#1	77	1025	10089	28228	59561	2736	101715	91547
		#2	127	872	7010	20941	72716	2523	104189	113030
		#3	130	3287	10624	43102	96949	2359	156451	162220
Fall	Oxide	#1	523	2335	17990	57063	31420	2566	111896	158099
		#2	130	636	7177	25448	28039	2091	63521	102900
		#3	208	1020	13127	38871	58069	4094	115389	133126

Tank 30A		Aluminum								
Season	Zone	Core	NSE	AS	PYRO	Rox	Rcd	Rres	Cum Tot	Total Digest
Initial		#1	BDL	25	84	n/a	n/a	911	1021	2116
Initial		#2	BDL	20	90	BDL	57	706	873	1332
Initial		#3	BDL	22	78	n/a	n/a	905	1006	1923
Initial		#4	BDL	21	48	BDL	41	484	594	1616
Summer	Sulfide	#1	3.0	71	102	n/a	n/a	986	1163	1388
		#2	BDL	29	75	n/a	n/a	815	918	1611
		#3	26	544	488	n/a	n/a	676	1734	n/a
Fall	Sulfide	#1	8.6	130	117	n/a	n/a	1152	1408	1755
		#2	6.0	219	217	n/a	n/a	737	1179	1171
		#3	2.4	73	100	n/a	n/a	702	877	713
Summer	Trans	#1	45	1636	1088	n/a	n/a	876	3645	2281
		#2	62	8305	3771	n/a	n/a	1565	13703	1421
		#3	29	9768	4811	n/a	n/a	1790	16398	13877
Fall	Trans	#1	39	26731	18139	n/a	n/a	17382	62291	20905
		#2	53	14368	9966	n/a	n/a	1755	26142	32312
		#3	25	38339	16300	n/a	n/a	5502	60167	50929
Summer	Oxide	#1	BDL	30389	9361	5804	165	1304	47023	29298
		#2	BDL	27853	12585	5037	503	1307	47286	31871
		#3	1599	7159	4363	2218	430	1805	17575	10026
Fall	Oxide	#1	BDL	13967	3533	2087	698	1954	22240	13263
		#2	BDL	10826	3621	1434	446	1847	18174	24965
		#3	BDL	4280	1428	1401	288	1783	9180	9497

Tank 36A		Aluminum								
Season	Zone	Core	NSE	AS	PYRO	Rox	Rcd	Rres	Cum Tot	Total Digest
Initial		#5	BDL	18	75	n/a	n/a	833	926	1209
Initial		#6	BDL	18	98	n/a	n/a	807	923	1815
Initial		#7	BDL	18	99	n/a	n/a	757	874	1107
Initial		#8	BDL	17	76	50	58	638	789	1769
Summer	Sulfide	#1	BDL	68	110	n/a	n/a	762	940	6942
		#2	17	365	393	n/a	n/a	1171	1946	2097
		#3	BDL	53	119	n/a	n/a	748	920	1202
Fall	Sulfide	#1	45	997	1230	n/a	n/a	1185	3457	4384
		#2	7.2	97	161	n/a	n/a	1099	1364	1661
		#3	65	1204	1666	n/a	n/a	1701	4636	3018
Summer	Trans	#1	69	2294	1259	n/a	n/a	1388	5010	4626
		#2	59	6741	2661	360	73	7260	17154	10497
		#3	15	27738	9679	n/a	n/a	2340	39771	25636
Fall	Trans	#1	10	17563	13873	n/a	n/a	5491	36938	44546
		#2	9.4	33979	17568	n/a	n/a	9593	61150	45129
		#3	1.3	19408	13287	n/a	n/a	8783	41480	37855
Summer	Oxide	#1	1500	24333	11241	5891	757	1337	45058	28497
		#2	996	16771	6366	1655	845	1580	28214	24659
		#3	1470	2377	1084	858	417	5816	12022	7555
Fall	Oxide	#1	974	1253	497	517	109	1631	4980	4574
		#2	1431	5388	3512	3533	195	1637	15696	10602
		#3	1026	3832	1757	1298	229	1824	9966	7101

BDL: below detection limit of ICP-OES (<0.003 mg·L^{-1} for Al and <0.001 mg·L^{-1} for Fe)
n/a: not analyzed

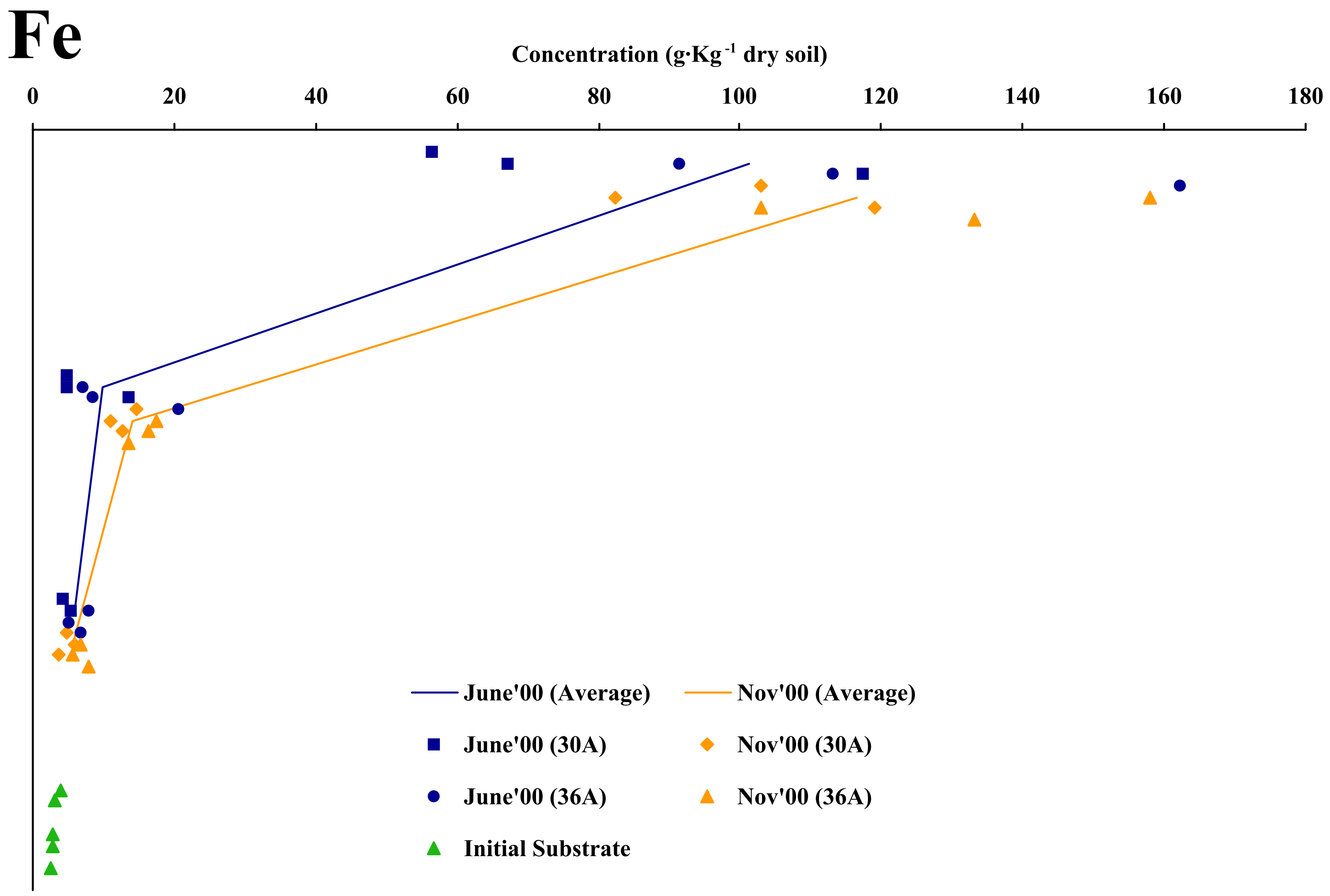

Figure 3.5a. Total digest data for iron in the three reaction zones compared to the composition of the initial substrate.

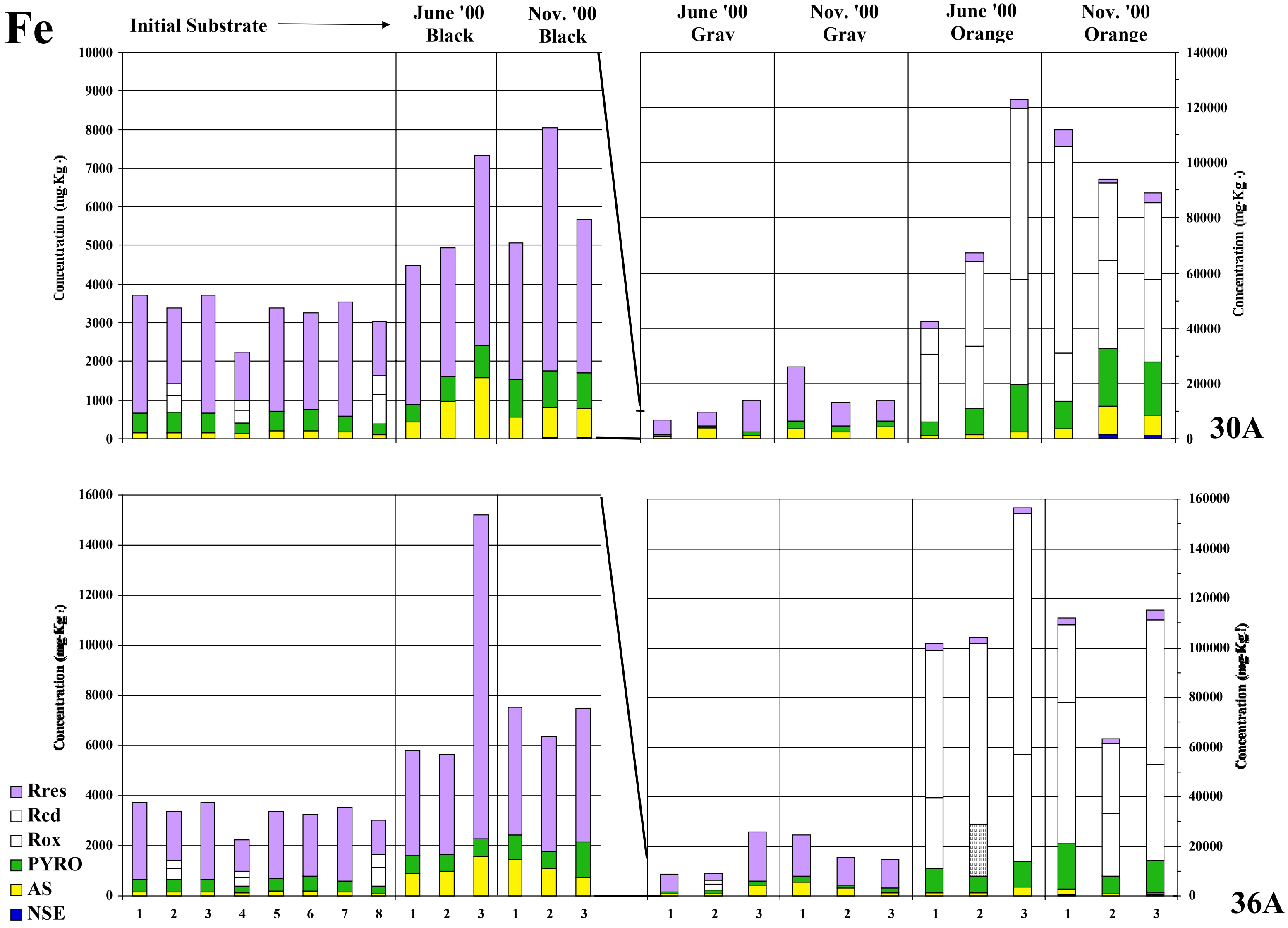

Figure 3.5b. Sequential extraction data for iron in the three reaction zones compared to the composition of the initial substrate.

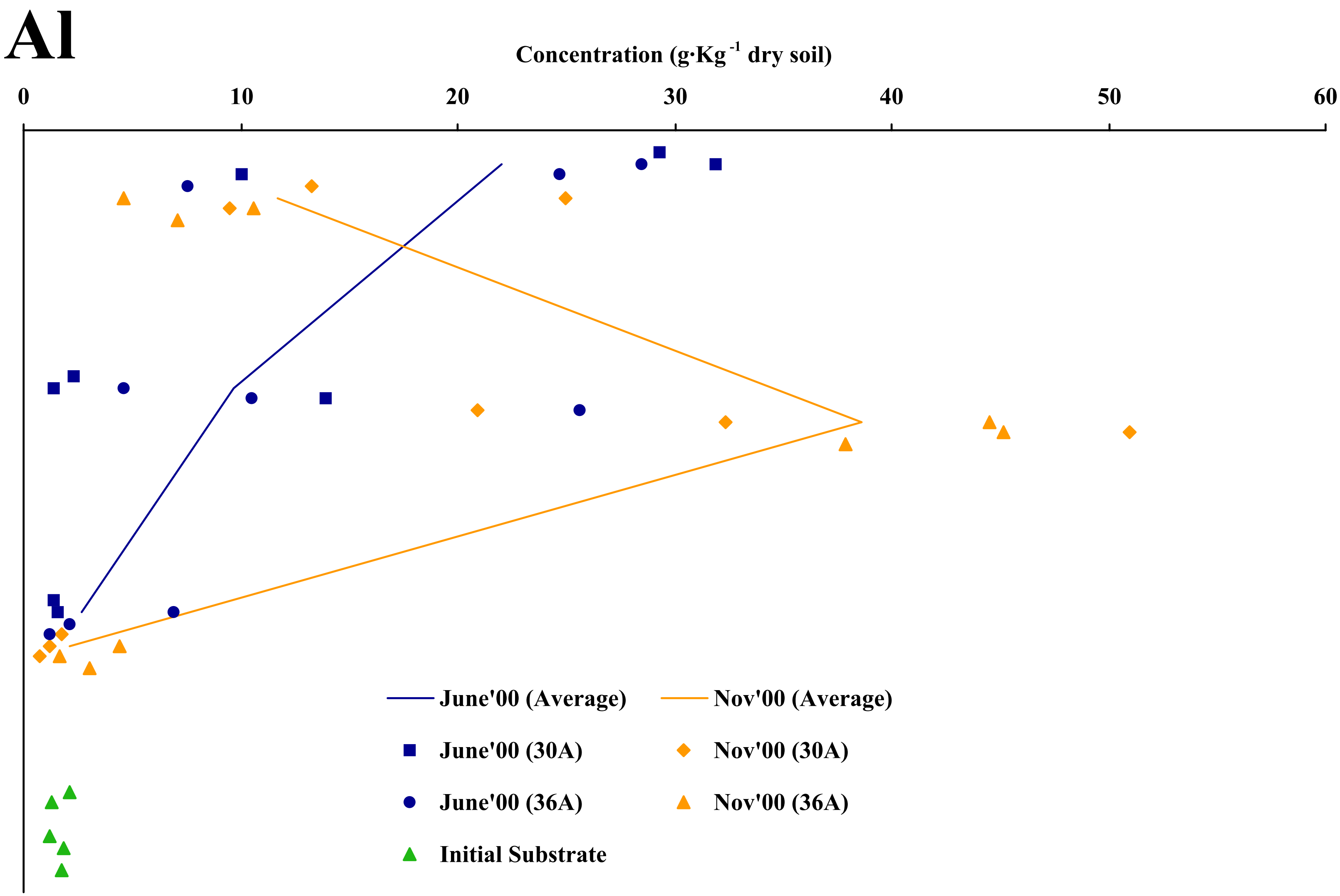

Figure 3.6a. Total digest data for aluminum in the three reaction zones compared to the composition of the initial substrate.

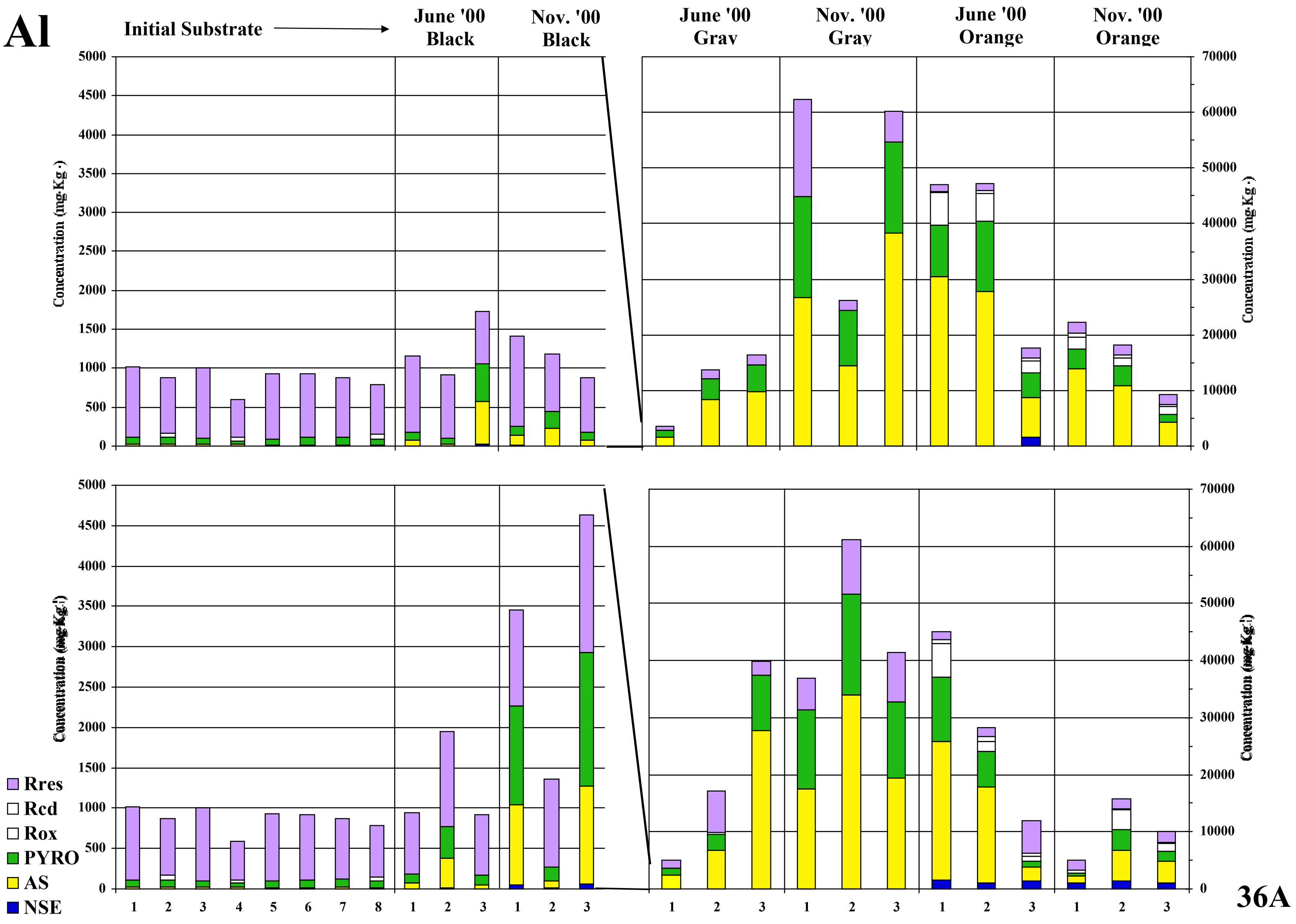

Figure 3.6b. Sequential extraction data for aluminum in the three reaction zones compared to the composition of the initial substrate.

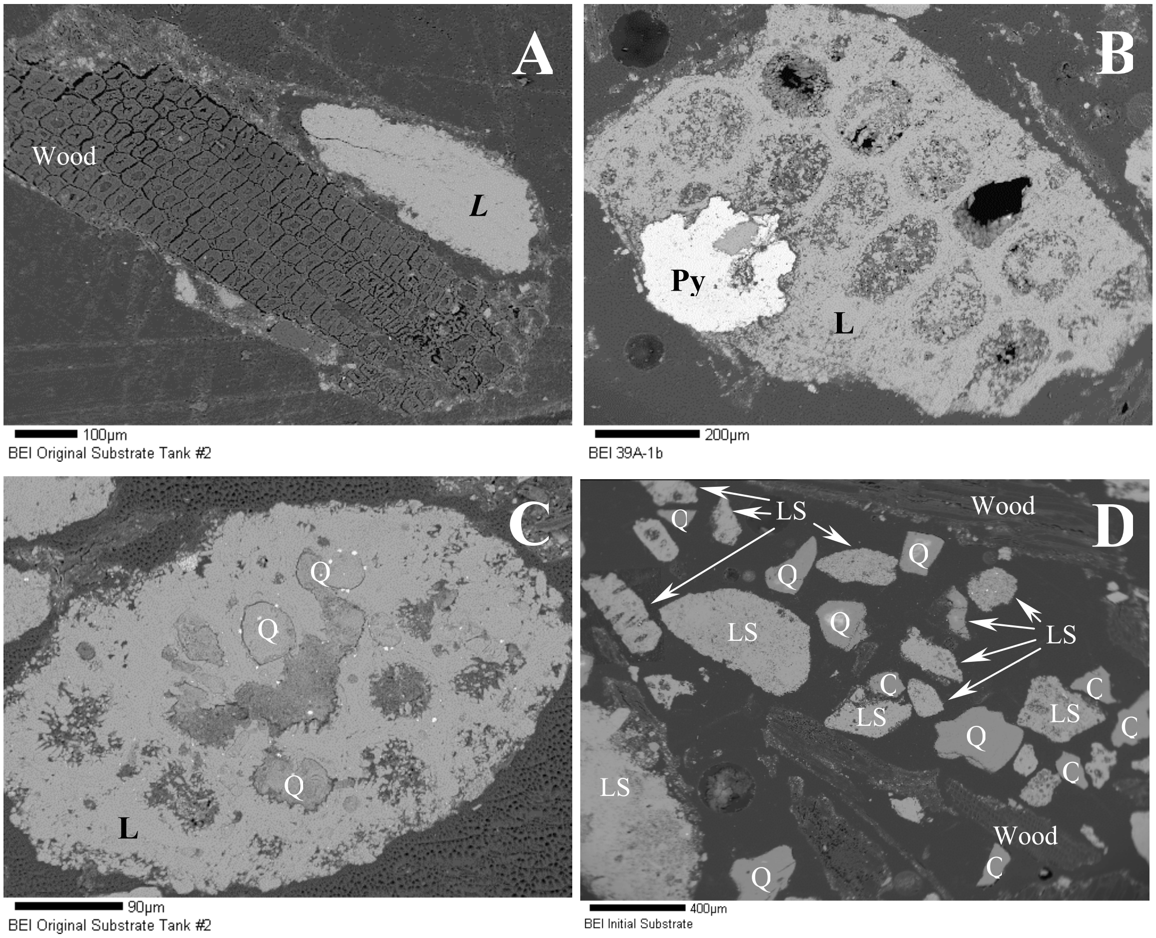

Figure 3.7. Back-scatter electron (BSE) images of the initial substrate showing limestone (LS), wood fragments (wood), quartz grains (Q), and pyrite (Py). (A) Small aggregate of limestone (LS) and wood. Note that fine-grained limestone fragments "coat" surfaces of the wood particle. (B) Fossil fragment containing anhedral pyrite (Py) grain. (C) Porous fossil fragment with quartz (Q) inclusions (i.e., trapped quartz). (D) Overview of the initial substrate showing limestone, wood fragments, and quartz.

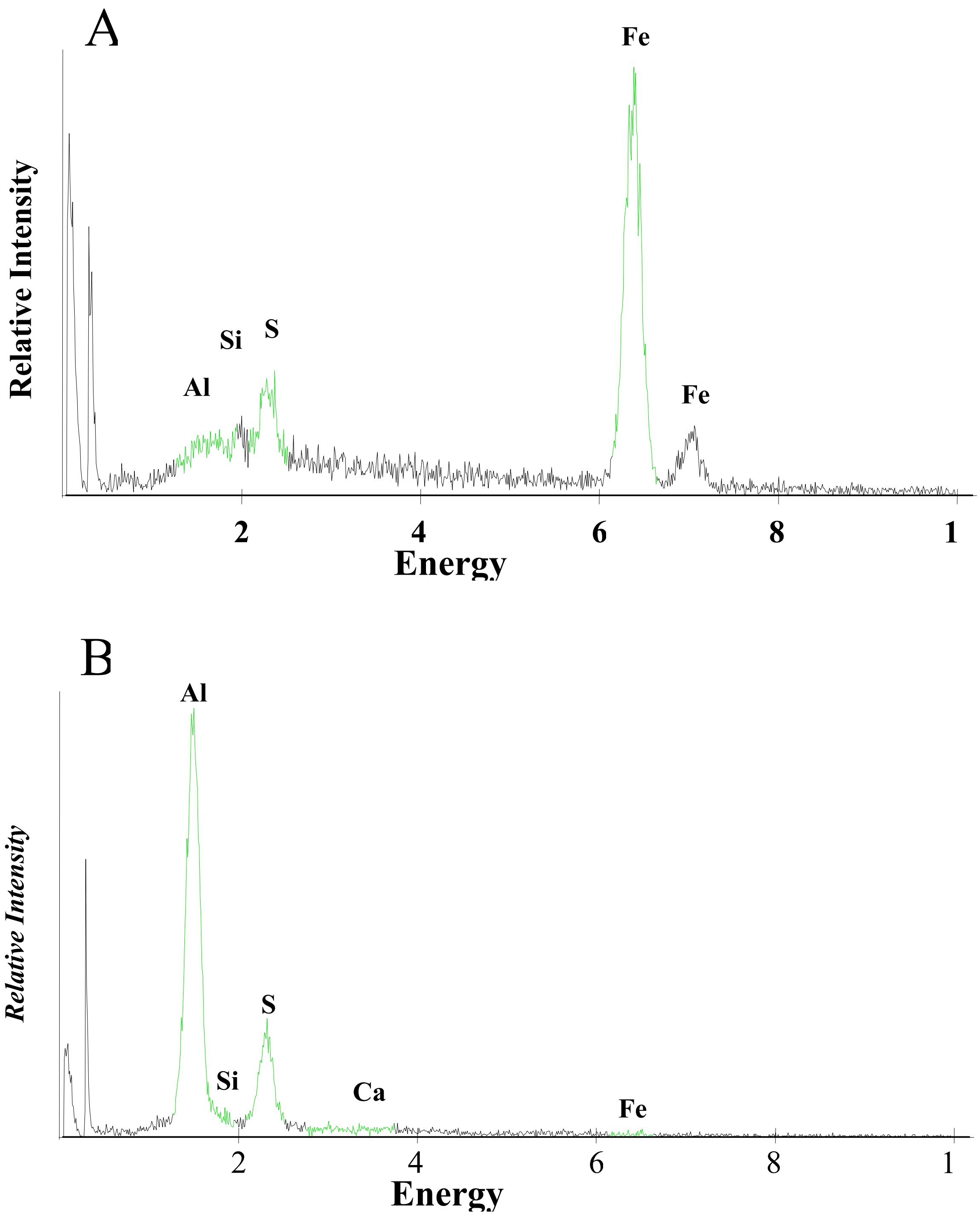

Figure 3.8. Qualitative energy dispersive spectroscopy (EDS) patterns of (A) iron-bearing precipitates from the orange zone and (B) aluminum-bearing precipitates from the gray zone.

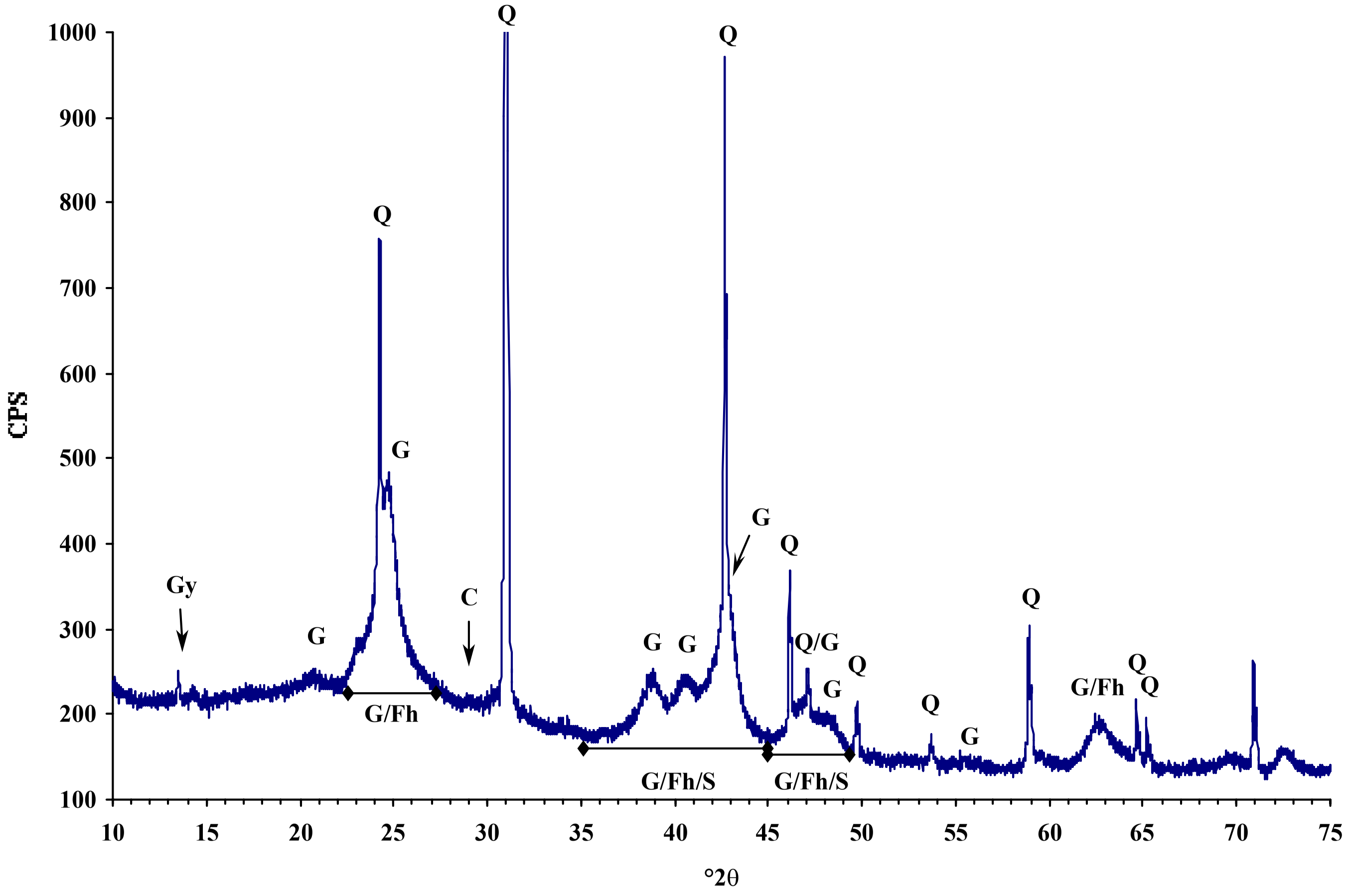

Figure 3.9. X-ray diffraction pattern from a representative sample of the orange zone showing reflections indicative of quartz (Q), and goethite (G), ferrihydrite (Fh), and schwertmannite (S). Broadening of the peaks, indicating poorly crystalline material, occurred in three regions (bars). These poorly crystalline materials were interpreted as ferrihydrite, schwertmannite, or poorly crystalline goethite. The location of the 100% relative intensity peaks for calcite (C) and gypsum (Gy) are also shown with arrows.

Figure 3.10. Back-scatter electron (BSE) images of the orange zone showing wood fragments, quartz grains (Q), iron-bearing precipitates (Fe), aluminum- and sulfur-bearing precipitate (Al-S), relict limestone grains (RLS), relict gypsum grains (RGy), and pyrite (Py). No limestone was detected in any BSE photomicrograph. (A) Textures of the upper orange zone showing only organic material (i.e., wood), quartz, and iron precipitate (colored arrows). Iron precipitates display colloidal textures (Ramdohr, 1980) indicative of rapid precipitation, including spherical (blue arrows), dendritic (orange arrows), and botryoidal (green arrows) textures. Note the sharp pattern of the dendritic textures indicate they formed along the boundary of former grain that has been dissolved away. Note also that most organic fragments are permineralized along the outer edges by rims of iron. (B) Iron precipitates coating quartz fragment and exhibiting dendritic growth texture. (C) Organic fragment (i.e., wood) permineralized by iron precipitate. (D) Complete skeletal replacement of former grains (i.e., limestone) by iron precipitate. Note overgrowth of botryoidal iron precipitates (green arrows). (E) Patch of aluminum- and sulfur-bearing precipitate in the lower orange zone outlining several relict limestone grains (dotted lines; RLS). (F) Large circular pattern of another relict limestone grain (dotted line) in the lower orange zone outlined by a primary phase of aluminum-sulfur precipitate (Al-S-1) and partially filled by a second phase of aluminum-sulfur precipitate (Al-S-2). The second, interior phase of aluminum-sulfur precipitate outlines sharp edges of former blocky grains (now void space filled with epoxy) within the relict limestone grain that have been dissolved away. These blocky grains are interpreted as relict gypsum grains (RGy).

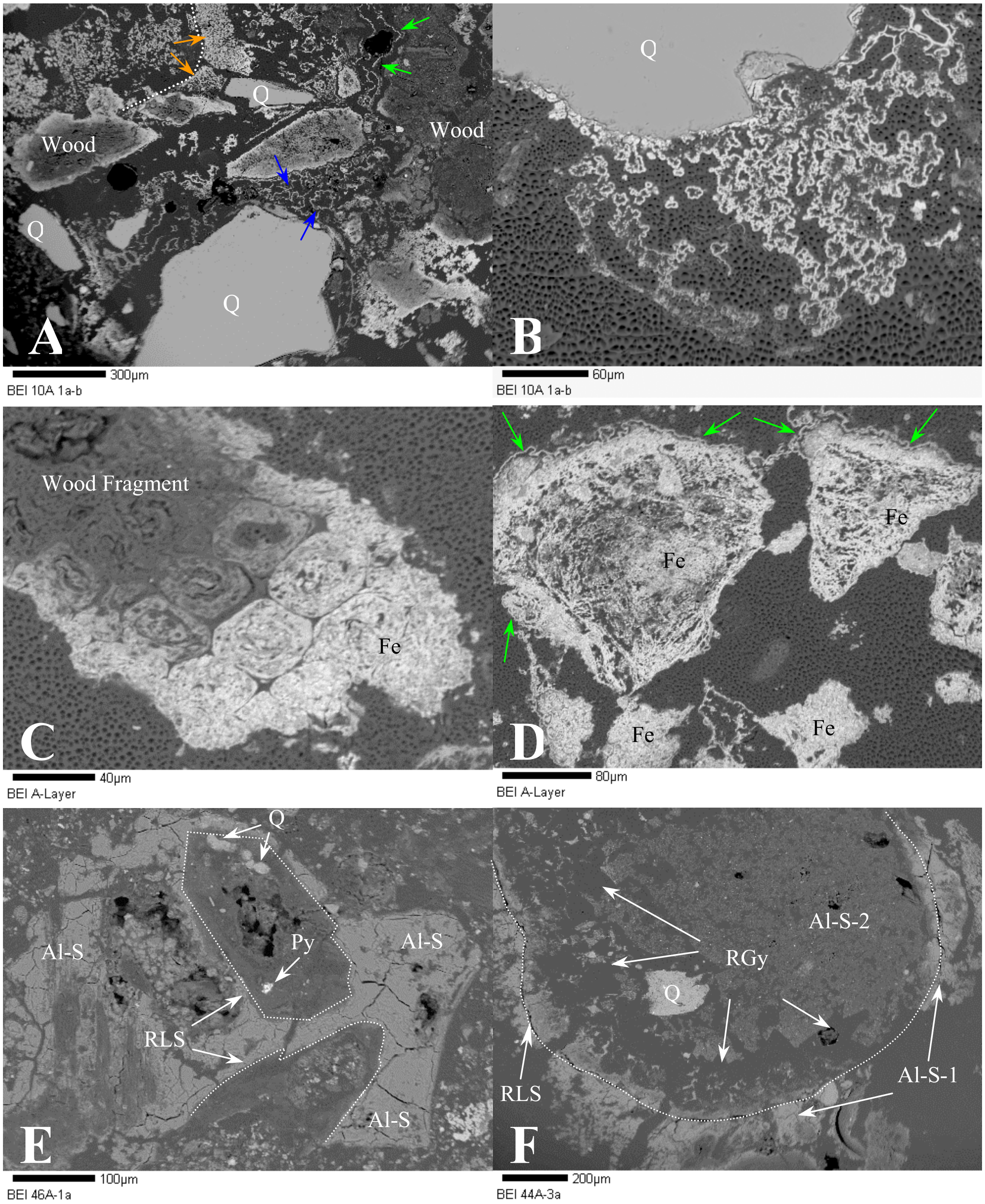
Q
Wood
Wood
Q
Q
Q
A
300µm
BEI 10A 1a-b
Q
B
60µm
BEI 10A 1a-b
Wood Fragment
Fe
C
40µm
BEI A-Layer
Fe
Fe
Fe
Fe
D
80µm
BEI A-Layer
Q
Al-S
Py
Al-S
RLS
Al-S
E
100µm
BEI 46A-1a
Al-S-2
RGy
Q
RLS
Al-S-1
F
200µm
BEI 44A-3a

Figure 3.10

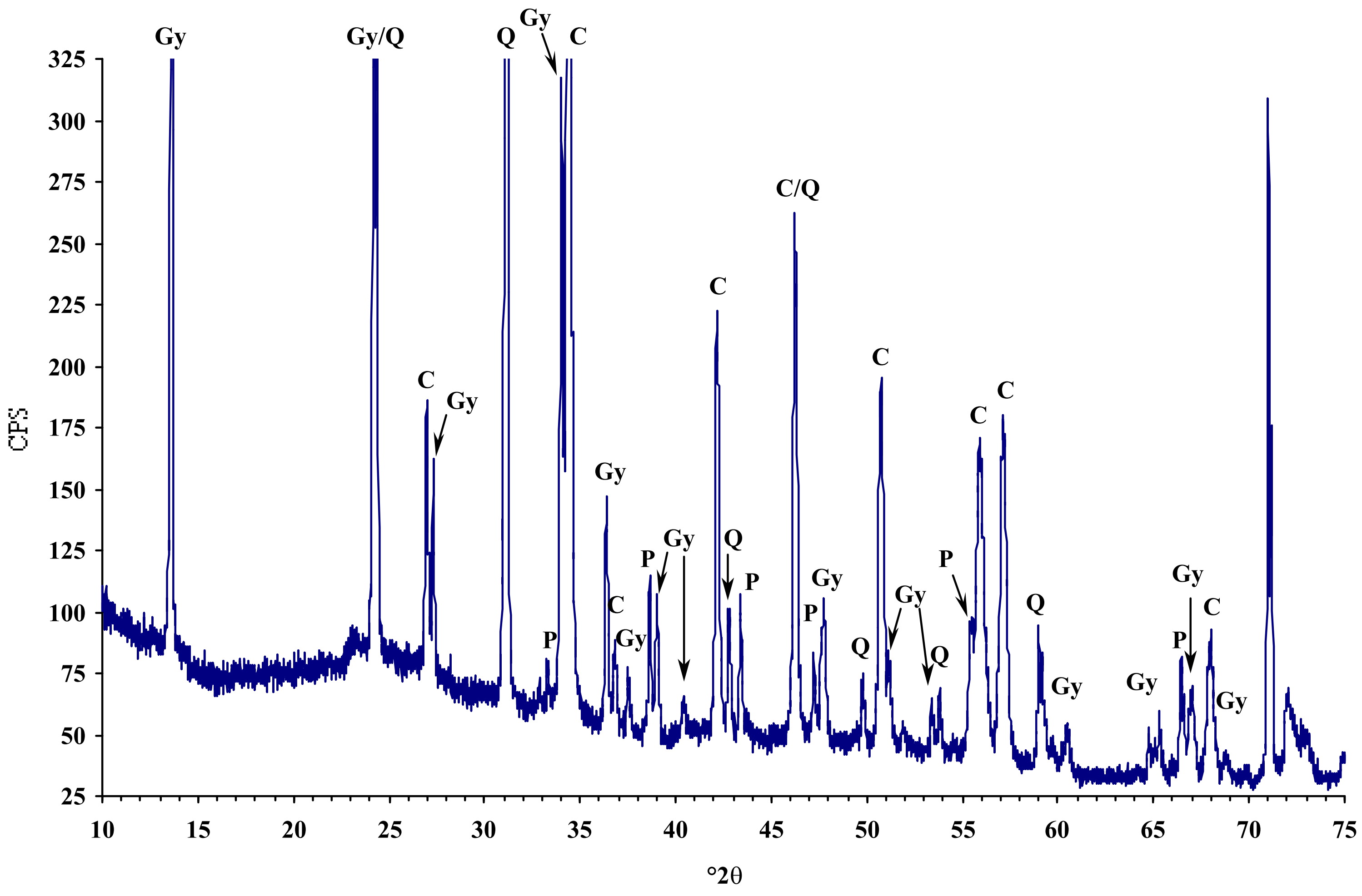

Figure 3.11. X-ray diffraction pattern from representative sample of the transitional zone showing reflections indicative of gypsum (Gy), quartz (Q), calcite (C), and pyrite (P).

Figure 3.12. Back-scatter electron (BSE) images of representative samples from the gray zone showing quartz grains (Q), aluminum- and sulfur-bearing precipitate (Al-S), relict limestone grains (former grain boundary outlined with dotted line), gypsum grains (Gy), and anhedral (Py) and framboidal (yellow arrows) pyrite. (A) Large circular pattern of a relict limestone grain (dotted lines) in the upper gray zone rimmed by aluminum- and sulfur-bearing precipitates (see Fig. 2.9b for typical EDS pattern). Minor amounts of framboidal pyrite are present (yellow arrows) and they are commonly engulfed by the aluminum precipitate. (B) Several relict limestone grains (dotted lines) in a patch of aluminum- and sulfur-bearing precipitate adjacent to a former limestone grain filled with blocky gypsum (Gy). Gypsum was identified by EDS (data not shown) and confirmed by XRD (see Fig. 2.12). (C) Relict limestone grain (dotted lines) outlined by a dense rim of aluminum- and sulfur-bearing precipitates. Note the aluminum- and sulfur-bearing compound and gypsum precipitated within the relict grain. (D) Partially replaced limestone grain (dotted lines) with gypsum replacement rim at the former grain boundary, remnant limestone (LS) in the grain interior, and a reaction rim of aluminum- and sulfur-bearing precipitates separated from the former limestone grain by approximately 5 – 10 μm. This grain is from approximately midway through the gray zone. (E) Close-up of the former limestone grain boundary displayed in panel (D) showing the gypsum replacement rim. Note the intergrowth of remnant limestone fragments. Limestone and gypsum were distinguished by EDS (data not shown) and the relatively high topographic relief of the limestone grains as seen in secondary electron images. (F) Partially replaced limestone fossil fragment from the lower gray zone rimmed by dendritic aluminum- and sulfur-bearing precipitates. Note the framboidal pyrite (yellow arrows) rimming the fossil fragment is surrounded by the aluminum precipitate. Bright grains in the fossil cavities are also pyrite framboids.

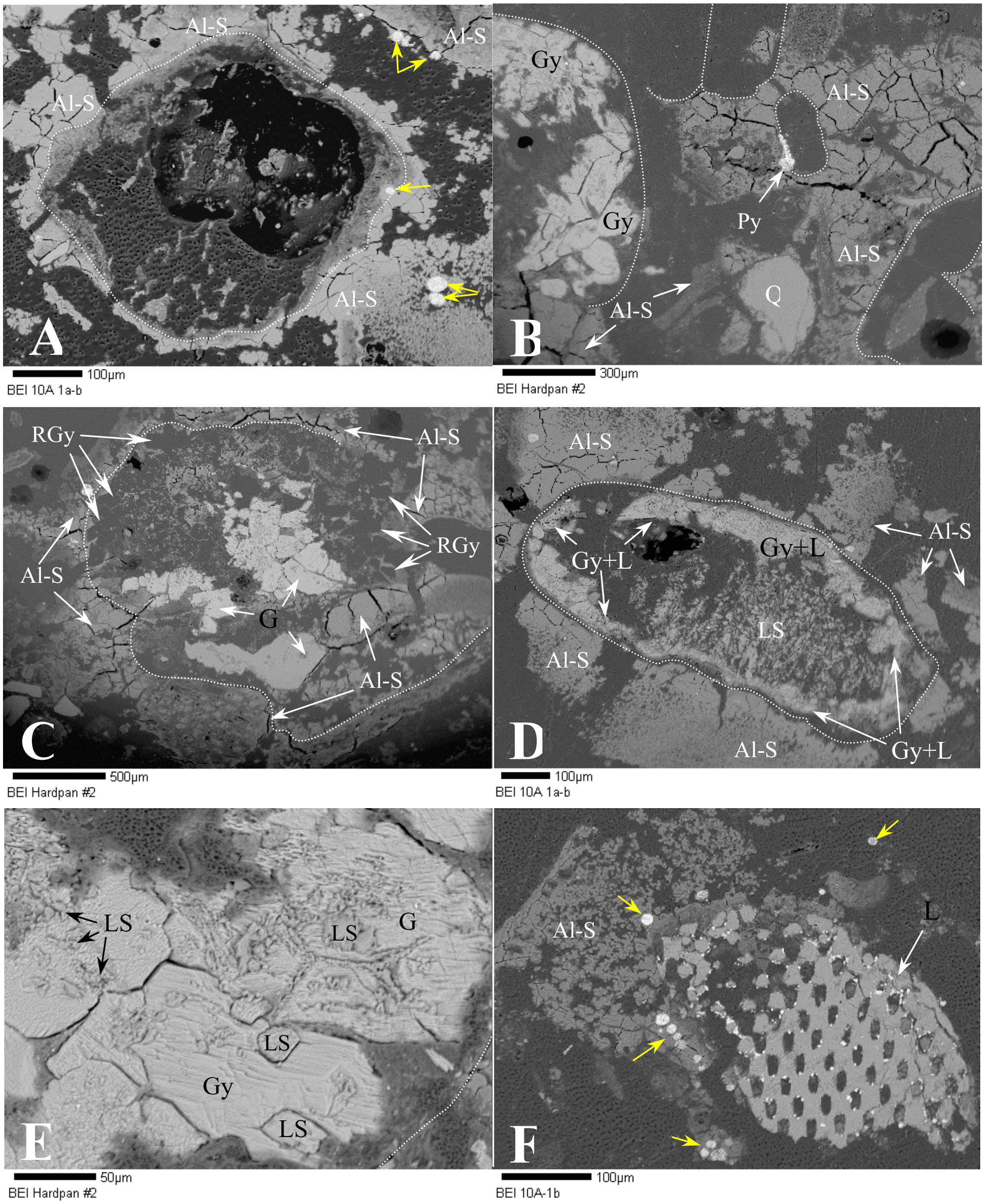
A
Al-S
Al-S
Al-S
Al-S
100µm
BEI 10A 1a-b
B
Gy
Gy
Al-S
Py
Al-S
Q
Al-S
300µm
BEI Hardpan #2
C
RGy
Al-S
RGy
Al-S
G
Al-S
500µm
BEI Hardpan #2
D
Al-S
Gy+L
Gy+L
Al-S
LS
Al-S
Al-S
Gy+L
100µm
BEI 10A 1a-b
E
LS
LS
G
LS
Gy
LS
50µm
BEI Hardpan #2
F
Al-S
L
100µm
BEI 10A-1b

Figure 3.12

Figure 3.13. Back-scatter electron images of the black zone showing organic material (organic), quartz grains (Q), aluminum- and sulfur-bearing precipitate (Al-S), anhedral pyrite (Py), pyrite crystallites (i.e., loose clusters of fine-grained [<1 μm] pyrite; green arrows), and framboidal pyrite (yellow arrows). (A) Band of aluminum- and sulfur-bearing precipitate showing dendritic growth away from the nucleation point. Note the inclusions of framboidal pyrite. (B) Organic matter surrounded by framboidal pyrite and permineralized or replaced with aluminum- and sulfur-bearing precipitates. (C) Large anhedral pyrite grain with clusters of secondary framboidal and individual pyrite crystallites. (D) Quartz grain coated with aluminum- and sulfur-bearing precipitates containing abundant framboidal pyrite inclusions. (E) Lower portion of the black zone showing pristine limestone and associated quartz. Note the abundance of very fine-grained limestone fragments and quartz lining the edge of the more massive limestone grain. (F) Pristine limestone grain showing close-up of associated framboidal pyrite grains. The small, bright specs in the limestone grain are primary pyrite grains associated with the initial limestone.

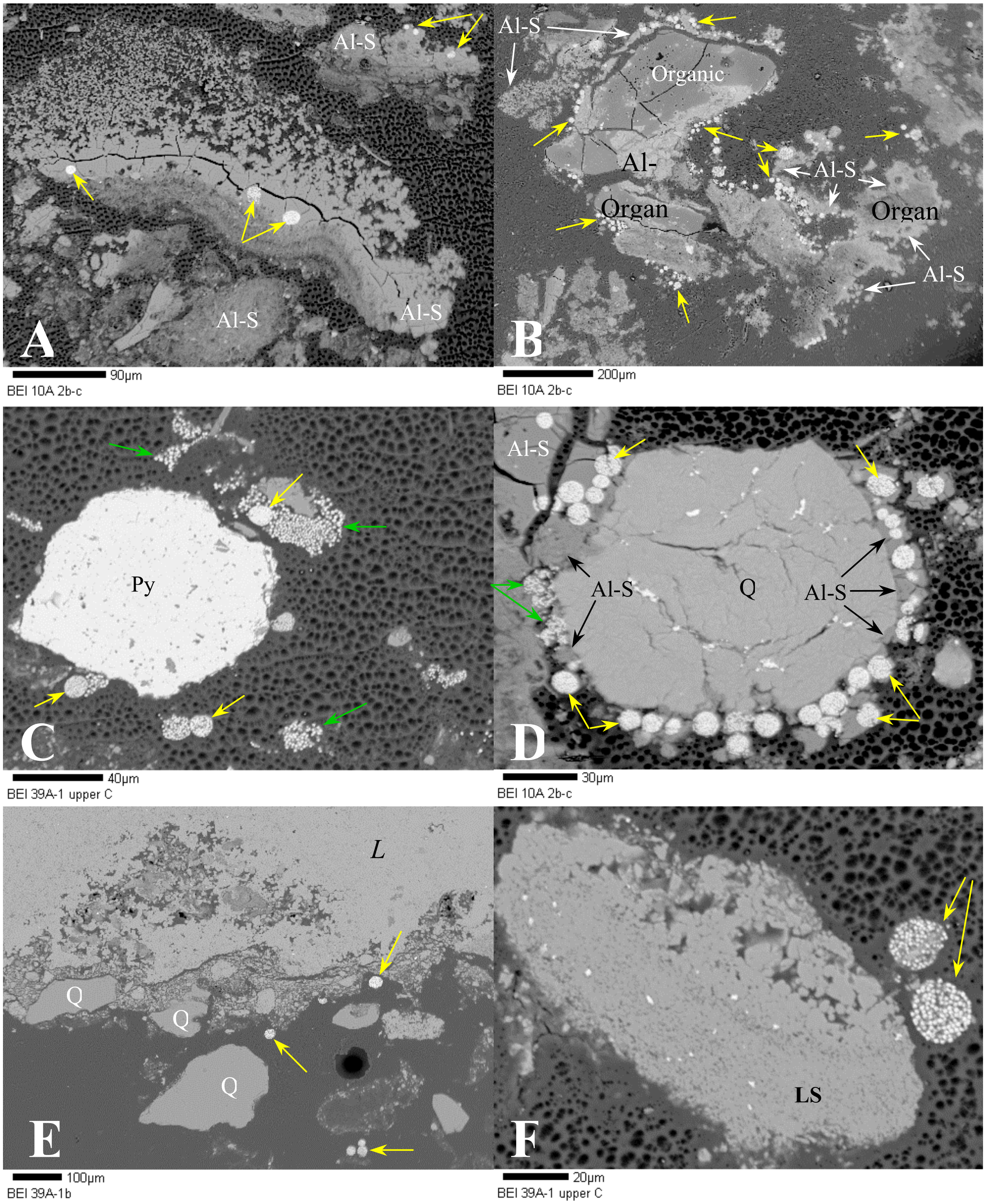
Al-S
Al-S
Al-S
A
90µm
BEI 10A 2b-c
Al-S
Organic
Al-
Al-S
Organ
Organ
Al-S
B
200µm
BEI 10A 2b-c
Py
C
40µm
BEI 39A-1 upper C
Al-S
Al-S
Q
Al-S
D
30µm
BEI 10A 2b-c
L
Q
Q
Q
E
100µm
BEI 39A-1b
LS
F
20µm
BEI 39A-1 upper C

Figure 3.13

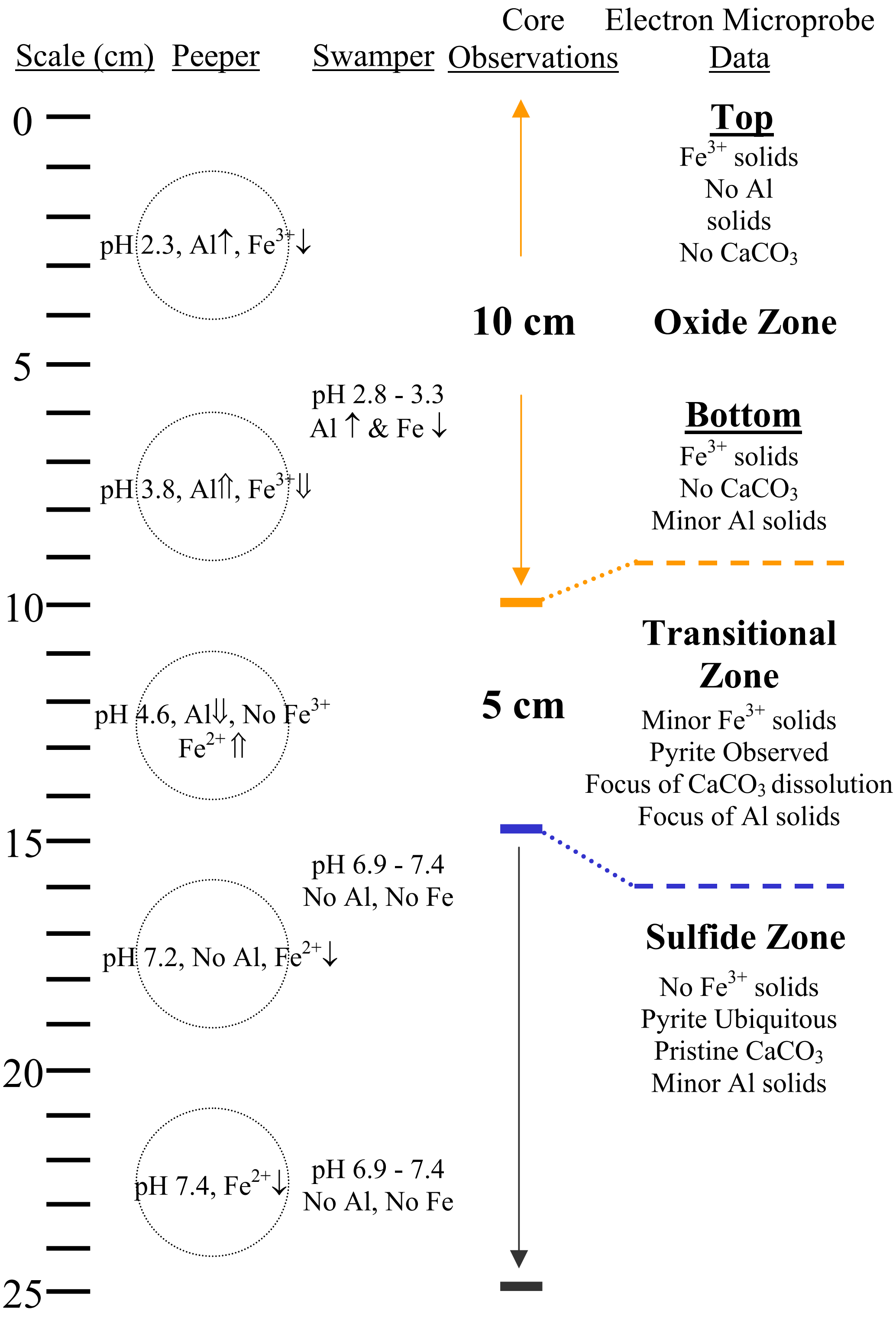

Figure 3.14. Correlation of the pore water data to the three reaction zones. Swamper pore water data are from chapter 2.

CHAPTER 4

TRACE METAL RETENTION IN VERTICAL FLOW CONSTRUCTED WETLANDS TREATING LOW PH, FERRIC IRON-DOMINATED ACID ROCK DRAINAGE[5]

---

[5] Thomas, R.C. and Romanek, C.S. 2002. To be submitted to *Geochimica Cosmochimica et Acta*

ABSTRACT

Remediation strategies employed for mitigation of low-pH, metal-sulfate drainage (i.e., acid rock drainage, ARD) may include passive treatment systems. While shown effective for neutralization of acid and removal of major ions (e.g., iron, aluminum, manganese), trace element removal during acid neutralization in passive systems is rarely investigated. The focus of this paper, therefore, is the fate of trace metals in one common type of passive treatment system, the vertical flow wetland (VFW). The experimental VFW contained a limestone buffered organic substrate (LBOS) and received low pH (<3), ferric iron-dominated ARD for two years. During this time, trace elements (As, Cd, Cr, Cu, U, Co, Ni, and Zn) were removed along a pH gradient controlled by a series of reaction zones that developed above a dynamic limestone dissolution front. Therefore, for the practical purpose of implementing LBOS to treat low pH, ferric iron-dominated ARD, high trace element removal efficiency can be expected as long as the limestone dissolution front does not pass completely through the substrate. With the exception of uranium, trace metal attenuation largely occurred above the limestone dissolution front in the transitional and oxide reaction zones. Trace metal removal was facilitated through sorption to primary organic matter and secondary hydrous iron and aluminum precipitates. The sorption selectivity within the LBOS follows the sequence:

$$As > Cu > Cr > Co = Ni = Zn = Cd > U.$$

Cadmium, copper, chromium, cobalt, nickel, zinc, and uranium were subject to remobilization as the pH decreased over time, although the degree of mobilization was trace element-dependent; arsenic was not remobilized. The following general order of trace element mobility can be applied to the LBOS:

$$U > Co = Zn \geq Cd = Ni > Cu > Cr > As.$$

1. INTRODUCTION

Passive treatment technologies, including constructed treatment wetlands, are widely used for the remediation of acid rock drainage (ARD) related to coal mining in the eastern United States. Because pH, total iron, total manganese, and total suspended solids are generally the only constituents regulated for ARD originating from coal mining activities (U.S. Code of Federal Regulations, 1991), evaluations of most passive treatment systems focus on the neutralization of acid and acid-generating contaminants, and the long-term retention of metals (e.g., iron and manganese). The ultimate fate of trace contaminants is rarely investigated despite the fact that elevated levels of some trace metals are commonly encountered in coal-related ARD (e.g., As, Cd, Co, Cr, Cu, Ni, Zn; Hyman and Watzlaf, 1997). The focus of this paper, therefore, is the fate of trace metals in low pH (<3) ferric iron-dominated ARD treated by one common type of passive system, the vertical flow wetland (VFW).

In VFWs, water flows downward by gravity, usually from a pond, through organic matter and limestone before flowing out through a drainage system. The limestone may be mixed with organic matter in a single layer (limestone buffered organic substrate or LBOS, see Chapter 2) or the VFW may be constructed in distinct layers consisting of organic matter overlying limestone (Kepler and McCleary, 1994). When VFWs containing LBOS are used to treat low pH (<3), ferric iron-dominated ARD, acid neutralization is ultimately controlled by limestone dissolution along a fairly narrow (2 – 5 cm) front that migrates through the substrate over time (Watzlaf, 1997; see chapter 2 and 3). Below the dissolution front, where pore water is buffered by limestone, pH is >6.5 and dissolved metal content approximates that of the final effluent. Within and above the dissolution front, pH and metal (i.e., iron and aluminum) mobility are ultimately controlled by a series of mineral dissolution-precipitation reactions that involves carbonates, aluminum hydroxysulfates, and iron oxyhydroxides (Blowes and Ptacek, 1994; see chapter 3). With continued influx of ARD through the LBOS, the dissolution front will migrate through LBOS and pore water pH and metal concentration will eventually approach that of the influent.

In chapter 3, a series of three mineralogical reaction zones were identified that characterize the reaction sequence through time: the oxide, transitional, and sulfide zones (Fig. 4.1). Furthermore, two stages were described which lead to the development of the three reaction zones and then described a paragenetic sequence for the continued evolution of the zones. With the first introduction of ARD into the water column overlying the LBOS, the ARD-substrate interface is the site of an initial "zone of active limestone dissolution". Dissolved ferric iron and aluminum initially precipitate together in the presence of limestone. Electron microprobe imaging of the upper oxide zone (2.5 cm) showed iron oxyhydroxide replacement of limestone indicating ferric iron initially precipitated at pH as high as 7.0 in the upper 2.5 cm (see chapter 3). Below the initial dissolution zone, after complete removal of ferric iron, pore water conditions were conducive to sulfate reduction (i.e., sulfate-rich, available organic material, pH > 6.5, Widdel, 1988) and the accumulation of sulfide precipitates. Thus initially, the LBOS would have consisted of two main zones, a zone of active limestone dissolution containing mixed ferric oxyhydroxides and aluminum sulfates and a zone of unreacted limestone containing sulfide (see chapter 3).

As the limestone buffering capacity in this initial dissolution zone is overwhelmed by the precipitation of iron and aluminum and depletion of limestone, the pH drops (<6.5), the limestone dissolution front advances, and development of the three reaction zones commence. In chapter 3, a paragenetic sequence for the development of the three reaction zones was described, which can be summarized as follows. The first reaction zone to develop is the sulfide zone. The sulfide zone is characterized by ubiquitous iron sulfides (e.g., pyrite), pristine limestone, and pore water near calcite saturation; it develops below the dissolution front where pore water pH is > 6.5. The sulfide zone is dynamic, “rolling” ahead of the limestone dissolution front as it advances. However, the sulfide zone is ephemeral in nature. At any fixed position within the sulfide zone, with the advancement of the limestone dissolution front, the sulfide zone is overprinted by a transitional zone. The transitional zone, which is defined by partially dissolved limestone and abundant aluminum and calcium hydroxysulfates, demarcates the advancing limits where limestone dissolution occurs. The pore water pH of the transitional zone is held steady between 3.8 and 4.6 by the dissolution of limestone and the precipitation of aluminum and calcium hydroxysulfates. Concurrent with the drop in pH, acid volatile sulfides of the sulfide zone are solubilized and leached while less reactive sulfides, such as pyrite remains. Similar to the sulfide zone, the transitional zone is also both dynamic and ephemeral, advancing with the limestone dissolution front while being overprinted by an overlying oxide zone. Encroachment of the oxide zone, which contains abundant iron oxyhydroxides and only minor aluminum hydroxysulfate in the lower portions, occurs as limestone is consumed completely within the transitional zone. Without the buffering capacity of limestone, pore water pH in the upper transitional – lower oxide zones drops and previously precipitated aluminum and calcium hydroxysulfates dissolve. Thus, the pore water pH of the oxide zone is held at a pH between the influent value and 3.8 by the dissolution of aluminum and calcium hydroxysulfates and the precipitation of iron oxyhydroxides. As part of the overprinting process, pyrite generated in the sulfide zone is dissolved in the oxide zone by ferric iron oxidation of the sulfide moiety. Moreover, aluminum and calcium hydroxysulfates dissolved in the oxide zone are reprecipitated in the advancing transitional zone (see chapter 3).

Thus, the oxide zone represents the final stage of LBOS evolution; all of the original limestone, as well as secondary aluminum and calcium hydroxysulfates and iron sulfides, have been removed. Previous studies (Watzlaf, 1997; see chapter 2) have indicated that, given enough time, the limestone dissolution front will eventually migrate completely through the organic layer and the entire column of substrate will eventually experience the breadth of reactions that culminate in the conversion of the LBOS to "oxide zone" material. Hence, trace metals retained in the oxide zone may be sequestered permanently, whereas trace metals removed in the transitional and sulfide zones, but solubilized in the oxide zone may represent transient retention and result in delayed release from the VFW. Based on this model, determining the ultimate trace element retaining capacity of the LBOS should be as simple as determining the total trace element content sequestered in the oxide zone.

The primary objectives of this study were: (1) to characterize the vertical distribution of As, Cr, Cu, Co, Ni, U, and Zn dissolved in pore water and retained as solids within the three reaction zones of LBOS treating low pH, ferric iron-dominated ARD, (2) to determine the key geochemical processes controlling the development of the observed trace metal profiles in the pore waters and LBOS relative to the three reaction zones, and (3) to predict the long-term sequestration of trace elements in the LBOS.

2. MATERIALS AND METHODS

The experimental set-up employed in this study was described previously (Thomas et al., 1999; see chapter 2 and 3). Briefly, eight plastic tanks (92 cm diameter by 122 cm tall) were used to simulate vertical flow wetlands. Each vertical flow wetland (VFW) tank was filled with 92 cm of limestone buffered organic substrate (LBOS) overlying 15 cm of coarse (#57; i.e. ~1.27 cm) limestone (Fig. 4.2a). Composition and physicochemical characteristics of the limestone buffered organic substrate (LBOS) are presented in Table 4.1.

The ARD was delivered continuously at an average rate of ~20 $mL{\cdot}min^{-1}$ to the top of each VFW tank for two years, starting in late December 1998 and ending in December 2000 (see chapter 2). Effluent drained from the bottom of the tanks through standpipes such that a 15-cm column of ARD was maintained over the LBOS. Influent

ARD had an average pH of 2.4 and was dominated by ferric iron (96% Fe^{3+}; 142 $mg \cdot L^{-1}$ total) and aluminum (84 $mg \cdot L^{-1}$) as primary contaminants (see chapter 2). Influent calcium averaged 52 $mg \cdot L^{-1}$ (chapter 2; see Table R3.1 for further detail).

2.1. Water Sampling and Analysis

Acid rock drainage was flushed through the VFW tanks for ~4 months prior to the onset of sampling. A single influent water sample was taken (weekly) from a manifold distributing water to the eight tanks and effluent water samples were taken from each tank from April 1999 to December 2000. To facilitate this study, trace element data were collected as splits from pore water samples that were previously characterized for iron, aluminum, and calcium (chapter 2 and 3). Fine-scale pore water samples were collected using a vacuum-operated pore-water extractor (i.e., swamper, Winger and Lasier, 1991) and acrylic pore-water diffusion samplers (i.e., peepers, Hesslein, 1976; Carignan, 1984; Carignan et al., 1985) at two different times (June and November, 2000) during the course of this study. Details of the sampling devices and technique can be found in chapters 2 and 3.

2.1.1. Pore Water Sampling

Swampers were basically tubes with a filter (e.g., air stone) at one end and connected to a vacuum flask at the other end. The filter-end of the tubing was placed in the soil and a pore water sample was drawn into the flask via a vacuum pump (see

Winger and Lasier, 1991 for details). Swamper samples were taken June 2000 from two different VFW tanks (30A and 36A). Three different areas, approximately 120° apart, were sampled in each tank. At each sampling area (-1, -2, -3), pore water was drawn at three depth horizons below the substrate-water interface (2-, 11-, and 19-cm; Fig. 4.2b). Samples 30A-2 and 36A-3 from the 2-cm depth horizon were lost during analysis. Approximately 100 mL of pore water was recovered at each horizon. In addition, a single sample of the ARD water column above the LBOS was taken with a syringe.

The peeper was a made using an acrylic (Plexiglas) plate with wells drilled in it (3cm diameter). The wells were filled with deionized water (~3 mL), covered with a 10 nm polycarbonate dialysis membrane, and secured by another matching plate containing 3 cm holes (Hesslein, 1976; Carignan, 1984; Carignan et al., 1985). The peeper contained a total of seven well horizons that provided a detailed pore water profile of the LBOS. Peeper pore water was collected from one tank (44A) between May 21 and June 6, 2000. The peeper was inserted in the LBOS such that the first two well horizons were situated in the water column above the LBOS with the bottom edge of the second well horizon positioned at the sediment-water interface (Fig. 4.2b). The remaining five well horizons provided a pore water profile of the LBOS at 2.5, 7.5, 12.5, 17.5, and 22.5 cm depth. The peeper was left in the LBOS for sixteen days. During this time, the pore water equilibrated with the deionized water through osmosis (Carignan, 1984; Carignan et al., 1985).

2.1.2. Water Analysis

All water samples collected for this study were analyzed for temperature, pH, and dissolved trace metal content (As, Cd, Co, Cu, Ni, U, Zn); further analysis of the same water samples is presented elsewhere (chapters 2 and 3). Temperature and pH were measured in the field (chapter 2). Influent, effluent, and swamper samples for dissolved trace-metal analysis were filtered (0.45 μm), while peeper samples did not require filtering due to the 10 nm pore size of the dialysis membrane (chapter 3). All samples for dissolved trace-metal analysis were acid preserved (1% HNO_3) prior to analysis by inductively coupled plasma mass spectrometry (ICP-MS, Elan 6000, Perkin-Elmer Corporation, Norwalk, CT). Instrument precision was generally < 3% and accuracy was within 10% based on second source calibration checks with certified standards. Lower detection limits of the ICP-MS are listed in Table 4.2 for the individual elements analyzed in this study.

2.2. Substrate Sampling and Analysis

Substrate cores were extracted from two tanks (30A and 36A). In each tank, three areas, 120° apart, were sampled in June 2000 followed by a second sampling event in November 2000 at approximately 60° from the first event. Each core sampled approximately ~20 – 25 cm of the upper LBOS. For the June 2000 sampling, swamper samples were taken concurrently.

Cores were extruded in an anaerobic glove bag and sectioned lengthwise (chapter 3). One half of the core was dried anaerobically and impregnated with epoxy for electron microprobe analysis following methods described in chapter 3, while the other half was divided according to the three reaction zones based on color and texture (see, Fig. 4.2). Material from each zone was sealed separately in an air-tight polyethylene bottle under nitrogen, and frozen for later analysis. At a later date, samples were thawed under nitrogen and physically homogenized. A subsample of each reaction zone was chemically analyzed using both total and sequential dissolution techniques (described below).

Samples of the initial substrate were also collected as the tanks were initially filled with LBOS. Each sample was air-dried, homogenized, and stored for later analysis. Dried, substrate was impregnated with epoxy (chapter 3) and examined by electron microprobe to establish textures and elemental associations specific to the starting materials. All samples of the initial LOBS were treated according to the methodologies outlined below for the core samples to provide baseline data on the solid phase.

2.2.1. Electron Microprobe Analysis

Oriented, polished sections (~0.5 cm thick) of each zone were prepared from the epoxy-impregnated samples. Polished substrate chips were examined with an electron microprobe (JOEL 8600) using back-scatter electron (BSE) imaging at an accelerating voltage of 15KeV and beam current of 5 nA. The elemental composition of precipitates was determined using an energy dispersive spectrometer (EDS; ~ 1 µm spot size).

Sodium is the element of lowest mass routinely detected using the EDS system on this particular instrument and the minimum detectable concentration for elements of higher mass was estimated at between 0.5 and 1 weight percent (Fleisher pers. comm., 2002). Thus, trace elements precipitated as discrete solids smaller than a few tenths of a micron or generally “associated” with primary or secondary solids (e.g., organic fragments or iron oxyhydroxides, respectively) in concentrations less than a few weight percent were not detected by this method.

2.2.2. Total Metal Digests

Five to ten gram splits of each reaction zone from each core were weighed, removed from the anaerobic glove bag, and air-dried for several days. The air-dried samples were then re-weighed to obtain a gravimetric water content. The dried samples were ground to a fine powder with a cryogenic grinder for total metal analysis. Eight samples of the initial substrate were also cryogenically ground. Approximately 0.5 g of each powdered sample was digested with 10mL of 50% trace-metal grade HNO_3 plus a few drops of 30% H_2O_2 at 105°C using a block digester according to EPA method 3050B for the acid digestion of sediments, sludges, and soils. Method 3050B is an “environmental digest” and does not completely solubilize refractory material such silicates and resistant organic matter. Therefore, small amounts of detritus (i.e., quartz) and clear organic fragments remained after the digest.

The digest was diluted to a final volume of 50 mL with deionized water and then filtered (0.45 µm) before analysis by inductively coupled plasma optical emission spectrometry (ICP-OES, Elan 4300DV, Perkin-Elmer Corporation, Norwalk, CT). The ICP-OES methodology and quality control procedures employed were based on the EPA method 6010 (SW 846). The ICP-OES calculated precision internally by collecting triplicate readings for each sample. The internal relative standard deviation (i.e., instrument precision) of these readings was usually < 2%. Similar to the ICP-MS procedure, samples were calibrated to certified standards as described above. In an effort to gauge sample heterogeneity and reproducibility (i.e., overall precision), several replicate, 0.5-g powdered samples were digested and analyzed; results were within 20% of each other.

2.2.3. Sequential Extraction Analysis

2.2.3.1. Sequential Extraction Scheme. A sequential extraction scheme, modified from Miller et al. (1986) and Clark et al. (1996), was employed in an effort to determine trace element partitioning to the various solids identified in the LBOS. This procedure used four successively aggressive dissolution steps to extract trace elements from the different LBOS solids. The final step was further subdivided into three additional sequential sub-steps for some samples. The reagents and extraction times employed and chemical forms targeted are listed in Fig. 4.3. In theory, the extraction scheme first releases: 1) weakly-bound, neutral-salt exchangeable (NSE) trace metals, followed by 2) acid soluble (AS) material such as carbonates, acid volatile sulfides, and some aluminum compounds, 3) pyrophosphate (PYRO) extractable materials such as humic substances or metals complexed with organic matter, and finally 4) recalcitrant material (R) such as iron oxides, sulfides, and refractory organic material. Silicate minerals are generally not dissolved in this extraction scheme.

Based on a prior knowledge of the mineralogical content of the substrate from each zone, the recalcitrant material from the oxide zone (R) was further extracted, so that trace elements associated with "iron oxides" could be distinguished from other recalcitrant phases (i.e., refractory organic material and sulfides); the sequence included: (1) oxalate-extractable iron (R_{ox}), which targets amorphous iron oxides, (2) citrate-dithionite extractable iron (R_{cd}), which targets crystalline iron oxides, and (3) residual material (R_{res}). For most samples from the transitional and sulfide zones, pyrite was the only mineral that could be extracted in the recalcitrant fraction, so only the residual step (R_{res}, Fig. 4.3) was performed for these reaction zones. However, because minor amounts of iron oxyhydroxide were observed in the transitional zone, and to provide some level of comparison, all three extraction steps (R_{ox}, R_{cd}, R_{res}) were performed on one core (#2) from the transitional zone of tank 36A. Thus, for the oxide zone samples and the transitional zone sample from core #2 of tank 36A, the recalcitrant fraction (R) is equal to the sum of the oxide steps (R_{ox} and R_{cd}) and the residual step (R_{res}).

Splits of the eight initial substrate samples were also subjected to sequential extraction. Samples of initial substrate were divided into two groups to determine baseline trace elemental concentrations in each step. The first group, which consisted of five samples, was only subjected to the four basic extraction procedures, while the second group, which consisted of the remaining three samples, was subjected to all six extraction steps.

2.2.3.2. Sequential Extraction Procedure. All samples were extracted in triplicate and all transfers were recorded by weight. Sequential extractions were performed on damp, unground samples to avoid chemical changes that might occur upon drying and cryogenic grinding (i.e., oxidation of iron monosulfides). Extraction of the initial substrate was conducted on dry unground material. Approximately 0.5 g of homogenized substrate was transferred to a 50 mL Oakridge tube having a rubber gasket cap. Extractants were prepared with trace metal-grade reagents and milli-Q water (see Fig. 4.3 for details). Twenty grams of extractant were added to each tube providing a 1:40 substrate to extractant ratio (by weight/weight). Neutral-salt exchangeable (NSE) and acid soluble (AS) extraction steps were conducted in an oxygen-free environment to prevent oxidation of any acid volatile sulfides (i.e., iron monosulfides). Solutions used in these steps were prepared and stored anaerobically. The Oakridge tubes were filled and sealed in an anaerobic glove bag prior to extraction. Extractions were carried out at room temperature (unless otherwise noted in Fig. 4.3) on a low-speed shaker table, except the R_{cd} and R_{res} recalcitrant extraction steps, which were performed in a water bath having a built in shaker. Samples were oriented vertically for the R_{cd} and R_{res} extraction steps; all other samples were shaken on their sides from end to end.

The NSE extractant was separated from the remaining solids by filtering with a 0.4 μm polycarbonate disposable vacuum-filtration kit in the anaerobic glove bag. The filter and residual solids were transferred back to the Oakridge tube and re-weighed for the AS extraction step. After the AS step, the filter was removed from the tube and any attached soil particles were carefully placed back in the Oakridge tube. The extractant was separated from the residual solid by centrifugation (10,000 rpm for 20 minutes) and the supernatant was decanted. The supernatant was acidified with concentrated ultra-pure nitric acid to a final concentration of 1% and stored in a polyethylene bottle for metal analysis. The residual solid was rinsed with de-ionized water to remove any remaining extractant before being filtered with a 0.4 μm polycarbonate filter via vacuum-filtration. The polycarbonate filter and residual solid sample were transferred back to the Oakridge tube and the procedure was repeated for the remaining extraction steps (PYRO, R_{ox}, R_{cd}, and R_{res}). Blanks were analyzed with polycarbonate filters.

The NSE and AS extractants were diluted 1:10 before analysis by ICP-OES, while the remaining extractants did not require dilution. All ICP-OES analyses were back calculated to dry weight by subtracting the water content of the sample. Methodology and quality control procedures were the same as those employed for the total metal digests.

3. RESULTS

3.1. Water Chemistry

3.1.1. Influent water chemistry

Influent and effluent chemistry is reported in Table 4.2. Influent trace metals with average concentrations significantly higher than the lower detection limit of the ICP-MS included (average concentration reported in parenthesis following each element): arsenic (29 $\mu g \cdot L^{-1}$), cadmium (6.2 $\mu g \cdot L^{-1}$), chromium (90 $\mu g \cdot L^{-1}$), copper (383 $\mu g \cdot L^{-1}$), uranium (12 $\mu g \cdot L^{-1}$), cobalt (356 $\mu g \cdot L^{-1}$), nickel (716 $\mu g \cdot L^{-1}$), and zinc (1647 $\mu g \cdot L^{-1}$). In the case where dissolved concentrations were below the ICP-MS detection limits, an operationally-defined value, equal to the lower detection limit, was entered for the purpose of calculating effluent average. Influent arsenic, cadmium, and uranium were frequently below the ICP-MS detection limit (Table 4.2), however the maximum concentration observed was at least two orders of magnitude greater. The concentration range of the remaining trace elements, Cr, Cu, Co, Ni, and Zn, was always above the ICP-MS detection limit.

3.1.2. Effluent water chemistry

Overall, the LBOS was very effective at removing trace metals from the influent ARD. In general, for all trace elements, the highest and lowest effluent values recorded for individual tanks were directly related to the fluctuations in influent concentration, so that the highest effluent concentrations occurred concurrent with the highest influent concentrations. For all trace elements, at least once during the study, the effluent concentration was below the detection of the ICP-MS; this was typically coupled to a relatively low influent concentration. To minimize the effect of fluctuations in influent trace element concentration over time, reductions in the trace element concentration were calculated as the percentage of trace element removed (avg. effluent/avg. influent).

The greatest reduction in effluent occurred with copper and cobalt with >99% average removal of both trace metals in all eight tanks. Ninety-nine percent of the influent nickel and 98% of the influent chromium were also removed on average in all eight tanks without much variation among the tanks. Cadmium removal was consistently below the detection limit of the ICP-MS in all eight tanks. There was slight variation in the range of average uranium and zinc removed among tanks with 97% to >99% uranium and 96 to 98% zinc removed. Finally, arsenic exhibited a 10% range in average removal between tanks with a minimum of 88% and a maximum of 98% for a single tank.

3.1.3. Pore water – swampers and peepers

Based on pH profiles of the swamper samples compared to the peepers, it was concluded in chapter 3 that the swamper actually sampled pore water approximately 4 cm deeper than the sampling depths indicated. Therefore, an adjustment of 4 cm was made to the swamper data to compare pore waters extracted by the two methods. Consequently, although the swamper sampling depths originally targeted three reaction zones, the final swamper data sampled pore waters of the middle oxide (6 cm) and sulfide (15 and 23 cm) zones.

For the peeper profile, it was determined (see chapter 3) that the first two well horizons (-7.5 and –2.5 cm) sampled the ARD water column overlying the LBOS. The third well horizon (2.5 cm), which was the first horizon in the substrate, sampled pore waters of the upper portion of the oxide zone. The fourth (7.5 cm) and fifth (12.5 cm) peeper sampling horizons represented the interface of the oxide and transitional zones and the bottom of the transitional zone, respectively, and the lower most two peeper well horizons (17.5 and 22.5 cm) sampled pore waters of the sulfide zone.

The pore water data collected with both the swamper and peeper samplers are presented in Fig. 4.4. In addition to pore water data, the influent ARD, sampled at the distribution manifold, and the effluent, sampled at the standpipe, are also plotted. For the swamper data, two influent and two effluent samples are shown. The influent samples were collected from the manifold eight days prior to and one day before sampling, while the effluent samples were collected, one from each tank, the day before sampling. For the peeper data, there are three influent and three effluent samples shown. Influent and effluent samples were collected the day before the peeper was installed, one week later, and after two weeks concurrent with removal of the peeper sampler.

3.1.3.1. pH. The influent pH measured at the manifold was ~2.4 the day before swamper sampling (June 27, 2000) and ranged between 2.4 and 2.9 during peeper sampling (May 21 – June 6, 2000; Fig. 4.4). The pH of the ARD water column overlying the LBOS measured during the swamper sampling was similar to the manifold influent with pH values of 2.3 and 2.4 measured in tanks 36A and 30A, respectively. In contrast, the peeper pH (~2.2) of the ARD water column overlying the LBOS was lower than the influent delivered to the tank over the peeper equilibration period. Swamper and peeper pore water data indicated that the oxide zone (0 – 10 cm deep) yielded a range of pH values that increased with depth. The first peeper well horizon within the substrate (2.5 cm) recorded a pH of 2.3. The four swamper samples collected at ~ 6 cm had pH values of 2.8, 2.9, 3.0, and 3.3. Finally, the second peeper well horizon (7.5 cm), indicative of the lower oxide/upper transitional zone, had a pH of 3.8. The transitional zone, which was only sampled by the peeper (12.5 cm), had a pH of 4.6. The 15 and 23 cm swamper sampling depths and the lower two peeper well horizons (17.5 and 22.5 cm), provided 14 samples of the sulfide zone with a fairly narrow pH range (6.8 – 7.6) for all samples.

Both pore water analysis techniques indicated that the pH in the sulfide zone was higher than the final effluent values.

3.1.3.2. As. Influent arsenic concentration measured at the manifold the day before swamper sampling was 92 $\mu g \cdot L^{-1}$ (Fig. 4.4). Influent samples taken from the ARD water column overlying the LBOS at the time of swamper sampling (8 and 14 $\mu g \cdot L^{-1}$ from tanks 36A and 30A, respectively) indicated that appreciable arsenic removal occurred at low pH (2.2 – 2.4) either in the piping system delivering the ARD to the tank or in the water column overlying the ARD. Swamper pore water analyses showed that arsenic concentrations in the oxide zone (6 cm) were similar to concentrations in the overlying ARD water column at a pH $\leq$ 3.3. Swamper samples from the sulfide zone (15 and 23 cm) indicated that arsenic concentrations were largely similar to the effluent concentrations at pH > 6.8, although arsenic levels as high as 5 – 6 $\mu g \cdot L^{-1}$ were measured at 15 cm. Even though the sulfide zone (i.e., 15 and 23 cm) average was similar, the range in arsenic values decreased with depth (0 – 4 $\mu g \cdot L^{-1}$ at 23 cm). Peeper pore water samples were not analyzed for arsenic.

3.1.3.3. Cr. Influent chromium concentration was 126 $\mu g \cdot L^{-1}$ the day before swamper sampling (Fig. 4.4), whereas influent chromium concentration ranged between 132 – 160 $\mu g \cdot L^{-1}$ during equilibration. Chromium concentrations of the ARD water column overlying the LBOS measured with both the swamper (100 – 127 $\mu g \cdot L^{-1}$) and the peeper (160 – 188 $\mu g \cdot L^{-1}$) were slightly lower than the manifold influent concentrations.

Swamper and peeper samples of the oxide zone exhibited a range of chromium values that was somewhat pH dependent. Pore water from the upper oxide zone (pH 2.3), collected at 2.5 cm with the peeper, contained dissolved chromium (208 $\mu g \cdot L^{-1}$) that was higher than the influent concentration. Swamper samples indicated that dissolved chromium in the oxide zone at 6 cm was similar to influent concentrations when the pH was between 2.8 and 3.3. Peeper pore water samples collected from the second well horizon (7.5 cm) indicated minor chromium retention in the bottom of the oxide zone at pH 3.8 (i.e., 22% of the influent concentration). Peeper data also showed that additional chromium removal occurred in the transitional zone (12.5 cm) between pH 3.8 and 4.6. The majority of swamper and peeper pore water samples from the sulfide zone (>15 cm) indicated that >96% of the dissolved chromium measured in the ARD water column was removed at pH < 6.8, which is similar to that removed when ratioing the final effluent concentration with the influent concentration (Table 4.2). As an exception, chromium in the lower most peeper well horizon was ~91 $\mu g \cdot L^{-1}$ at pH 7.4.

3.1.3.4. Cu. Influent copper concentration was 467 $\mu g \cdot L^{-1}$ the day before swamper sampling (Fig. 4.4), while influent concentration ranged between 567 – 713 $\mu g \cdot L^{-1}$ during peeper equilibration. Both swamper and peeper samples of the ARD water column overlying the LBOS contained copper concentrations similar to influent concentration.

The range in dissolved copper concentrations obtained from the oxide zone was largely pH dependent. Peeper data showed there was no major change in the pore water copper concentration in the upper oxide zone (2.5 cm; pH 2.3) compared with the overlying ARD water column (pH 2.2). In contrast, dissolved copper concentrations in swamper samples (6 cm) nearly doubled relative to the influent levels between pH 2.8 – 3.3 with a maximum concentration of 1291 $\mu g \cdot L^{-1}$ obtained at pH 2.9. Peeper data from the bottom of the oxide zone (7.5 cm) exhibited >90% copper removal from the pore water relative to the influent by pH 3.8. According to peeper data, most of the remaining copper was removed in the transitional zone (12.5 cm) to near effluent concentrations by pH 4.6. There was only minimal dissolved copper (0 – 8 $\mu g \cdot L^{-1}$) detected in the sulfide zone pore water (> 15 cm) collected with either technique or in the corresponding effluent samples.

3.1.3.5. U. Influent uranium concentration was 15 $\mu g \cdot L^{-1}$ the day before swamper sampling (Fig. 4.4). Analysis of the ARD water column overlying the LBOS indicated uranium concentrations were similar to the ARD source. Pore water collected from the oxide zone with the swamper (6 cm; pH 2.8 – 3.3) yielded uranium concentrations higher than the ARD overlying the substrate (23 – 32 $\mu g \cdot L^{-1}$). Swamper samples from the sulfide zone (15 and 23 cm) indicated that uranium was completely removed from the pore water by pH 6.8, as concentrations were largely similar to the effluent concentrations (although uranium levels as high as 1 $\mu g \cdot L^{-1}$ were measured). Peeper pore water samples were not analyzed for uranium.

3.1.3.6. Cd. Influent cadmium concentration was approximately 8 $\mu g \cdot L^{-1}$ the day before swamper sampling. In contrast, the influent cadmium concentration was below the detection limit the week prior to and during the first week of peeper equilibration, while it increased to ~9 $\mu g \cdot L^{-1}$ by the last week of peeper equilibration. Cadmium concentration in the ARD water column overlying the LBOS measured during the swamper sampling was similar to influent concentration. The ARD water-column cadmium measured with the peepers ranged between ~12 and 14 $\mu g \cdot L^{-1}$. Swamper and peeper pore water data displayed different cadmium profiles. On average, the swamper data showed that the oxide zone (6 cm) cadmium concentrations increased four-fold (39

$\mu g \cdot L^{-1}$). Increases were pH-dependent with average increases between pH 2.8 – 3.0 (i.e. 33 – 37 $\mu g \cdot L^{-1}$) and a maximum increase (51 $\mu g \cdot L^{-1}$) at pH of 3.3. In contrast, the peeper data showed there was no major change in the pore water cadmium concentration in the upper oxide zone (at pH 2.3) compared with the overlying ARD water column (pH 2.2). Moreover, peeper data showed >50% removal of water column cadmium by pH 3.8 (bottom of the oxide zone). According to peeper data, complete removal of cadmium was accomplished by pH 4.6 (transitional zone). There was no dissolved cadmium detected in the sulfide zone pore water collected with either technique or in the corresponding effluent samples.

3.1.3.7. Co, Ni, Zn. Cobalt, nickel, and zinc concentrations all exhibited similar behaviors within swamper and peeper pore water profiles (Fig. 4.4). Influent concentrations of cobalt, nickel, and zinc were 383, 743, 1545 $\mu g \cdot L^{-1}$, respectively the day before swamper sampling (Fig. 4.4). Influent cobalt, nickel, and zinc concentrations were consistent during peeper equilibration (560 – 568, 1146 – 1165, 2339 – 2378 $\mu g \cdot L^{-1}$, respectively). Analysis of swamper samples indicated that the ARD water column overlying the LBOS contained cobalt, nickel, and zinc concentrations roughly similar to the corresponding influent values. The concentrations of cobalt, nickel, and zinc measured in the two peeper samples of the overlying ARD water column were similar to the respective influent concentration measured during peeper equilibration.

Analysis of swamper and peeper samples from the oxide zone (0 – 10 cm) showed that concentrations of cobalt, nickel, and zinc increased in the upper oxide zone at low pH followed by precipitation in the transitional zone at higher pH. Peeper samples showed minor solubilization occurred just below the ARD-substrate interface (2.5 cm) at pH 2.3. In general, the swamper samples (6 cm) indicated that concentrations increased with increasing pH, although at pH 2.8 there was no change in cobalt and nickel concentrations, and only a slight increase in zinc relative to the influent concentrations. However, swamper (6 cm) cobalt, nickel, and zinc concentrations increased with pH between 2.9 – 3.3 with peak values observed at pH 3.3. The peeper sample collected from the oxide – transitional zone interface (7.5 cm) indicated that the trend of increasing cobalt, nickel, and zinc concentration continued up to pH 3.8 (811, 1798, 5194 $\mu g \cdot L^{-1}$, respectively). According to peeper data, cobalt, nickel, and zinc removal to near effluent concentrations was accomplished by pH 4.6 (transitional zone, 12.5 cm). Both peeper and swamper samples indicated that cobalt concentrations remained ~10 – 20 $\mu g \cdot L^{-1}$ between pH 4.6 and 6.8. Above pH 6.8, cobalt concentrations were similar to the final effluent (< 10 $\mu g \cdot L^{-1}$). Swamper and peeper data showed that, above pH 6.8, nickel concentrations varied from below detection up to 64 $\mu g \cdot L^{-1}$ without correlation to pH. Zinc concentrations exhibited the greatest variability above pH 6.8, ranging from below effluent concentrations (i.e., <91 μgL^{-1}) up to five times the effluent concentration (448 $\mu g \cdot L^{-1}$).

3.2. Substrate Analysis

3.2.1. Electron Microprobe Analysis

In general, trace elements were not identified during EDS analysis of the LBOS reaction zone samples indicating that trace elemental concentrations were lower than the

EDS detection limits (~0.5 – 1%) at the spatial scale of sample analysis. However, rare grains containing measurable amounts of copper, nickel, cobalt, and zinc were observed in the LBOS. All of these grains were small, averaging 10 – 20 μm in diameter.

Microprobe analysis of the initial substrate revealed small discrete grains of copper-nickel in the vesicle of a wood fragment (Fig. 4.5a) and zinc sulfide with another wood fragment (not shown). Rare iron- and sulfur-bearing (e.g., pyrite; chapter 3) grains were found associated with the limestone, although their trace element content was below the detection limit. Only rare grains containing trace metals were identified in the oxide and transitional zones (Fig. 4.5b,c). They were probably detrital grains originating from tools used to prepare the limestone screenings or the wood chips from the composted stable waste. Trace metals were found solely associated with sulfur in the sulfide zone. Sulfur-bearing, nickel-cobalt grains occurred as thin bands associated with framboidal (spherical) pyrite (Fig. 4.5d-f). Zinc sulfide was also observed (Fig. 4.5e-f).

3.2.2. Total and Sequential Extraction Data

Total digest data are presented in Fig. 4.6 and Table 4.3 for core samples from each reaction zone and the initial LBOS. Total digest data were only collected for arsenic, chromium, copper, cobalt, and zinc; cadmium, nickel, and uranium were not collected due to analytical error. The total concentrations of cadmium, nickel, and uranium were derived from the sum of the four sequential extraction steps (NSE, AS, PYRO, and R series; Table 4.3). These cumulative sequential totals are presented in Fig. 4.6 for cadmium, nickel, and uranium in lieu of the single-step total digests.

For arsenic, chromium, copper, cobalt, and zinc, the cumulative sequential total data (Table 4.3) were compared to the total concentrations obtained from the single-step digestion. Both techniques produced similar results. Most totals were within 30% of one another, with the totals from the cumulative sequential extractions typically yielding the higher concentration.

Sequential extraction data are presented in Fig. 4.7 and Table 4.3. Since the extractions were conducted in triplicate, the data shown in Fig. 4.7 is the average of three sub-samples taken from each reaction zone within each core. Eight samples of the initial substrate were also extracted in triplicate.

To provide baseline data, total trace element concentrations of the initial LBOS were determined (Fig. 4.6; Table 4.3). Based on the trace element content of the limestone screenings and the known mixing ratio of organic matter to limestone (52.9% $CaCO_3$), the trace element contribution from the limestone was determined (Table 4.1). The trace element content of the organic matter component was determined by subtracting the limestone contribution from the total (Table 4.1).

3.2.2.1. As. Total digests of the initial substrate indicated that arsenic concentrations in the LBOS at the start of the experiment were relatively low, averaging 2.5 $mg \cdot kg^{-1}$ with a total range from below detection to 4.6 $mg \cdot kg^{-1}$ (Fig. 4.6). Sequential extractions of the initial substrate showed that arsenic partitioning was bimodal, but sporadic, at the start of the experiment (Fig. 4.7). Approximately 5 to 50% of the arsenic in initial LBOS resided in the NSE fraction, while the remaining mass was removed in the recalcitrant fraction. Subdivision of the recalcitrant fraction indicated that 60 to 75%

of the recalcitrant arsenic (i.e., 50 to 70% of the total) was attributable to the R_{cd} phase with the remaining balance accounted for in the residual (R_{res}) fraction.

Total digests indicated arsenic concentrations in core material from the transitional and sulfide zones were similar to initial LBOS over the course of the project (Fig. 4.6). However, sequential extraction data demonstrated that arsenic concentrations in these zones were lower. Temporal comparison of sulfide and transitional zone core material indicates that active leaching occurred over the six months between core sampling events. Most of the removal occurred in the recalcitrant fraction (Fig. 4.7).

Total digests of core samples collected in June 2000 showed that arsenic concentrations in the oxide zone increased from initial concentrations to an average of 21 $mg \cdot kg^{-1}$ during the first eighteen months of the project (range of 13 – 30 $mg \cdot kg^{-1}$; Fig. 4.6). Average of the total digests from oxide zone samples taken November 2000 (35 $mg \cdot kg^{-1}$) indicated the total arsenic concentration continued to increase over the next six months. Sequential extractions showed that the majority of arsenic sequestered in the June 2000 samples of both tanks (70 to >90%) resided in the recalcitrant fractions (Fig. 4.7). Within the recalcitrant fraction, 30 to 55% was extracted in the R_{ox} fraction, 10 to 45% in the R_{cd} fraction, and 0 to 30% in the R_{res} fraction. Sequential extractions showed that arsenic distribution did not change greatly over time (Fig. 4.7).

3.2.2.2. Cr. Total digests of the initial substrate indicated that the starting chromium concentrations were fairly consistent (5.0 – 9.4 $mg \cdot kg^{-1}$), averaging 6.7 $mg \cdot kg^{-1}$ (Fig. 4.6). According to sequential extraction data of the initial substrate, chromium was predominantly distributed among the recalcitrant (45 – 70%), the AS (17 – 35%), and the PYRO (~15%) fractions (Fig. 4.7). Subdivision of the recalcitrant fraction indicated that approximately half of the recalcitrant chromium was attributable to the R_{ox} and R_{cd} phases and the other half to the R_{res} fraction. Within the R_{ox} and R_{cd} half of the recalcitrant fraction, the R_{ox} to R_{cd} ratio was 1 to 3.

Total digest data showed that chromium concentrations in the sulfide zone were equal to or slightly higher than the initial substrate and they were consistent between June and November 2000 sampling events (Fig. 4.6). Sequential extractions indicated that the chromium distribution in the sulfide zone was similar to the distribution within the initial substrate and that it did not change over time (Fig. 4.7).

June 2000 core material from the transitional zone exhibited greater than a four-fold increase in total chromium on average (34 $mg \cdot kg^{-1}$) relative to the initial LBOS, although the total range among cores was large (6.3 to 83 $mg \cdot kg^{-1}$; Fig. 4.6). Sequential extractions showed these increases occurred in the AS (12 – 50%), PYRO (5 – 20%), and recalcitrant fractions (30 – 85%). Core collected in November 2000 were slightly higher in chromium (42 $mg \cdot kg^{-1}$) relative to those collected in June 2000 or the initial LBOS (Fig. 4.6). The increase was primarily attributed to the AS step (Fig. 4.7).

Total digests of June 2000 core samples from the oxide zone showed that chromium concentrations increased an order of magnitude (80 $mg \cdot kg^{-1}$ average) compared to the initial LBOS during the first eighteen months of the project (Fig. 4.6). Sequential extractions showed that increase largely occurred in the AS, PYRO and recalcitrant fractions (Fig. 4.7). Within the recalcitrant fraction, most of the observed increase occurred in the R_{ox} and R_{cd} fractions. Total digests of the November 2000 core samples indicated the average chromium concentration in the oxide zone (94 $mg \cdot kg^{-1}$) increased between sampling events but that chromium partitioning changed very little.

Chromium was extracted primarily in the recalcitrant (40 – 60%), PYRO (20 – 25%), and AS (15 – 35%) fractions, with approximately two-thirds of the recalcitrant fraction being attributed to the R_{ox} and R_{cd} fractions.

3.2.2.3. Cu. Total digests of the initial substrate indicated that the copper concentration in the LBOS at the start of the experiment was relatively low, averaging 4.5 $mg \cdot kg^{-1}$ (range 3.8 – 5.8 $mg \cdot kg^{-1}$). Sequential extractions of the initial substrate indicated that copper was distributed in the recalcitrant (60 – 65%), PYRO (25 – 30%), and NSE (<10%) fractions. Subdivision of the recalcitrant fraction showed approximately even partitioning of recalcitrant copper into the R_{ox} and R_{res} fractions.

Copper in June 2000 cores from the sulfide zone was generally similar or slightly elevated in concentration compared to the LBOS with an average 11 $mg \cdot kg^{-1}$ and a range of 4 to 31 $mg \cdot kg^{-1}$. Sequential extractions showed copper partitioning in the sulfide zone was generally similar to the initial substrate, although there was a loss of copper in the NSE fraction and a slight increase in the recalcitrant fraction (70 – 85% of total). Little change occurred over the six months between he June and November 2000 sampling events except for a relative increase in the PYRO and recalcitrant fractions over time.

Two thirds of the June 2000 transitional zone samples contained copper concentrations similar to the sulfide zone (6 – 26 $mg \cdot kg^{-1}$), while the remaining samples showed a large increase (94 and 182 $mg \cdot kg^{-1}$). Extractions indicated that all of the increase in total copper occurred in the PYRO (3 – 25%) and recalcitrant (65 – 97%) steps. Subdivision of the recalcitrant fraction indicated that the R_{res} was the overwhelmingly dominant carrier of copper in this zone. Digests of November 2000 samples exhibited an increase in total copper (192 $mg \cdot kg^{-1}$) approximately 3.5 times greater than cores collected in June 2000. Moreover, the highest values in the range (105 – 299 mg·kg^{-1}) were within the range of copper concentrations observed in the oxide zone (see below). The temporal increase in total copper occurred primarily in the recalcitrant fraction.

Copper in digests of June 2000 core samples from the oxide zone increased approximately two orders of magnitude in concentration (305 mg·kg^{-1} average) compared to the initial substrate during the first eighteen months of the project with a total range of 204 – 473 mg·kg^{-1}. Sequential extractions of the June 2000 cores showed that although an increase was noted in all fractions, recalcitrant copper was the dominant phase (50 – 85%). The R_{res} step accounted for most of the recalcitrant fraction; the balance was largely extracted in the R_{ox} step. The remainder of copper in the oxide zone resided in the PYRO (5 – 25%) and AS (15 – 32%) extraction steps. Total digests of core material sampled in November 2000 indicated a slightly higher average copper concentration (338 mg·kg^{-1}) compared to June 2000 cores. The relative distribution of copper among extraction steps remained constant between June and November 2000, with the recalcitrant fraction, accounting for 50 – 75% of the total copper, and the PYRO (12 – 18%) and AS (10 – 40%) fractions making up the difference. The majority of recalcitrant copper was extracted in the R_{res} phase.

3.2.2.4. U. Total uranium concentrations of the initial substrate and the core material were calculated using cumulative sequential extraction data, instead of total digest data. Initial uranium concentration in the LBOS was 23 mg·kg^{-1} and was fairly consistent (22 – 25 mg·kg^{-1} range). Sequential extractions of the initial substrate showed that ~90% of the total uranium at the start of the experiment was partitioned to the AS fraction and the remaining 10% was subequally divided between the NSE, PYRO, and recalcitrant fractions.

Total uranium in June 2000 cores from the sulfide zone was slightly higher than the initial substrate with uranium concentrations falling in a fairly narrow range (27 – 31 $mg \cdot kg^{-1}$). Sequential extractions indicated that the majority of this increase (i.e., >90%) occurred in the AS fraction. Comparison of totals from the June and November 2000 sampling events revealed no difference in average content (29 and 31 $mg \cdot kg^{-1}$, respectively), although the range of values was larger in November 2000 (23 – 40 $mg \cdot kg^{-1}$). Uranium distribution in the various fractions of the sequential extraction did not differ across the two sampling events.

The majority of June 2000 transitional zone samples exhibited a range of values from 24 to 31 $mg \cdot kg^{-1}$ similar to sulfide zone concentrations, with one exception (80 $mg \cdot kg^{-1}$). As with the sulfide zone, most of the uranium (>85%) was liberated in the AS fraction of the sequential extractions. There was a decrease in uranium between June and November 2000 sampling events. Totals from November 2000 averaged 9 $mg \cdot kg^{-1}$, while June 2000 samples averaged 36 $mg \cdot kg^{-1}$. In fact, the values from the November 2000 samples were more similar to the oxide zone samples than the June 2000 samples (see below). Sequential extractions indicated this reduction occurred primarily in the AS fraction.

Totals from the June 2000 oxide zone samples displayed a four-fold decrease in uranium concentration over the initial LBOS (6 $mg \cdot kg^{-1}$ average). Sequential extractions indicated this occurred through the removal of AS material from the oxide zone. The remaining uranium was variably distributed in the PYRO (40 – 95%), NSE (up to 50%), and recalcitrant (up to 30%; mainly the R_{cd}) fractions. Totals from the November 2000 cores did not differ from those collected in June 2000. Sequential extractions conducted on November 2000 samples indicated further evolution of the oxide zone. The AS phase was completely removed from all but one core and the remaining material was retained in the PYRO extractable fraction (78 – 98%).

3.2.2.5. Cd. Total cadmium concentrations of the initial substrate and the core material were calculated using cumulative sequential extraction data, instead of total digest data. Initial cadmium concentration in the LBOS was low (0.9 $mg \cdot kg^{-1}$; Fig 3.6). Sequential extractions of the initial substrate showed that cadmium was partitioned primarily in the recalcitrant fraction (55 – 70%), followed by the PYRO fraction (25 – 30%), and finally to AS fraction (5 – 17%; Fig. 4.7). Almost all of the recalcitrant cadmium was attributed to the R_{res} extraction step.

Cadmium concentration in the sulfide zone did not differ greatly from the initial substrate (0.5 – 4.3 $mg \cdot kg^{-1}$ range; Fig. 4.6) nor did they vary between June and November 2000. Sequential extractions showed little change in the distribution of cadmium with the exception of a single core (#3 in tank 36A; Fig. 4.7).

Cadmium concentrations in the June 2000 samples from the transitional zone showed minor accumulations of cadmium (2.7 $mg \cdot kg^{-1}$ average, 1.0 – 5.7 $mg \cdot kg^{-1}$ range; Fig. 4.6) compared to the initial LBOS and the sulfide zone, while the November 2000 samples showed large gains in total cadmium. Sequential extractions showed that this increase was largely manifested in an increase in AS-extractable cadmium for most cores (Fig. 4.7).

Totals from the oxide zone of the June 2000 cores exhibited a one and a half order of magnitude increase (22 – 56 mg·kg^{-1} range) in cadmium concentration compared to the initial LBOS (40 mg·kg^{-1} average; Fig. 4.6). Sequential extractions showed that much of this increase occurred in the recalcitrant fraction (65 – 80% of the total cadmium in the oxide zone). Almost all recalcitrant cadmium was extracted with R_{ox} (30 – 60%) or R_{cd} (10 – 45%) reagents (Fig. 4.7). Increases in the PYRO extraction step (15 – 25%) were also noted, whereas cadmium from the AS step decreased (<5% of the total). Totals from the November 2000 cores indicated that cadmium concentration in the oxide zone did not change during the six months between core sampling events (Fig. 4.6). Likewise, sequential extraction of the oxide zone from November 2000 cores showed that cadmium distribution did not change over time (Fig. 4.7).

3.2.2.6. Co. Total cobalt concentrations in the initial substrate were relatively low (0.9 mg·kg^{-1} average) with little variation (0.6 – 1.1 mg·kg^{-1}). Sequential extractions indicated that cobalt was predominantly distributed among the recalcitrant (60 – 75%) and the AS (17 – 33%) fractions at the start of the experiment. Subdivision of the recalcitrant fraction indicated that approximately one third to one half was attributable to the R_{cd} phase with the remainder extracted during the R_{res} step.

Total digests of the core samples from the sulfide zone were an order of magnitude higher than initial substrate levels (9 mg·kg^{-1}) with a wide range of values (1.2 – 29 mg·kg^{-1}). Relative increases were noted primarily in the PYRO fraction with minor increases observed in the AS and recalcitrant fractions. Average values for cobalt from the June and November 2000 samples did not differ. Sequential extractions, in general, also showed little change in the amount of cobalt extracted in each step (Table 4.3).

Average cobalt from the June 2000 transitional zone samples (47 mg·kg^{-1}) was approximately 50 times higher than the initial substrate concentration, although values varied widely among cores (5 – 102 mg·kg^{-1}). Sequential extractions showed that in transitional zone samples with total cobalt concentrations similar to the sulfide zone, cobalt partitioning was similar to the sulfide zone. For the transitional zone samples that showed a large increase in total cobalt, increases consistently occurred in the AS (6 – 32%), PYRO (20 – 68%), and recalcitrant (25 – 55%) fractions (Table 4.3). Digests of November 2000 transitional zone samples indicated that cobalt concentration increased compared to the June 2000 sampling event. By the end of the project, total cobalt concentrations were 100 – 250 times greater than the initial substrate (i.e., 85 – 228 mg·kg^{-1}). These increases occurred primarily in the PYRO step.

Total digests of June 2000 oxide zone core samples showed that, on average, cobalt concentrations increased approximately two orders of magnitude (65 mg·kg^{-1}) above initial LBOS, but was only slightly higher than average transitional zone values from the same sampling event. Sequential extractions indicated cobalt partitioning was similar to transitional zone samples. In contrast to results from the transitional zone, average total cobalt from November 2000 (44 mg·kg^{-1}) was less than that from the June 2000 sampling data. Sequential extractions indicated the largest decreases occurred in the PYRO and R_{ox} phases, although decreases were observed in all fractions.

3.2.2.7. Ni. Total nickel concentrations of the initial substrate and the core material were calculated using cumulative sequential extraction data, instead of total digest data. The initial concentration of nickel in LBOS was higher than the other trace elements (93 mg·kg^{-1} average), with a much large range (23 – 186 mg·kg^{-1}). Sequential extractions indicated that nickel primarily resided in the recalcitrant fraction followed by lesser amounts in the AS and PYRO steps. The R_{res} step consistently comprised the majority of the recalcitrant fraction.

Nickel concentrations in the sulfide zone of the June 2000 cores were variable (39 $mg \cdot kg^{-1}$ average), with the majority of samples having values lower than the initial substrate level. As with the initial substrate, much of the variability in total nickel was attributed to variability in the recalcitrant fraction. With the exception of two samples (244 and 289 $mg \cdot kg^{-1}$), nickel concentrations from November 2000 sampling event were similar to June 2000 concentrations.

The average nickel concentration from June 2000 samples of the transitional zone (166 $mg \cdot kg^{-1}$) was higher than the initial substrate average, but the range of values observed was relatively large (i.e., 26 – 460 $mg \cdot kg^{-1}$). Sequential extractions showed that both the AS and PYRO fractions displayed net relative increases compared to initial substrate. Average nickel concentration from transitional zone samples in November 2000 (362 $mg \cdot kg^{-1}$) were ~4 times greater than those in June 2000. Comparison of June and November 2000 samples showed that the concentration of nickel continued to increase in the AS and PYRO fractions over time, although the PYRO fraction exhibited the greatest relative increase overall (20 – 90% of the total). Additionally, a large increase in NSE nickel was noted in one core (#3, tank 36A).

Total nickel in the oxide zone (269 $mg \cdot kg^{-1}$) was higher than the initial LBOS. No difference was observed in total concentration between June and November 2000. However, similar to trends observed in cobalt and zinc (below), within a single core, samples from June 2000 were generally higher in nickel than the underlying transitional zone. Likewise, in November 2000 samples, the oxide zone nickel totals were generally lower than the underlying transitional zone samples. Sequential extractions showed that for November 2000 oxide zone samples, the nickel concentration extracted in the PYRO and AS fractions decreased compared to June 2000, while an increase was noted in the recalcitrant (15 – 88%) fraction. Within the recalcitrant fraction, the R_{ox} (0 – 42%) and R_{res} (0 – 85%) phases accounted for the observed increase; the R_{cd} fraction was similar to the initial substrate.

3.2.2.8. Zn. Average total zinc concentrations in the initial substrate were 35 $mg \cdot kg^{-1}$ (23 – 58 $mg \cdot kg^{-1}$ range). Zinc partitioning within the initial substrate was fairly consistent with the majority extracted in the AS step (65 – 80%) and the remaining extracted in the PYRO (5 – 17%) and recalcitrant (10 – 30%) steps. Subdivision of the recalcitrant fraction showed variability among the three phases (R_{ox}, R_{cd}, R_{res}) with no distinct trend.

The majority of total digests conducted on June 2000 cores from the sulfide zone produced zinc concentrations that were similar to initial levels (40 $mg \cdot kg^{-1}$ average). When increases in zinc above the initial concentration were noted, they largely occurred in the PYRO and recalcitrant fractions. Average total zinc concentration (40 $mg \cdot kg^{-1}$) from the November 2000 digests was identical to the June 2000 average. Likewise, November 2000 sequential extractions exhibited similar distribution patterns relative to June 2000; increases were focused in the PYRO and recalcitrant fractions.

Total zinc concentrations in transitional zone samples from the June 2000 cores exhibited a bimodal distribution. Three cores had zinc concentrations that were similar to the sulfide zone and equal to or slightly greater than the initial substrate values (29, 50, and 73 mg·kg^{-1}), whereas, the remaining three cores had total zinc concentrations more than seven times higher than the average initial zinc concentration (257, 357, and 485 mg·kg^{-1}). Sequential extractions showed that the increase occurred variably between the AS (<1% - 35%), PYRO (5 – 60%), and recalcitrant (25 – 75%) fractions. Sequential extractions showed that the R_{res} step accounted for most (84%) of the increase in recalcitrant zinc. Average total zinc concentration (744 mg·kg^{-1}) from the November 2000 digests was three times greater than the June 2000 average. Increases were mainly attributed to the PYRO (25 – 60%) and recalcitrant fractions (25 – 68%).

Total digests of oxide zone samples from the June 2000 cores showed that, on average, zinc concentrations (380 mg·kg^{-1}) increased an order of magnitude over initial concentrations. However, the range in oxide zone zinc concentrations, similar to cobalt, was extensive and bimodal. Two cores had zinc concentrations (75 and 133 mg·kg^{-1}) that were comparable to sulfide zone, whereas, the remaining four cores had total zinc concentrations more than ten times higher than the average initial zinc concentration (526 – 566 mg·kg^{-1}) and similar to the high zinc concentrations observed in the transitional zone. Sequential extractions, however, showed that at least minor increases occurred in every fraction compared to the initial substrate. The majority (>80%) of the recalcitrant zinc occurred in the R_{ox} and R_{cd} fractions with one exception. Similar to the initial substrate, distribution between the R_{ox} and R_{cd} phases was variable, ranging from subequal to the R_{ox} fraction dominating. Total digests of the November 2000 zone samples showed that the average zinc concentration decreased (~43%) during the six months between sampling (215 mg·kg^{-1}). Sequential extractions indicated that the decrease occurred variably in all extraction phases.

4. DISCUSSION

Effluent samples from the tanks indicated that the LBOS was highly effective at removing trace contaminants from low pH, ferric iron-dominated ARD over the two years of the study. In general, the data presented indicate that removal occurred within a fairly narrow pH range above a limestone dissolution front (transitional and oxide zones). However, it was demonstrated in chapter 3 that the pH in the substrate gradually approach influent levels, as the limestone dissolution front advances, and trace element precipitation shifts deeper into the LBOS. With time, the limestone dissolution front will break through the LBOS (chapter 2) and the trace element removal capacity of the substrate will be exceeded. Moreover, column studies on acid neutralization in mine tailings demonstrated that decreases in pH resulted in remobilization of previously sequestered trace elements (Jurjovec et al., 2002). Jurjovec et al. (2002) found that cobalt, nickel, and zinc were mobilized at pH 5.7; cadmium and chromium were mobilized at pH 4.0; while copper was unaffected by changes in pH. These column study results were also similar to field observations at two different mine tailings sites pertaining to the order of metal mobility during acid neutralization where Zn > Ni ≥ Co > Cu (Blowes and Jambor, 1990) and Co = Ni > Zn > Cu (Dubrovsky, 1986).

Therefore, as the pH in the substrate above the limestone dissolution front drops, the long-term retention of previously sequestered trace elements must be considered. Studies have shown that as the pH drops above the limestone dissolution front, previously precipitated aluminum solids are dissolved, only to precipitate deeper in the substrate at a higher pH (Watzlaf, 1997; see chapter 3). Consequently, aluminum removal is transient;

aluminum migrates with the limestone dissolution front through the LBOS. Upon break through of the limestone dissolution front, all of the aluminum sequestered over time will be released from the LBOS in a large, concentrated pulse (see chapter 3).

While pore water data for several trace elements showed concentrations above influent levels, indicating the dissolution of previously precipitated trace element solids, the most compelling evidence for the migration of previously precipitated trace elements was changes in the oxide zone solid phase over time. It is important to reiterate that the oxide zone formed over a range of pH values. In chapter 3, it was found that at the start of the experiment, iron and aluminum both precipitated in an initial zone of limestone dissolution at circumneutral pH. It is logical, therefore, to conclude that most of the initial trace element precipitation also took place in this initial zone. Following complete removal of limestone, the pH dropped as the buffering capacity of the oxide zone shifted to the dissolution of aluminum hydroxysulfate. In chapter 3, it was found that in the June 2000 cores, approximately 70% of the total aluminum sequestered in the LBOS resided in the oxide zone, whereas by the November 2000 core sampling event, <25% of the total aluminum in the LBOS remained in the oxide zone. Therefore, by comparing the trace element concentration in the oxide zone over time, coupled with the pore water data, it is possible to determine which trace elements were mobilized following the drop in oxide zone pH.

4.1. Identification of trace element removal mechanisms

Given the increase in pH, the precipitation of discrete trace element bearing solids (e.g., oxides or sulfides) was theoretically possible (Stumm and Morgan, 1981; Langmuir, 1997) and minor amounts of cobalt, nickel, and zinc sulfides were noted in specific zones (i.e., sulfide) with electron microprobe analysis. Based on the comparably higher total cobalt, nickel, and zinc concentrations in some transitional zone samples, these discrete precipitates were anticipated. However, discrete trace metal precipitates, in general, were rarely observed, indicating trace element removal was dominantly controlled by coprecipitation with major metals, aluminum and iron, and sorption reactions involving the major reactive surfaces in the LBOS. Sorption can involve predominantly electrostatic (non-specific) or predominantly chemical (specific) interactions. In the case of non-specific sorption, the surface charge of the sorbent controls the sorption process and the identity of the sorbate is relatively unimportant (Smith, 1999). Alternatively, specific adsorption involves the chemical bonding of a particular sorbate to the sorbent surface and the identity of the sorbate is often very important (Mcbride, 1994; Smith, 1999). The major sorbents in the LBOS above the limestone dissolution front were organic matter and aluminum and iron hydroxy-minerals. Both groups of sorbents show a high degree of selectivity for divalent transition metal cations (Jenne, 1968; Kinniburgh and Jackson, 1981; Stumm and Morgan, 1981; Dzombak and Morel, 1990; McBride, 1994; Langmuir, 1997; Smith, 1999; Walton-Day, 1999).

4.1.1. Non-specific adsorption. Non-specific adsorption (also referred to as ion exchange) is a relatively weak interaction between particle surfaces and ions and most attached ions can be easily removed from the surface under appropriate conditions (Smith, 1999). It is rapid and usually reversible (e.g., Stumm and Morgan, 1981) and thus, is not reliable mechanism for long-term retention of metals in treatment wetlands (Walton-Day, 1999). In the sequential extraction scheme employed in this study, elements bound to reactive surfaces through cation exchange were targeted with the NSE extraction step.

4.1.2. Specific adsorption – organic matter. The affinity of metals for organic matter is well documented (Fraser, 1961; Szalay, 1964; Ong and Swanson, 1966; Bascomb, 1968; Davis, 1984; Langmuir, 1997). In general, the stability of divalent-metal-organic complexes decreases as follows: Cu > Ni > Co > Zn > Cd > Fe > Mn (McBride, 1994; Walton-Day, 1999). Studies of wetlands rich in organic matter have demonstrated that copper and nickel, in particular, exhibit an especially strong affinity to the organic fraction (Fraser, 1961; Ong and Swanson, 1966; Walton-Day et al., 1990; Sobolewski, 1999). However, aberrations from this sequence have also been observed. In particular, some studies have shown that uranium and chromium also show a strong affinity for organic matter (Makos and Hrncir, 1995; Sobolewski, 1999).

In the sequential extraction scheme employed herein, elements complexed to organic matter were extracted in the PYRO and R_{res} steps. Pyrophosphate solutions are known to extract metals complexed to labile organic substances (Bascomb, 1968; McLaren and Crawford, 1973; Jarvis, 1985; Walton-Day et al., 1990; Papp et al., 1991). Aluminum hydroxysulfate was another possible phase extracted in PYRO. Distinction between pyrophosphate-extractable trace elements associated with labile organic matter and aluminum hydroxysulfate is addressed below. In contrast to PYRO step, metals bound to more refractory organic material generally require much harsher chemical treatment for effective extraction and are therefore, not extracted until the R_{res} step. Previous studies noted that chromium and copper, in particular, formed strong complexes with refractory organic matter and require harsh chemical treatment for their release (i.e., Makos and Hrncir, 1995; Sobolewski, 1999). In addition to extracting trace elements associated with refractory organic matter, the R_{res} step also dissolved refractory sulfides (i.e., pyrite) and any associated trace elements. However, results from chapter 3 demonstrated that sulfides were generally absent from the oxide zone and concentrations were relatively low in the transitional and sulfide zones. They concluded that sulfide precipitation was overall a minor process in the LBOS.

4.1.3. Specific adsorption – hydrous oxides. Similar to organic matter, the affinity of metals for metal-oxide minerals is well documented and it is widely accepted that metal-oxide minerals comprise some of the most important sorbent minerals in natural systems (i.e., Jenne, 1968; Kinniburgh and Jackson, 1981; Stumm and Morgan, 1981; Blowes and Jambor, 1990; Dzombak and Morel, 1990; Blowes and Ptacek, 1994; Langmuir, 1997; Smith, 1999; Jurjovec et al., 2002). Sorption of cations and anions on oxide minerals is strongly pH dependent. Cations and anions sorb with opposite pH dependence in that sorption of cations increases proportionally with pH whereas sorption of anions decrease with increasing pH (Dzombak and Morel, 1990; Jenne, 1968; Stumm and Morgan, 1981; Smith, 1999). Thus, for elements such as arsenic that tend to form oxyanions (e.g., AsO_4^{3-}), adsorption was theoretically maximized at low pH. Kinniburgh et al. (1976) defined the pH_{50} as an indicator of the relative affinity of metals for a mineral surface. The pH_{50} is defined as the pH at which 50% of the cations in solution are adsorbed and is commonly invoked as a reference point for comparative purposes between studies. Sorption experiments with iron oxyhydroxide indicate that pH_{50} is between 3.0 – 4.0 for uranium (as uranyl ion, UO_2^{2+}), 3.5 – 4.5 for chromium (Cr^{3+}), 4.0 – 5.5 for copper (Cu^{2+}), and 5.0 – 7.0 for cadmium (Cd^{2+}), nickel (Ni^{2+}), cobalt (Co^{2+}), zinc (Zn2+, Kinniburgh et al., 1976; Dzombak and Morel, 1990; Langmuir, 1997; Smith et al., 1998).

The distinction between the iron oxyhydroxide and aluminum hydroxysulfate precipitates was fairly straightforward with the extraction scheme employed. Amorphous and crystalline iron oxyhydroxides were extracted during the R_{ox} and R_{cd} steps, respectively. Given the sequence of the extraction scheme, no other source of trace elements was identified for these two steps. Results from chapter 3 showed that aluminum hydroxysulfates were largely extracted in the AS (pH 2.2) and PYRO (pH 10) extraction steps due to the amphoteric nature of aluminum hydroxysulfate with the majority extracted in the AS step. Thus, trace elements associated with aluminum hydroxysulfate were dominantly extracted in the AS step with possible occurrence in the PYRO step. Trace elements extracted only in the PYRO step were most likely bound to labile organic matter. Association with acid volatile sulfides (AVS) is another possible source of trace elements extracted in the AS step. Coprecipitation of trace elements with AVS is well established (e.g., Huerta-Diaz and Morse, 1992; Huerta-Diaz et al., 1993; Saunders et al., 1996; Saunders et al., 1997; Huerta-Diaz et al., 1998; Lee et al., 2000); however, within the LBOS this phase plays only a minor role in metal retention (see chapter 3). Other possible sources in the AS step are discussed with the individual trace elements below.

4.2. Individual Trace Element Removal Trends

4.2.1. As. Based on the calculated contribution of the limestone component to the total arsenic content of the initial substrate, limestone generally accounted for the majority of the initial arsenic (Table 4.1). However, sequential extractions indicated that arsenic was associated with limestone and organic components. Within the limestone, arsenic was most likely associated with randomly distributed trace pyrite fragments and therefore, it was extracted in the R_{res} fraction of the sequential extraction procedure. Arsenic was most likely associated with the organic component through ion exchange (NSE) and coprecipitation with minor crystalline iron oxyhydroxides present in the organic material (R_{cd}).

Analysis of the ARD water column overlying the LBOS indicated that greater than 85% of the arsenic measured at the ARD source was removed at influent pH levels (i.e., 2.2 – 2.4). The main sorbent in contact with the influent ARD was iron oxyhydroxide. Results presented in chapter 3 demonstrated that iron oxyhydroxide precipitation occurred around the tank inlet (Fig 3.8) and within the ARD water column. Because arsenic tends to form oxyanions (e.g., arsenate), which strongly adsorb to iron hydroxy-minerals at low pH (Dzombak and Morel, 1990; McBride, 1994), removal of arsenic was most likely facilitated by the low pH of the ARD water column through adsorption to iron oxyhydroxides. Total digest data, which showed that the majority of the arsenic sequestered in the LBOS was retained in the oxide zone (Fig. 4.6), and sequential extractions of the oxide zone, which indicated that over 80% of the extractable arsenic resided in the R_{ox} and R_{cd} fractions (Fig. 4.7), further supports this interpretation. Moreover, because arsenic oxyanions desorb at higher pH ($pH_{50} = 11 – 12$; Dzombak and Morel, 1990), much of the arsenic extracted in the PYRO fraction (pH 10) may reflect partial desorption from iron oxyhydroxides rather than arsenic associated with labile organic matter.

While the majority of the influent arsenic was likely removed as an oxyanion through adsorption to iron oxyhydroxides at low pH, pore water data from the middle oxide zone (6 cm; pH ≤ 3.3), which showed that arsenic concentrations remained unchanged from the overlying water column, indicate not all of the arsenic was amenable to this removal mechanism. Pore water data did indicate arsenic was removed to effluent concentrations by 15 cm (pH ≥ 6.8). However, total digest and sequential extractions indicated accumulation in the transitional and sulfide zones was minor compared to the initial substrate, indicating removal occurred in the lower oxide (6 – 7.5 cm; pH 3.3 – 3.8). However, distinction of a mechanism for arsenic removal in the lower oxide zone at higher pH (>3.3) from removal in the upper oxide zone (pH 2.3) was not possible.

Given that most of the dissolved arsenic was removed at influent pH through adsorption to iron oxyhydroxides, remobilization was not expected as the pH of the substrate dropped over time. Pore water, which did not show any increase above influent concentrations, and total digest data, which did not show any migration of arsenic deeper in the substrate, support this conclusion. In fact, because arsenic removal through adsorption to iron oxyhydroxides was favored by low pH, decreases in the LBOS pH over time should promote further arsenic removal and prevent any significant mobilization of arsenic.

4.2.2. Cr. Total digests and sequential extractions showed that the initial chromium concentration in the LBOS was low and mainly divided among the AS, PYRO, and recalcitrant extraction steps. Because more than half of the initial chromium could be attributed to the limestone component of the LBOS (Table 4.1), chromium extracted in the AS fraction was likely liberated from the limestone. The PYRO and recalcitrant fractions were derived from solids associated with the organic component of the LBOS. The PYRO extractable chromium was attributed to labile organic matter. Within the recalcitrant fraction, approximately half of the chromium was associated with amorphous or crystalline iron oxyhydroxides (i.e., R_{ox} and R_{cd} steps), while the remaining was extracted in the R_{res} fraction. Previous studies of chromium removal in wetlands found that chromium was tightly bound to refractory organic matter and was only released after harsh chemical treatment (Makos and Hrncir, 1995). Based on the findings of Makos and Hrncir (1995), R_{res} chromium was likely associated with refractory organic matter.

Total digests indicated that the chromium concentration in the sulfide zone was only slightly higher than the initial substrate and there was little change in the sulfide zone chromium concentration over time. Based on these results, all of the chromium was probably removed from the pore water prior to reaching the sulfide zone. In fact, pore water data showed that chromium removal occurred in the transitional and oxide zones between pH 3.3 – 6.5 with the highest concentration occurring at the lowest pH in the oxide zone.

Although pore water data indicated chromium precipitation in the transitional zone (pH 3.8 – 4.6), only two thirds of the cores extracted in June 2000 showed increase in total chromium relative to the initial substrate and sulfide zone, indicating chromium precipitation in the transitional zone was recent. November 2000 digests showed that chromium accumulation within the transitional zone continued over time. Sequential extractions showed that most of the chromium increase in the transitional zone was associated with the AS fraction. At $pH > 4$, chromium precipitates as insoluble $Cr(OH)_3$; however below pH 4, $Cr(OH)_3$ is highly soluble (Sass, 1987). Therefore, chromium extracted in the AS step resided as Cr^{3+} sorbed to aluminum hydroxysulfate or $Cr(OH)_3$ precipitated on LBOS surfaces. In addition, increases were observed in chromium bound to labile (PYRO fraction) and refractory (R_{res} fraction) organic matter.

Total digest of the June 2000 samples indicated that the oxide zone accounted for most of the chromium removed in the first eighteen months of the study. Pore water extracted concurrently from the upper oxide zone (2.5 cm) contained a chromium concentration higher than the influent, indicating that chromium previously precipitated at a higher pH was dissolved from the LBOS as the pH (2.3) approached influent levels. However, the solubilization of chromium from the upper oxide zone must have been fairly match by reprecipitation within the lower oxide zone, because total chromium concentrations in the oxide zone were constant between June and November 2000 sampling events. In fact, pore water data showed that some dissolved chromium was removed by the lower half of the oxide zone, where pore water pH (3.3 – 3.8) approximated the pH_{50} for chromium (III) adsorption to iron oxyhydroxide (i.e., between 3.5 and 4.5; Dzombak and Morel, 1990).

Sequential extractions of both June and November 2000 samples of the oxide zone exhibited appreciable, yet similar, amounts of chromium bound to iron oxyhydroxide (i.e., R_{ox} and R_{cd}). As with the transitional zone, chromium was bound to labile (PYRO fraction), and refractory (R_{res} fraction) organic matter. Chromium, most likely present as a $Cr(OH)_3$ surface precipitate on iron oxyhydroxide (Sass, 1987), was also extracted in the AS fraction. However, whereas, the PYRO and R_{res} fractions showed increase relative to the transitional zone, the AS fraction remained constant or decreased slightly. Acid soluble, $Cr(OH)_3$ likely precipitated in the oxide zone prior to the complete dissolution of limestone (i.e., pH>4). Moreover, the spike in dissolved chromium observed at pH 2.3 (2.5 cm) was likely due to the dissolution of $Cr(OH)_3$. Although the pH of the entire oxide zone was favorable for $Cr(OH)_3$ dissolution (i.e., <4), the rate $Cr(OH)_3$ dissolution may be kinetically limited and therefore did not occur until the pH dropped to influent concentrations. Because the pH in the lower oxide zone was too low for additional $Cr(OH)_3$ precipitation, over time chromium associated with the AS step would be completely removed from the oxide zone. However, chromium sequestered in the AS fraction was apparently the only fraction effected by changing pH. Chromium associated with organic matter (PYRO and R_{res}) or coprecipitated with iron oxyhydroxides (R_{ox} and R_{cd}), was expected to be largely unaffected by decreasing pH over time. Therefore, only a portion of the chromium sequestered in the LBOS was remobilized with changing pH conditions over time.

4.2.3. Cu. Total digests and sequential extractions of the initial substrate showed that the LBOS originally contained minor amounts of copper largely associated with labile organic matter (PYRO) and a more recalcitrant fraction (R_{res}), either copper tightly bound to refractory organic matter or copper sulfide. Of the transitional elements studied, copper has the highest affinity for organic matter (Stumm and Morgan, 1981; McBride, 1994; Sobolewski, 1999; Walton-Day, 1999). Moreover, organically complexed copper is typically bound more tightly than any other divalent transitional metal (McBride, 1994; Sobolewski, 1999). In studies of wetland sediments removing copper, Sobolewski (1999) noted that this strong affinity required harsh chemical treatment for total copper extraction indicating it was bound to recalcitrant rather than labile organic compounds. Given the small amount of sulfide material identified in the initial substrate by electron microscopy, recalcitrant organic matter was the most likely source of copper (R_{res} step).

Total digests of the sulfide zone showed only very minor increases in total copper and only minor changes over time. The extractions showed that the small increases were attributed to copper bound to labile (PYRO) and recalcitrant (R_{res}) organic matter. Similar to chromium, pore water data explains why the total copper concentration was so low in the sulfide zone. Dissolved copper concentrations were equivalent to effluent values by the time pore water migrated to the sulfide zone and therefore, the amount of copper loading on the sulfide zone was very low.

In fact, pore water samples showed very little dissolved copper made it into the transitional zone. Consequently, most of the copper concentrations from the June 2000 transitional zone digests were similar to the sulfide zone. However, the large increase in copper concentration between June and November 2000 transitional zone samples indicate that copper removal was shifting from total removal in the lower oxide zone to greater removal in the transitional zone. Sequential extractions indicated the increases were due to the binding of copper with organic matter. Minor increases in copper bound to labile organic matter (PYRO) were observed, but most of the increases were to refractory organic matter (R_{res}).

Pore water data indicated that copper, previously precipitated in the oxide zone at higher pH, was resolubilized as the pH dropped below 3.3. The lack of above-influent-copper concentrations at 2.5 cm may be due to the fact that all of the mobile copper previously precipitated had been removed by the time the pH dropped to 2.3. Although previously precipitated copper was dissolved from the upper oxide zone, most of it was reprecipitated in the lower oxide zone between pH 3.3 and 3.8. As a consequence of this recycling of copper within the oxide zone, digest data do not exhibit any discernible temporal changes in total copper over time and therefore give no indication as to the magnitude of copper mobility below pH 3.3.

Sequential extractions, however, indicated that much of the copper extracted from cores in June and November 2000 was partitioned to either labile (PYRO) or refractory (R_{res}) organic matter and therefore, may not be remobilized. In fact, the AS fraction, which was only extracted in the oxide zone, was the only source of potentially mobile copper observed in the LBOS, indicating that less than half of the total copper retained was soluble. The source of the AS copper is unknown. Additionally, a small amount of copper was immobilized through coprecipitated with iron oxyhydroxides (R_{ox} and R_{cd}). However, the amount of copper in the R_{ox} and R_{cd} steps did not change over time. Moreover, the pH_{50} for copper (4.0 and 5.5) indicated the pH of the oxide zone was too low for effective copper adsorption to iron oxyhydroxides. Therefore, copper extracted in the R_{ox} and R_{cd} steps was likely coprecipitated with iron oxyhydroxides at higher pH before the development of distinct reaction zones. Additional coprecipitation with iron oxyhydroxides was not expected for the remainder of the project.

4.2.4. U. Total digests showed that the LBOS originally contained an appreciable amount of uranium (23 mg·Kg^{-1}) that was largely associated with the organic component (Table 4.1). The limestone component of the LBOS contributed only ~ 1 mg·kg^{-1} of the total uranium measured in the initial substrate. Sequential extractions showed that nearly all of the initial uranium resided in an acid soluble phase associated with the organic component or was leached from organic matter in a low pH environment.

Total digests and sequential extractions showed that uranium was sequestered in the sulfide zone over the course of the experiment. Uranium accumulation was apparently slow based on the small average increase relative to the initial substrate and the lack of a measurable difference between cores collected in June and November 2000. The slow accumulation was likely due to the low level of dissolved uranium measured in the influent (22 μg·L^{-1} maximum) and the relatively small amount that resided in the initial LBOS.

Total digests indicated that uranium was solubilized from the transitional zone between June and November 2000. Unfortunately, pore water data were not available for the transitional zone. The depletion of uranium from the transitional zone was driven by the penetration of more oxidizing (i.e., ferric iron-bearing), lower pH water deeper into the substrate. This liberated uranium from acid sensitive materials (AS step).

Similar to the transitional zone, digests of both June and November 2000 core samples from the oxide zone showed removal of uranium from the initial substrate. Notably, as the total concentration of uranium in the AS step approached depletion, the amount of uranium in the R_{cd} and PYRO fractions increased. The minor amount of R_{cd} uranium extracted in the oxide zone samples likely represented uranium adsorbed to goethite surfaces. Within the sequential extraction scheme employed, hexavalent uranium (U^{6+}) was preferably extracted in the PYRO extraction step (Bertsch pers. comm., 2002), due to the high pH of the extraction and the formation of uranyl-carbonate complexes (Langmuir, 1997). Therefore, although uranium has a strong affinity for organic matter (Langmuir, 1997; Sobolewski, 1999), the association with labile organic matter (PYRO step) can not be resolved with the extraction scheme employed herein.

The depletion of uranium from the oxide and transitional zones and apparent accumulation in the sulfide zone is analogous to the formation of uranium roll front deposits (Nash et al., 1981; Langmuir, 1997). The formation of roll fronts can be summarized as follows: trace amounts of uranium are leached from reduced sediments (e.g., LBOS organic material), by oxidized water (e.g., ferric-iron dominated influent ARD). Uranium is transported as the uranyl ion (UO_2^{2+}) under oxidizing and mildly acidic conditions. When the uranyl-bearing water encounters a redox interface, such as the boundary between the transitional zone and the sulfide zone (based on the presence/absence of active sulfide precipitation, i.e., chapter 3), U(VI) is reduced to U(IV) and precipitated as a solid such as pitchblende [$UO_{2(am)}$] (Langmuir, 1997). Reduction is typically accomplished by reaction with organic carbon, S^{2-}, or solid sulfides (Nash et al., 1981).

In the LBOS, pore water data indicated that uranium mobility was related to pH changes in the oxide zone. However, development of the oxide zone resulted from the ingress of fairly oxidizing ARD (i.e., ferric iron-dominated). Therefore, uranium inherited from the initial substrate was oxidatively leached from the oxide zone and, based on total digest data, from the transitional zone over time. This solubilized uranium, coupled with influent-ARD uranium, was then precipitated, initially in the transitional zone. However, as oxidizing fluids penetrated into the transitional zone, uranium was again mobilized and ultimately accumulated in the sulfide zone. Hence, no uranium retention is expected in the oxide and transitional zones; all of the uranium is predicted to migrate in advance of the limestone dissolution front (i.e., in the sulfide zone) and may accumulate over time. A large spike of dissolved uranium in the effluent would be the first indication that the transitional zone (i.e., limestone dissolution front) is about to break through the LBOS.

4.2.5. Cd. Cadmium concentrations in the initial substrate were low and largely associated with the organic material (Fig. 4.7; Table 4.1). Within the organic component of the LBOS, cadmium was most likely complexed to labile organic matter (PYRO) and a recalcitrant compound (R_{res}). Association with refractory organic matter as a possible source of cadmium extracted in the R_{res} step can be ruled out, because cadmium generally adsorbs rather weakly on organic matter (McBride, 1994). Therefore, cadmium extracted in the R_{res} step was most likely coprecipitated with rare iron sulfide grains associated with wood fragments or found intergrown in the limestone. Small amounts of cadmium coprecipitated directly with the carbonate material was likely extracted in the AS step.

Total cadmium concentrations of the sulfide zone were similar to the initial LBOS and changed very little over the course of the project. This can be largely attributed to the fact that dissolved cadmium was removed from the pore water above the sulfide zone (i.e., 15 cm; Fig. 4.4). Minor increases were occasionally noted in the R_{res} and AS fraction from June 2000 samples, indicating cadmium was associated with the ubiquitous framboidal pyrite (R_{res}) present in this zone. Potential acid soluble phases that could have sequestered cadmium include carbonate (Fuller and Davis, 1987) or acid volatile sulfide (Huerta-Diaz et al., 1998; Lee et al., 2000). In November 2000, cores generally showed small increases in cadmium, however the increases were associated with labile organic matter (PYRO).

June 2000 samples from the transitional zone, which showed cadmium largely associated with labile organic matter (PYRO) and the recalcitrant fraction (R_{res}, i.e. pyrite), experienced only slight increases in total cadmium compared to the sulfide zone and initial LBOS. Swamper pore water, which showed cadmium concentrations above influent levels at pH <3.3, indicated that previously precipitated cadmium was dissolved from the upper oxide zone, but precipitated above pH 3.3 in the lower oxide and/or transitional zones. In contrast, peeper data apparently exhibited no dissolution of previously precipitated cadmium solids in the upper oxide zone and indicated that cadmium was completely removed at pH 4.6. However, the validity of the peeper data is questionable due to the lack of cadmium in the influent during the week prior to and the first week of peeper equilibration. In fact, the entire dissolved cadmium profile measured with the peeper may only represent solubilization of previously precipitated cadmium. Consequently, relative to the peeper influent concentration measured at the end of equilibration, the pore water profile may be shifted to lower concentrations due to the lack of influent cadmium. Thus, a pH range more precise than the 3.3 – 6.5 range for the bulk of cadmium precipitation can not be ascertained. It is noteworthy that: 1) the average influent cadmium concentration was the lowest of the trace elements studied, 2) it was one of only three trace elements (arsenic, cadmium, and uranium) in the influent ARD recorded below detection over the course of this study, and 3) it was the only trace element studied that was below detection during either pore water sampling events.

While pore water data could not distinguish between precipitation in the lower oxide or transitional zone, total digests of November 2000 samples indicated the majority of cadmium precipitation occurred in the transitional zone. Increases in cadmium in the transitional zone over time largely occurred in the acid soluble phase. This can be attributed to cadmium weakly adsorbed to iron oxyhydroxides found in minor abundance or, more likely, adsorption/coprecipitation with the ubiquitous aluminum hydroxysulfates.

Total digest and sequential extraction indicated that the majority of cadmium removed in the LBOS for the first 18 months of the project (June 2000 cores) occurred in the oxide zone and was coprecipitated with amorphous and/or crystalline iron oxyhydroxides (i.e., R_{ox} and R_{cd}) or complexed with labile organic matter (PYRO). However, data presented in chapter 3 showed that, in pore water collected concurrent with the June 2000 cores, dissolved ferric iron precipitated (as an oxyhydroxide) at pH <3.8, well below the experimental pH_{50} for cadmium (5.0 – 7.0). Therefore, coprecipitation with iron oxyhydroxides may have occurred during the initial formation of the oxide zone at higher pH.

Although pore water data indicated solubilization of cadmium from the upper oxide zone (>6 cm; Fig. 4.4), core data also showed the highest cadmium concentration of three zones investigated. One possible explanation for the positive correlation between pore water and solids is that cadmium dissolved from the upper oxide zone at pH <3.3 was reprecipitated in the lower oxide zone at a slightly higher pH (3.8) and therefore cadmium was recycled internally within this zone. Alternatively, the amount of variability in oxide zone cadmium totals between cores (June and November 2000) may mask any changes over time. The variability in the total cadmium concentration was most likely attributable to the frequent paucity in influent dissolved cadmium over the course of the project, as the measured concentration was commonly below the ICP-MS lower detection limit (Table 4.1). Therefore, it can not be determined if the apparent equality in oxide zone cadmium between June and November 2000 was due to internal recycling of cadmium within the oxide zone or if the decreases were so subtle that they were masked by the variability.

It is likely that, because most of the cadmium was associated with iron oxyhydroxides, very little will be mobilized from the oxide zone with continued ingress of low pH ARD. However, cadmium associated with aluminum hydroxysulfate in the transitional zone (AS fraction) may represent only transient retention. As the aluminum hydroxysulfates are dissolved and mobilized, any associated cadmium would migrate as well.

4.2.6. Co. Initial cobalt in the LBOS was low and can largely be attributed to the limestone component (Table 4.1). Therefore, cobalt extracted in the AS step was likely sequestered in the carbonate fraction (i.e., limestone), while cobalt in the R_{res} step was likely extracted from pyrite associated with the limestone. Some cobalt was also associated with organic matter in the LBOS, as measurable cobalt was extracted in the PYRO step. Additionally, some of the initial cobalt was coprecipitated with iron oxides (mainly crystalline, i.e., R_{cd}).

Total digest and sequential extractions indicated that the increase noted in the sulfide zone was attributable to organic matter binding (PYRO) and the coprecipitation in the sulfide fraction. Cobalt coprecipitation with acid volatile sulfide (AS fraction) and pyrite (R_{res} fraction) has been previously documented (Huerta-Diaz et al., 1993; McBride, 1994; Huerta-Diaz et al., 1998) and, albeit rare, cobalt-bearing sulfides were identified during electron microprobe analysis (Fig. 4.5). The low levels of cobalt in the sulfide zone and the lack of change over time was largely due to the fact that, as indicated by pore water analysis, dissolved cobalt was removed to effluent concentrations above the sulfide zone and therefore, very little cobalt entered the sulfide zone.

Pore water data showed that, in June 2000, cobalt was liberated from the oxide zone (discussed below) and largely reprecipitated in the transitional zone between pH 3.8 – 4.6. Cobalt sequestration in the transitional zone was confirmed with the total digest data, which showed appreciable accumulation that increased from June to November 2000. Sequential extractions indicated most of the cobalt increases in the transitional zone were due to labile organic binding of cobalt (PYRO), although increases also occurred in the other mobile fractions (NSE, AS). Although some of the cobalt from the AS step can be attributed to coprecipitation with AVS inherited from the sulfide zone, geochemical conditions prevalent in the transitional zone were conducive to AVS dissolution and therefore other processes were likely responsible for the slight increases in AS cobalt observed. Given the possibilities within the transitional zone, most of the cobalt extracted in the AS step was likely associated with aluminum hydroxysulfate through adsorption and/or coprecipitation.

Pore water data indicated that cobalt was actively leached from the oxide zone below pH 3.8, while total digests of cores taken concurrently (June 2000) indicated that a large amount of oxide zone cobalt, previously precipitated at higher pH, remained. However, sequential extractions indicated most of the cobalt retained in the June 2000 oxide zone samples was highly mobile, occurring mainly as acid soluble (AS), organically bound (PYRO), or exchangeable (NSE) cobalt. The relatively high concentration of cobalt in the pore water samples coupled with the potential mobility of cobalt observed in the June 2000 oxide zone samples was realized in the November 2000 analysis. Total cobalt concentrations in the oxide zone decreased slightly over time. Sequential extractions showed that this decrease occurred in the readily mobile fractions (NSE, AS, PYRO). While other trace elements bound to labile organic matter (PYRO) were generally resistant to changing pH conditions over time, cobalt retained in the PYRO fraction decreased over time and was attributed to the fact that organically bound cobalt is readily soluble at low pH (McBride, 1994). In addition to the mobile cobalt in the oxide zone, an appreciable amount was found coprecipitated with iron oxyhydroxides (R_{ox} and R_{cd} fractions). Because the pH_{50} for cobalt sorption is high (5.0 – 7.0), it is likely that this coprecipitation occurred prior to the formation of distinct reaction zones. With the exception of cobalt associated with iron oxyhydroxides, most of the cobalt may be solubilized and removed from the oxide zone over time.

4.2.7. Ni. The total nickel concentration of the initial substrate was the highest of all the trace elements studied. Digests of the initial limestone component of the LBOS indicated that nickel was the most abundant trace metal as well (Table 4.1). Therefore, a small portion of the total nickel in the initial substrate (~9.5 $mg \cdot kg^{-1}$; Table 4.1) was attributable to the original limestone (AS fraction), whereas the bulk of the initial nickel was mainly associated with recalcitrant material within the organic matter (i.e., R_{res} fraction). Nickel extracted in the R_{res} fraction was most likely bound in sulfide or tightly bound to refractory organic matter. Given the general lack of non-limestone related sulfide material in the initial substrate (Fig 3.5) and the strong affinity of nickel for organic matter (McBride, 1994; Sobolewski, 1999), the R_{res} fraction in the initial substrate was most likely nickel bound to refractory organic matter.

The concentration of nickel in the sulfide zone samples did not vary from the initial LBOS and there were no noticeable changes over time. This was largely due to the fact that nickel was removed to effluent concentrations in the transitional zone at $pH < 4.6$. Sequential extractions indicated that, similar to the initial substrate, nickel concentration in the sulfide zone varied considerably from core to core. While nickel tightly bound to refractory organic matter likely accounted for most of the R_{res} nickel, rare nickel-cobalt sulfides were observed during electron microprobe analysis (Fig. 4.5). Any nickel associated with sulfides in the LBOS would have been extracted in the AS (i.e., precipitation as an acid volatile sulfide) and/or R_{res} (i.e., coprecipitation with pyrite) steps.

Similar to cobalt, nickel exhibited a trend towards enrichment within the transitional zone over time. While refractory organic matter still played a role, most of the increase occurred in nickel associated with labile organic matter bound (PYRO) and acid soluble material (AS). The acid soluble nickel was most likely related to adsorption/coprecipitation with aluminum hydroxysulfates.

Samples from the oxide zone further reinforce the suggested shift from initial precipitation of nickel in the oxide zone to continued precipitation in the transitional zone. In all cores, except one (core #3, tank 36A), the June 2000 oxide zone totals were higher than the underlying transitional zone samples, even when the transitional zone samples displayed moderate increases in total nickel. Over time, accumulation in the transitional zone was greater, so that, for any given core in November 2000, the oxide zone samples contained less nickel than the underlying transitional zone samples. Although the oxide zone average nickel concentration was similar in June and November 2000, given the variability of total nickel in the initial substrate, the shift in the distribution patterns between the oxide and transitional zone are consistent with pore water data, which indicated dissolution from the oxide zone with reprecipitation in the transitional zone. Sequential extractions indicated that dissolved nickel in the pore water data was accommodated by a decrease in the mobile nickel fraction (i.e., NSE, AS, and PYRO steps). For nickel totals from the oxide zone, much of the variability was due to differences in the R_{res} fraction. Most of this variation was likely attributed to the initial organic material (nickel binding to refractory organic matter); however some may be due to additional nickel binding to organic matter during the initial stages of the oxide zone when the pH was circumneutral. Likewise, nickel coprecipitated with iron oxyhyroxides (R_{ox} and R_{cd}) was likely a relict of initial conditions when iron oxyhydroxides precipitated at near-neutral pH. This is supported by the high pH_{50} of nickel (5.0 to 7.0) and the fairly constant to slightly reduced amount of R_{ox} and R_{cd} nickel over time.

4.2.8. Zn. Total digests of the limestone component of the LBOS indicated that the limestone fraction contributed a maximum of approximately 2.0 $mg \cdot kg^{-1}$ zinc to the total concentration of the initial LBOS (35 mg·kg^{-1}; Table 4.1) and therefore, the bulk of the initial zinc was associated with the organic component. A minor amount of the initial zinc was associated with iron oxides (R_{ox} and R_{cd} fractions) or labile organic matter (PYRO), and the majority was present in the acid soluble (AS) fraction. The source of the AS zinc is unknown, although it possibly resulted from desorption of zinc from iron oxyhydroxides associated with the organic matter or desorption from the organic matter.

As with all trace elements studied, pore water data showed that zinc was largely removed above the limestone dissolution front, prior to the sulfide zone. Therefore, June 2000 sulfide zone core samples showed only minor increases in total zinc. When increases were noted, sequential extractions indicated that zinc was associated with labile organic matter (PYRO) or sulfide (R_{res}; either direct precipitation as ZnS or a coprecipitate with pyrite). Precipitation of zinc sulfide in the sulfide zone was observed in electron microprobe imaging, which showed rare sulfur-bearing zinc grains (Fig. 4.5). Total digest and sequential extractions of November 2000 sulfide zone samples showed little change over time.

Similar to cobalt and nickel, pore water data showed that, in June 2000, zinc was liberated from the oxide zone (discussed below) and largely reprecipitated in the transitional zone between pH 3.8 – 4.6. The bimodal distribution of zinc concentrations in the June 2000 samples demonstrated the initial stages of zinc sequestration in the transitional zone. In the six months between the June and November 2000 sampling events, the zinc concentration in the transitional zone exceeded the concentration accumulated in the oxide zone during the first eighteen months of the project. This demonstrates that not only did the site of zinc precipitation shift completely to the transitional zone, but also zinc previously precipitated in the oxide zone must have been dissolved and relocated in the transitional zone. Sequential extractions showed that transitional zone samples containing low levels of zinc were characteristically similar to the sulfide zone, while samples containing elevated zinc concentrations (June and November 2000) exhibited an increase in zinc partitioned to organic matter (PYRO) and recalcitrant (R_{res}) zinc. The source of R_{res} zinc is discussed below.

Total digests of the June and November 2000 cores supported a temporal trend of zinc dissolution from the oxide zone coupled to accumulation in the transitional zone. Sequential extractions of the oxide zone in June 2000 showed that zinc was initially sequestered in the labile organic fraction (PYRO) and an acid soluble (AS) phase. Additionally, June 2000 extractions indicated some exchangeable zinc (NSE) and minor coprecipitation with iron oxyhydroxides (R_{ox} and R_{cd} fractions). Under acidic, oxidizing conditions, zinc is commonly retained only in exchangeable forms on organic matter; it does not complex tightly with organic matter at low pH (McBride, 1994). Thus, into addition to the PYRO step, the AS and NSE fractions may represent zinc weakly bound to organic matter. Over time, the amount of zinc coprecipitated with iron oxyhydroxides remained constant or decreased slightly, indicating the incorporation of zinc was largely limited to initial oxide zone conditions (i.e., circumneutral pH). Zinc coprecipitation with iron oxyhydroxides optimally occurs between pH of 5.0 to 7.0 (pH_{50}). Decreases in zinc concentrations of the oxide zone between June and November 2000 occurred largely through removal of zinc associated with organic matter (PYRO) and acid soluble (AS) zinc.

5. CONCLUSIONS

Few studies of passive treatment systems have addressed trace element removal during acid neutralization, although elevated levels of some trace elements are commonly encountered in coal-related ARD (e.g., As, Cd, Co, Cr, Cu, Ni, Zn; (Hyman and Watzlaf, 1995). Results from this study show that, for the practical purpose of implementing LBOS to treat low pH, ferric iron-dominated ARD, high trace element removal efficiency can be expected as long as the limestone dissolution front does not pass completely through the substrate. With the exception of uranium, trace metal attenuation largely occurs above the limestone dissolution front in the transitional and oxide zones. Trace metal removal is facilitated through sorption to primary organic matter and secondary hydrous iron and aluminum precipitates. With the exception of arsenic, iron oxyhydroxide is apparently not a major sorbent for trace element removal once the pH in the oxide zone drops below 3.8. Thus, trace element sorption is controlled by either organic matter or aluminum hydroxysulfate and the dominant sorbent is trace element specific.

Although the sorptive behavior of these two sorbent types is generally very different, they both exhibit an overriding dependence on pH. Only arsenic, which adsorbs to iron oyxhydroxides, is retained at influent pH values. All other trace elements require an increase in pH to at least 3.3 before they are sequestered. Therefore, trace element removal is confined to either the lower oxide zone concomitant with ferric iron precipitation (pH 3.3 – 3.8) or the transitional zone concurrent with aluminum hydroxysulfate precipitation (pH 3.8 – 4.6). Based largely on pH considerations, the sorption selectivity within the LBOS follows the sequence:

$$\mathrm{As} > \mathrm{Cu} > \mathrm{Cr} > \mathrm{Co} = \mathrm{Ni} = \mathrm{Zn} = \mathrm{Cd} > \mathrm{U}.$$

Given that there were two distinct types of surfaces present (organic matter and hydrous oxide minerals), the selectivity sequence was in general agreement with those published for oxide ($\mathrm{Cr} \geq \mathrm{Cu} \geq \mathrm{Co} \geq \mathrm{Zn}$ and $\mathrm{Ni} \geq \mathrm{Cd}$; e.g., Smith, 1999) and organic ($\mathrm{Cu} > \mathrm{Ni} > \mathrm{Co} > \mathrm{Zn} > \mathrm{Cd}$; e.g., Walton-Day, 1999) sorbents.

Given the pH constraints, only a portion of the dissolved copper and chromium are actively sequestered in the lower oxide zone, while the remaining copper and chromium, cadmium, cobalt, nickel, and zinc are sequestered in the transitional zone. Uranium, which is more dependent on the redox conditions of the LBOS than the pore water pH, is not removed from the pore water until the sulfide zone. Because the location of the transitional zone within the LBOS is dynamic depending on the depth of the limestone dissolution front, the site of active trace element sequestration (i.e., $\mathrm{pH} > 3.3$) is constantly migrating deeper into the LBOS over time. Thus, if the LBOS is implemented to the point where the limestone dissolution front is permitted to pass completely through the substrate and the neutralization potential is completely consumed, then trace elements (except arsenic) can no longer be sequestered and will pass through the substrate.

However, of greater concern is the fate of trace elements precipitated behind the limestone dissolution front after all of the neutralization potential has been consumed.

Results from this study show that all trace elements sequestered at $\mathrm{pH} > 3.3$ are subject to remobilization as the pH decreases over time, although the degree of mobilization is trace element-dependent. These remobilized trace elements coupled with influent concentrations may accumulate in solution at the pH-dependent point of maximum mobility. If the LBOS continues to receive ARD after the limestone dissolution front passes completely through the substrate, dissolved trace elements (with the exception of arsenic) will be released in the effluent as the pH drops to influent levels and at concentrations potentially orders of magnitude higher than the influent concentration. Based on the pH of solubilization and the amount of total trace element solubilized, the following general order of trace element mobility can be applied to the LBOS:

$$\mathrm{U} > \mathrm{Co} = \mathrm{Zn} \geq \mathrm{Cd} = \mathrm{Ni} > \mathrm{Cu} > \mathrm{Cr} > \mathrm{As}$$

Of particular practical interest, results from this study demonstrate that several trace elements are directly related to aluminum chemistry and may even coprecipitate with aluminum hydroxysulfate (i.e., Zn). This raises concerns over the recent practice of flushing vertical flow wetlands (VFW) systems. Recently, as a part of a preventative maintenance plan, VFWs are being flushed in an attempt to remove aluminum precipitates that potentially reduce substrate permeability. If large quantities of aluminum precipitates are flushed from a LBOS, then considerations should be made to test the trace element content.

ACKNOWLEDGEMENTS

This research was funded by Financial Assistance Award Number De-FC09-96SR18546 between the United States Department of Energy and The University of Georgia as a part of the US DOE National Water Research Center. The authors would like to thank the principle investigators of this grant, Dr. Rebbecca Sharitz, Dr. J Vaun McArthur, and Dr. Beverly Collins for their continued support and assistance. The authors would also like to acknowledge Linda Paddock, Daniel Coughlin, Matt Opdyke, and Morris Jones for their technical assistance in sample and chemical analysis.

REFERENCES

Bascomb C. L. (1968) Distribution of pyrophosphate-extractable iron and organic carbon in soils of various groups. *Journal of Soil Science* **19**(2), 251 - 268.

Blowes D. W. and Jambor J. L. (1990) The pore-water chemistry and the mineralogy of the vadose zone of sulfide tailings, Waite Amulet, Quebec. *Applied Geochemistry* **5**, 327 - 346.

Blowes D. W. and Ptacek C. J. (1994) Acid-neutralization mechanisms in inactive mine tailings. In *The Environmental Geochemistry of Sulfide Mine-Wastes, Short Course Handbook*, Vol. 22 (ed. J. L. Jambor and D. W. Blowes), pp. 271 - 292. Mineralogical Association of Canada.

Carignan R. (1984) Interstitial water sampling by dialysis: Methodoligical notes. *Limnol. Oceanogr.* **29**(3), 667-670.

Carignan R., Rapin F., and Tessier A. (1985) Sediment porewater sampling for metal analysis: A comparison of techniques. *Geochimica Cosmochimica et Acta* **49**, 2493-2497.

Clark S. B., Johnson W. H., Malek M. A., Serkiz S. M., and Hinton T. G. (1996) A comparison of sequential extraction techniques to estimate geochemical controls on the mobility of fission product, actinide and heavy metal contamination in soils. *Radiochimica Acta* **74**, 173 - 179.

Davis J. A. (1984) Complexation of trace metals by adsorbed natural organic matter. *Geochimica Cosmochimica et Acta* **48**, 679 - 691.

Dubrovsky N. M. (1986) Geochemical evolution of inactive pyritic tailings in the Elliot Lake uranium district. Ph.D., University of Waterloo.

Dzombak D. A. and Morel F. M. M. (1990) *Surface Complexation Modeling - Hydrous Ferric Oxide*. John Wiley and Sons.

Fraser D. C. (1961) Organic sequestration of copper. *Economic Geology* **56**, 1063 - 1078.

Fuller C. C. and Davis J. A. (1987) Processes and kinetics of Cd^{2+} sorption by a calcareous aquifer sand. *Geochimica Cosmochimica et Acta* **51**(6), 1491 - 1502.

Hesslein R. H. (1976) An in situ sampler for close interval pore water studies. *Limnol. Oceanogr.* **21**, 912-914.

Huerta-Diaz M. A., Carignan R., and Tessier A. (1993) Measurement of trace metals associated with acid volatile sulfides and pyrite in organic freshwater sediments. *Environmental Science and Technology* **27**, 2367 - 2372.

Huerta-Diaz M. A. and Morse J. W. (1992) Pyritization of trace metals in anoxic marine sediments. *Geochimica Cosmochimica et Acta* **56**, 2681 - 2702.

Huerta-Diaz M. A., Tessier A., and Carignan R. (1998) Geochemistry of trace metals associated with reduced sulfur in freshwater sediments. *Applied Geochemistry* **13**, 213 - 233.

Hyman D. M. and Watzlaf G. R. (1995) Mine Drainage Characterization for the Successful Implementation of Passive Treatment Systems. *17th Annual National Association of Abandoned Mine Lands Conference*, 170 - 185.

Hyman D. M. and Watzlaf G. R. (1997) Metals and Other Components of Coal Mine Drainage as Related to Aquatic Life. *National Meeting of the American Society of Surface Mining and Reclamation*.

Jarvis S. C. (1985) Forms of aluminum in some acid permanent grassland soils. *Journal of Soil Science* **37**, 211 - 222.

Jenne E. A. (1968) Controls on Mn, Fe, Co, Ni, Cu, and Zn concentrations in soils and water: the significant role of hydrous Mn and Fe oxides. In *Trace Inorganics in Water*, Vol. 73 (ed. R. F. Gould), pp. 337 - 387. American Chemical Society.

Jurjovec J., Ptacek C. J., and Blowes D. W. (2002) Acid neutralization mechanisms and metal release in mine tailings: A laboratory column experiment. *Geochimica Cosmochimica et Acta* **66**(9), 1511 - 1523.

Kepler D. A. and McCleary E. C. (1994) Successive alkalinity-producing systems (SAPS) for the treatment of acidic mine drainage. *Proc. Int. Land Reclamation and Mine Drainage Conference and Third Int. Conference on the Abatement of Acidic Drainage*, 195-204.

Kinniburgh D. G. and Jackson M. L. (1981) Cation adsorption by hydrous metal oxides and clay. In *Adsorption of Inorganics at Solid-Liquid Interfaces* (ed. M. A. Anderson and A. J. Rubin), pp. 91 - 160. Ann Arbor Science.

Kinniburgh D. G., Jackson M. L., and Syers J. K. (1976) Adsorption of alkali earth, transition, and heavy metal cations by hydrous oxide gels of iron and aluminum. *Soil Science Society of America Journal* **40**, 796 - 799.

Langmuir D. (1997) *Aqueous Environmental Geochemistry*. Prentice Hall.

Lee J.-S., Lee B.-G., Luoma S. N., Choi H. J., Koh C.-H., and Brown C. L. (2000) Influence of acid volatile sulfides and metal concentrations on metal partitioning in contaminated sediments. *Environmental Science and Technology* **34**, 4511 - 4516.

Makos J. D. and Hrncir D. C. (1995) Chemistry of Cr(VI) in a constructed wetland. *Environmental Science and Technology* **29**, 2414 - 2419.

McBride M. B. (1994) *Environmental Chemistry of Soils*. Oxford University Press.

McLaren R. G. and Crawford D. V. (1973) Studies on soil copper I. The fractionation of copper in soils. *Journal of Soil Science* **24**(2), 172 - 181.

Miller W. P., Martens D. C., and Zelazny L. W. (1986) Effect of Sequence in the extraction of trace metals from soils. *Soil Science Society of America Journal* **50**(3), 598 - 601.

Nash J. T., Granger H. C., and Adams S. S. (1981) Geology and concepts of genesis of important types of uranium deposits. *Economic Geology* **75th ann. vol**, 63 - 116.

Ong H. L. and Swanson V. E. (1966) Adsorption of copper by peat. lignite, and bituminous coal. *Economic Geology* **61**, 1214 - 1231.

Papp C. S. E., Filipek L. H., and Smith K. S. (1991) Selectivity and effectiveness of extractants used to release metals associated with organic matter. *Applied Geochemistry* **6**, 349 - 353.

Sass B. M. a. D. R. (1987) Solubility of amorphous chromium(III)-iron(III) hydroxide solid solutions. *Inorganic Chemistry* **26**, 2228 - 2232.

Saunders J. A., Cook R. B., Thomas R. C., and Crowe D. E. (1996) Coprecipitation of trace metals in biogenic pyrite: Implications for enhanced intrinsic bioremediation. In *Proceedings of the 4th International Symposium on the Geochemistry of the Earth's Surface* (ed. S. H. Bottrell), pp. 470-474.

Saunders J. A., Thomas R. C., Lee M.-K., and Wolf L. (1997) Geologic evidence for the utility of using sulfate reducing bacteria for in situ anaerobic bioremediation of heavy-metal contaminated groundwater. In *Proceedings of the 4th International Symposium on In Situ and On Site Bioremediation*, Vol. v. 5, pp. 583-588. Battelle Press.

Smith K. S. (1999) Metal sorption on mineral surfaces - An overview with examples relating to mineral deposits. In *The Environmental Geochemistry of Mineral Deposits, Part A: Processes, Techniques, and Health Issues*, Vol. 6A (ed. G. S. Plumlee and M. K. Logsdon), pp. 161 -182. Society of Economic Geologists.

Smith K. S., Ranville J. F., Plumlee G. S., and Macalady D. L. (1998) Predictive double-layer modeling of metal sorption in mine-drainage systems. In *Adsorption of Metals by Geomedia* (ed. E. A. Jenne), pp. 521 - 547. Academic Press.

Sobolewski A. (1999) A review of processes responsible for metal removal in wetlands treating contaminated mine drainage. *International Journal of Phytoremediation* **1**(1), 19 - 51.

Stumm W. and Morgan J. J. (1981) *Aquatic Chemistry*. John Wiley & Sons.

Szalay A. (1964) Cation ion exchange properties of humic acids and their importance in the geochemical enrichment of UO_2^{++} and other cations. *Geochimica Cosmochimica et Acta* **28**, 1605 - 1614.

Thomas R. C., Romanek C. S., Coughlin D. P., and Crow D. E. (1999) Treatment of acid mine drainage using anaerobic constructed treatment wetlands: predicting longevity with substrate neutralization potential. *Proceedings Sudbury '99 - Mining and the Environment II*, 449-458.

U.S. Code of Federal Regulations. (1991) Title 40 -- Protection of the Environment; Chapter I -- Environmental Protection Agency; Subchapter N -- Effluent Guidelines and Standards; Part 434 - Coal mining point source category; July 1.

Walton-Day K. (1999) Geochemistry of the processes that attenuate acid mine drainage in wetlands. In *The Environmental Geochemistry of Mineral Deposits, Part A: Processes, Techniques, and Health Issues*, Vol. 6A (ed. G. S. Plumlee and M. K. Logsdon), pp. 215 - 228. Society of Economic Geologists.

Walton-Day K., Filipek L. H., and Papp C. S. E. (1990) Mechanisms controlling Cu, Fe, Mn, and Co profiles in peat of the Filson Creek Fen, northeastern Minnesota. *Geochimica Cosmochimica et Acta* **54**, 2933 - 2946.

Watzlaf G. R. (1997) Passive treatment of acid mine drainage in down-flow limestone systems. *Proceedings of the 14th Annual National Meeting of the American Society of Surface Mining and Reclamation.*, 611-622.

Widdel F. (1988) Microbiology and Ecology of Sulfate- and Sulfur-Reducing Bacteria. In *Biology of Anaerobic Microorganisms* (ed. A. J. B. Zehnder), pp. 469-585. Wiley Interscience.

Winger P. V. and Lasier P. J. (1991) A vacuum-operated pore-water extractor for estuarine and freshwater sediments. *Arch. Environ. Contam. Toxicol.* **21**, 321-324.

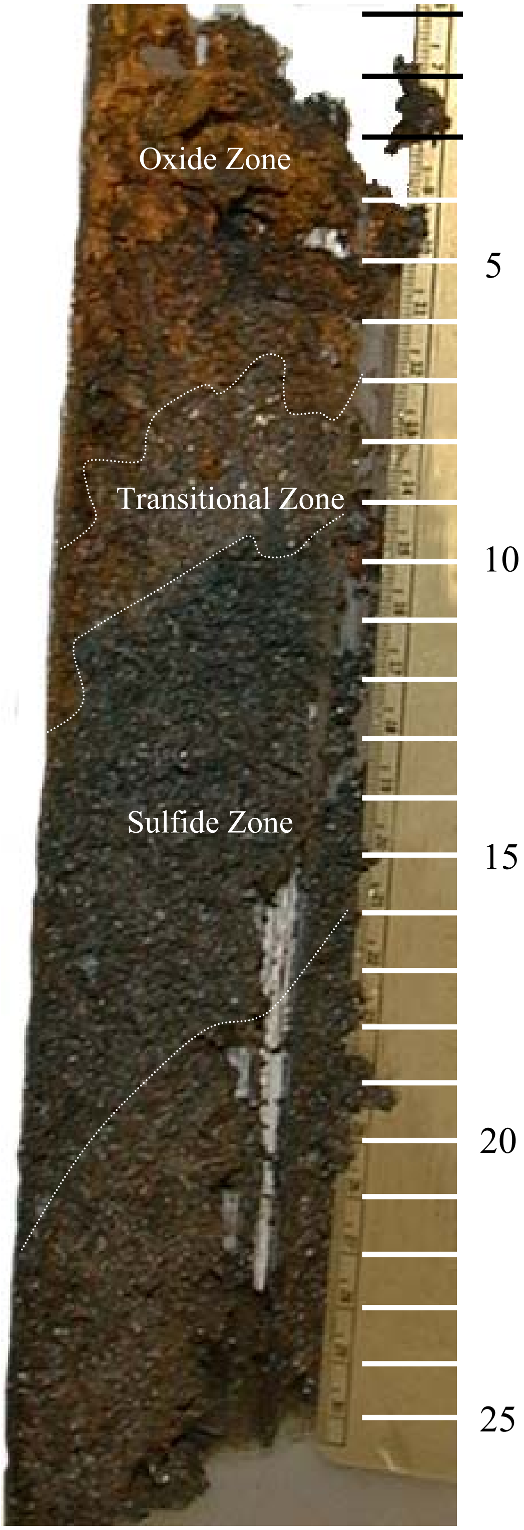

Figure 4.1. Photograph of a cores taken from the LBOS showing the three reaction zones. Scale to the right is in centimeters.

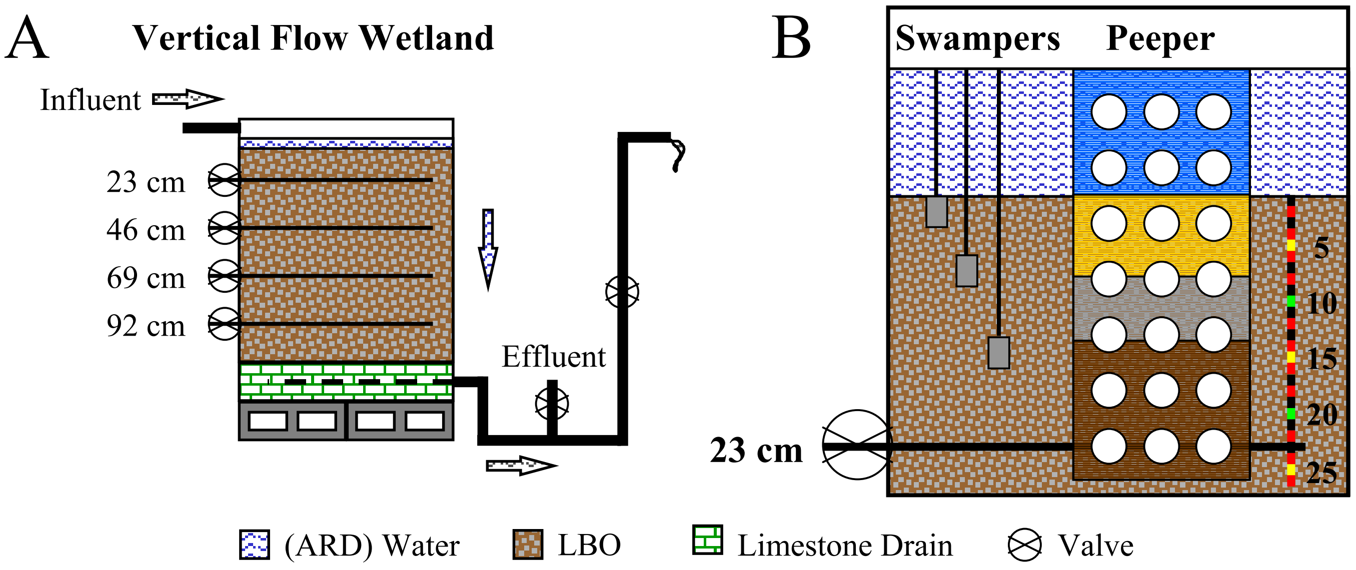

Figure 4.2. Cross section of the vertical flow wetland (VFW) tank. A. Overview of the tank set up. B. Close-up of substrate above 23 cm showing the sampling location of the swamper and peeper pore water samples. The scale to the right is in centimeters.

Table 4.1. Composition and physicochemical attributes of the limestone buffered organic substrate (LBOS).

LBOS Composition (by volume)	**Physicochemical Attributes**[†]	
• 25% Limestone Screenings • 72% Composted Stable Waste • 3% Spent Brewing Grains • <1% Kricket Krap ®	**• CEC:** **83.29 meq·100 gm^{-1} soil** **• NP:** **529 g $CaCO_3$·Kg^{-1} soil**	
	• Paste pH 7.61 **• Density: 0.741 g·cm^{-3}**	**• Carbon 36 %** **• C:N 28.8**

all values in mg·kg^{-1}	**Fe**	**Al**	**Ca**	**Mn**	**As**	**Cr**	**Cu**	**U**	**Cd**	**Co**	**Ni**	**Zn**
LBOS Total	2805	1611	217048	135	2.5	6.7	4.5	23	0.9	0.9	93	35
Limestone Total	546	543	694339	143	6.0	7.1	1.2	2.5	0.6	2.3	18	4
Limestone Contribution [a]	289	287	367305	76	3.2	3.8	0.6	1.3	0.3	1.2	10	2
Org. Matter Contribution [b]	2516	1324	-	59	-	3.0	3.8	22	0.6	-	84	33

Limestone Screenings - Grain Size Distribution

(mm)	**9.5 - 4.8**	**4.8 - 2.4**	**2.4 - 1.2**	**1.2 - 0.6**	**0.6 - 0.3**	**0.3 - 0.15**	**0.15 - 0.07**	**< 0.07**
Percent	**2.50%**	**22.2%**	**31.5%**	**27.0%**	**13.4%**	**3.12%**	**0.32%**	**0.03%**

[†] Physicochemical attributes are from Thomas et al. (1999)

[a] Limestone contribution was determined by multiplying the limestone total metal concentration by the proportion of limestone in the LBOS (i.e., 0.529)

[b] Organic matter contribution was determined by difference. Values are not given where the metal concentration measured in the limestone was greater than the concentration measured in the final LBOS.

Table 4.2. Influent and effluent pH and trace metal chemistry for the individual VFW tanks. Values in parenthesis are the range over the 2 year study; where only one value is given, the lower value is below detection limits of the ICP-MS. Data for Ca, Fe, Al, SO_4, and H_2S are from chapter 3.

	pH Std Units	Ca (mg·L^{-1})	Fe (mg·L^{-1})	Al (mg·L^{-1})	As (µg·L^{-1})	Cd (µg·L^{-1})	Cr (µg·L^{-1})	Cu (µg·L^{-1})	U (µg·L^{-1})	Co (µg·L^{-1})	Ni (µg·L^{-1})	Zn (µg·L^{-1})	Sulfate (mg·L^{-1})	Sulfide (mg·L^{-1})
L.D.L		0.023	0.00139	0.0026	0.16	0.1	0.82	0.3	0.03	0.07	0.22	0.83	0.5	0.05
Influent	2.4	52	142	84	29.2	6.2	89.8	383	11.6	356	716	1647	1521	n/a
ARD	(1.6 to 3.0)	(23 to 114)	(92 to 237)	(39 to 274)	(134)	(12)	(58 to 188)	(190 to 792)	(22)	(186 to 770)	(377 to 1548)	(741 to 3417)	(926 to 3385)	n/a
Tank 2A	6.48	570	12.9	0.17	2.6	0.10	1.6	0.8	0.1	1.2	6.7	35	1248	1.2
	(5.9 to 6.9)	(268 to 807)	(40)	(9.3)	(16)	(0.2)	(8.7)	(5.4)	(0.5)	(12)	(21)	(154)	(696 to 1817)	(15)
Tank 10A	6.42	611	11.6	0.02	1.2	0.10	2.2	1.2	0.1	1.1	8	45	1275	3.2
	(5.9 to 6.9)	(371 to 1003)	(0.1 to 90)	(0.2)	(6.3)	(0.1)	(39)	(8.9)	(0.7)	(13)	(34)	(174)	(495 to 2732)	(20)
Tank 13A	6.34	610	32.8	0.07	0.7	0.1	1.8	1.6	0.1	1.0	9.4	59	1277	0.7
	(5.5 to 6.9)	(392 to 921)	(0.6 to 123)	(4.2)	(6.9)	(0.2)	(23)	(16)	(0.7)	(7.4)	(72)	(250)	(876 to 1938)	(15)
Tank 24A	6.40	619	16.7	0.03	1.4	0.10	1.5	1.0	0.4	1.1	7.0	47	1273	4.0
	(6.0 to 6.9)	(373 to 888)	(120)	(0.4)	(9.9)	(0.2)	(6.1)	(8.2)	(11)	(7.3)	(22)	(370)	(541 to 2257)	(40)
Tank 30A	6.42	616	14.1	0.02	3.5	0.10	1.5	0.9	0.2	1.2	7.3	44	1302	1.6
	(5.9 to 6.8)	(380 to 943)	(0.01 to 76)	(0.3)	(20)	(0.5)	(7.4)	(7.6)	(5.8)	(15)	(24)	(180)	(678 to 2323)	(15)
Tank 36A	6.33	604	19.2	0.02	1.9	0.10	1.7	1.5	0.1	1.5	9.0	62	1186	2.8
	(5.5 to 6.8)	(372 to 853)	(58)	(0.3)	(13)	(0.1)	(17)	(7.1)	(0.7)	(21)	(44)	(336)	(627 to 2098)	(20)
Tank 39A	6.5	609	2.3	0.02	2.5	0.10	2.1	0.9	0.05	1.3	7.4	33	1113	9.4
	(6.0 to 7.0)	(398 to 915)	(11)	(0.2)	(17)	(0.1)	(15)	(10)	(0.5)	(18)	(25)	(135)	(263 to 1585)	(1 to 30)
Tank 44A	6.50	558	6.8	0.05	2.4	0.10	1.9	1.6	0.1	1.3	9.3	44	936	15.6
	(5.2 to 7.1)	(362 to 907)	(48)	(2.2)	(27)	(0.2)	(8.3)	(10)	(1.6)	(26)	(56)	(148)	(427 to 1569)	(0.1 to 50)
Average	6.42	600	14.5	0.05	2.0	0.10	1.8	1.2	0.13	1.2	8.0	46	1201	4.8
Min	6.33	558	2.3	0.02	0.7	0.10	1.5	0.8	0.05	1.0	6.7	33	936	0.7
Max	6.50	619	32.8	0.17	3.5	0.10	2.2	1.6	0.36	1.5	9.4	62	1302	15.6

L.D.L = lower detection limits of the ICP-MS, n/a = not analyzed

Average, minimum, and maximum were calculated from the individual tank averages

Figure 4.3. Flow diagram for total digest and sequential extraction of the LBOS samples. Damp samples from the LBOS were used in sequential extractions, while samples from the initial substrate were extracted dry. All total digest samples were conducted on dried, cryogenicaly ground material. Total digests were conducted using a block digestor (105°C) instead of shaking in a water bath.

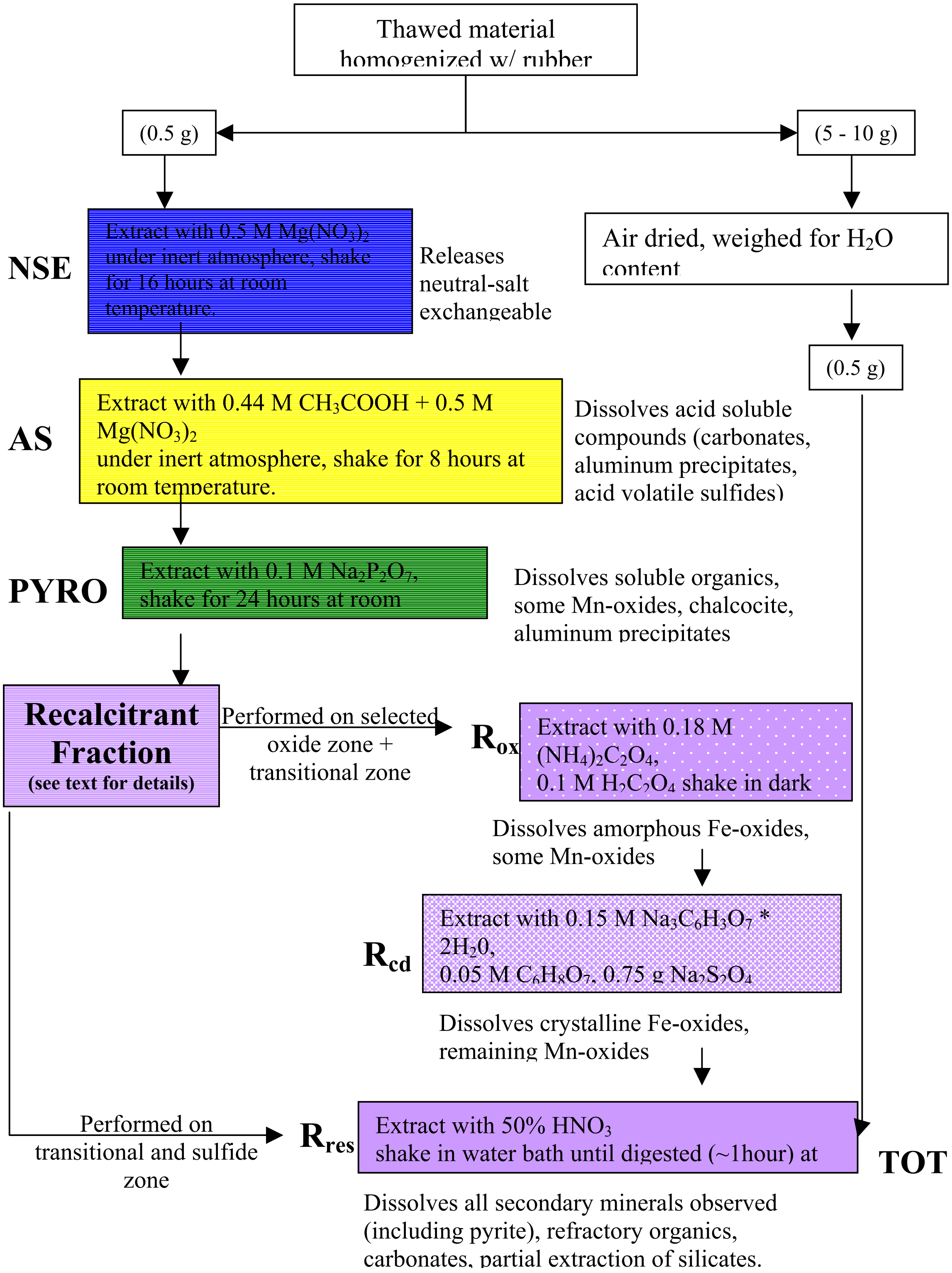
Thawed material homogenized w/ rubber
(0.5 g)
(5 - 10 g)
NSE
Extract with 0.5 M $Mg(NO_3)_2$ under inert atmosphere, shake for 16 hours at room temperature.
Releases neutral-salt exchangeable
Air dried, weighed for H_2O content
(0.5 g)
AS
Extract with 0.44 M CH_3COOH + 0.5 M $Mg(NO_3)_2$ under inert atmosphere, shake for 8 hours at room temperature.
Dissolves acid soluble compounds (carbonates, aluminum precipitates, acid volatile sulfides)
PYRO
Extract with 0.1 M $Na_2P_2O_7$, shake for 24 hours at room
Dissolves soluble organics, some Mn-oxides, chalcocite, aluminum precipitates
Recalcitrant Fraction
(see text for details)
Performed on selected oxide zone + transitional zone
R_{ox}
Extract with 0.18 M $(NH_4)_2C_2O_4$, 0.1 M $H_2C_2O_4$ shake in dark
Dissolves amorphous Fe-oxides, some Mn-oxides
R_{cd}
Extract with 0.15 M $Na_3C_6H_5O_7$ * $2H_20$, 0.05 M $C_6H_8O_7$, 0.75 g $Na_2S_2O_4$
Dissolves crystalline Fe-oxides, remaining Mn-oxides
Performed on transitional and sulfide zone
R_{res}
Extract with 50% HNO_3 shake in water bath until digested (~1hour) at
TOT
Dissolves all secondary minerals observed (including pyrite), refractory organics, carbonates, partial extraction of silicates.

Figure 4.4. Dissolved trace element concentrations and pH profiles from the upper 25 cm of the LBOS. The vertical axes are sampling depth; negative values indicate samples were collected from the ARD water column overlying the substrate or the influent. Swamper samples (blue circles and squares) were collected from two tanks (30A and 36A) in June 2000 at three depths in LBOS. The 6 cm sampling depth was representative of the middle oxide zone, while the 15 and 23 cm depths were from the sulfide zone (see chapter 3). One sample of the ARD water column overlying the LBOS was taken from each tank during swamper sampling and is shown with the first sampling area (i.e., -1). Peeper samples (green triangles) were collected from tank 44A in May 2000. The first two peeper well horizons (-7.5 and -2.5 cm) sampled the ARD overlying the LBOS. The first well horizon in the LBOS (2.5 cm) sampled the upper oxide zone, the second horizon (7.5 cm) collected pore water at the oxide – transitional zone interface, the third horizon (12.5 cm) sampled the transitional zone, and finally the fourth and fifth well horizons in the LBOS (17.5 and 22.5 cm) collected pore water from the sulfide zone. In addition to samples of the ARD water column overlying the LBOS, the influent ARD from the manifold and the tank effluent samples were collected immediately prior to swamper and peeper sampling (see text for details).

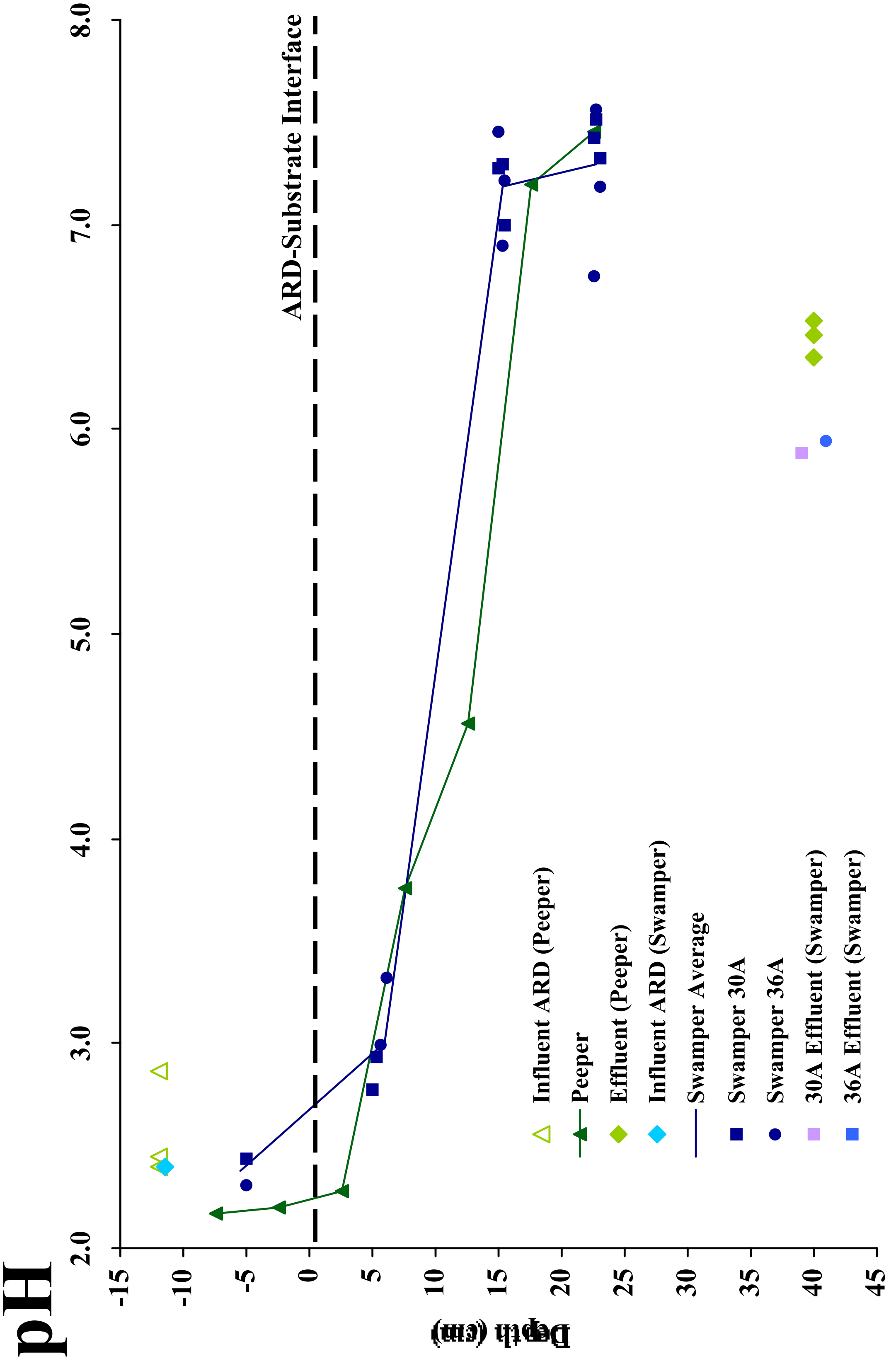
pH
ARD-Substrate Interface
Depth (cm)
-15
-10
-5
0
5
10
15
20
25
30
35
40
45
2.0
3.0
4.0
5.0
6.0
7.0
8.0
Influent ARD (Peeper)
Peeper
Effluent (Peeper)
Influent ARD (Swamper)
Swamper Average
Swamper 30A
Swamper 36A
30A Effluent (Swamper)
36A Effluent (Swamper)

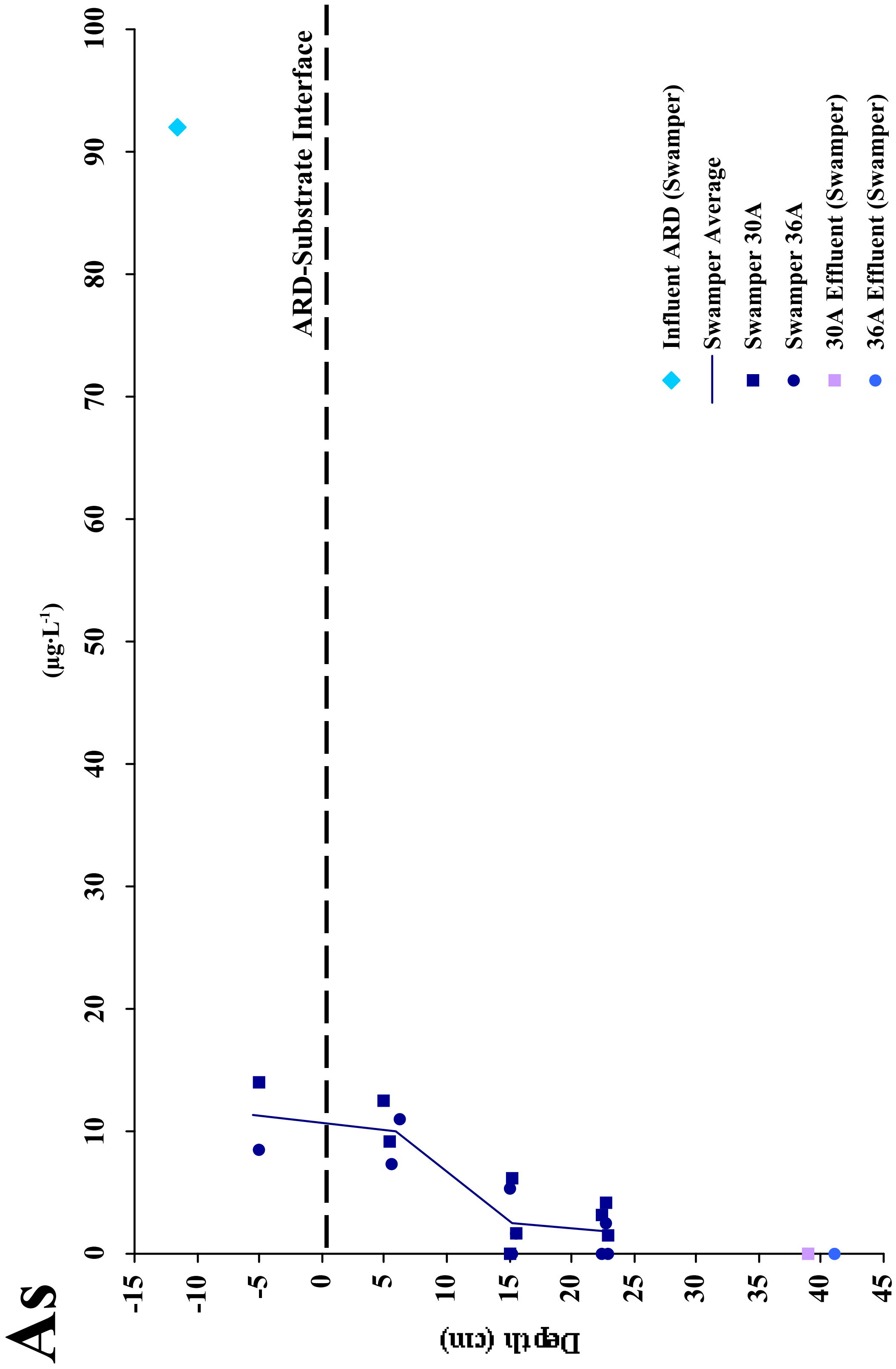
As
(µg·L-1)
0
10
20
30
40
50
60
70
80
90
100
Depth (cm)
-15
-10
-5
0
5
10
15
20
25
30
35
40
45
ARD-Substrate Interface
Influent ARD (Swamper)
Swamper Average
Swamper 30A
Swamper 36A
30A Effluent (Swamper)
36A Effluent (Swamper)

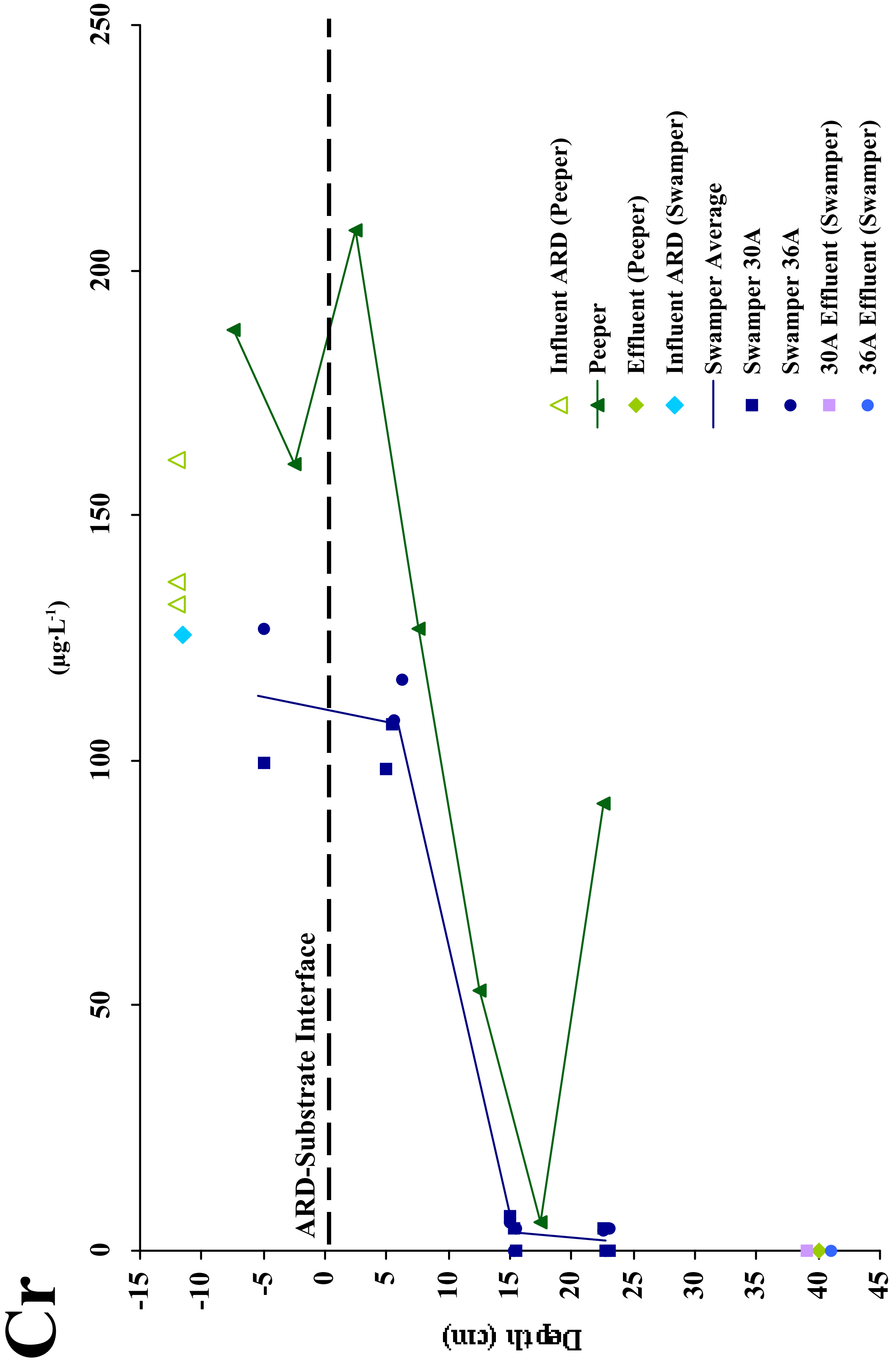
Cr
(µg·L⁻¹)
0
50
100
150
200
250
Depth (cm)
-15
-10
-5
0
5
10
15
20
25
30
35
40
45
ARD-Substrate Interface
Influent ARD (Peeper)
Peeper
Effluent (Peeper)
Influent ARD (Swamper)
Swamper Average
Swamper 30A
Swamper 36A
30A Effluent (Swamper)
36A Effluent (Swamper)

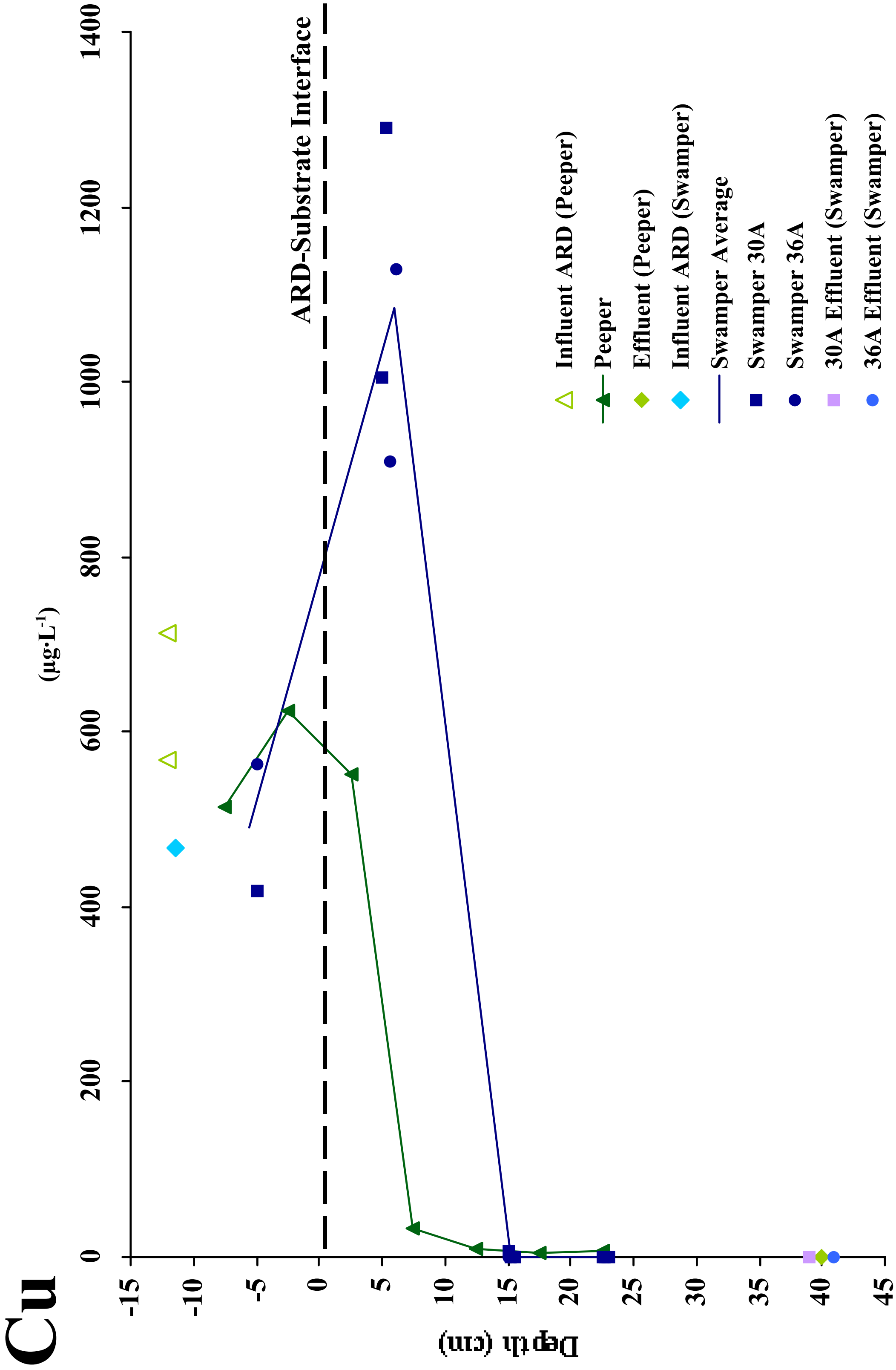

Cu
(µg·L^{-1})
0
200
400
600
800
1000
1200
1400
Depth (cm)
-15
-10
-5
0
5
10
15
20
25
30
35
40
45
ARD-Substrate Interface
Influent ARD (Peeper)
Peeper
Effluent (Peeper)
Influent ARD (Swamper)
Swamper Average
Swamper 30A
Swamper 36A
30A Effluent (Swamper)
36A Effluent (Swamper)

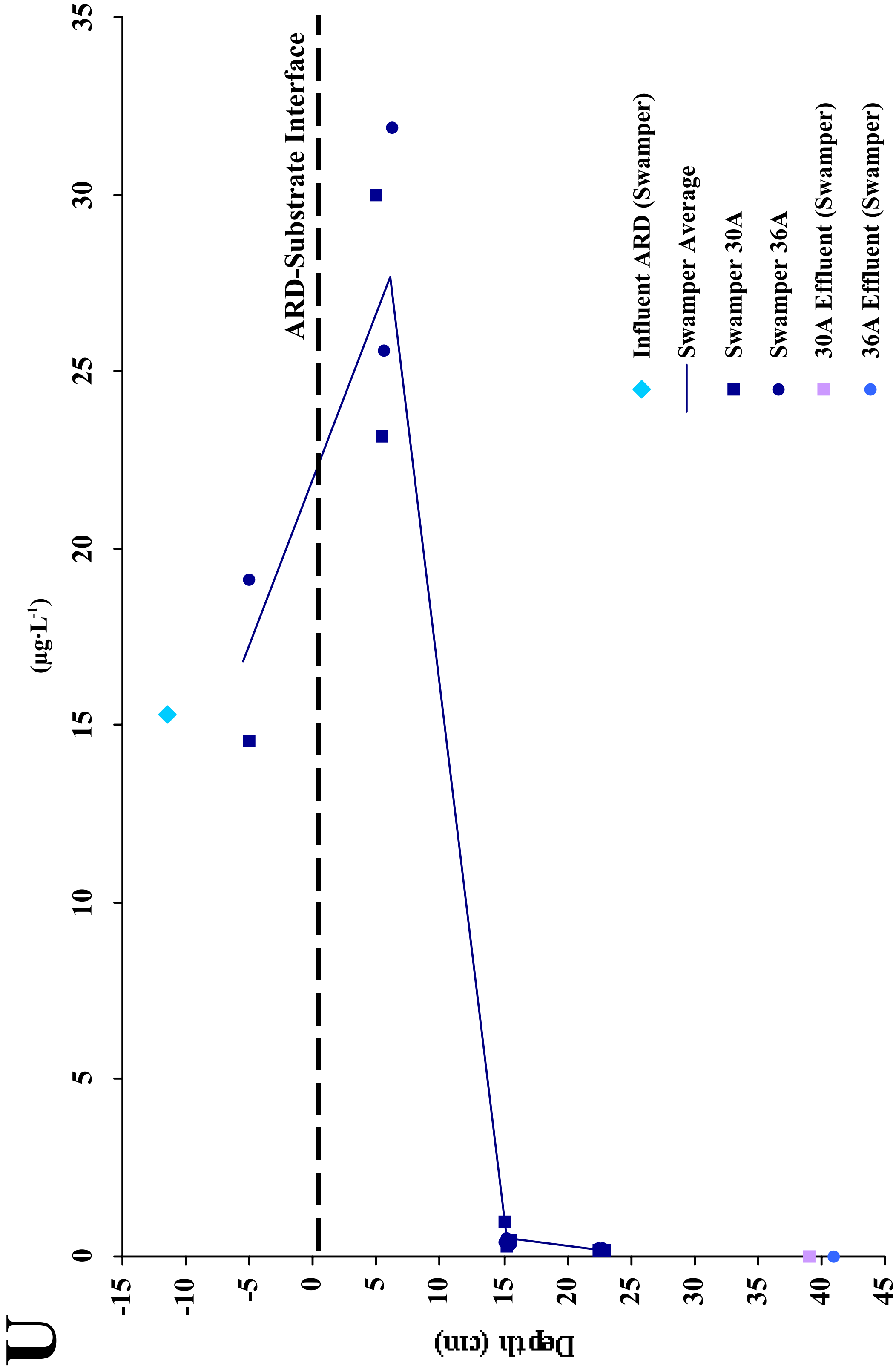
U
ARD-Substrate Interface
Influent ARD (Swamper)
Swamper Average
Swamper 30A
Swamper 36A
30A Effluent (Swamper)
36A Effluent (Swamper)
(µg·L-1)
0
5
10
15
20
25
30
35
Depth (cm)
-15
-10
-5
0
5
10
15
20
25
30
35
40
45

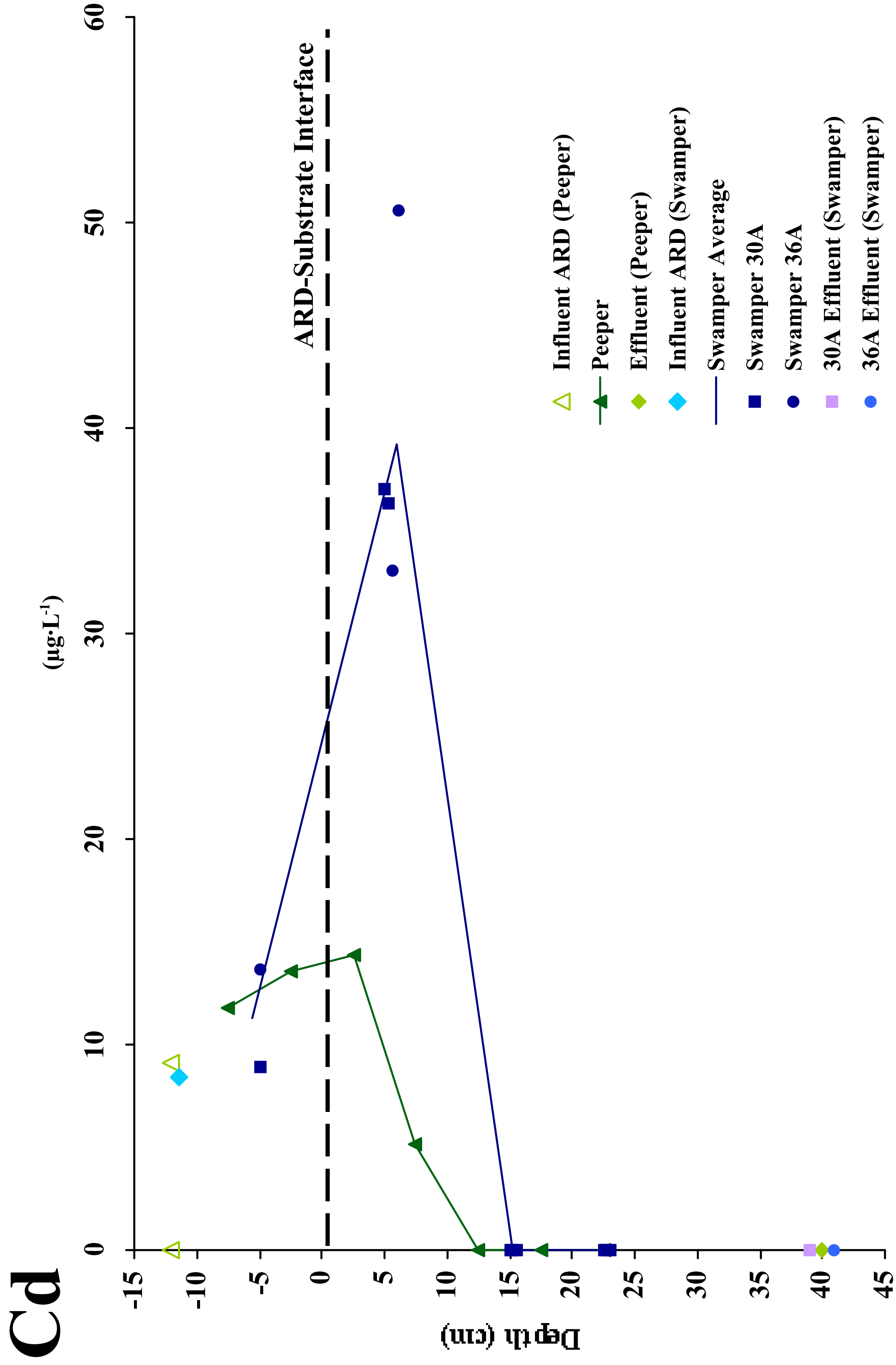
Cd
ARD-Substrate Interface
(µg·L-1)
Depth (cm)
0
10
20
30
40
50
60
-15
-10
-5
0
5
10
15
20
25
30
35
40
45
Influent ARD (Peeper)
Peeper
Effluent (Peeper)
Influent ARD (Swamper)
Swamper Average
Swamper 30A
Swamper 36A
30A Effluent (Swamper)
36A Effluent (Swamper)

Co

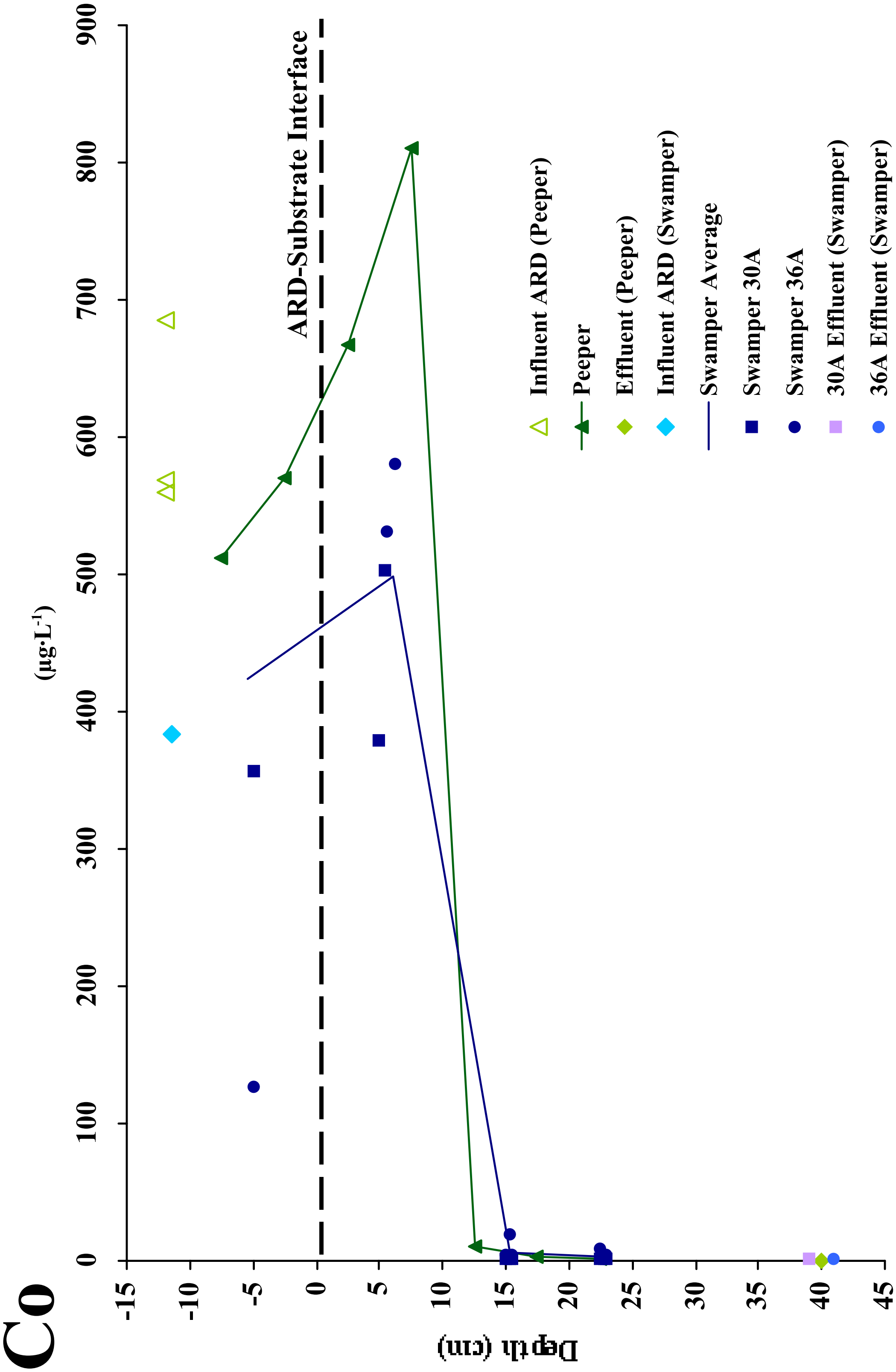
(µg·L-1)
0
100
200
300
400
500
600
700
800
900
Depth (cm)
-15
-10
-5
0
5
10
15
20
25
30
35
40
45
ARD-Substrate Interface
△ Influent ARD (Peeper)
Peeper
◆ Effluent (Peeper)
◆ Influent ARD (Swamper)
Swamper Average
■ Swamper 30A
● Swamper 36A
■ 30A Effluent (Swamper)
● 36A Effluent (Swamper)

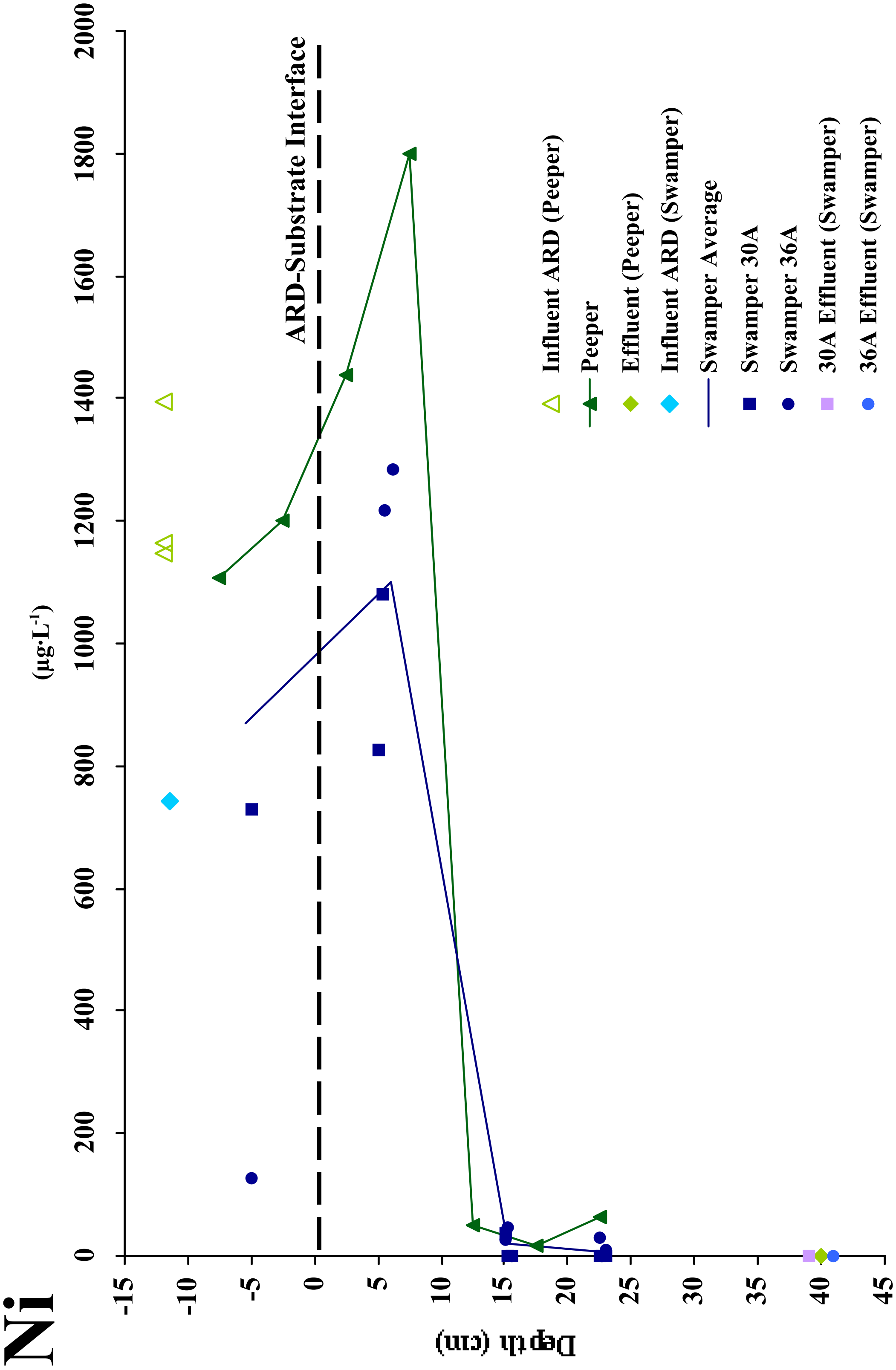
Ni
(µg·L⁻¹)
0
200
400
600
800
1000
1200
1400
1600
1800
2000
Depth (cm)
-15
-10
-5
0
5
10
15
20
25
30
35
40
45
ARD-Substrate Interface
Influent ARD (Peeper)
Peeper
Effluent (Peeper)
Influent ARD (Swamper)
Swamper Average
Swamper 30A
Swamper 36A
30A Effluent (Swamper)
36A Effluent (Swamper)

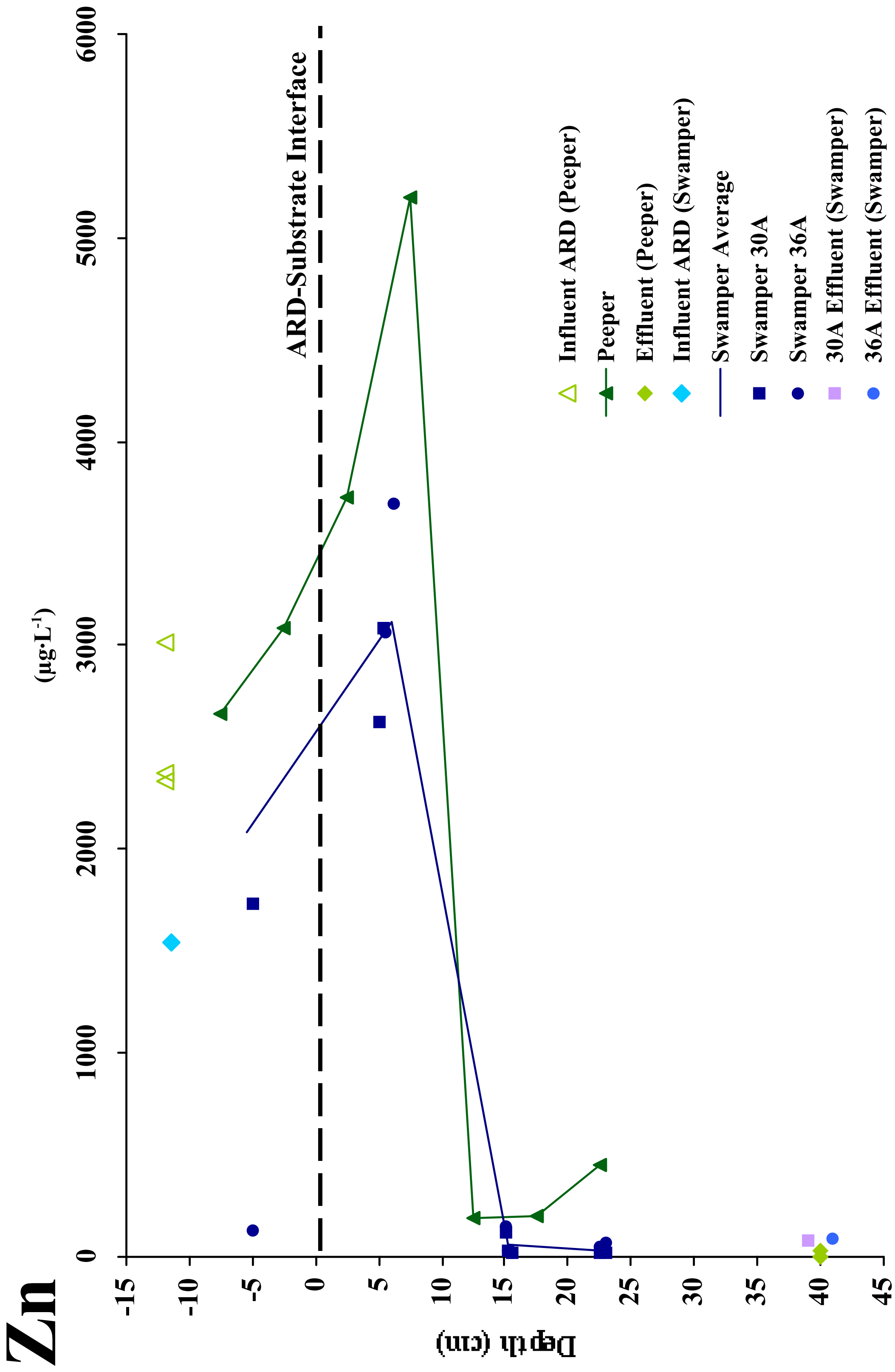
Zn
Depth (cm)
(µg·L-1)
-15
-10
-5
0
5
10
15
20
25
30
35
40
45
0
1000
2000
3000
4000
5000
6000
ARD-Substrate Interface
Influent ARD (Peeper)
Peeper
Effluent (Peeper)
Influent ARD (Swamper)
Swamper Average
Swamper 30A
Swamper 36A
30A Effluent (Swamper)
36A Effluent (Swamper)

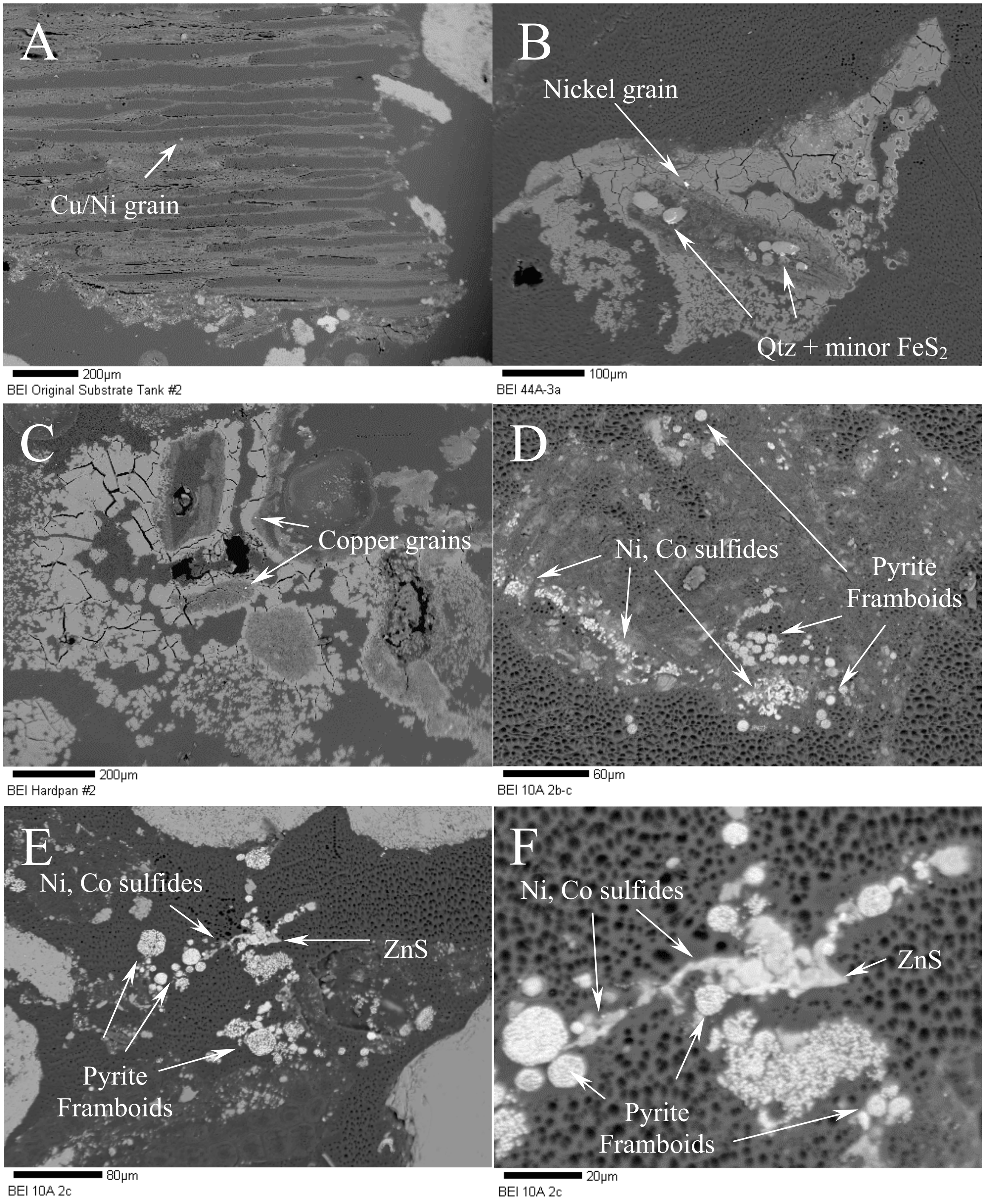

Figure 4.5. Electron microprobe images showing discrete trace metal precipitates in the LBOS. Detailed analysis of LBOS textures are presented in chapter 3. (A) Wood fragment from the initial substrate showing associated copper-nickel grain (B) nickel grain with minor associated phosphate observed in the oxide zone. (C) Copper grains in the interior of former limestone. (D) Band of nickel, cobalt sulfides precipitated along the edge of a wood fragment. Secondary framboidal pyrite (spheres) is also noted. (E) Band of nickel, cobalt sulfides with framboidal pyrite (spheres) and anhedral zinc sulfide. (F) Close-up of sulfides in (E)

Figure 4.6. Total trace element analysis of LBOS. Data are divided by reaction zone (oxide, transitional, and sulfide), date of collection (blue and orange), and finally by tank (30A or 36A) and core number (-1, -2, -3). The lines connect average values for each zone. Eight replicates of the initial substrate are provided (green triangles). Total digests were conducted following the procedure outlined on the right side of Figure 3.3. For cadmium, uranium, and nickel, cumulative totals, calculated from sequential digest data (Table 3.3), are plotted (see text for details).

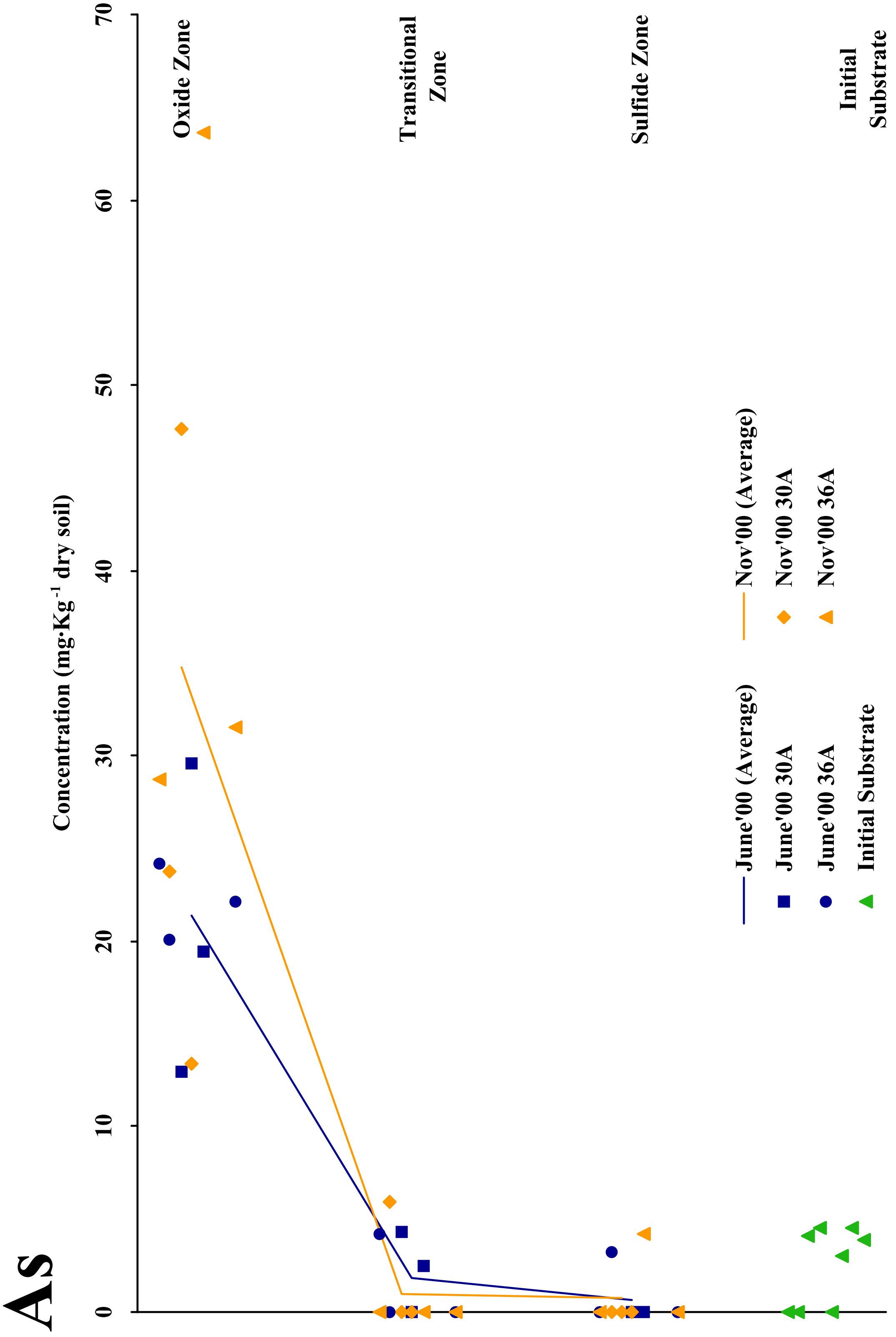
As
Concentration (mg·Kg-1 dry soil)
0
10
20
30
40
50
60
70
Oxide Zone
Transitional Zone
Sulfide Zone
Initial Substrate
June'00 (Average)
June'00 30A
June'00 36A
Initial Substrate
Nov'00 (Average)
Nov'00 30A
Nov'00 36A

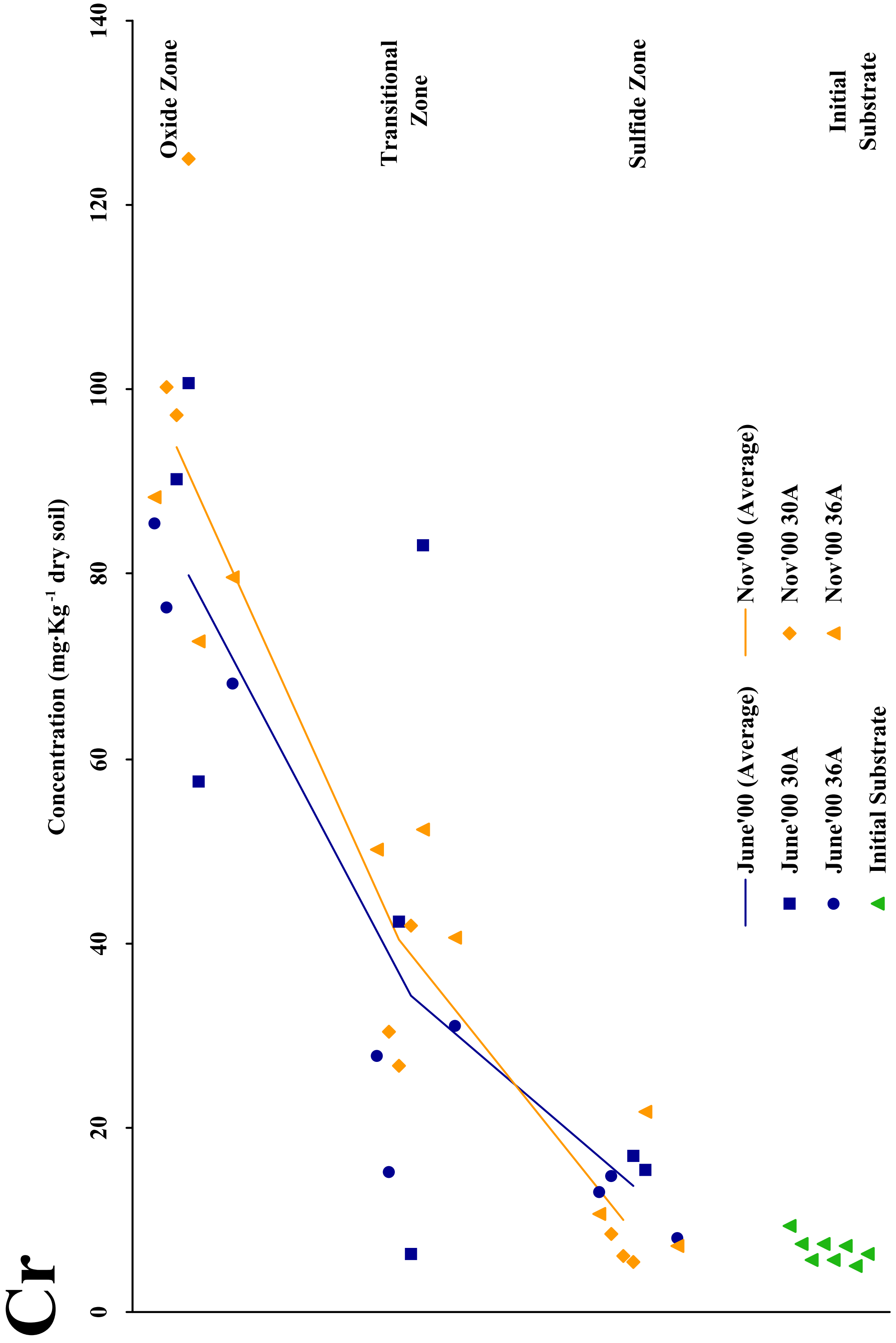

Cr

Concentration (mg·Kg^{-1} dry soil)
0
20
40
60
80
100
120
140
Oxide Zone
Transitional Zone
Sulfide Zone
Initial Substrate
June'00 (Average)
June'00 30A
June'00 36A
Initial Substrate
Nov'00 (Average)
Nov'00 30A
Nov'00 36A

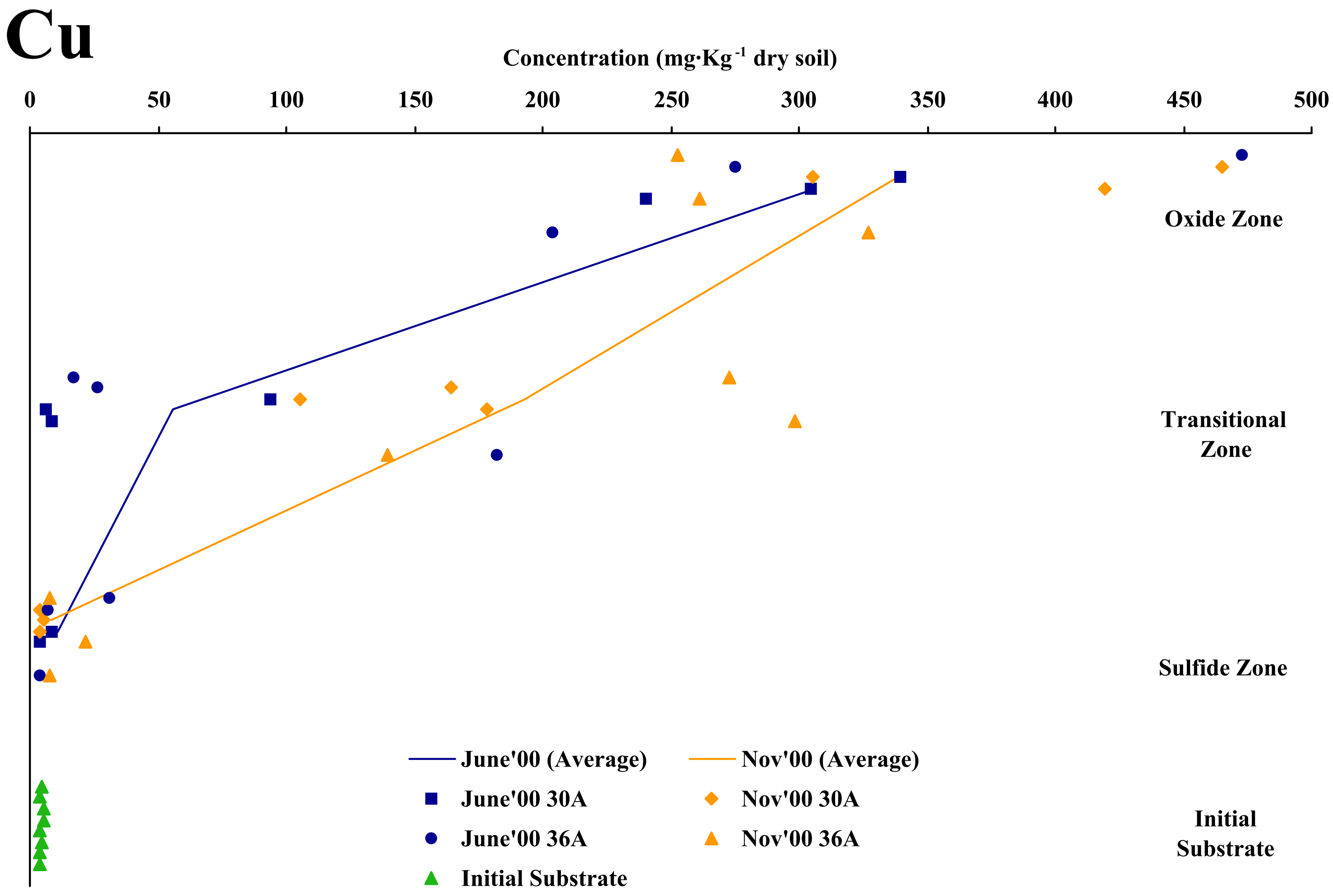
Cu
Concentration (mg·Kg^{-1} dry soil)
0
50
100
150
200
250
300
350
400
450
500
Oxide Zone
Transitional Zone
Sulfide Zone
Initial Substrate
June'00 (Average)
June'00 30A
June'00 36A
Initial Substrate
Nov'00 (Average)
Nov'00 30A
Nov'00 36A

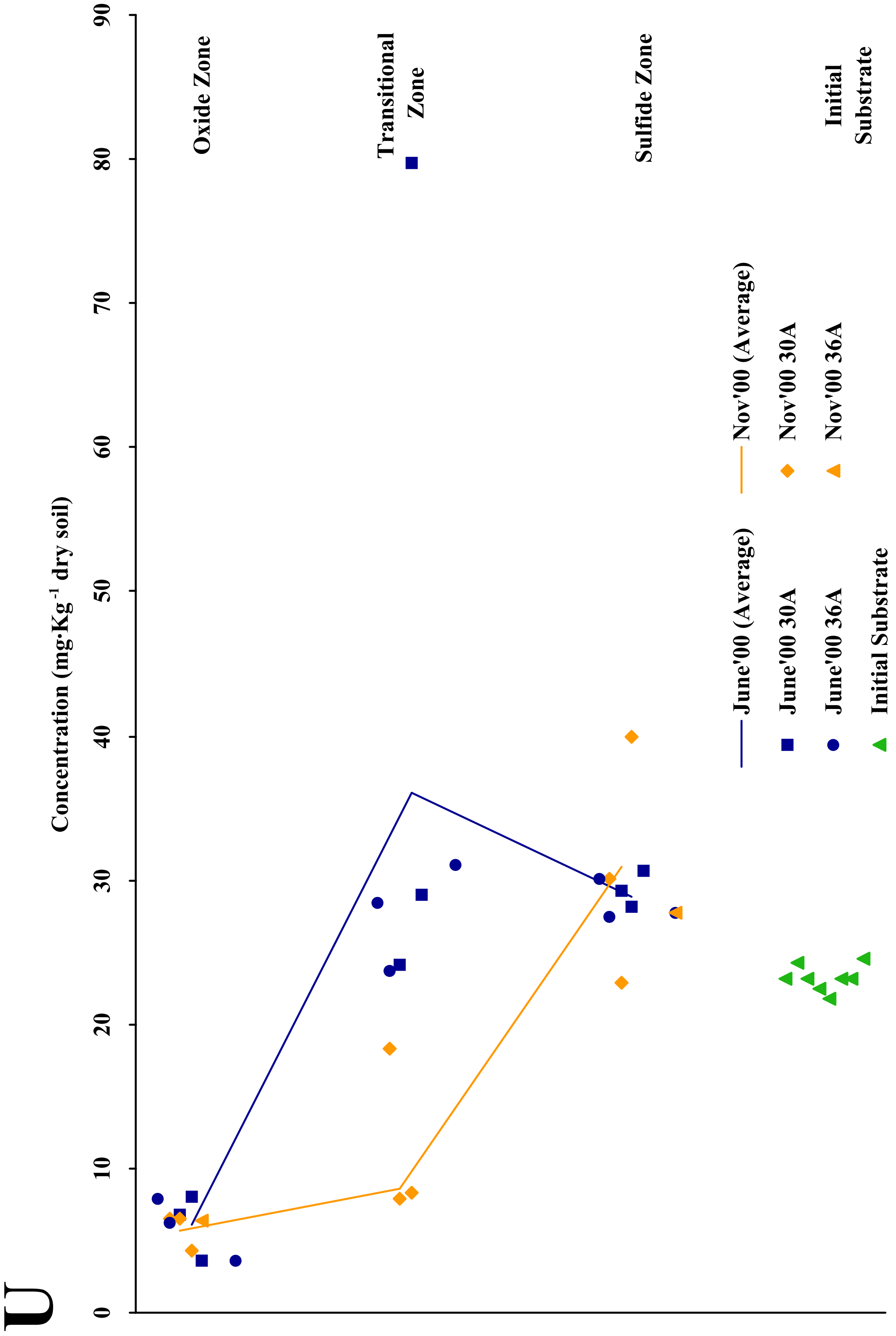
U
Concentration (mg·Kg⁻¹ dry soil)
0
10
20
30
40
50
60
70
80
90
Oxide Zone
Transitional Zone
Sulfide Zone
Initial Substrate
June'00 (Average)
June'00 30A
June'00 36A
Initial Substrate
Nov'00 (Average)
Nov'00 30A
Nov'00 36A

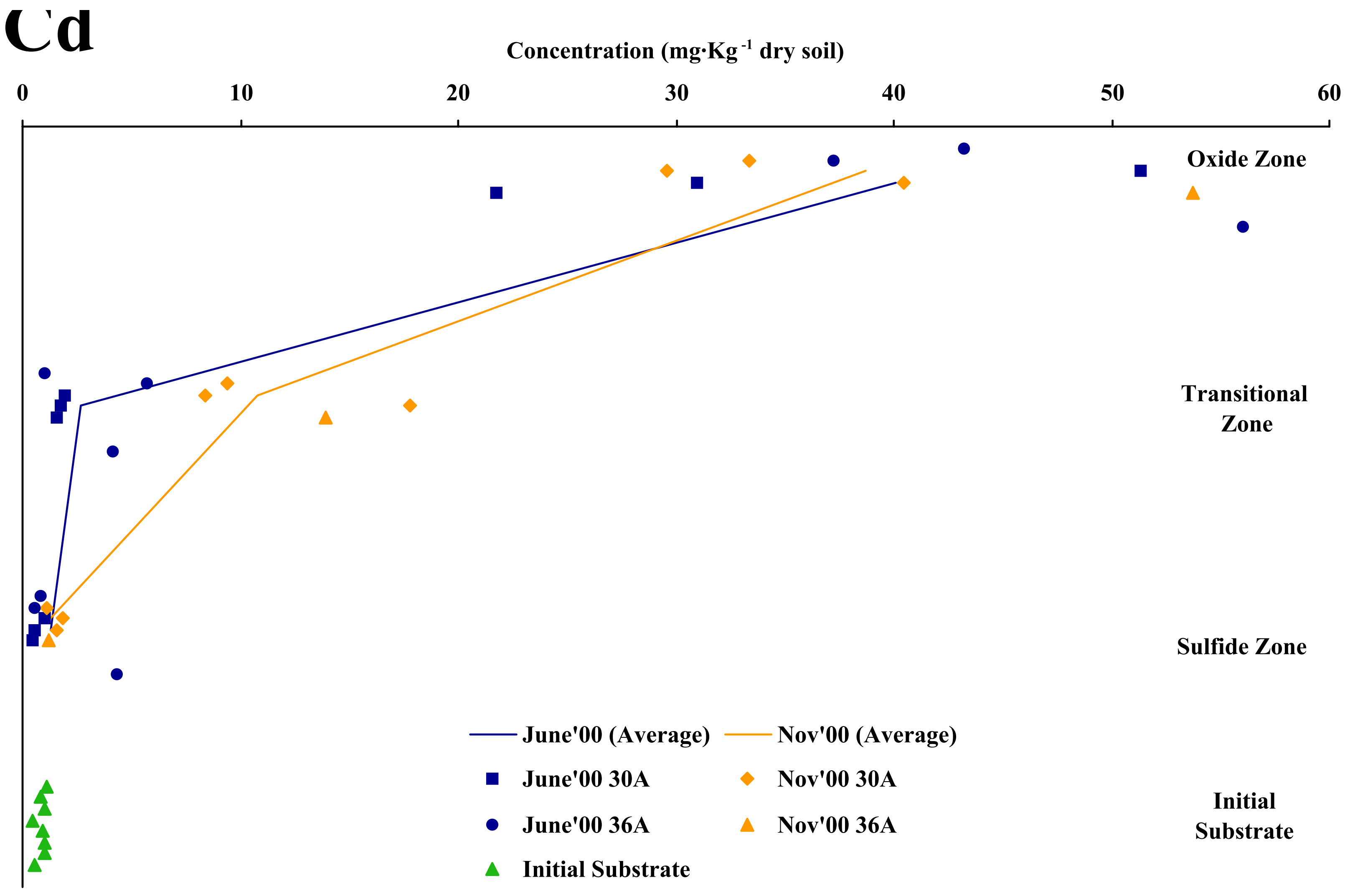
Cd
Concentration (mg·Kg -1 dry soil)
0
10
20
30
40
50
60
Oxide Zone
Transitional Zone
Sulfide Zone
Initial Substrate
June'00 (Average)
Nov'00 (Average)
June'00 30A
Nov'00 30A
June'00 36A
Nov'00 36A
Initial Substrate

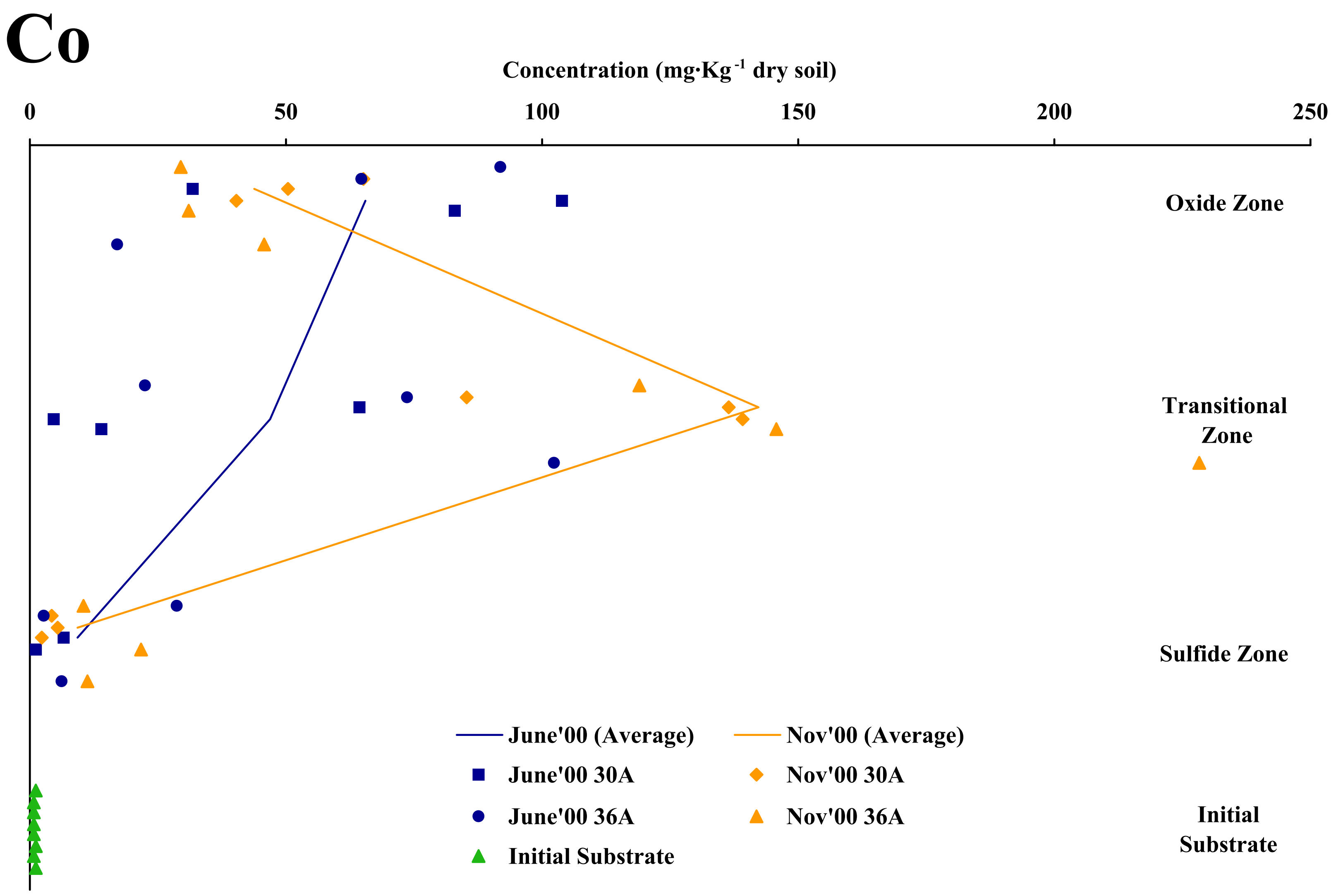
Co
Concentration (mg·Kg^{-1} dry soil)
0
50
100
150
200
250
Oxide Zone
Transitional Zone
Sulfide Zone
Initial Substrate
June'00 (Average)
June'00 30A
June'00 36A
Initial Substrate
Nov'00 (Average)
Nov'00 30A
Nov'00 36A

Ni

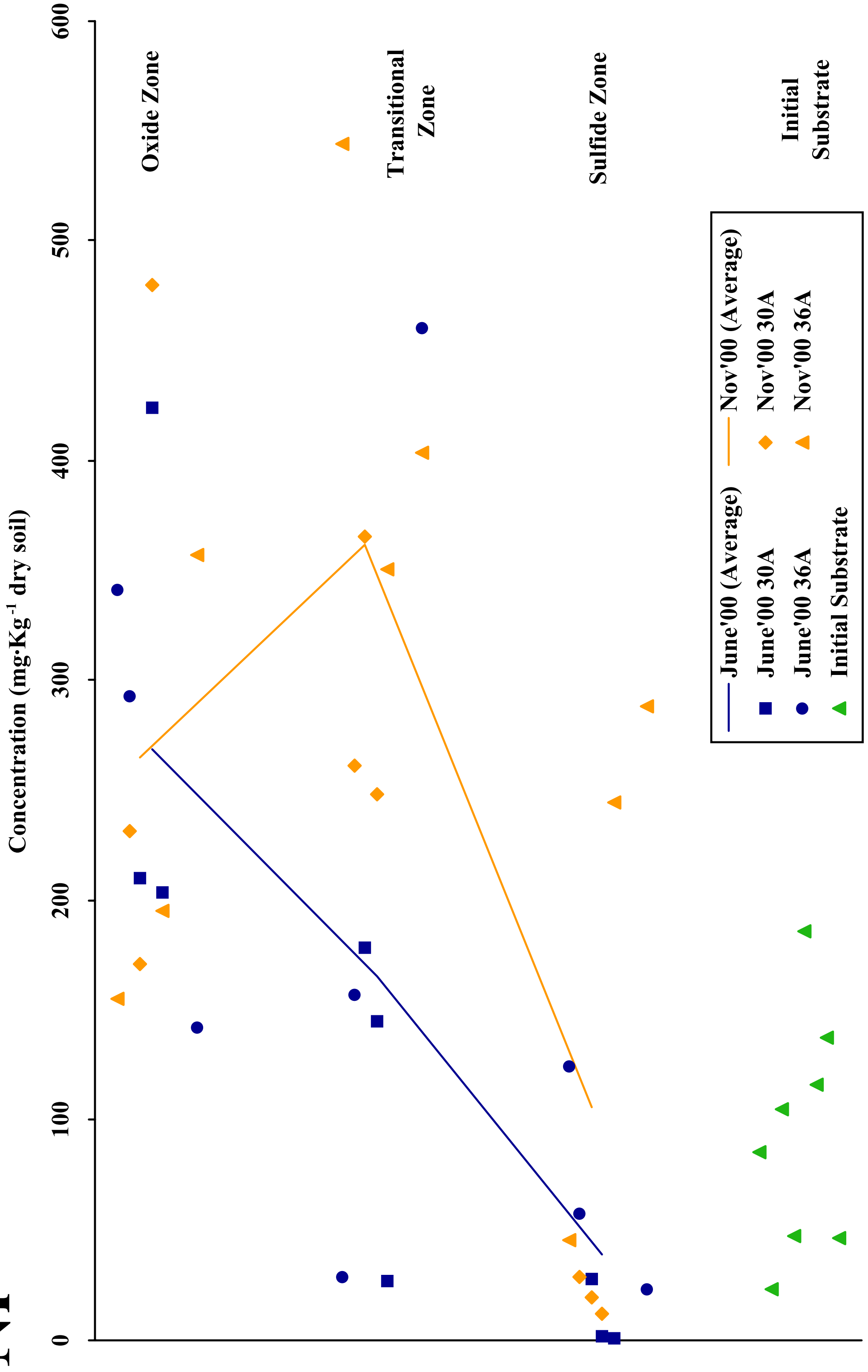
Concentration (mg·Kg-1 dry soil)
0
100
200
300
400
500
600
Oxide Zone
Transitional Zone
Sulfide Zone
Initial Substrate
June'00 (Average)
June'00 30A
June'00 36A
Initial Substrate
Nov'00 (Average)
Nov'00 30A
Nov'00 36A

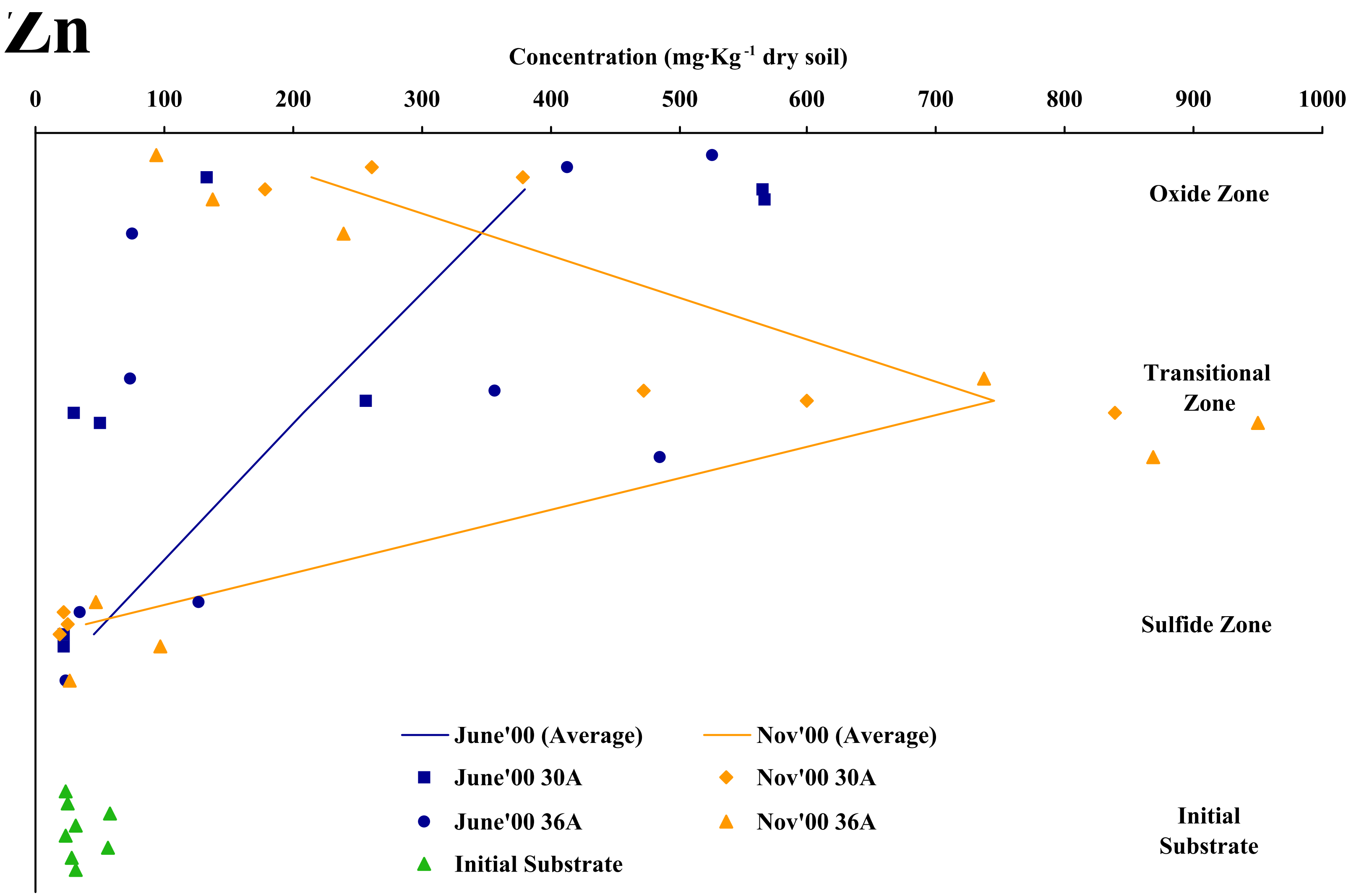
Zn
Concentration (mg·Kg^{-1} dry soil)
0
100
200
300
400
500
600
700
800
900
1000
Oxide Zone
Transitional Zone
Sulfide Zone
Initial Substrate
June'00 (Average)
June'00 30A
June'00 36A
Initial Substrate
Nov'00 (Average)
Nov'00 30A
Nov'00 36A

Table 4.3. Sequential extraction results from the LBOS. All values are given as mg·kg^{-1}

Tank 36A Arsenic

Season	Zone	Core	NSE	AS	PYRO	Rox	Rcd	Rres	Cum Tot	Total Digest
Initial		#1	0.21	0.00	0.00	n/a	n/a	2.11	2.32	0.00
Initial		#2	0.94	0.00	0.00	0.00	3.33	2.27	6.54	0.00
Initial		#3	1.19	0.00	0.00	n/a	n/a	2.11	3.30	4.12
Initial		#4	0.62	0.00	0.00	0.00	2.30	1.50	4.42	4.54
Summer	Sulfide	#1	0.22	0.00	0.09	n/a	n/a	0.00	0.31	0.00
		#2	2.11	0.00	0.00	n/a	n/a	0.00	2.11	3.28
		#3	0.00	0.00	0.00	n/a	n/a	0.00	0.00	0.00
Fall	Sulfide	#1	0.00	0.00	0.06	n/a	n/a	1.29	1.36	4.25
		#2	0.40	0.00	0.22	n/a	n/a	0.00	0.62	0.00
		#3	1.28	0.00	0.39	n/a	n/a	0.00	1.67	0.00
Summer	Trans	#1	1.12	0.00	0.00	n/a	n/a	0.00	1.12	4.20
		#2	2.59	0.00	0.00	0.18	0.56	0.00	3.33	0.00
		#3	0.45	0.00	0.00	n/a	n/a	0.05	0.49	0.00
Fall	Trans	#1	0.00	0.00	0.00	n/a	n/a	0.48	0.48	0.00
		#2	0.00	0.00	0.00	n/a	n/a	0.00	0.00	0.00
		#3	1.52	0.00	0.00	n/a	n/a	0.00	1.52	0.00
Summer	Oxide	#1	1.34	0.00	0.00	10.07	1.72	5.49	18.62	24.18
		#2	3.09	0.00	0.62	10.48	3.24	4.85	22.27	20.09
		#3	0.00	0.01	2.50	11.74	8.80	4.40	27.46	22.12
Fall	Oxide	#1	0.00	0.00	14.42	27.32	28.53	5.01	75.28	63.59
		#2	0.44	0.00	3.16	12.69	20.47	2.15	38.91	31.58
		#3	0.00	0.00	7.10	16.75	25.68	6.17	55.70	28.76

Tank 30A Arsenic

Season	Zone	Core	NSE	AS	PYRO	Rox	Rcd	Rres	Cum Tot	Total Digest
Initial		#5	1.79	0.00	0.00	n/a	n/a	1.91	3.70	0.00
Initial		#6	0.34	0.00	0.00	n/a	n/a	1.64	1.98	3.07
Initial		#7	0.45	0.00	0.00	n/a	n/a	2.58	3.03	4.59
Initial		#8	0.27	0.00	0.00	0.00	4.05	1.43	5.76	3.84
Summer	Sulfide	#1	0.94	0.38	0.00	n/a	n/a	0.00	1.33	0.00
		#2	0.94	0.00	0.00	n/a	n/a	0.00	0.94	0.00
		#3	0.00	0.00	0.00	n/a	n/a	0.00	0.00	n/a
Fall	Sulfide	#1	0.71	0.00	0.55	n/a	n/a	0.00	1.26	0.00
		#2	0.00	0.20	0.00	n/a	n/a	0.00	0.20	0.00
		#3	0.00	0.00	0.00	n/a	n/a	0.00	0.00	0.00
Summer	Trans	#1	1.52	0.00	0.00	n/a	n/a	2.19	3.71	2.54
		#2	0.00	0.00	0.00	n/a	n/a	0.00	0.00	0.00
		#3	1.05	0.00	0.00	n/a	n/a	0.00	1.05	4.29
Fall	Trans	#1	0.55	0.00	0.00	n/a	n/a	1.08	1.63	5.99
		#2	0.00	0.00	0.00	n/a	n/a	0.00	0.00	0.00
		#3	1.76	0.00	0.00	n/a	n/a	0.00	1.76	0.00
Summer	Oxide	#1	0.26	4.75	0.00	5.70	9.00	0.00	19.70	19.39
		#2	2.65	0.00	2.97	18.22	5.80	5.44	35.09	29.61
		#3	3.56	0.00	1.47	8.10	3.21	0.91	17.25	12.98
Fall	Oxide	#1	0.00	0.00	1.03	2.68	14.12	1.82	19.65	23.79
		#2	4.66	0.00	16.20	17.58	26.47	0.00	64.91	47.64
		#3	0.00	0.00	3.33	4.53	18.73	0.00	26.60	13.39

Tank 36A Cadmium

Season	Zone	Core	NSE	AS	PYRO	Rox	Rcd	Rres	Cum Tot	Total Digest
Initial		#1	0.00	0.04	0.28	n/a	n/a	0.74	1.07	n/a
Initial		#2	0.00	0.03	0.32	0.00	0.00	0.51	0.87	n/a
Initial		#3	0.00	0.04	0.28	n/a	n/a	0.71	1.04	n/a
Initial		#4	0.00	0.05	0.15	0.00	0.00	0.31	0.51	n/a
Summer	Sulfide	#1	0.00	0.00	0.61	n/a	n/a	0.22	0.8	n/a
		#2	0.00	0.01	0.35	n/a	n/a	0.24	0.6	n/a
		#3	0.00	1.92	0.55	n/a	n/a	1.84	4.3	n/a
Fall	Sulfide	#1	0.00	0.00	0.72	n/a	n/a	0.48	1.2	n/a
		#2	0.00	0.00	0.63	n/a	n/a	0.13	0.8	n/a
		#3	0.00	0.24	1.11	n/a	n/a	0.19	1.5	n/a
Summer	Trans	#1	0.00	0.27	0.58	n/a	n/a	0.13	1.0	n/a
		#2	0.00	0.20	1.26	0.82	0.33	3.06	5.7	n/a
		#3	0.00	0.00	2.03	n/a	n/a	2.14	4.2	n/a
Fall	Trans	#1	0.00	8.32	2.38	n/a	n/a	3.24	14	n/a
		#2	0.00	6.37	1.00	n/a	n/a	2.49	10	n/a
		#3	0.00	0.71	2.59	n/a	n/a	2.08	5	n/a
Summer	Oxide	#1	2.74	2.39	7.98	15.64	13.78	0.68	43	n/a
		#2	0.50	1.91	5.93	11.47	16.70	0.75	37	n/a
		#3	1.01	0.57	8.46	22.24	22.87	0.94	56	n/a
Fall	Oxide	#1	1.39	0.83	13.76	29.38	7.81	0.59	54	n/a
		#2	1.60	0.66	6.03	13.65	6.41	0.48	29	n/a
		#3	0.45	0.64	10.06	20.98	13.45	0.60	46	n/a

Tank 30A Cadmium

Season	Zone	Core	NSE	AS	PYRO	Rox	Rcd	Rres	Cum Tot	Total Digest
Initial		#5	0.00	0.09	0.31	n/a	n/a	0.54	0.94	n/a
Initial		#6	0.00	0.12	0.32	n/a	n/a	0.53	0.97	n/a
Initial		#7	0.00	0.10	0.25	n/a	n/a	0.63	0.98	n/a
Initial		#8	0.00	0.10	0.14	0.02	0.00	0.31	0.58	n/a
Summer	Sulfide	#1	0.00	0.06	0.26	n/a	n/a	0.15	0.5	n/a
		#2	0.00	0.01	0.39	n/a	n/a	0.12	0.5	n/a
		#3	0.00	0.00	0.65	n/a	n/a	0.32	1.0	n/a
Fall	Sulfide	#1	0.00	0.17	0.79	n/a	n/a	0.15	1.1	n/a
		#2	0.00	0.92	0.63	n/a	n/a	0.26	1.8	n/a
		#3	0.00	0.67	0.71	n/a	n/a	0.20	1.6	n/a
Summer	Trans	#1	0.40	0.29	0.66	n/a	n/a	0.20	1.6	n/a
		#2	0.00	0.00	0.81	n/a	n/a	0.96	1.8	n/a
		#3	0.00	0.10	1.36	n/a	n/a	0.45	1.9	n/a
Fall	Trans	#1	0.00	0.48	2.75	n/a	n/a	6.16	9.4	n/a
		#2	0.00	5.17	1.26	n/a	n/a	1.94	8.4	n/a
		#3	0.00	8.99	1.79	n/a	n/a	7.04	17.8	n/a
Summer	Oxide	#1	0.00	1.32	4.50	13.25	2.02	0.67	21.8	n/a
		#2	0.00	2.18	8.28	12.12	7.19	1.18	31.0	n/a
		#3	1.39	1.26	13.74	20.77	13.84	0.33	51.3	n/a
Fall	Oxide	#1	0.00	2.14	7.89	3.30	19.40	0.60	33.3	n/a
		#2	0.35	1.61	17.48	3.19	6.08	0.91	29.6	n/a
		#3	0.18	1.97	14.58	16.13	7.22	0.38	40.4	n/a

Tank 36A Chromium

Season	Zone	Core	NSE	AS	PYRO	Rox	Rcd	Rres	Cum Tot	Total Digest
Initial		#1	0.39	3.08	1.15	n/a	n/a	3.86	8.49	9.43
Initial		#2	0.21	3.11	1.35	0.75	1.77	2.24	9.43	7.38
Initial		#3	0.26	2.63	1.03	n/a	n/a	3.62	7.54	5.71
Initial		#4	0.20	1.25	0.43	0.44	1.01	1.23	4.57	7.35
Summer	Sulfide	#1	0.01	1.28	0.69	n/a	n/a	3.54	5.5	13.07
		#2	0.25	1.31	1.28	n/a	n/a	4.34	7.2	14.77
		#3	0.00	0.67	0.56	n/a	n/a	2.98	4.2	8.01
Fall	Sulfide	#1	0.23	1.89	1.29	n/a	n/a	5.01	8.4	21.62
		#2	0.11	1.18	0.69	n/a	n/a	4.55	6.5	7.23
		#3	0.38	2.30	1.57	n/a	n/a	4.40	8.6	10.70
Summer	Trans	#1	0.76	2.27	1.05	n/a	n/a	5.98	10.1	27.83
		#2	0.36	4.14	1.18	2.82	0.57	25.94	35.0	15.09
		#3	0.08	24.61	6.27	n/a	n/a	16.07	47.0	30.97
Fall	Trans	#1	0.00	20.01	11.63	n/a	n/a	20.53	52	52.41
		#2	0.06	19.12	6.28	n/a	n/a	12.93	38	40.50
		#3	0.08	18.06	8.02	n/a	n/a	16.88	43	50.11
Summer	Oxide	#1	0.90	22.49	30.59	28.69	9.16	11.37	103	85.63
		#2	1.06	14.56	18.13	17.01	9.00	11.90	72	76.44
		#3	3.41	9.42	12.34	24.44	11.08	24.59	85	68.20
Fall	Oxide	#1	0.13	9.13	16.04	17.80	4.43	14.49	62	72.72
		#2	0.67	11.24	16.92	19.44	6.12	14.79	69	79.63
		#3	0.75	11.12	17.91	23.19	9.59	14.32	77	88.30

Tank 30A Chromium

Season	Zone	Core	NSE	AS	PYRO	Rox	Rcd	Rres	Cum Tot	Total Digest
Initial		#5	0.16	1.62	0.87	n/a	n/a	4.55	7.20	5.57
Initial		#6	0.27	1.19	0.86	n/a	n/a	3.89	6.21	7.23
Initial		#7	0.34	0.96	0.68	n/a	n/a	3.01	4.99	5.01
Initial		#8	0.05	0.84	0.60	0.42	1.26	1.65	4.82	6.21
Summer	Sulfide	#1	0.23	0.85	0.59	n/a	n/a	4.29	6.0	15.50
		#2	0.03	1.10	1.03	n/a	n/a	3.79	5.9	16.94
		#3	0.13	2.21	0.88	n/a	n/a	2.67	5.9	n/a
Fall	Sulfide	#1	0.47	1.35	0.70	n/a	n/a	4.79	7.3	8.38
		#2	0.02	0.60	0.58	n/a	n/a	3.13	4.3	5.99
		#3	0.00	1.02	0.53	n/a	n/a	3.05	4.6	5.45
Summer	Trans	#1	1.94	1.88	1.00	n/a	n/a	3.83	8.6	83.20
		#2	0.12	8.31	3.45	n/a	n/a	5.02	16.9	6.31
		#3	0.32	6.55	2.84	n/a	n/a	9.13	18.8	42.34
Fall	Trans	#1	0.75	25.84	11.03	n/a	n/a	19.73	57.4	30.42
		#2	0.00	11.72	6.23	n/a	n/a	7.54	25.5	26.72
		#3	0.00	38.20	9.09	n/a	n/a	12.25	59.5	41.79
Summer	Oxide	#1	1.04	15.15	13.08	20.95	2.99	8.14	61.3	57.57
		#2	0.33	27.17	18.23	17.08	13.33	11.08	87.2	100.66
		#3	0.46	15.26	29.23	30.42	10.20	14.12	99.7	90.35
Fall	Oxide	#1	0.39	40.40	25.04	20.31	10.97	16.55	113.7	100.31
		#2	1.77	25.77	27.05	34.66	8.84	21.37	119.5	97.19
		#3	0.43	27.18	22.13	34.20	7.06	12.75	103.8	125.11

Table 4.3. Continued

Tank 36A **Copper**

Season	Zone	Core	NSE	AS	PYRO	Rox	Rcd	Rres	Cum Tot	Total Digest
Initial		#1	0.3	0.0	1.2	n/a	n/a	2.9	4.4	4.4
Initial		#2	0.3	0.0	1.4	1.3	0.0	1.4	4.4	3.8
Initial		#3	0.3	0.0	1.1	n/a	n/a	2.7	4.1	5.8
Initial		#4	0.2	0.0	0.8	0.7	0.0	1.1	2.8	5.6
Summer	Sulfide	#1	0.0	0.0	1.5	n/a	n/a	3.2	4.8	31
		#2	0.0	0.0	1.7	n/a	n/a	10	11	6.7
		#3	0.0	0.0	1.3	n/a	n/a	3.2	4.4	4.1
Fall	Sulfide	#1	0.0	0.0	3.0	n/a	n/a	13	16	22
		#2	0.0	0.0	2.7	n/a	n/a	4.6	7.3	8.1
		#3	0.0	0.0	5.1	n/a	n/a	11	16	8.1
Summer	Trans	#1	0.0	0.0	2.0	n/a	n/a	11	13	17
		#2	0.0	0.0	5.7	4.7	1.2	398	410	26
		#3	0.0	0.0	37	n/a	n/a	172	209	182
Fall	Trans	#1	0.0	0.0	55	n/a	n/a	288	343	299
		#2	0.0	0.0	21	n/a	n/a	148	169	140
		#3	0.0	6.1	51	n/a	n/a	192	249	273
Summer	Oxide	#1	4.5	98	72	57	12	208	451	473
		#2	0.7	44	46	32	5.7	128	255	275
		#3	4.8	51	15	21	12	397	501	204
Fall	Oxide	#1	11	50	30	42	6.1	99	238	262
		#2	3.9	50	45	34	6.1	121	259	327
		#3	3.3	84	34	29	6.9	89	246	253

Tank 30A **Copper**

Season	Zone	Core	NSE	AS	PYRO	Rox	Rcd	Rres	Cum Tot	Total Digest
Initial		#5	0.4	0.0	1.7	n/a	n/a	3.9	6.0	3.8
Initial		#6	0.5	0.0	1.3	n/a	n/a	3.0	4.8	4.3
Initial		#7	0.4	0.0	1.3	n/a	n/a	3.3	5.1	4.1
Initial		#8	0.4	0.0	1.2	1.2	0.1	1.5	4.5	4.0
Summer	Sulfide	#1	0.0	0.0	1.4	n/a	n/a	7.1	8.5	3.8
		#2	0.0	0.0	1.6	n/a	n/a	4.3	5.9	8.2
		#3	0.0	0.0	2.6	n/a	n/a	6.9	9.5	n/a
Fall	Sulfide	#1	0.0	0.0	3.5	n/a	n/a	4.4	7.9	4.1
		#2	0.0	0.0	1.8	n/a	n/a	4.4	6.2	5.2
		#3	0.0	0.0	1.7	n/a	n/a	2.1	3.9	3.5
Summer	Trans	#1	1.1	0.0	3.5	n/a	n/a	9.1	14	8.3
		#2	0.0	0.0	14	n/a	n/a	41	55	5.9
		#3	0.0	0.0	18	n/a	n/a	63	81	93
Fall	Trans	#1	0.0	3.8	27	n/a	n/a	275	306	164
		#2	0.0	0.0	16	n/a	n/a	136	152	106
		#3	0.0	0.0	18	n/a	n/a	402	421	178
Summer	Oxide	#1	0.0	80	51	36	3.5	83	253	241
		#2	0.0	40	58	31	8.1	135	271	305
		#3	19	89	44	43	10	122	327	340
Fall	Oxide	#1	0.0	206	67	50	7.0	192	522	465
		#2	0.0	32	58	49	12	197	348	305
		#3	0.0	87	40	41	7.5	147	323	419

Tank 36A **Uranium**

Season	Zone	Core	NSE	AS	PYRO	Rox	Rcd	Rres	Cum Tot	Total Digest
Initial		#1	0.9	21	0.8	n/a	n/a	0.9	23	n/a
Initial		#2	0.7	22	0.7	0.9	0.0	0.1	24	n/a
Initial		#3	0.9	21	0.7	n/a	n/a	0.5	23	n/a
Initial		#4	0.6	21	0.4	0.5	0.0	0.2	22	n/a
Summer	Sulfide	#1	0.4	28	1.4	n/a	n/a	0.3	30	n/a
		#2	1.7	24	1.3	n/a	n/a	0.3	27	n/a
		#3	0.7	27	0.0	n/a	n/a	0.5	28	n/a
Fall	Sulfide	#1	0.6	30	1.1	n/a	n/a	0.0	31	n/a
		#2	0.3	29	1.2	n/a	n/a	0.0	31	n/a
		#3	0.6	29	0.9	n/a	n/a	0.0	31	n/a
Summer	Trans	#1	2.0	25	1.4	n/a	n/a	0.0	28	n/a
		#2	2.5	20	0.7	0.0	0.1	0.4	24	n/a
		#3	2.1	28	0.9	n/a	n/a	0.0	31	n/a
Fall	Trans	#1	1.1	0.2	0.6	n/a	n/a	0.2	2.2	n/a
		#2	3.2	1.4	0.0	n/a	n/a	0.0	4.5	n/a
		#3	1.4	8.6	0.3	n/a	n/a	0.0	10	n/a
Summer	Oxide	#1	0.0	0.9	6.0	0.0	1.0	0.0	7.9	n/a
		#2	0.0	0.0	4.3	0.0	2.0	0.0	6.3	n/a
		#3	0.6	0.1	1.7	0.0	1.0	0.1	3.6	n/a
Fall	Oxide	#1	0.3	0.4	5.0	0.0	0.5	0.2	6.4	n/a
		#2	0.2	0.0	4.9	0.0	0.0	0.0	5.2	n/a
		#3	0.0	0.0	4.5	0.0	0.6	0.0	5.1	n/a

Tank 30A **Uranium**

Season	Zone	Core	NSE	AS	PYRO	Rox	Rcd	Rres	Cum Tot	Total Digest
Initial		#5	1.1	20	0.4	n/a	n/a	0.5	22	n/a
Initial		#6	1.2	21	0.8	n/a	n/a	0.3	23	n/a
Initial		#7	1.2	21	0.5	n/a	n/a	0.3	23	n/a
Initial		#8	0.9	22	0.5	0.8	0.0	0.3	25	n/a
Summer	Sulfide	#1	1.7	27	1.4	n/a	n/a	0.1	31	n/a
		#2	1.3	25	1.3	n/a	n/a	0.1	28	n/a
		#3	1.0	26	1.6	n/a	n/a	0.3	29	n/a
Fall	Sulfide	#1	0.4	29	1.0	n/a	n/a	0.2	30	n/a
		#2	0.7	22	0.0	n/a	n/a	0.2	23	n/a
		#3	0.2	39	0.2	n/a	n/a	0.2	40	n/a
Summer	Trans	#1	1.4	26	1.0	n/a	n/a	0.1	29	n/a
		#2	0.5	77	1.7	n/a	n/a	0.3	80	n/a
		#3	2.4	21	0.8	n/a	n/a	0.0	24	n/a
Fall	Trans	#1	1.6	13	3.4	n/a	n/a	0.0	18	n/a
		#2	0.6	7.1	0.2	n/a	n/a	0.1	8.0	n/a
		#3	0.6	3.8	3.7	n/a	n/a	0.2	8.4	n/a
Summer	Oxide	#1	0.2	0.0	3.4	0.0	0.0	0.0	3.7	n/a
		#2	3.9	0.0	3.5	0.0	0.6	0.0	8.0	n/a
		#3	2.8	0.3	2.7	0.0	1.1	0.0	6.8	n/a
Fall	Oxide	#1	0.1	0.0	5.1	0.6	0.6	0.1	6.5	n/a
		#2	0.0	0.0	6.4	0.0	0.0	0.0	6.5	n/a
		#3	0.0	0.0	3.6	0.0	0.5	0.1	4.3	n/a

Tank 36A **Cobalt**

Season	Zone	Core	NSE	AS	PYRO	Rox	Rcd	Rres	Cum Tot	Total Digest
Initial		#1	0.0	0.2	0.1	n/a	n/a	0.8	1.1	1.1
Initial		#2	0.0	0.2	0.1	0.0	0.3	0.5	1.1	0.7
Initial		#3	0.0	0.3	0.1	n/a	n/a	0.8	1.2	0.6
Initial		#4	0.0	0.3	0.0	0.0	0.2	0.3	0.8	0.6
Summer	Sulfide	#1	0.0	1.0	2.1	n/a	n/a	2.1	5.1	29
		#2	0.1	1.0	0.9	n/a	n/a	2.0	4.0	2.8
		#3	0.0	1.0	6.5	n/a	n/a	2.4	10	6.4
Fall	Sulfide	#1	0.1	1.2	16	n/a	n/a	8.0	26	22
		#2	0.1	2.1	11	n/a	n/a	4.4	17	11
		#3	1.3	6.2	6.6	n/a	n/a	5.0	19	10
Summer	Trans	#1	1.3	5.3	4.9	n/a	n/a	14	26	23
		#2	11	19	21	8.0	1.5	6.5	67	74
		#3	0.5	8.6	92	n/a	n/a	34	135	102
Fall	Trans	#1	1.1	16	97	n/a	n/a	51	164	146
		#2	0.8	6.3	161	n/a	n/a	35	203	228
		#3	61	50	64	n/a	n/a	32	206	119
Summer	Oxide	#1	47	6.2	59	15	4.1	5.3	137	92
		#2	19	4.1	44	12	3.5	1.6	85	65
		#3	4.2	2.3	5.0	3.0	0.8	1.7	17	17
Fall	Oxide	#1	3.9	3.1	21	11	0.9	1.9	42	31
		#2	32	3.7	14	4.3	1.2	1.8	57	46
		#3	4.6	2.5	17	7.2	0.9	1.6	33	29

Tank 30A **Cobalt**

Season	Zone	Core	NSE	AS	PYRO	Rox	Rcd	Rres	Cum Tot	Total Digest
Initial		#5	0.0	0.4	0.1	n/a	n/a	0.9	1.4	0.9
Initial		#6	0.1	0.4	0.1	n/a	n/a	0.8	1.4	1.1
Initial		#7	0.0	0.3	0.1	n/a	n/a	1.4	1.8	0.7
Initial		#8	0.0	0.3	0.1	0.0	0.4	0.4	1.2	1.1
Summer	Sulfide	#1	0.1	1.0	0.4	n/a	n/a	0.8	2.2	1.2
		#2	0.3	1.7	2.2	n/a	n/a	2.8	7.0	6.6
		#3	0.0	1.1	3.6	n/a	n/a	1.3	6.0	n/a
Fall	Sulfide	#1	0.2	2.0	2.6	n/a	n/a	2.0	6.8	4.3
		#2	0.0	0.6	4.4	n/a	n/a	3.4	8.5	5.3
		#3	0.0	1.0	2.0	n/a	n/a	2.1	5.1	2.2
Summer	Trans	#1	0.9	5.4	4.9	n/a	n/a	5.5	17	14
		#2	0.1	4.9	26	n/a	n/a	13	44	4.8
		#3	3.7	6.7	37	n/a	n/a	25	72	64
Fall	Trans	#1	6.9	16	102	n/a	n/a	50	175	85
		#2	0.0	1.4	92	n/a	n/a	29	123	136
		#3	0.0	1.7	101	n/a	n/a	42	144	139
Summer	Oxide	#1	37	8.0	27	16	1.9	6.8	96	83
		#2	29	21	61	24	8.2	5.2	149	104
		#3	16	6.9	16	6.3	2.0	2.0	50	32
Fall	Oxide	#1	6	21	22	21	3.8	2.6	77	65
		#2	2.1	3.4	44	15	3.1	3.0	70	51
		#3	3.7	8.8	15	9	1.9	2.0	40	40

Table 4.3. Continued

Tank 36A		Nickel								
Season	Zone	Core	NSE	AS	PYRO	Rox	Rcd	Rres	Cum Tot	Total Digest
Initial		#1	0.00	17.87	0.51	n/a	n/a	67	85	n/a
Initial		#2	0.00	10.97	2.98	0.00	7.50	1.6	23	n/a
Initial		#3	0.00	1.28	0.83	n/a	n/a	103	105	n/a
Initial		#4	0.00	22.39	2.65	16.09	1.48	4.68	47	n/a
Summer	Sulfide	#1	0.0	41.8	10.8	n/a	n/a	72	125	n/a
		#2	0.0	0.6	1.2	n/a	n/a	56	57	n/a
		#3	0.0	18.8	4.9	n/a	n/a	0.0	24	n/a
Fall	Sulfide	#1	0.0	0.0	31.8	n/a	n/a	213	244	n/a
		#2	0.0	0.0	6.3	n/a	n/a	283	289	n/a
		#3	0.5	11.7	6.6	n/a	n/a	27	46	n/a
Summer	Trans	#1	1.1	16.1	8.3	n/a	n/a	3.6	29	n/a
		#2	16	70	35	33	2.2	0.0	157	n/a
		#3	0.2	68	182	n/a	n/a	209	460	n/a
Fall	Trans	#1	1.1	85	217	n/a	n/a	47	350	n/a
		#2	1.9	52	350	n/a	n/a	0.0	404	n/a
		#3	103	173	109	n/a	n/a	159	544	n/a
Summer	Oxide	#1	121	19	117	46	5.7	33	341	n/a
		#2	53	14	81	41	1.3	104	293	n/a
		#3	10	6.2	8.1	9.7	1.2	107	143	n/a
Fall	Oxide	#1	14	1.4	47.5	35.5	2.3	95	196	n/a
		#2	79	7.3	23.3	2.9	4.2	241	358	n/a
		#3	14	1.9	33.0	4.5	1.7	101	156	n/a

Tank 30A		Nickel								
Season	Zone	Core	NSE	AS	PYRO	Rox	Rcd	Rres	Cum Tot	Total Digest
Initial		#5	0.00	18.60	7.92	n/a	n/a	159.80	186	n/a
Initial		#6	0.00	28.00	2.84	n/a	n/a	85	116	n/a
Initial		#7	0.00	15.63	3.66	n/a	n/a	118.60	138	n/a
Initial		#8	1.09	20.93	3.41	7.98	8.66	4.31	46	n/a
Summer	Sulfide	#1	0.0	0.5	0.4	n/a	n/a	0.0	0.9	n/a
		#2	0.0	0.7	0.8	n/a	n/a	0.0	1.5	n/a
		#3	0.0	13.2	14.3	n/a	n/a	0.0	27.6	n/a
Fall	Sulfide	#1	0.0	0.0	2.5	n/a	n/a	25.9	28.4	n/a
		#2	0.0	5.9	13.3	n/a	n/a	0.0	19.2	n/a
		#3	0.0	3.1	9.1	n/a	n/a	0.0	12.3	n/a
Summer	Trans	#1	0.8	18.4	7.4	n/a	n/a	0.0	26.5	n/a
		#2	0.0	37.9	47.3	n/a	n/a	59.7	144.9	n/a
		#3	5.8	29.5	68.1	n/a	n/a	75.0	178.4	n/a
Fall	Trans	#1	9.7	45.9	205.7	n/a	n/a	0.0	261.4	n/a
		#2	0.0	17.8	200.4	n/a	n/a	147.5	365.7	n/a
		#3	0.0	12.1	224.2	n/a	n/a	11.7	248.0	n/a
Summer	Oxide	#1	98.1	32.9	46.0	22.7	3.6	0.0	203.3	n/a
		#2	91.1	83.2	117.1	63.7	11.1	57.9	424.2	n/a
		#3	38.7	20.8	26.3	18.0	2.6	103.9	210.4	n/a
Fall	Oxide	#1	13.1	54.3	37.6	41.7	5.3	79.9	231.9	n/a
		#2	2.6	6.2	81.2	70.9	10.0	0.0	170.9	n/a
		#3	5.8	24.5	25.8	0.0	3.9	419.6	479.6	n/a

Tank 36A		Zinc								
Season	Zone	Core	NSE	AS	PYRO	Rox	Rcd	Rres	Cum Tot	Total Digest
Initial		#1	0.0	19	2.8	n/a	n/a	2.8	25	23
Initial		#2	0.0	18	3.2	1.0	1.3	1.4	25	24
Initial		#3	0.0	15	2.7	n/a	n/a	4.1	22	58
Initial		#4	0.00	17.74	1.54	3.04	4.76	0.7	28	32
Summer	Sulfide	#1	11	18.8	24.2	n/a	n/a	8.9	63	127
		#2	2.2	21.9	10.2	n/a	n/a	4.3	39	35
		#3	0.0	7.8	19.6	n/a	n/a	13	41	23
Fall	Sulfide	#1	0.0	16.5	61.7	n/a	n/a	96	175	97
		#2	0.0	16.5	27.4	n/a	n/a	8.4	52	27
		#3	0.0	57.7	23.2	n/a	n/a	23	104	48
Summer	Trans	#1	0.0	80.9	25.8	n/a	n/a	26	133	73
		#2	0.0	182.1	56.8	101.8	14.6	612	967	357
		#3	7.8	36.8	348	n/a	n/a	179	571	485
Fall	Trans	#1	0.0	17.1	496	n/a	n/a	326	839	949
		#2	0.0	16.6	455	n/a	n/a	424	895	869
		#3	1.0	315	329	n/a	n/a	228	873	736
Summer	Oxide	#1	324	246	166	91.7	78.6	6.7	913	526
		#2	127	204	140	70.9	44.4	21	608	413
		#3	22.6	31.5	7.5	26.3	30.7	461	580	75
Fall	Oxide	#1	76.1	52.0	28.8	48.2	0.0	8.8	214	138
		#2	157.2	63.7	61.4	38.2	2.2	5.0	328	240
		#3	30.6	56.7	27.1	24.3	0.0	2.0	141	94

Tank 30A		Zinc								
Season	Zone	Core	NSE	AS	PYRO	Rox	Rcd	Rres	Cum Tot	Total Digest
Initial		#5	0.00	25.47	5.42	n/a	n/a	1.7	33	24
Initial		#6	0.0	22	3.1	n/a	n/a	1.8	27	56
Initial		#7	0.00	19.53	3.29	n/a	n/a	2.9	26	28
Initial		#8	0.00	21.96	4.06	6.55	1.60	0.0	34	32
Summer	Sulfide	#1	0.0	15.5	6.1	n/a	n/a	4.0	26	22
		#2	0.0	20.6	11.8	n/a	n/a	2.0	34	22
		#3	2.1	15.8	30.2	n/a	n/a	7.9	56	n/a
Fall	Sulfide	#1	0.0	33.2	12.7	n/a	n/a	7.9	54	22
		#2	0.0	4.2	22.4	n/a	n/a	8.7	35	25
		#3	0.0	5.9	20.0	n/a	n/a	4.5	30	19
Summer	Trans	#1	0.0	47.0	11.5	n/a	n/a	14	72	50
		#2	0.3	1.1	161.8	n/a	n/a	120	283	29
		#3	0.0	86.6	98.6	n/a	n/a	62	247	257
Fall	Trans	#1	3.9	115.4	431.6	n/a	n/a	1182	1733	473
		#2	0.0	2.1	191.4	n/a	n/a	312	505	600
		#3	0.0	0.0	369.3	n/a	n/a	640	1009	840
Summer	Oxide	#1	42.5	204.1	163.5	152.7	13.3	17	593	566
		#2	4.4	349	287	176	149	41	1007	565
		#3	76.5	127.4	43.7	75.3	40.4	3.5	367	133
Fall	Oxide	#1	0.0	159.0	55.3	51.2	12.8	1.6	280	261
		#2	0.0	134.9	64.2	194.2	18.7	6.3	418	378
		#3	1.2	104.2	23.5	77.8	15.5	9.6	232	179

Figure 4.7. Sequential extraction results from the initial LBOS and the three reaction zones over time. Data are divided by tank (30A or 36A), reaction zone (oxide, transitional, and sulfide), date of collection, and finally core number (-1, -2, -3). Results from the initial samples (n=8) are duplicated next to each tank for reference. The vertical axes represent the elemental concentration (mg·kg^{-1}). In general, the vertical scale of the left panel (i.e., initial substrate and the sulfide zone) is much lower than the vertical scale of the right panel (i.e., oxide and transitional zones). Note that for some trace elements, the scales are different between tanks. Sequential extractions were conducted following the procedure outlined on the left side of Figure 3.3.

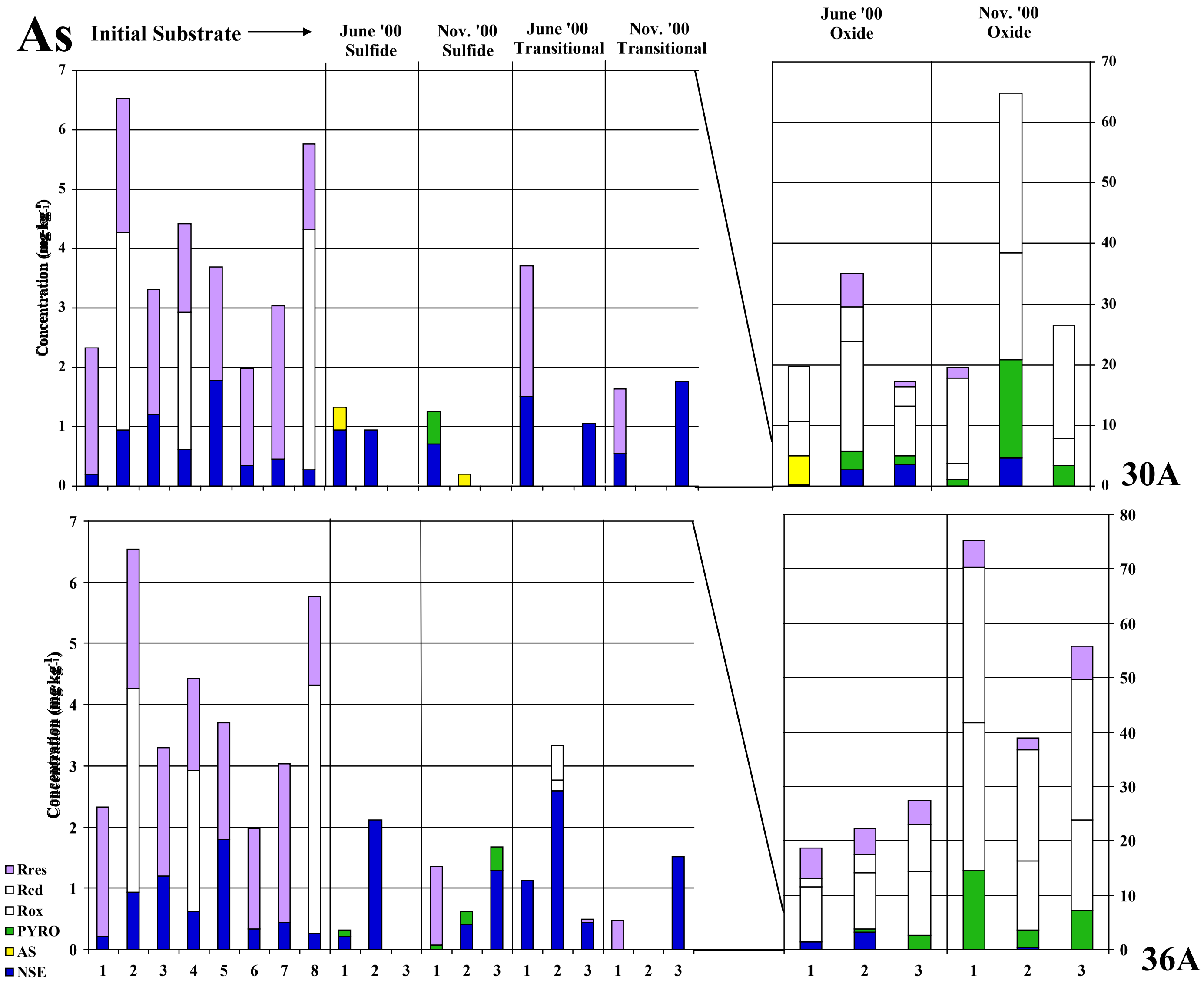
As
Initial Substrate
June '00 Sulfide
Nov. '00 Sulfide
June '00 Transitional
Nov. '00 Transitional
June '00 Oxide
Nov. '00 Oxide
Concentration (mg kg-1)
30A
36A
0
1
2
3
4
5
6
7
10
20
30
40
50
60
70
80
1
2
3
4
5
6
7
8
Rres
Red
Rox
PYRO
AS
NSE

Figure 4.7a

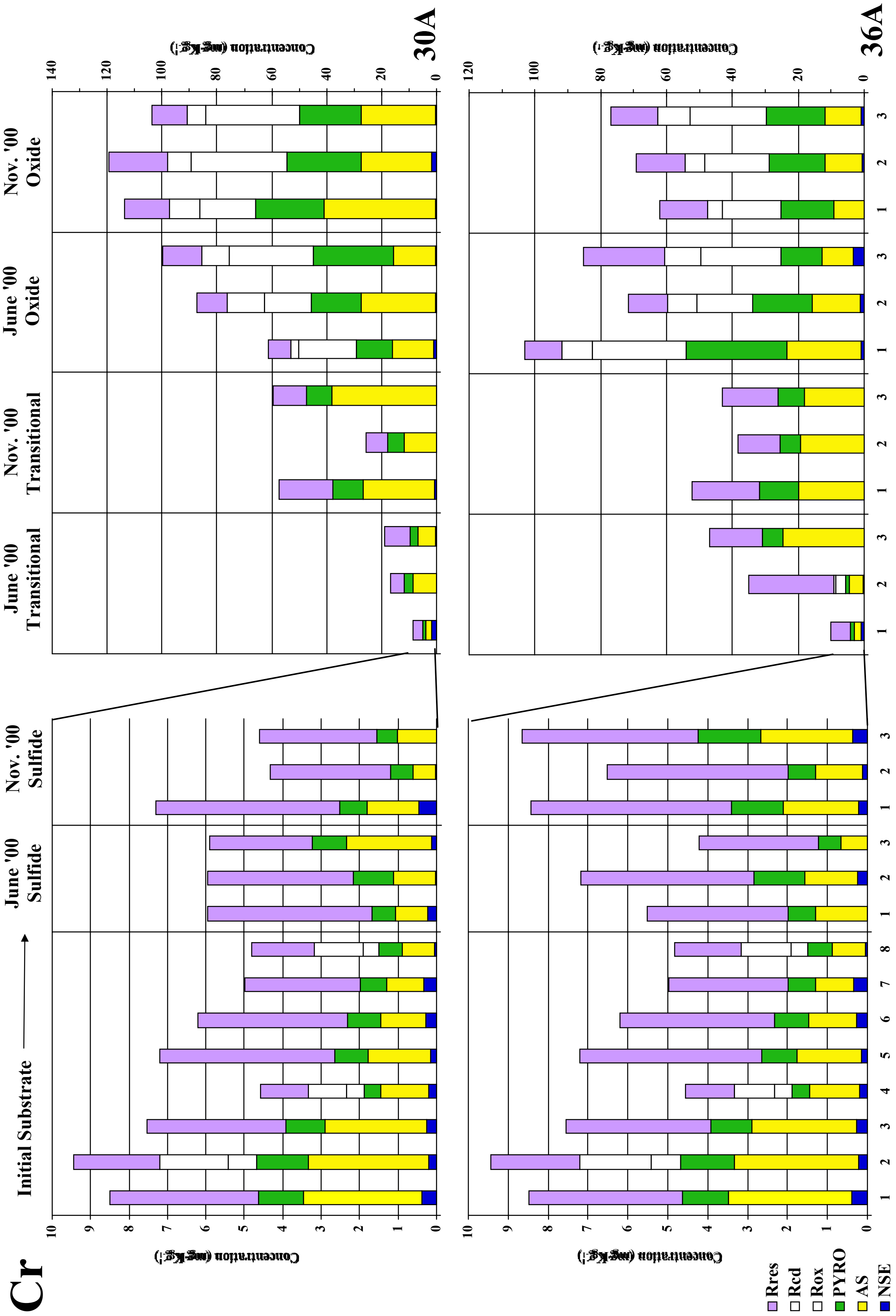
Cr
30A
36A
Initial Substrate
June '00 Sulfide
Nov. '00 Sulfide
June '00 Transitional
Nov. '00 Transitional
June '00 Oxide
Nov. '00 Oxide
Concentration (mg-kg-1)
0
1
2
3
4
5
6
7
8
9
10
20
40
60
80
100
120
140
1
2
3
4
5
6
7
8
Rres
Rcd
Rox
PYRO
AS
NSE

Figure 4.7b

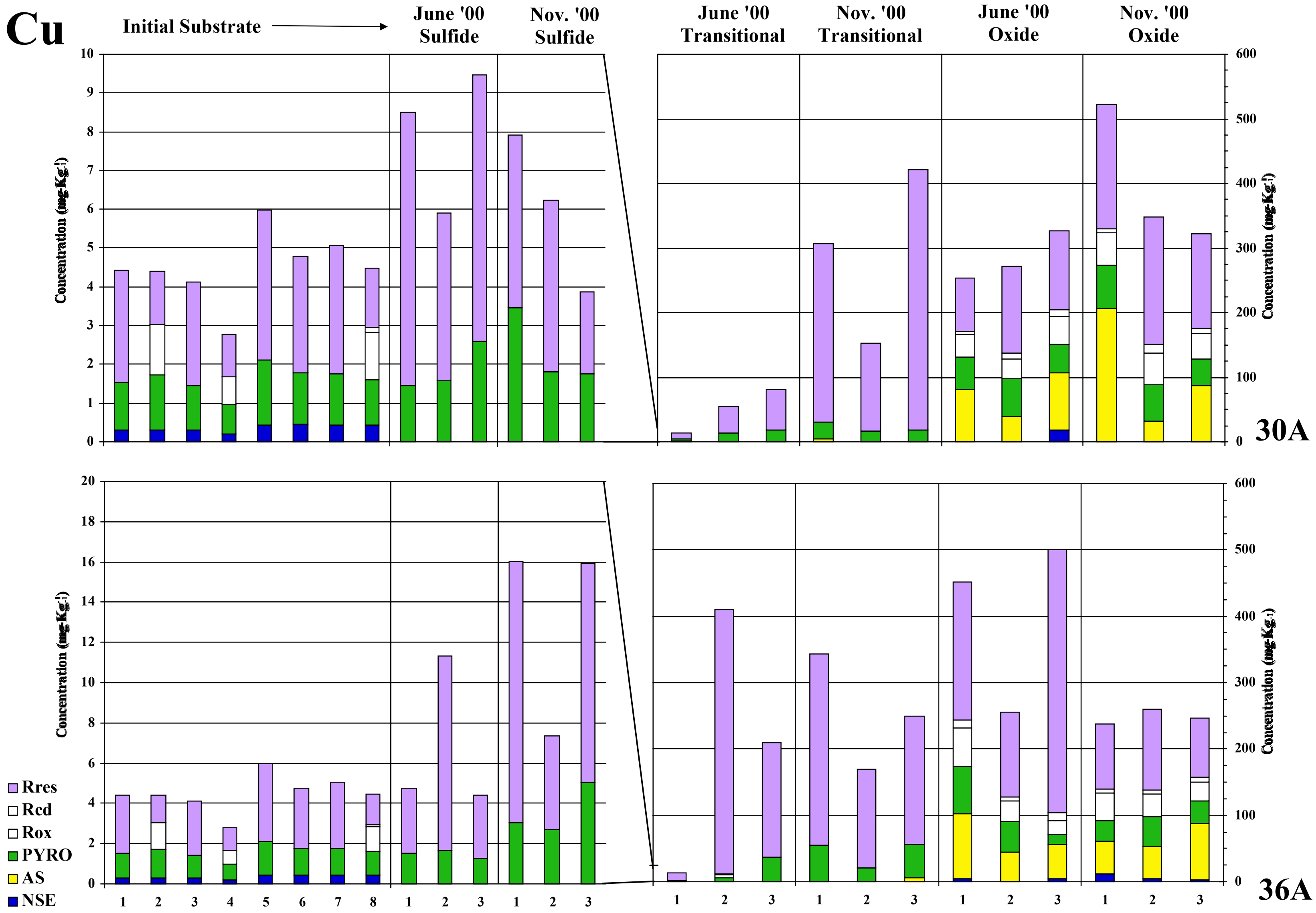
Cu
Initial Substrate
June '00 Sulfide
Nov. '00 Sulfide
June '00 Transitional
Nov. '00 Transitional
June '00 Oxide
Nov. '00 Oxide
Concentration (mg·Kg⁻¹)
0
1
2
3
4
5
6
7
8
9
10
0
100
200
300
400
500
600
30A
0
2
4
6
8
10
12
14
16
18
20
36A
1
2
3
4
5
6
7
8
Rres
Rcd
Rox
PYRO
AS
NSE

Figure 4.7c

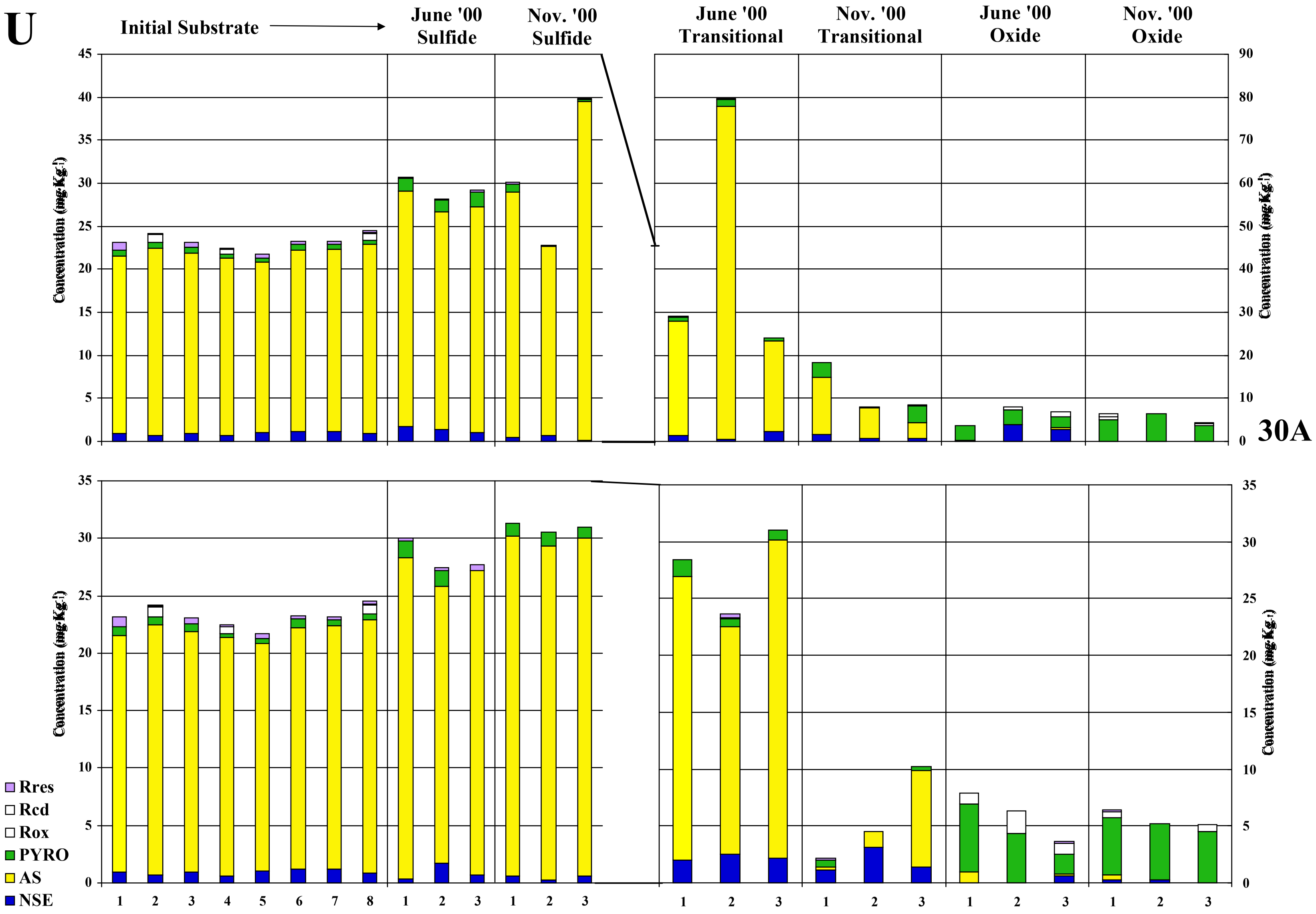
U
30A
Initial Substrate
June '00 Sulfide
Nov. '00 Sulfide
June '00 Transitional
Nov. '00 Transitional
June '00 Oxide
Nov. '00 Oxide
Concentration (mg Kg-1)
0
5
10
15
20
25
30
35
40
45
0
10
20
30
40
50
60
70
80
90
0
5
10
15
20
25
30
35
1
2
3
4
5
6
7
8
1
2
3
Rres
Rcd
Rox
PYRO
AS
NSE

Figure 4.7d

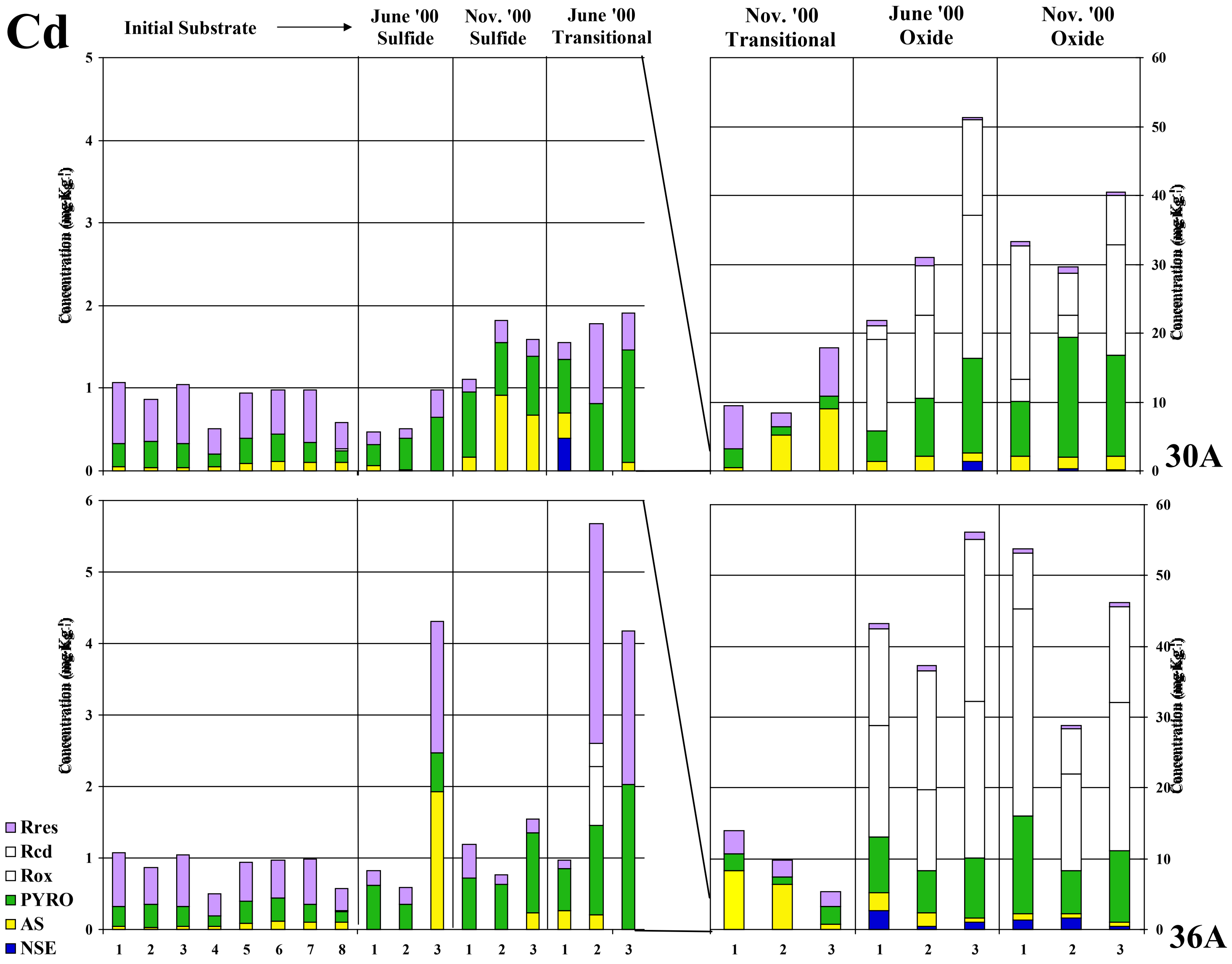
Cd
Initial Substrate
June '00 Sulfide
Nov. '00 Sulfide
June '00 Transitional
Nov. '00 Transitional
June '00 Oxide
Nov. '00 Oxide
Concentration (mg Kg-1)
0
1
2
3
4
5
6
10
20
30
40
50
60
30A
36A
1
2
3
4
5
6
7
8
Rres
Rcd
Rox
PYRO
AS
NSE

Figure 4.7e

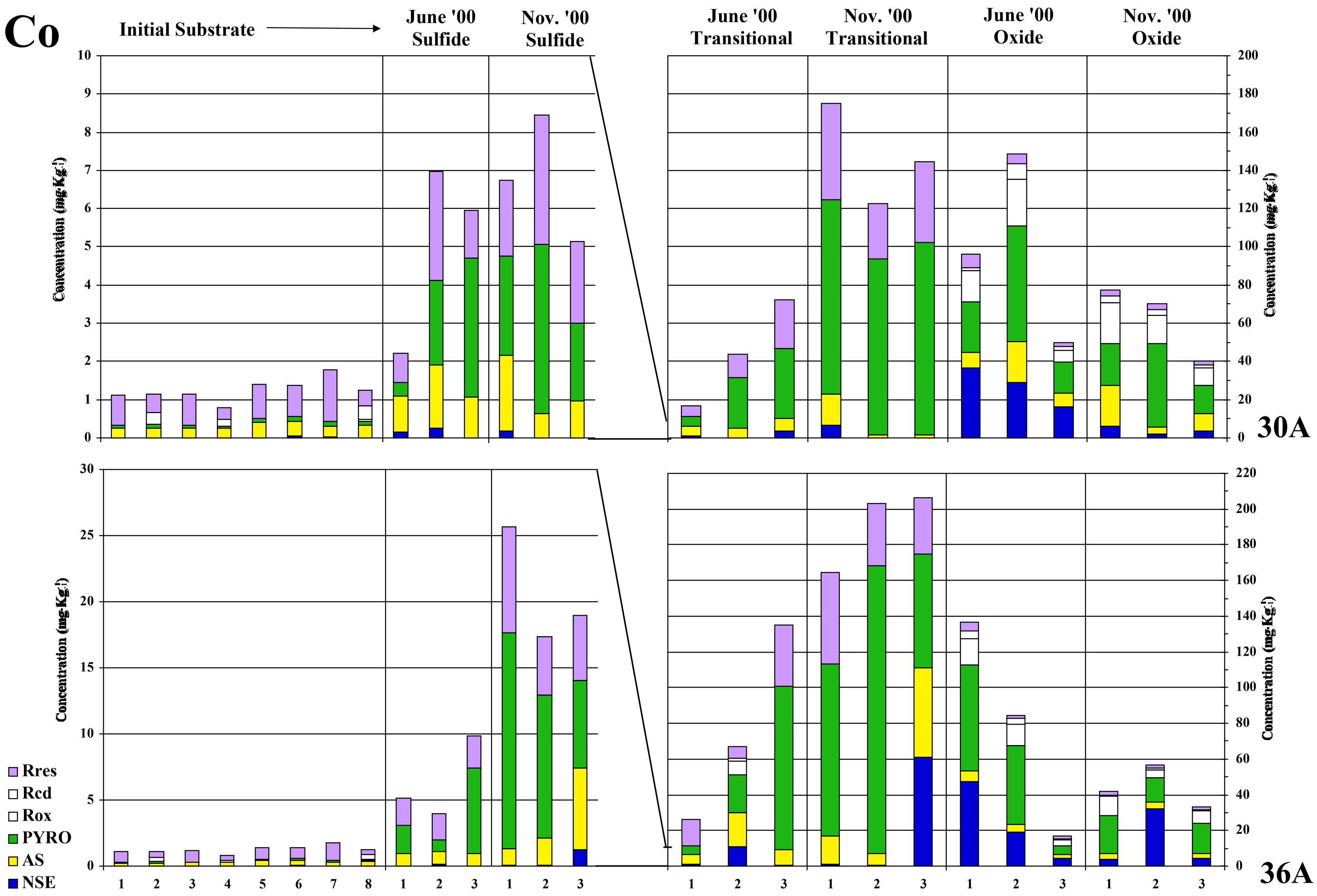
Co
Initial Substrate
June '00 Sulfide
Nov. '00 Sulfide
June '00 Transitional
Nov. '00 Transitional
June '00 Oxide
Nov. '00 Oxide
Concentration (mg·Kg⁻¹)
30A
36A
0
1
2
3
4
5
6
7
8
9
10
20
40
60
80
100
120
140
160
180
200
15
25
30
220
Rres
Rcd
Rox
PYRO
AS
NSE

Figure 4.7f

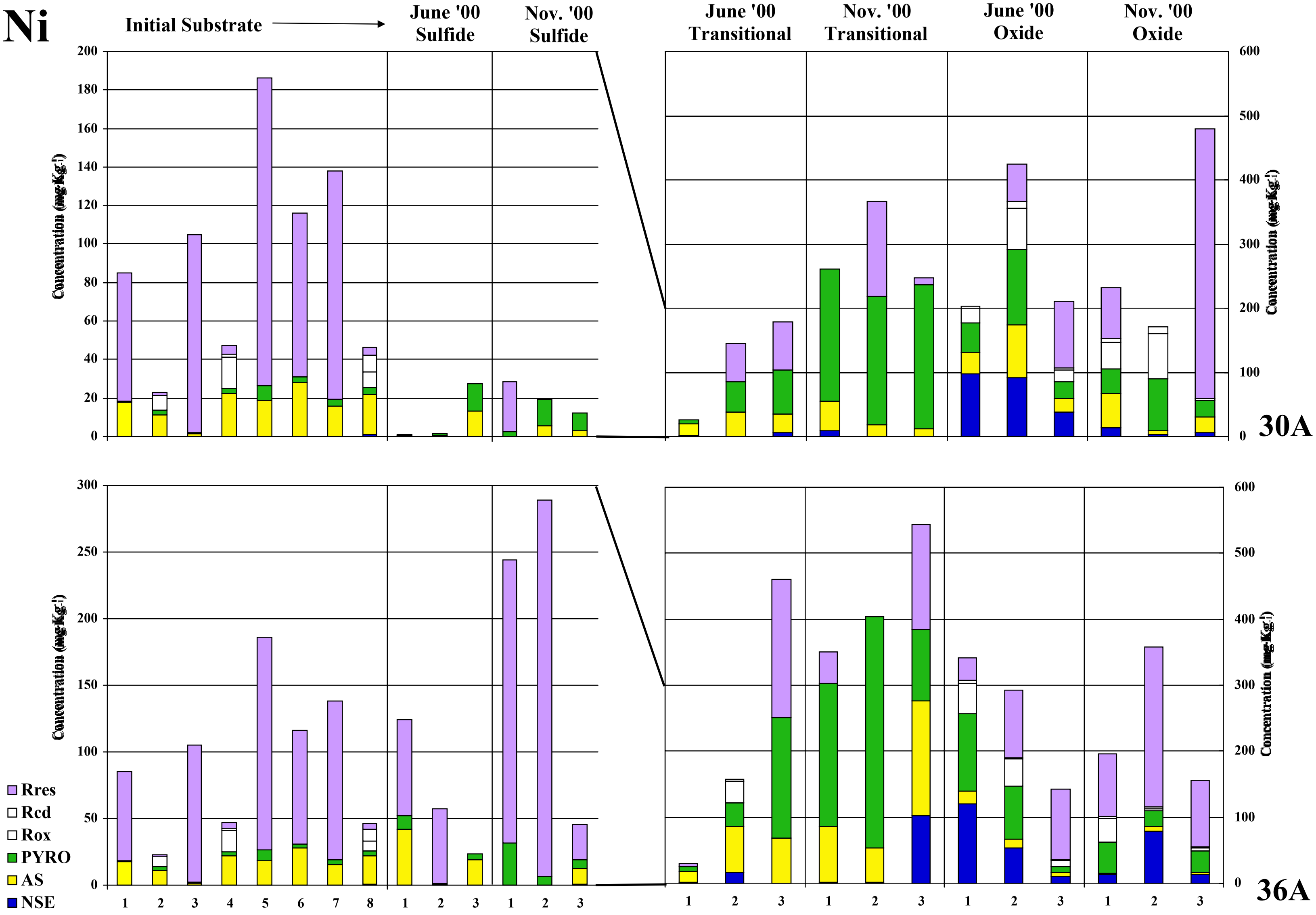
Ni
Initial Substrate
June '00 Sulfide
Nov. '00 Sulfide
June '00 Transitional
Nov. '00 Transitional
June '00 Oxide
Nov. '00 Oxide
30A
36A
Concentration (mg Kg-1)
0
20
40
60
80
100
120
140
160
180
200
0
50
100
150
200
250
300
0
100
200
300
400
500
600
1
2
3
4
5
6
7
8
Rres
Rcd
Rox
PYRO
AS
NSE

Figure 4.7g

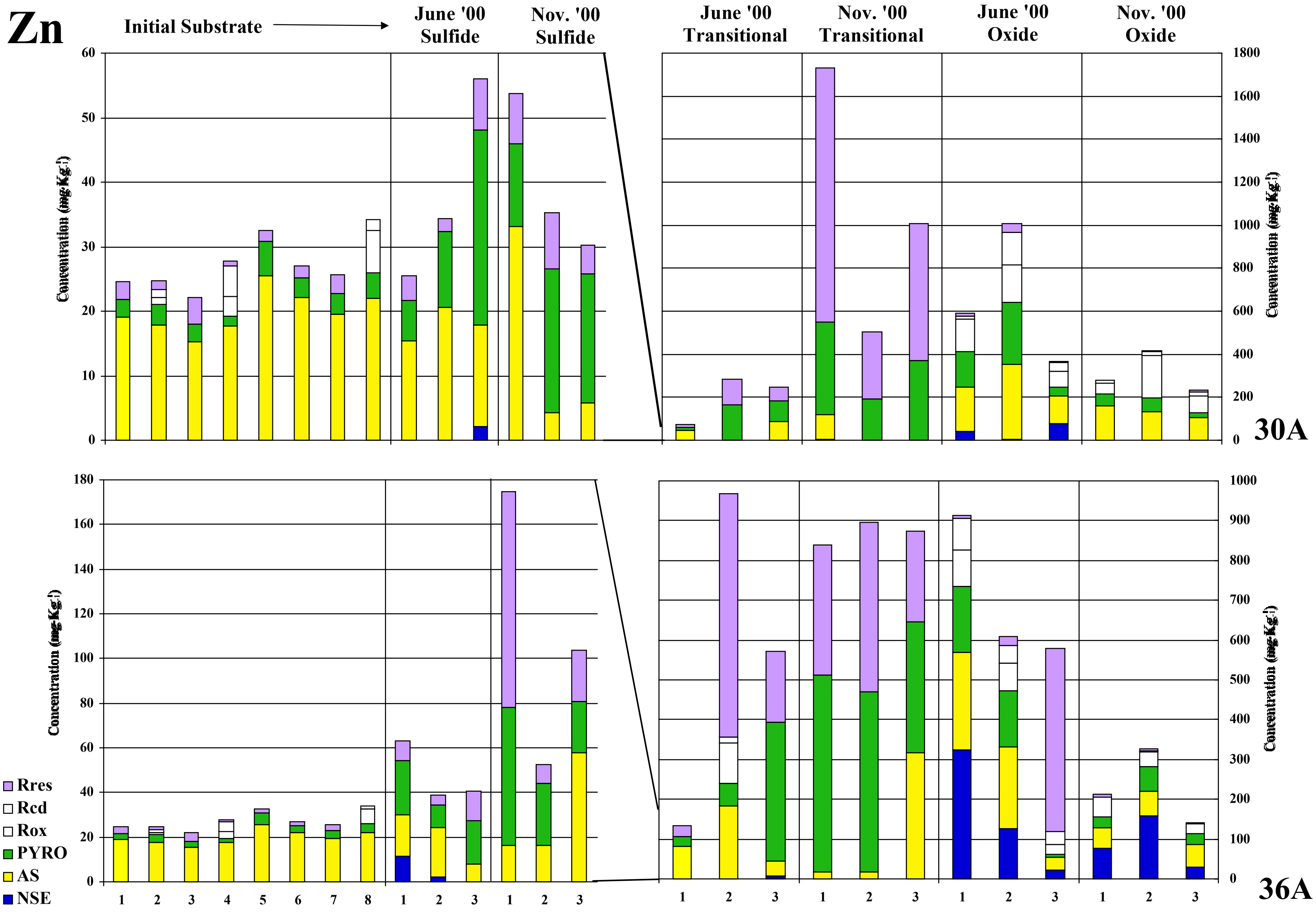
Zn
Initial Substrate
June '00 Sulfide
Nov. '00 Sulfide
June '00 Transitional
Nov. '00 Transitional
June '00 Oxide
Nov. '00 Oxide
Concentration (mg Kg-1)
0
10
20
30
40
50
60
0
200
400
600
800
1000
1200
1400
1600
1800
30A
0
20
40
60
80
100
120
140
160
180
0
100
200
300
400
500
600
700
800
900
1000
36A
1
2
3
4
5
6
7
8
1
2
3
1
2
3
1
2
3
1
2
3
1
2
3
1
2
3
Rres
Rcd
Rox
PYRO
AS
NSE

Figure 4.7h

Figure 4.8. Photographs of the tank influent orifice showing iron oxyhydroxide crust precipitated at pH ~2.4. These low pH iron oxyhydroxides crusts may have played a significant role in the sorption and retention of arsenic from the influent ARD.

CHAPTER 5

CONCLUSIONS

One of the main limitations to passive treatment of net acidic ARD (i.e. proton acidity + mineral acidity > alkalinity) is the ability of treatment systems to generate sufficient alkalinity to completely neutralize the influent acidity. While influent proton acidity is commonly neutralized within a typical limestone-based passive system, the system is generally designed to permit mineral acidity to pass through unaffected. Because <15% of the total acidity in ARD related to coal mining is attributed to proton acidity (Hedin et al., 1994), by design, the majority of the influent acidity must be neutralized *ex situ* through oxidation and hydrolysis of ferrous iron in an aerobic wetland.

Results from this study show that by treating fully oxidized (i.e. ferric » ferrous iron) ARD in a passive treatment system amended with a limestone-buffered organic substrate (LBOS), >97% of the influent acidity can be neutralized *in situ* and an alkaline effluent maintained. Mineral acidity (as dissolved ferric iron and aluminum) was removed above a limestone dissolution front. The precipitation of iron and aluminum concomitant with limestone dissolution buffers the pore water pH (<4.5) at a level conducive for rapid limestone dissolution and subsequent alkalinity generation. Thus, the ferric iron – aluminum hydrolysis and precipitation process is one of the key mechanisms of acid neutralization in the upper LBOS, because it essentially converts all of the mineral acidity to proton acidity above the limestone dissolution front. If the ferrous iron component of the ARD used in this study had been larger, then the level of alkalinity attained could not have been realized.

Moreover, the LBOS allows for the near permanent removal of iron and aluminum from low pH ferric iron-dominated ARD if the system is properly monitored and decommissioned in a timely manner. Iron was removed as both oxyhydroxides and sulfides; fine-grained iron sulfides were likely transient while the oxyhydroxides were possibly more a permanent removal phase. The circumneutral pH below the limestone dissolution front assured that aluminum removal was complete. However, when the limestone dissolution front moves completely through the substrate, a pulse of aluminum is expected, after which aluminum will no longer be retained.

Few studies of passive treatment systems have addressed trace element removal during acid neutralization, although elevated levels of some trace elements are commonly encountered in coal-related ARD (e.g., As, Cd, Co, Cr, Cu, Ni, Zn). Results from this study show that, for the practical purpose of implementing LBOS to treat low pH, ferric iron-dominated ARD, high trace element removal efficiency can be expected as long as the limestone dissolution front does not pass completely through the substrate. With the exception of uranium, trace metal attenuation largely occurs above the limestone dissolution front in the transitional and oxide zones. Trace metal removal is facilitated through sorption to primary organic matter and secondary hydrous iron and aluminum precipitates. With the exception of arsenic, iron oxyhydroxide is apparently not a major sorbent for trace element removal once the pH in the oxide zone drops below 3.8. Thus, trace element sorption is controlled by either organic matter or aluminum hydroxysulfate and the dominant sorbent is trace element specific.

Results from this study show that all trace elements sequestered at pH > 3.3 are subject to remobilization as the pH decreases over time, although the degree of mobilization is trace element-dependent. These remobilized trace elements coupled with influent concentrations may accumulate in solution at the pH-dependent point of maximum mobility. If the LBOS continues to receive ARD after the limestone dissolution front passes completely through the substrate, dissolved trace elements (with the exception of arsenic) will be released in the effluent as the pH drops to influent levels and at concentrations potentially orders of magnitude higher than the influent concentration.

REFERENCES

American Public Health Association. (1998) *Standard Methods for the Examination of Water and Wastewater*. APHA.

Anderson M. A. (1990) A Hydrogeochemical Investigation of Metalliferous Coal Pile Runoff and Its Interaction with Soil and Groundwater. Ph.D., Virginia Polytechnic Institute and State University.

Anderson M. A., Bertsch P. M., Feldman S. B., and Zelazny L. W. (1991) Interactions of acidic metal-rich coal pile runoff with a subsoil. *Environ. Sci. Technol.* **25**(12), 2038-2046.

Banks R. S. (1977) Stratigraphy of the Eocene Santee Limestone in three quarries of the Coastal Plain of South Carolina. *South Carolina Geological Survey Geological Notes* **21**(3), 88 - 149.

Barton P. and Vatanatham T. (1976) Kinetics of limestone neutralization of acid waters. *Environ. Sci. Technol.* **10**(3), 262-266.

Bascomb C. L. (1968) Distribution of pyrophosphate-extractable iron and organic carbon in soils of various groups. *Journal of Soil Science* **19**(2), 251 - 268.

Blowes D. W. and Jambor J. L. (1990) The pore-water chemistry and the mineralogy of the vadose zone of sulfide tailings, Waite Amulet, Quebec. *Applied Geochemistry* **5**, 327 - 346.

Blowes D. W. and Ptacek C. J. (1994) Acid-neutralization mechanisms in inactive mine tailings. In *The Environmental Geochemistry of Sulfide Mine-Wastes, Short*

Course Handbook, Vol. 22 (ed. J. L. Jambor and D. W. Blowes), pp. 271 - 292. Mineralogical Association of Canada.

Booth J., Hong Q., Compton R. G., Prout K., and Payne R. M. (1997) Gypsum overgrowths passivate calcite to acid attack. *Journal of Colloid and Interface Science* **192**, 207 - 214.

Canfield D. E., Raiswell R., and Bottrell S. (1992) The reactivity of sedimentary iron minerals toward sulfide. *American Jounral of Science* **292**, 659-683.

Carignan R. (1984) Interstitial water sampling by dialysis: Methodoligical notes. *Limnol. Oceanogr.* **29**(3), 667-670.

Carignan R., Rapin F., and Tessier A. (1985) Sediment porewater sampling for metal analysis: A comparison of techniques. *Geochimica Cosmochimica et Acta* **49**, 2493-2497.

Chou L., Garrels R. M., and Wollast R. (1989) Comparative study of the kinetics and mechanisms of dissolution of carbonate minerals. *Chemical Geology* **78**, 269-282.

Clark S. B., Johnson W. H., Malek M. A., Serkiz S. M., and Hinton T. G. (1996) A comparison of sequential extraction techniques to estimate geochemical controls on the mobility of fission product, actinide and heavy metal contamination in soils. *Radiochimica Acta* **74**, 173 - 179.

Cornwell J. C. and Morse J. W. (1987) The characterization of iron sulfide minerals in anoxic marine sediments. *Marine Chemistry* **22**, 193 - 206.

Cravotta III C. A. and Trahan M. K. (1999) Limestone drains to increase pH and remove dissolved metals from acidic mine drainage. *Applied Geochemistry* **14**, 581 - 606.

Davis J. A. (1984) Complexation of trace metals by adsorbed natural organic matter. *Geochimica Cosmochimica et Acta* **48**, 679 - 691.

Demchak J., Morrow T., and Skousen J. (2001) Treatment of acid mine drainage by vertical flow wetlands in Pennsylvania. *Geochemistry: Exploration, Environment, and Analysis* **1**, 71-80.

Dietz J. M. and Stidinger D. M. (1996) Acidic mine drainage abatement in an anaerobic sub-surface flow wetland environment - case history of the treatment system at Corsica, PA. *Proceedings of the 13th Annual National Meeting of the American Society of Surface Mining and Reclamation*, 531-540.

Dubrovsky N. M. (1986) Geochemical evolution of inactive pyritic tailings in the Elliot Lake uranium district. Ph.D., University of Waterloo.

Dvorak D. H., Hedin R. S., Edenborn H. M., and McIntire P. E. (1992) Treatment of metal-contaminated water using bacterial sulfate reduction: results from pilot-scale reactors. *Biotechnol. Bioeng.* **40**, 609-616.

Dzombak D. A. and Morel F. M. M. (1990) *Surface Complexation Modeling - Hydrous Ferric Oxide*. John Wiley and Sons.

Eger P. (1992) The use of sulfate reduction to remove metals from acid mine drainage. *Proceedings of the 9th Annual National Meeting of the American Society of Surface Mining and Reclamation*, 563-578.

Ehrlich H. L. (1990) *Geomicrobiology*. Marcel Dekker.

Evangelou V. P. (1995) *Pyrite Oxidation and Its Control*. CRC Press.

Fraser D. C. (1961) Organic sequestration of copper. *Economic Geology* **56**, 1063 - 1078.

Fuller C. C. and Davis J. A. (1987) Processes and kinetics of Cd^{2+} sorption by a calcareous aquifer sand. *Geochimica Cosmochimica et Acta* **51**(6), 1491 - 1502.

Garrett Jr. W. E., Bartolucci A. A., and Vermace M. E. (2001) Constructed wetland research for the treatment of the Plant Gorgas coal pile runoff. *Proceedings of the 18th Annual National Meeting of the American Society of Surface Mining and Reclamation*, 558-568.

Gusek J. (1998) Three case histories of passive treatment of metal mine drainage. *Proceedings of the 19th Annual West Virginia Surface Mine Drainage Task Force Symposium*.

Hedin R. S., Nairn R. W., and Kleinmann R. L. P. (1994a) Passive treatment of coal mine drainage, pp. 35. US Dept. of Interior, Bureau of Mines.

Hedin R. S. and Watzlaf G. R. (1994) The effects of anoxic limestone drains on mine water chemistry. *Proc. Int. Land Reclamation and Mine Drainage Conference and Third Int. Conference on the Abatement of Acidic Drainage*, 185-194.

Hedin R. S., Watzlaf G. R., and Nairn R. W. (1994b) Passive treatment of acid mine drainage with limestone. *J. Environ. Qual.* **23**, 1338-1345.

Hellier W. W. (1996) The Bark Camp Run constructed wetlands: Findings and recommendations for future design criteria. *Proceedings of the 13th Annual National Meeting of the American Society of Surface Mining and Reclamation.*, 550-559.

Hem J. D. (1992) *Study and interpretation of the chemical characteristics of natural water*. U.S. Geol. Surv. Water Supply Paper 2254.

Herlihy A. T., Kaufmann P. R., Mitch M. E., and Brown D. D. (1990) Regional estimates of acid mine drainage impact on streams in the mid-Atlantic and southeastern United States. *Water Air Soil Pollution* **50**, 91 - 107.

Hesslein R. H. (1976) An in situ sampler for close interval pore water studies. *Limnol. Oceanogr.* **21**, 912-914.

Huerta-Diaz M. A., Carignan R., and Tessier A. (1993) Measurement of trace metals associated with acid volatile sulfides and pyrite in organic freshwater sediments. *Environmental Science and Technology* **27**, 2367 - 2372.

Huerta-Diaz M. A. and Morse J. W. (1992) Pyritization of trace metals in anoxic marine sediments. *Geochimica Cosmochimica et Acta* **56**, 2681 - 2702.

Huerta-Diaz M. A., Tessier A., and Carignan R. (1998) Geochemistry of trace metals associated with reduced sulfur in freshwater sediments. *Applied Geochemistry* **13**, 213 - 233.

Hyman D. M. and Watzlaf G. R. (1995) Mine Drainage Characterization for the Successful Implementation of Passive Treatment Systems. *17th Annual National Association of Abandoned Mine Lands Conference*, 170 - 185.

Hyman D. M. and Watzlaf G. R. (1997) Metals and Other Components of Coal Mine Drainage as Related to Aquatic Life. *National Meeting of the American Society of Surface Mining and Reclamation*.

Ineson P. R. (1989) *Introduction to Practical Ore Microscopy*. Wiley & Sons.

Jage C. R., Zipper C. E., and Hendricks A. C. (2000) Factors affecting performance of successive alkalinity-producing systems. *Proceedings of the 17th Annual National Meeting of the American Society of Surface Mining and Reclamation.*, 451-458.

Jarvis S. C. (1985) Forms of aluminum in some acid permanent grassland soils. *Journal of Soil Science* **37**, 211 - 222.

Jenne E. A. (1968) Controls on Mn, Fe, Co, Ni, Cu, and Zn concentrations in soils and water: the significant role of hydrous Mn and Fe oxides. In *Trace Inorganics in Water*, Vol. 73 (ed. R. F. Gould), pp. 337 - 387. American Chemical Society.

Jurjovec J., Ptacek C. J., and Blowes D. W. (2002) Acid neutralization mechanisms and metal release in mine tailings: A laboratory column experiment. *Geochimica Cosmochimica et Acta* **66**(9), 1511 - 1523.

Kennedy L. G., Everett J. W., Ware K. J., Parsons R., and Green V. (1998) Iron and sulfur mineral analysis methods for natural attenuation assessments. *Bioremediation Journal* **2**, 259-276.

Kepler D. A. and McCleary E. C. (1994) Successive alkalinity-producing systems (SAPS) for the treatment of acidic mine drainage. *Proc. Int. Land Reclamation and Mine Drainage Conference and Third Int. Conference on the Abatement of Acidic Drainage*, 195-204.

Kinniburgh D. G. and Jackson M. L. (1981) Cation adsorption by hydrous metal oxides and clay. In *Adsorption of Inorganics at Solid-Liquid Interfaces* (ed. M. A. Anderson and A. J. Rubin), pp. 91 - 160. Ann Arbor Science.

Kinniburgh D. G., Jackson M. L., and Syers J. K. (1976) Adsorption of alkali earth, transition, and heavy metal cations by hydrous oxide gels of iron and aluminum. *Soil Science Society of America Journal* **40**, 796 - 799.

Kleinmann R. L. P. (1990) Acid mine drainage in the United States. *Proceedings of the First Midwestern Region Reclamation Conference*.

Kleinmann R. L. P., Hornberger R., Leavitt B., and Hyman D. (2000) Introduction and recommendations. In *Prediction of Water Quality at Surface Coal Mines* (ed. R. L. P. Kleinmann), pp. 1-7. National Mine Land Reclamation Center.

Koch A. L. (1994) Growth Measurement: Most Probable Numbers. In *Methods for General and Molecular Bacteriology* (ed. P. Gerhardt, R. G. E. Murray, W. A. Wood, and N. R. Krieg), pp. 257 - 260. American Society for Microbiology.

Langmuir D. (1997) *Aqueous Environmental Geochemistry*. Prentice Hall.

Lee J.-S., Lee B.-G., Luoma S. N., Choi H. J., Koh C.-H., and Brown C. L. (2000) Influence of acid volatile sulfides and metal concentrations on metal partitioning in contaminated sediments. *Environmental Science and Technology* **34**, 4511 - 4516.

Makos J. D. and Hrncir D. C. (1995) Chemistry of Cr(VI) in a constructed wetland. *Environmental Science and Technology* **29**, 2414 - 2419.

May H. M. and Nordstrom D. K. (1991) Assessing the solubilities and reaction kinetics of aluminous minerals in soils. In *Soil Acidity* (ed. B. Ulrich and M. E. Sumner), pp. 125 - 148. Springer-Verlag.

McBride M. B. (1994) *Environmental Chemistry of Soils*. Oxford University Press.

McLaren R. G. and Crawford D. V. (1973) Studies on soil copper I. The fractionation of copper in soils. *Journal of Soil Science* **24**(2), 172 - 181.

Miller W. P., Martens D. C., and Zelazny L. W. (1986) Effect of Sequence in the extraction of trace metals from soils. *Soil Science Society of America Journal* **50**(3), 598 - 601.

Millings V. E. (1999) Stable isotopes as groundwater tracers at the D-Area Coal Pile Runoff Basin of the Savannah River Site, Aiken, SC. MS, University of Georgia.

Morin K. A., Cherry J. A., Dave N. K., Lim T. P., and Vivyurka A. J. (1988) Migration of acidic groundwater seepage from uranium-tailings impoundments, 1. Field study and conceptual hydrogeochemical model. *Journal of Contaminant Hydrology* **2**, 271 - 303.

Nairn R. W., Mercer M. N., and Lipe S. A. (2000) Alkalinity generation and metals retention in vertical-flow treatment wetlands. *Proceedings of the 17th Annual National Meeting of the American Society of Surface Mining and Reclamation.*, 412-420.

Nash J. T., Granger H. C., and Adams S. S. (1981) Geology and concepts of genesis of important types of uranium deposits. *Economic Geology* **75th ann. vol**, 63 - 116.

Nordstrom D. K. and Alpers C. N. (1999) Geochemistry of acid mine waters. In *The Environmental Geochemistry of Mineral Deposits, Part A: Processes, Techniques, and Health Issues*, Vol. 6A, pp. 133 - 160. Society of Economic Geologists.

Ong H. L. and Swanson V. E. (1966) Adsorption of copper by peat. lignite, and bituminous coal. *Economic Geology* **61**, 1214 - 1231.

Papp C. S. E., Filipek L. H., and Smith K. S. (1991) Selectivity and effectiveness of extractants used to release metals associated with organic matter. *Applied Geochemistry* **6**, 349 - 353.

Phipps T. T., Fletcher J. J., Fiske W., and Skousen J. G. (1991) A methodology for evaluating the costs of alternative AMD treatment systems. *Proceedings of the 12th Annual West Virginia Surface Mine Drainage Task Force Symposium*.

Plummer L. N., Wigley T. M. L., and Parkhurst D. L. (1978) The kinetics of calcite dissolution in CO_2-water systems at 5° to 60°C and 0.0 to 1.0 ATM CO_2. *American Journal of Science* **278**, 179-216.

Plummer L. N., Wigley T. M. L., and Parkhurst D. L. (1979) Critical review of the kinetics of calcite dissolution and precipitation. In *Chemical Modeling in Aqueous Systems - Speciation, Sorption, Solubility, and Kinetics*, Vol. 93 (ed. E. A. Jenne), pp. 537-573. Am. Chem. Soc. Symp. Ser. 93.

Powell J. D. (1988) Origin and influence of coal mine drainage on streams of the United States. *Environ. Geol. Water Sci.* **11**, 141 - 152.

Raiswell R., Canfield D. E., and Berner R. A. (1994) A comparison of iron extraction methods for the determination of degree of pyritisation and the recognition of iron-limited pyrite formation. *Chemical Geology* **111**, 101 - 110.

Ramdohr P. (1980) *The Ore Minerals and their Intergrowths*. Pergamon Press.

Rickard D. T. (1974) Kinetics and mechanism of the sulfidation of goethite. *American Jounral of Science* **274**, 941-952.

Robbins E. I., G.L. Nord J., Savela C. E., Eddy J. I., Livi K. J. T., Gullett C. D., Nordstrom D. K., Chou I.-M., and Briggs K. M. (1996) Microbial and mineralogical analysis of aluminum-rich precipitates that occlude porosity in a failed anoxic limestone drain, Monongalia County, West Virginia. *Thirteenth Annual International Pittsburgh Coal Conference*, 761-767.

Romanek C. S. (1991) Carbon isotope fractionation and precipitation kinetics of synthetic aragonite and calcite grown in dilute solutions. Dissertation, Texas A&M University.

Rose A. W. (1999) Chemistry and kinetics of calcite dissolution in passive treatment systems. *Proceedings of the 16th Annual National Meeting of the American Society of Surface Mining and Reclamation.*, 599-608.

Rose A. W. and Cravotta III C. A. (1998) Geochemistry of Coal Mine Drainage. In *Coal Mine Drainage Prediction and Pollution Prevention in Pennsylvania* (ed. K. B. C. Brady, M. W. Smith, and J. Schueck), pp. 1-1 to 1-22. The Pennsylvania Department of Environmental Protection.

Sass B. M. a. D. R. (1987) Solubility of amorphous chromium(III)-iron(III) hydroxide solid solutions. *Inorganic Chemistry* **26**, 2228 - 2232.

Saunders J. A., Cook R. B., Thomas R. C., and Crowe D. E. (1996) Coprecipitation of trace metals in biogenic pyrite: Implications for enhanced intrinsic bioremediation. In *Proceedings of the 4th International Symposium on the Geochemistry of the Earth's Surface* (ed. S. H. Bottrell), pp. 470-474.

Saunders J. A., Thomas R. C., Lee M.-K., and Wolf L. (1997) Geologic evidence for the utility of using sulfate reducing bacteria for in situ anaerobic bioremediation of heavy-metal contaminated groundwater. In *Proceedings of the 4th International Symposium on In Situ and On Site Bioremediation*, Vol. v. 5, pp. 583-588. Battelle Press.

Schwertmann U. and Cornell R. M. (2000) *Iron Oxides in the Laboratory*. Wiley-VCH.

Skousen J., Rose A., Geidel G., Foreman J., Evans R., and Hellier W. (1998) *A Handbook of Technologies for the Avoidance and Remediation of Acid Mine Drainage*. Acid Drainage Technology Initiative (ADTI).

Smith K. S. (1999) Metal sorption on mineral surfaces - An overview with examples relating to mineral deposits. In *The Environmental Geochemistry of Mineral Deposits, Part A: Processes, Techniques, and Health Issues*, Vol. 6A (ed. G. S. Plumlee and M. K. Logsdon), pp. 161 -182. Society of Economic Geologists.

Smith K. S., Ranville J. F., Plumlee G. S., and Macalady D. L. (1998) Predictive double-layer modeling of metal sorption in mine-drainage systems. In *Adsorption of Metals by Geomedia* (ed. E. A. Jenne), pp. 521 - 547. Academic Press.

Sobek A. A., Schuller W. A., Freeman J. R., and Smith R. M. (1978) Field and laboratory methods applicable to overburdens and minesoils, pp. 203. U.S. Gov. Print. Office.

Sobolewski A. (1999) A review of processes responsible for metal removal in wetlands treating contaminated mine drainage. *International Journal of Phytoremediation* **1**(1), 19 - 51.

Stanton M. R. and Goldhaber M. B. (1991) An experimental study of goethite sulfidation - Relationships to the diagnesis of iron and sulfur. In *Geochemical, Biogeochemical, and Sedimentological Studies of the Green River Formation, Wyoming, Utah, and Colorado* (ed. M. L. Tuttle). U.S. Geological Survey Bulletin 1973E.

Sterner P., Skousen J., and Donovan J. (1998) Geochemistry of laboratory anoxic limestone drains. *Proceedings of the 15th Annual National Meeting of the American Society of Surface Mining and Reclamation*, 214-234.

Stumm W. and Morgan J. J. (1981) *Aquatic Chemistry*. John Wiley & Sons.

Szalay A. (1964) Cation ion exchange properties of humic acids and their importance in the geochemical enrichment of UO_2^{++} and other cations. *Geochimica Cosmochimica et Acta* **28**, 1605 - 1614.

Thomas R. C., Romanek C. S., Coughlin D. P., and Crow D. E. (1999) Treatment of acid mine drainage using anaerobic constructed treatment wetlands: predicting longevity with substrate neutralization potential. *Proceedings Sudbury '99 - Mining and the Environment II*, 449-458.

To T. B., Nordstrom D. K., Cunningham K. M., Ball J. W., and McCleskey R. B. (1999) New method for the direct determination of dissolved Fe(III) concentration in acid mine waters. *Environ. Sci. Technol.* **33**(5), 807-813.

Turner D. and McCoy D. (1990) Anoxic alkaline drain treatment system, a low cost acid mine drainage treatment alternative. *Proc. 1990 Nat. Symp. on Mining*, 73-75.

U.S. Code of Federal Regulations. (1991) Title 40 -- Protection of the Environment; Chapter I -- Environmental Protection Agency; Subchapter N -- Effluent Guidelines and Standards; Part 434 - Coal mining point source category; July 1.

Walton-Day K. (1999) Geochemistry of the processes that attenuate acid mine drainage in wetlands. In *The Environmental Geochemistry of Mineral Deposits, Part A: Processes, Techniques, and Health Issues*, Vol. 6A (ed. G. S. Plumlee and M. K. Logsdon), pp. 215 - 228. Society of Economic Geologists.

Walton-Day K., Filipek L. H., and Papp C. S. E. (1990) Mechanisms controlling Cu, Fe, Mn, and Co profiles in peat of the Filson Creek Fen, northeastern Minnesota. *Geochimica Cosmochimica et Acta* **54**, 2933 - 2946.

Watzlaf G. R. (1997) Passive treatment of acid mine drainage in down-flow limestone systems. *Proceedings of the 14th Annual National Meeting of the American Society of Surface Mining and Reclamation.*, 611-622.

Watzlaf G. R. and Hedin R. S. (1993) A method for predicting the alkalinity generated by anoxic limestone drainage. *Proceedings of the 14th Annual West Virginia Surface Mine Drainage Task Force Symposium*.

Watzlaf G. R. and Hyman D. M. (1995) Limitations of Passive Systems for the Treatment of Mine Drainage. *17th Annual Association of Abandoned Mine Lands Conference*, 186-199.

Watzlaf G. R., Schroeder K. T., and Kairies C. (2000) Long-term performance of alkalinity-producing passive systems for the treatment of mine drainage. *Proceedings of the 17th Annual National Meeting of the American Society of Surface Mining and Reclamation.*, 262 - 274.

Watzlaf G. R., Schroeder K. T., Kleinmann R. L. P., Kairies C. L., and Nairn R. W. (2002) The passive treatment of coal mine drainage. *Workshop presented at the 2002 Annual National Meeting of the American Society of Mining and Reclamation.*

Wentzler T. H. and Aplan F. F. (1972) Kinetics of limestone dissolution by acid waters. In *Environmental Control* (ed. C. Rampacek), pp. 513 - 523. AIME.

Widdel F. (1988) Microbiology and Ecology of Sulfate- and Sulfur-Reducing Bacteria. In *Biology of Anaerobic Microorganisms* (ed. A. J. B. Zehnder), pp. 469-585. Wiley Interscience.

Widdel F. and Bak F. (1992) Gram-Negative Mesophilic Sulfate-Reducing Bacteria. In *The Prokaryotes*, Vol. IV (ed. A. Balows, H. G. Truper, M. Dworkin, W. Harder, and K.-H. Schleifer), pp. 3352 - 3378. Springer-Verlag.

Wildeman T., Brodie G., and Gusek J. (1993) *Wetland Design for Mining Operations*. BiTech Publishers Ltd.

Winger P. V. and Lasier P. J. (1991) A vacuum-operated pore-water extractor for estuarine and freshwater sediments. *Arch. Environ. Contam. Toxicol.* **21**, 321-324.

Ziemkiewicz P. F., Skousen J. G., Brant D. L., Sterner P. L., and Lovett R. J. (1997) Acid mine drainage treatment with armored limestone in open limestone channels. *Journal of Environmental Quality* **26**, 1017 - 1024.

Zipper C. E. and Jage C. R. (2001) Passive treatment of acid-mine drainage with vertical-flow systems, pp. 1-16. Powell River Project/Virginia Cooperative Extension.

APPENDIX A

PHYSICOCHEMISTRY OF INFLUENT AND EFFLUENT WATER

The following nine spreadsheets contain the weekly physicochemical data of the influent and effluent for the two years of the project. A single sample taken from the distribution manifold was used as the influent for all eight tanks. Effluent from each individual tank is also given. For various reasons, some data were occasionally not collected. These data have been designated "n/a" for "not analyzed" and are highlighted in light blue. In the case where cation concentrations were below the ICP-MS detection limits, an operationally-defined value, equal to the lower detection limit, was entered. These values are highlighted in light green. Sodium – Ammonium Acetate was added to tanks 2A, 24A, 30A, and 39A beginning on July 26, 2000. These values are in red.

The flow rate for each tank was collected weekly from the effluent standpipe using a graduate cylinder and stopwatch. At very low and very high flows, the rate generally had to be estimated. Estimated values for flow rate are highlighted in brown. Occasionally, there was no flow at the time of measurement. If the pipe was completely dry the rate was entered as zero. These values are highlighted in orange. If the pipe was wet, but no flow was measurable, a value of 0.005 $mL{\cdot}min^{-1}$ was entered. These values are highlighted in purple. The flow was increased to > 200 $mL{\cdot}min^{-1}$ on tanks 2A and 10A on October 10, 2000. These values are in blue. To view the spreadsheets, click on the link below:

Individual Tank Summary.xls

APPENDIX B

PHYSICOCHEMISTRY OF PORT PORE WATER DATA

Ports were installed at 23, 46, 69, and 92 centimeters in each tank. They were attached to 1.3-cm diameter, slotted PVC pipe that extended horizontally 72 cm into the organic layer. A “gravel packing” was created by placing a thin layer of very-coarse, clean quartz sand around the slotted PVC pipe. The packing was prevented clogging of the slotted PVC pipe and aided in the collection of a homogenized water sample across the port horizon.

Port samples were also collected weekly between April 2000 and November 2000. They were generally collected two days after the influent and effluent samples were taken. Ports were sampled progressively from top-down to minimize disturbance of unsampled ports due to draw-down during sampling. The tanks were paired into four groups and sampled on a weekly progressive rotation, such that all four ports on two tanks were sampled once every four weeks. This sampling strategy helped to minimize the development of preferential flow due to sampling.

However, despite these preventative measures core observations indicate that the ports may have been sampling along a preferential flow path that developed in the LBOS. The occurrence of a second orange layer adjacent to the gravel packing of the first port implied that preferential flow developed as a result of sampling the ports (Fig. B.1). It is likely that the preferential flow paths developed along the contact between the rigid walls of the tank and the LBOS substrate.

Once preferential flow paths were established the ports behaved in manner predicted by the migration of a reaction boundary (see Chapters 2 and 3). Therefore, while the port data are still valid, the changes in the LBOS pore water over time were recorded at an accelerated rate that was not representative of the development of the typical color zonation observed.

The following eight spreadsheets contain the physicochemical data of the pore water measured at the ports. For various reasons, some data were occasionally not collected. In particular, sulfide and alkalinity were not measured when the pH was < 4.5, because they are operationally defined as zero below this pH based on the methods employed for their determination (see Chapters 2 and 3). These data have been designated "n/a" for "not analyzed" and are highlighted in light blue. In the case where cation concentrations were below the ICP-MS detection limits, an operationally-defined value, equal to the lower detection limit, was entered. These values are highlighted in light green. Sodium – Ammonium Acetate was added to tanks 2A, 24A, 30A, and 39A beginning on July 26, 2000. These values are in red. The flow was increased to > 200 mL·min^{-1} on tanks 2A and 10A on October 10, 2000. These values are in blue. To view the spreadsheets, click on the link below:

Port Data.xls

Fig. B.1. Photograph of a core that intercepted the gravel packing of port #1. The formation of the second orange layer in the upper portions of the gravel packing indicates that preferential flow was bringing overlying ARD into the gravel packing. The pore water trends measured from the ports, therefore, are not representative of the three color reaction boundaries observed in all tanks, but are representative of the reactions that take place along a give flow path over time.

APPENDIX C

TOTAL DIGEST AND SEQUENTIAL EXTRACTION DATA

Total digest and sequential extractions were performed on core samples taken from the LBOS. Six cores were extracted from two tanks (30A and 36A; three from each tank) in June 2000. Another six cores were extracted from the two tanks in November 2000 (see Appendix D for schematic showing the sampling locations in tanks 30A and 36A). Total digest and sequential extraction data obtained from tank 30A and 36A core samples are presented in chapters 2,3, and 4. In addition to these data, total digests and sequential extractions were conducted on additional core samples taken from other tanks in December 2000. One core each was taken from tanks 2A, 13A, and 24A, while two cores were taken each from tanks 10A, 39A, and 44A.

All cores were divided into three sections based on the color reaction zones described in chapters 2,3, and 4. Samples were identified based on the tank number, then the core number, then the reaction zone, where “a” is oxide zone, “b” is the transitional zone, and “c” is the sulfide zone. For example, a sample with identification “44A-2a” is from tank 44A, the second core, the oxide zone.

The sequential extraction data is divided so that each extraction step is on a separate spreadsheet. Sequential extractions were conducted on damp samples. All values given have been back-calculated to $mg \cdot kg^{-1}$ dry weight of the sample. To view the spreadsheets, click on the link below:

Total Digest and Sequential Extraction Data

APPENDIX D

ELECTRON MICROPROBE IMAGES

Back-scatter electron microprobe images are presented in chapters 2, 3, and 4. In this appended section additional images are presented. Yellow arrows are used in all figures of this appended section to identify fine-grained pyrite (Py). Solids identified by green and blue arrows are identified in the figure captions. Fig. D.1 contains images of the initial LBOS. The main components of the initial substrate are organic fragments (OF), limestone (LS), and quartz (Qtz). Minor pyrite (Py) is also found, mainly associated with the limestone. Images of the oxide zone are presented in Fig. D.2. The oxide zone contains hydrous ferric iron compounds (HFO; mainly goethite and ferrihydrite, see chapter 3), organic fragments (OF), quartz (Qtz), and minor aluminum hydroxysulfate (Al-S). Images of the upper transitional zone are presented in Fig. D.3. The upper transitional zone contains organic fragments (OF), quartz (Qtz), minor HFO (proximal to the contact with the oxide zone), aluminum hydroxysulfate (Al-S), and pyrite (yellow arrows). Most of the initial limestone was dissolved from the upper transitional zone; however, the outline of former limestone grains is preserved by compounds that coated the limestone before it dissolved. These outlined grains are referred to as relict limestone grains (RLS; see chapters 2 and 3 for details). With depth limestone (LS) appears with increasing frequency. Images of the middle transitional zone are presented in Fig. D.4. In addition to the components identified in the upper transitional zone, the middle transitional zone contains abundant gypsum. Moreover, HFO is no longer present and framboidal pyrite is common. Images of the lower transitional zone are presented in Fig. D.5, while miscellaneous pictures from the transitional zone are presented in Fig. D.6. Finally, images of the sulfide zone are presented in Fig. D.7.

Figure D.1. Electron microprobe images of the initial LBOS. (A) Pyrite rimming limestone grain. Pyrite was occasionally observed with the initial limestone. (B) Pyrite found along fractures in the limestone grain shown in (A). (C) More pyrite rimming initial limestone. (D) Organic fragment with small limestone grains attached to the surface (all light colored material in the photograph is limestone). Also small limestone fossil shown at top. (E) Porous and vuggy fragment of fossiliferous limestone with fine-grained pieces of limestone in the vugs. Two pyrite framboids were identified in one of the vugs. (F) Close-up of the pyrite framboids identified in (E). (G) Limestone fragment with sub-rounded quartz inclusions, which in turn have pyrite inclusions. (H) Limestone grain with abundant sub-angular pyrite inclusions. (I) Limestone with minor associated pyrite. (J) Limestone fossil fragment showing abundant fine-grained limestone in cavities.

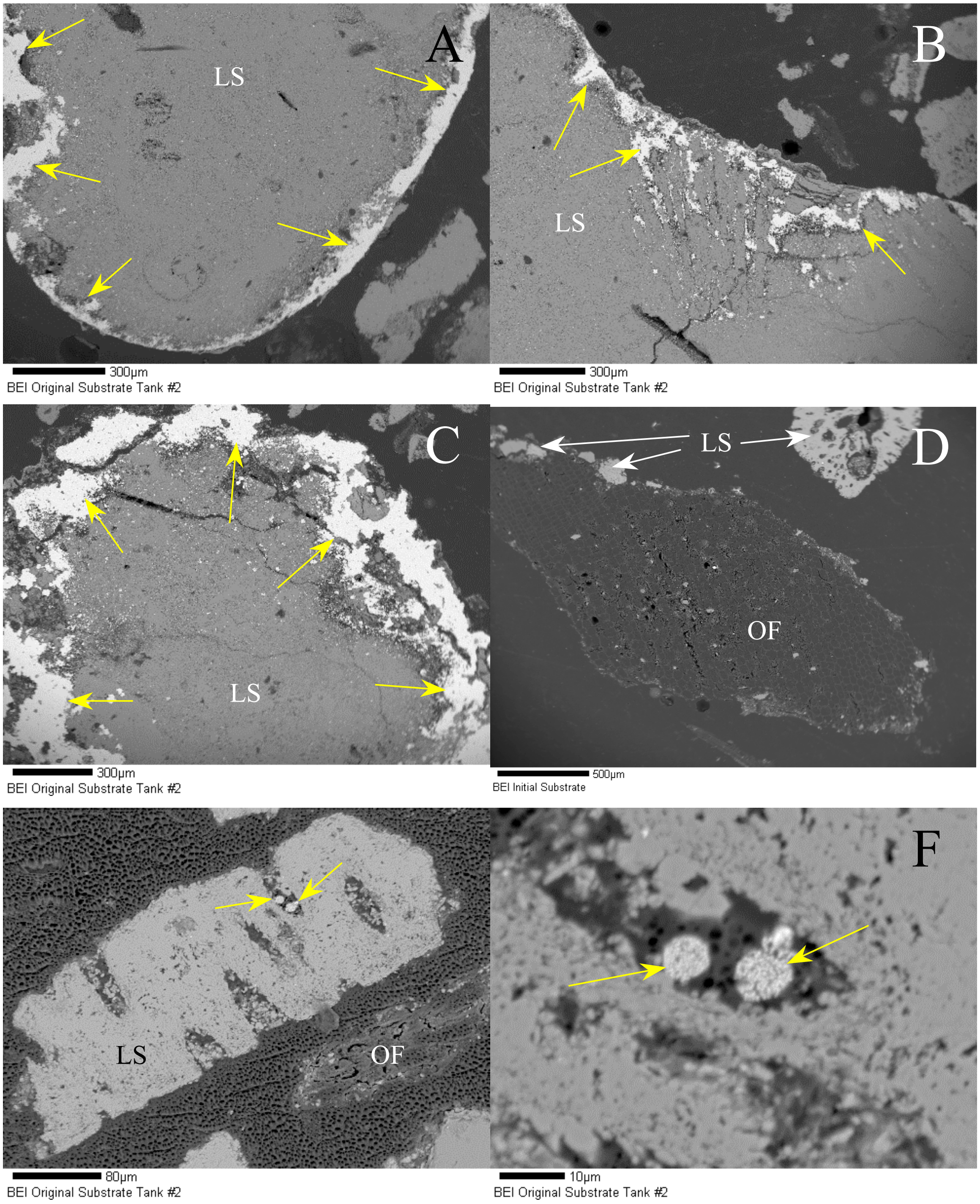
A
LS
300µm
BEI Original Substrate Tank #2
B
LS
300µm
BEI Original Substrate Tank #2
C
LS
300µm
BEI Original Substrate Tank #2
D
LS
OF
500µm
BEI Initial Substrate
LS
OF
80µm
BEI Original Substrate Tank #2
F
10µm
BEI Original Substrate Tank #2

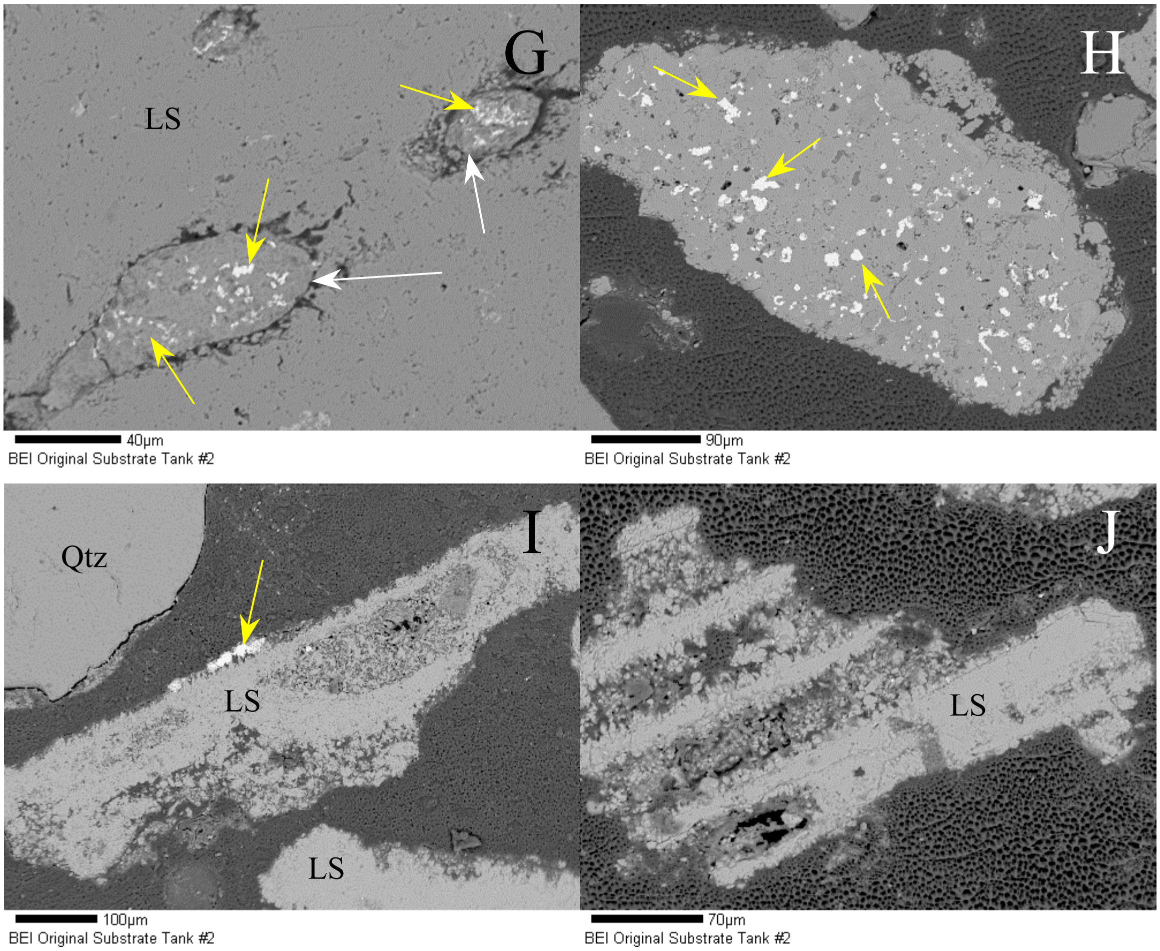
G
LS
40µm
BEI Original Substrate Tank #2
H
90µm
BEI Original Substrate Tank #2
I
Qtz
LS
LS
100µm
BEI Original Substrate Tank #2
J
LS
70µm
BEI Original Substrate Tank #2

Figure D.2. Electron microprobe images of the oxide zone. (A) Copy of Fig. 3.10a (see chapter 3) presented to orient the photograph shown in (B). (B) Close-up of blue rectangular area shown in (A). Green arrows point to "gel" textures (see Ramdohr, 1980) of hydrous ferric oxides (HFO) found in the oxide zone. (C) More HFO "gel" textures. (D) Former limestone grains replaced by HFO. The HFO contains minor amount of sulfur, indicating sulfate. (E) "Gel" texture of HFO precipitate. All material is HFO with minor sulfur. The difference in brightness is due to variations in the sulfate content and/or possibly the hydroxyl content (Fleischer, pers. comm., 2001) of the HFO. (F). Additional gel precipitation textures of HFO with varying sulfur content. Color variations are caused by the same factors discussed in (E). The sharp, flat edge on one side of the HFO indicates that this precipitated along a former surface and has either become dislodged from that surface or the surface (i.e., limestone) has dissolved away. (G) Quartz grain with HFO coating exhibiting a dendritic growth habit (green arrows). (H) Additional HFO coatings (green arrows) on quartz grain. (I) Patch of HFO extending from the surface of an organic fragment indicating growth from the surface. Organic fragment also has precipitated HFO lining cavities (former cell walls). Blue arrow points to a zircon grain. (J) Aluminum hydroxysulfate enveloping a quartz grain. Also minor amounts of aluminum and sulfur-bearing HFO. (K) Organic fragments completely devoid of attached fine-grained limestone commonly observed in the initial substrate. HFO in the lower left corner. (L) More organic fragments completely devoid of fine-grained limestone. Bright grains in the upper left corner are HFO. (M) Organic fragment showing complete removal of fine-grained limestone. Bright grain (blue arrow) is a titanium-bearing compound, most likely rutile (TiO_2). (N) Organic fragment with HFO grains around the rim, but no fine-grained limestone. (O) Cluster of pyrite framboids within a band of HFO. HFO contains subordinate amounts of sulfate and no aluminum.

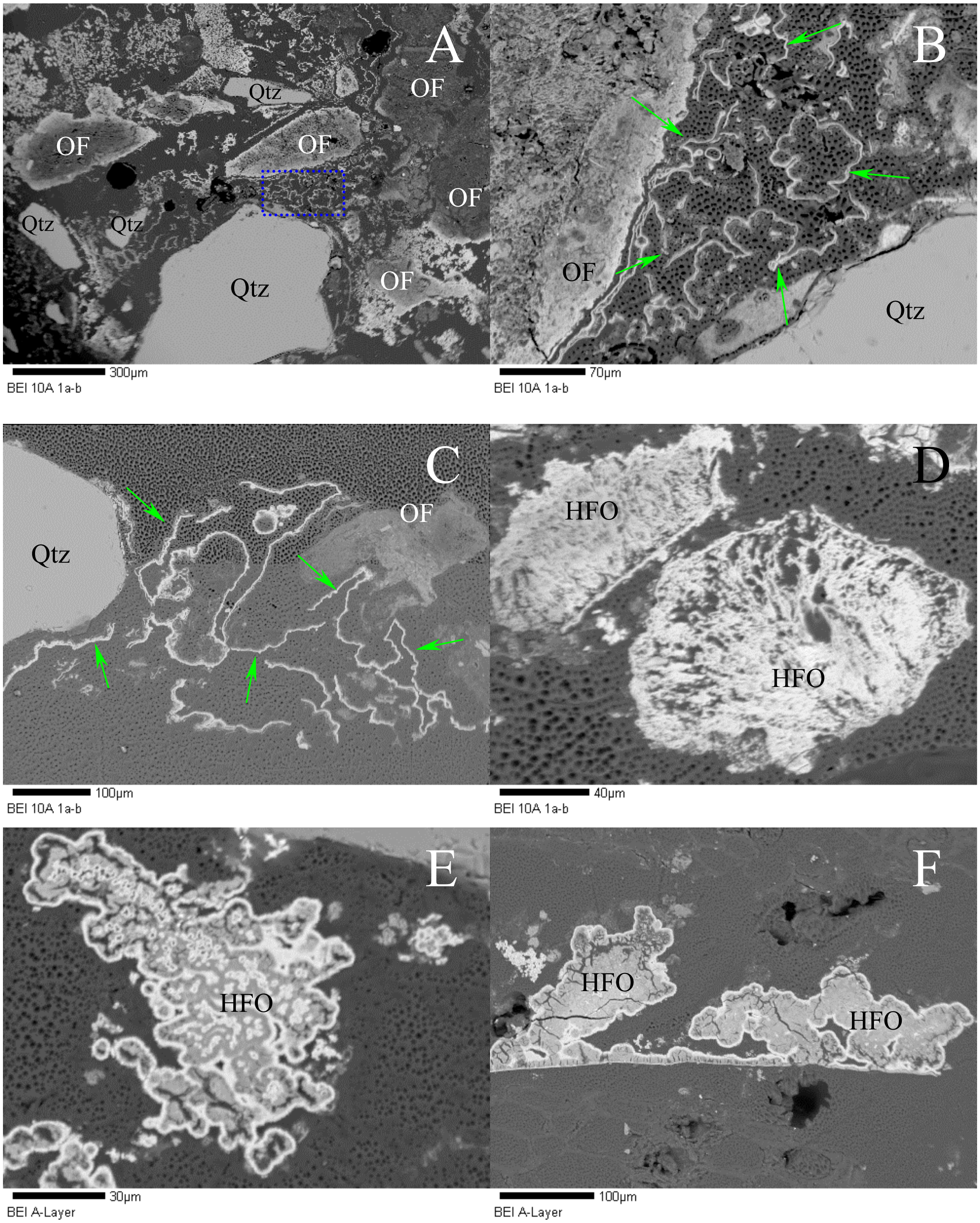
A
Qtz
OF
OF
OF
Qtz
Qtz
OF
Qtz
OF
300µm
BEI 10A 1a-b
B
OF
Qtz
70µm
BEI 10A 1a-b
C
OF
Qtz
100µm
BEI 10A 1a-b
D
HFO
HFO
40µm
BEI 10A 1a-b
E
HFO
30µm
BEI A-Layer
F
HFO
HFO
100µm
BEI A-Layer

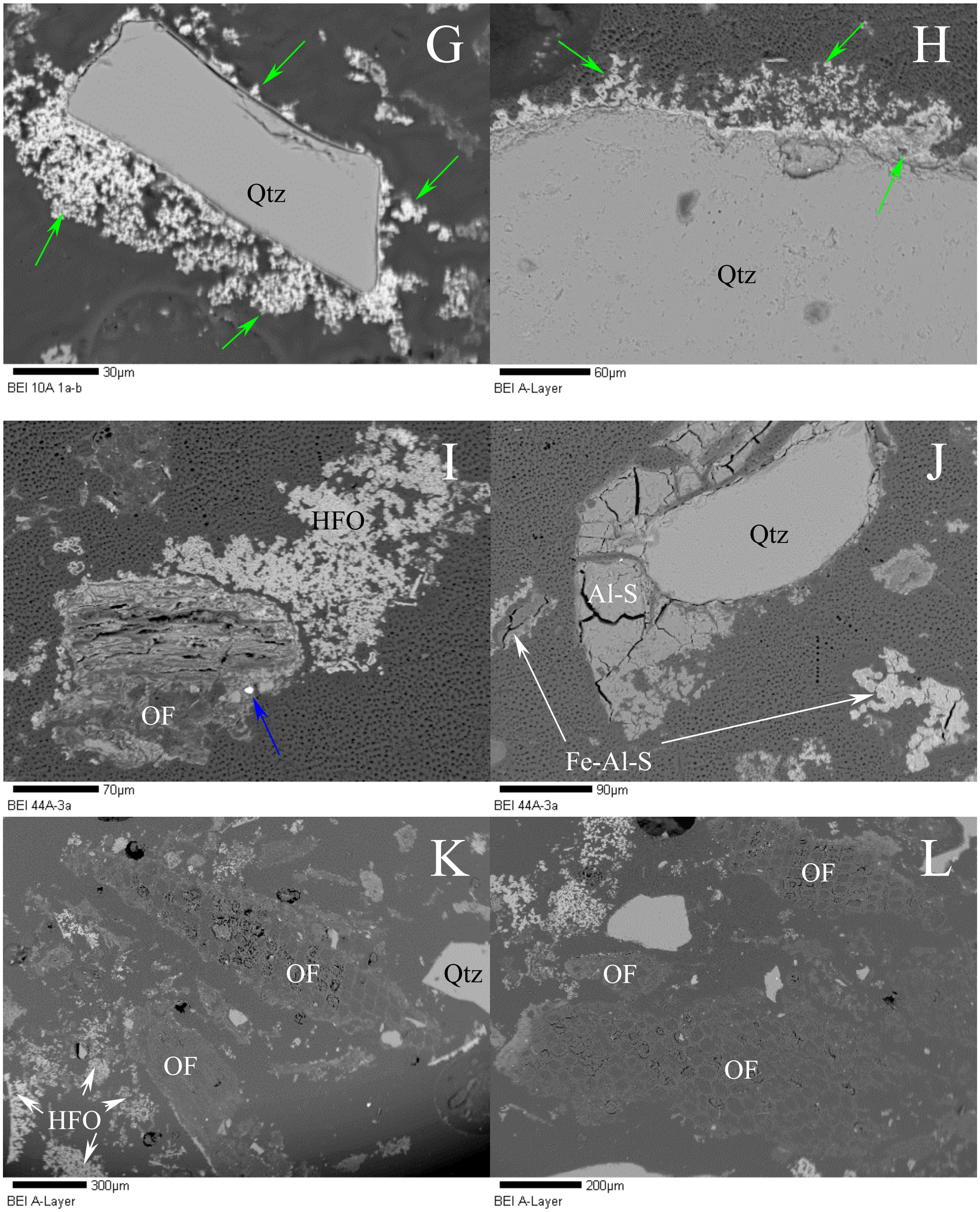
G
Qtz
30µm
BEI 10A 1a-b
H
Qtz
60µm
BEI A-Layer
I
HFO
OF
70µm
BEI 44A-3a
J
Qtz
Al-S
Fe-Al-S
90µm
BEI 44A-3a
K
OF
Qtz
OF
HFO
300µm
BEI A-Layer
L
OF
OF
OF
200µm
BEI A-Layer

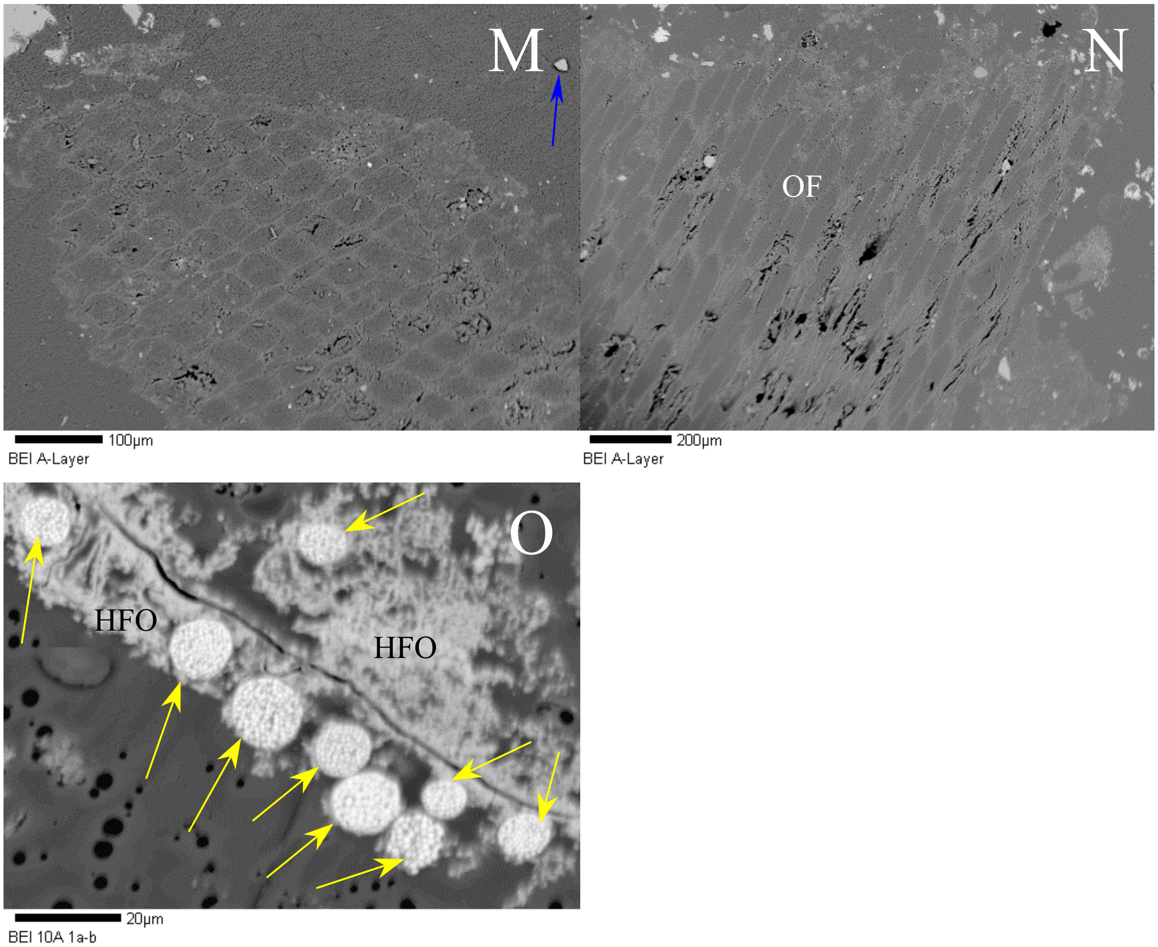
M
N
OF
100µm
BEI A-Layer
200µm
BEI A-Layer
O
HFO
HFO
20µm
BEI 10A 1a-b

Figure D.3. Electron microprobe images of the upper transitional zone. (A) Organic fragment and quartz grain with an overgrowth of mixed HFO and minor aluminum hydroxysulfate precipitate. (B) Organic fragment with HFO overgrowth. (C) Aluminum hydroxysulfate at left with HFO at right. Most of the bright material is HFO. (D) Organic fragment with HFO coatings. (E) Quartz grain with a thin overgrowth of HFO mixed with minor amounts of aluminum. (F) Close-up of blue rectangular box shown in (E). Note the two pyrite clusters embedded in the HFO-Al mixed precipitate. (G) Aluminum hydroxysulfate outlining a relict limestone grain (RLS) with interior pyrite. (H) Two relict limestone grains outlined by aluminum hydroxysulfate reaction rims. Quartz with pyrite inclusions is present in the interior of the RLS. (I) Patch of aluminum precipitate that contains a low sulfur content indicating possibly an oxyhydroxide precipitate. Also minor limestone occurs in the lower reaches of the upper transitional zone. (J) Aluminum hydroxysulfate coating an organic fragment. (K) Limestone grain with aluminum hydroxysulfate reaction halo. (L) Organic fragment with aluminum hydroxysulfate reaction rim. Quartz grain associated with the organic fragment contained irregular pyrite inclusions. Minor framboidal pyrite was also observed (yellow arrows). Some limestone present.

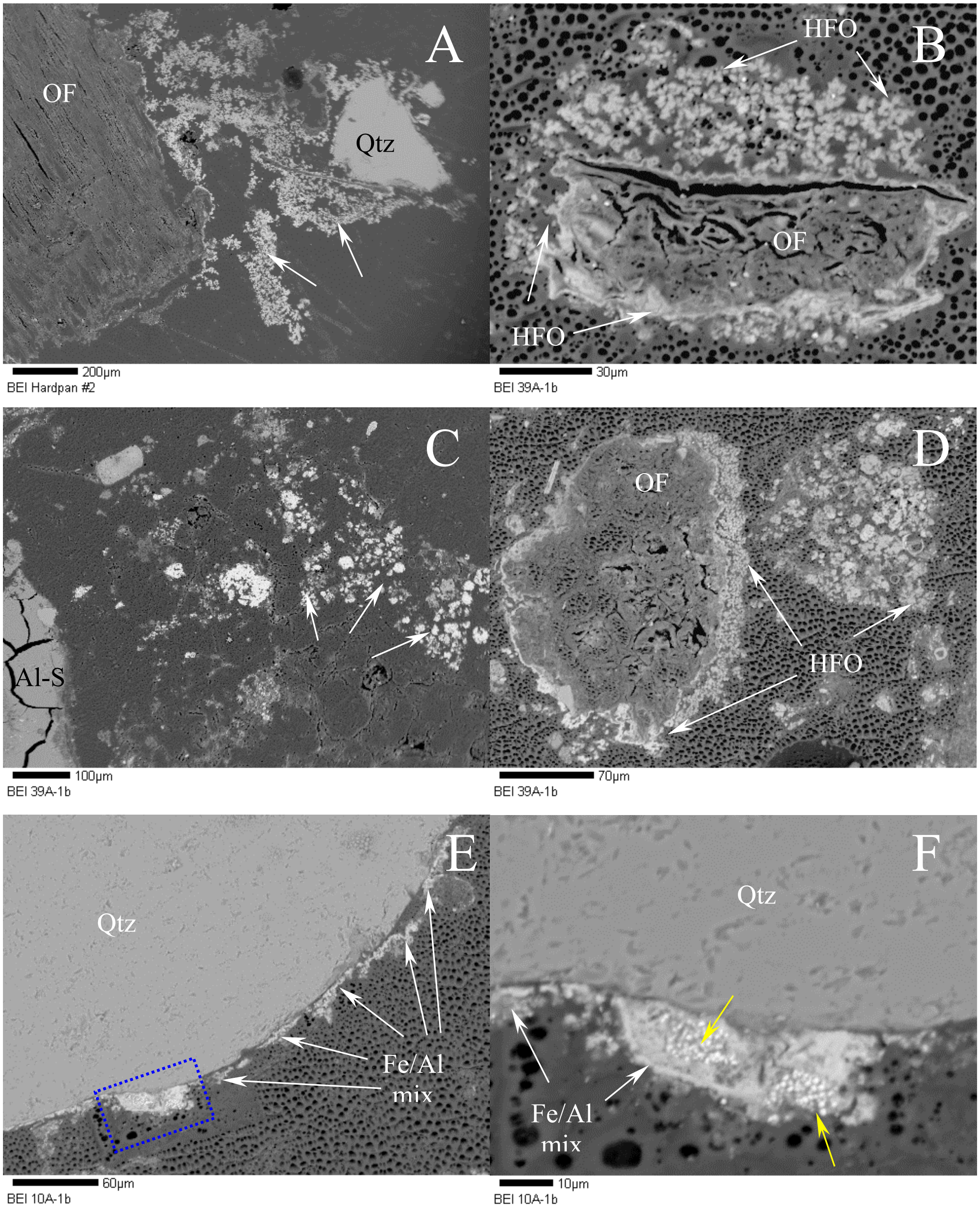
A
OF
Qtz
200µm
BEI Hardpan #2
B
HFO
OF
HFO
30µm
BEI 39A-1b
C
Al-S
100µm
BEI 39A-1b
D
OF
HFO
70µm
BEI 39A-1b
E
Qtz
Fe/Al mix
60µm
BEI 10A-1b
F
Qtz
Fe/Al mix
10µm
BEI 10A-1b

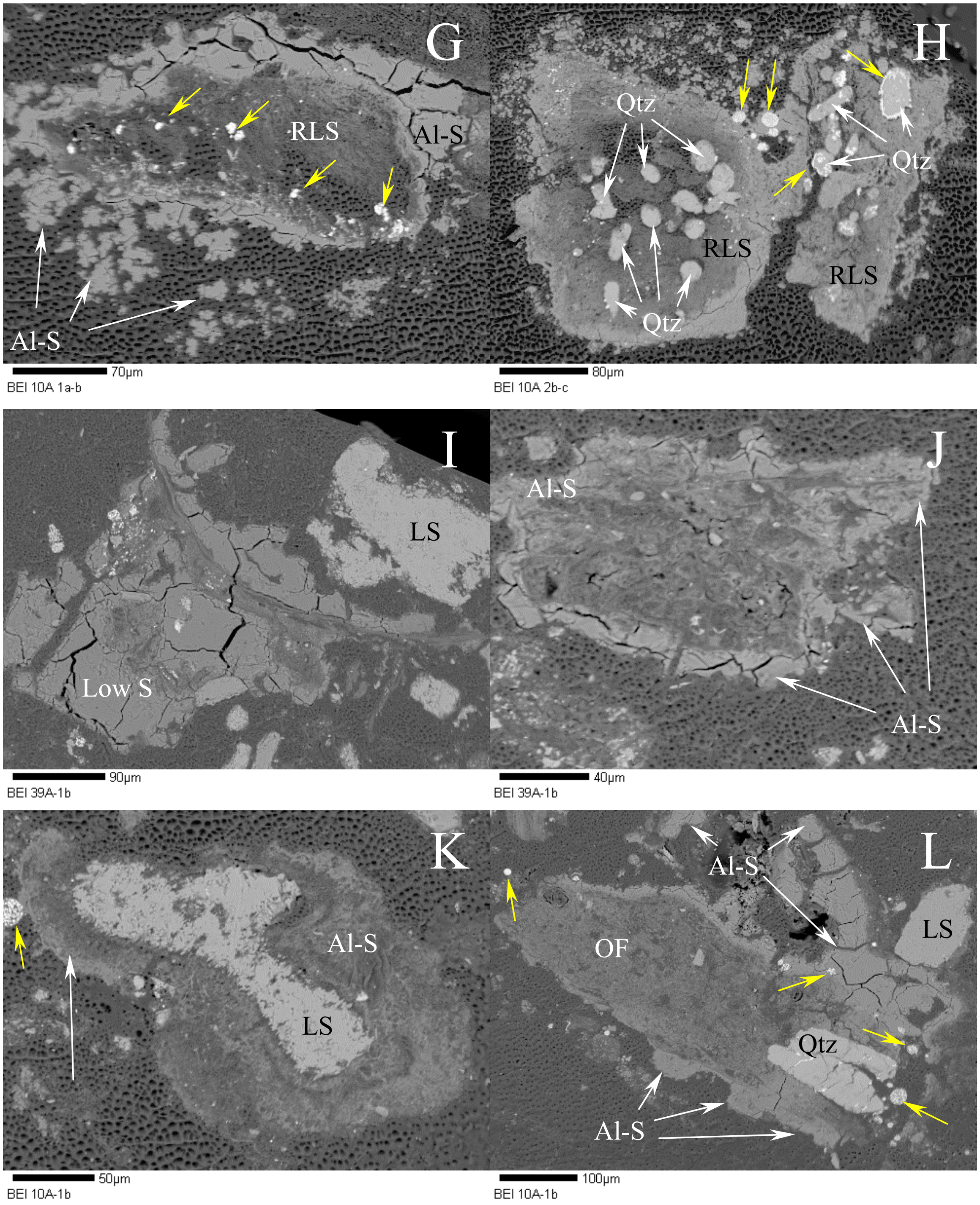
G
RLS
Al-S
Al-S
70µm
BEI 10A 1a-b
H
Qtz
Qtz
RLS
RLS
Qtz
80µm
BEI 10A 2b-c
I
LS
Low S
90µm
BEI 39A-1b
J
Al-S
Al-S
40µm
BEI 39A-1b
K
Al-S
LS
50µm
BEI 10A-1b
L
Al-S
LS
OF
Qtz
Al-S
100µm
BEI 10A-1b

Figure D.4. Electron microprobe images of the middle transitional zone. (A) Copy of Fig. 3.12d (see chapter 3) presented to orient the photograph shown in (B). (B) Close-up of blue rectangular area in (A) showing gypsum precipitation at the former surface of a limestone grain and a reaction rim of aluminum hydroxysulfate that coated the former limestone grain. (C) Close-up of gypsum at the former limestone grain surface showing small fragments of remnant limestone indicating gypsum replacement of limestone. (D) Secondary electron image (SEI) of the same gypsum-limestone intergrowth shown in (C). The SEI image displays topography and therefore allows further distinction between the very soft gypsum grains and the harder, higher relief limestone fragments. (E) Cluster of relict limestone grains outlined by aluminum hydroxysulfate reaction rims. Gypsum occurs as intergranular growth. (F) Close-up of blue rectangular box in (E) showing gypsum and aluminum hydroxysulfate. Small rounded fragments in gypsum are limestone grains. (G) Portion of the transitional zone containing limestone, organic matter, aluminum hydroxysulfate, gypsum, and minor pyrite framboids. (H) Organic fragment with aluminum hydroxysulfate reaction rim. In the center of photograph is partially plucked gypsum. The gypsum was likely plucked from the sample during preparation. (I) Organic fragment with aluminum hydroxysulfate reaction rim. Minor gypsum is present, along with quartz and limestone. (J) Gypsum cluster. (K) Limestone fossil fragment surrounded by gypsum reaction, which is, in turn, surrounded by an aluminum hydroxysulfate reaction rim. (L) Close-up of blue rectangular box in (K) showing gypsum reaction rim. Note the fine-grained fragments of limestone to the right of the photograph. (M) Organic fragment with small (white) sub-angular grains of gypsum. SEI imaging shows that these grains are not surface features but are actually precipitated within the organic material. (N) Close-up of blue rectangular box in (M). (O) Organic fragment with a dark gray reaction rim of gypsum (i.e., calcium sulfate). (P) Close-up of blue rectangular box in (O) showing the gypsum reaction rim and a rhombic shaped calcite crystal. (Q) Organic fragment with gypsum “chips”. (R) Close-up of blue rectangular box in (Q) showing the gypsum chips. (S) Dark gray band of gypsum associated with organic material. (T) Close-up of blue rectangular box in (S) showing gypsum band and associated framboidal pyrite. (U) Two isolated fragments of gypsum adjacent to large patch of aluminum hydroxysulfate and a grain of “pristine” limestone. (V) Close-up of blue rectangular box in (U) showing the pristine limestone. (W) Organic fragment with gypsum precipitates.

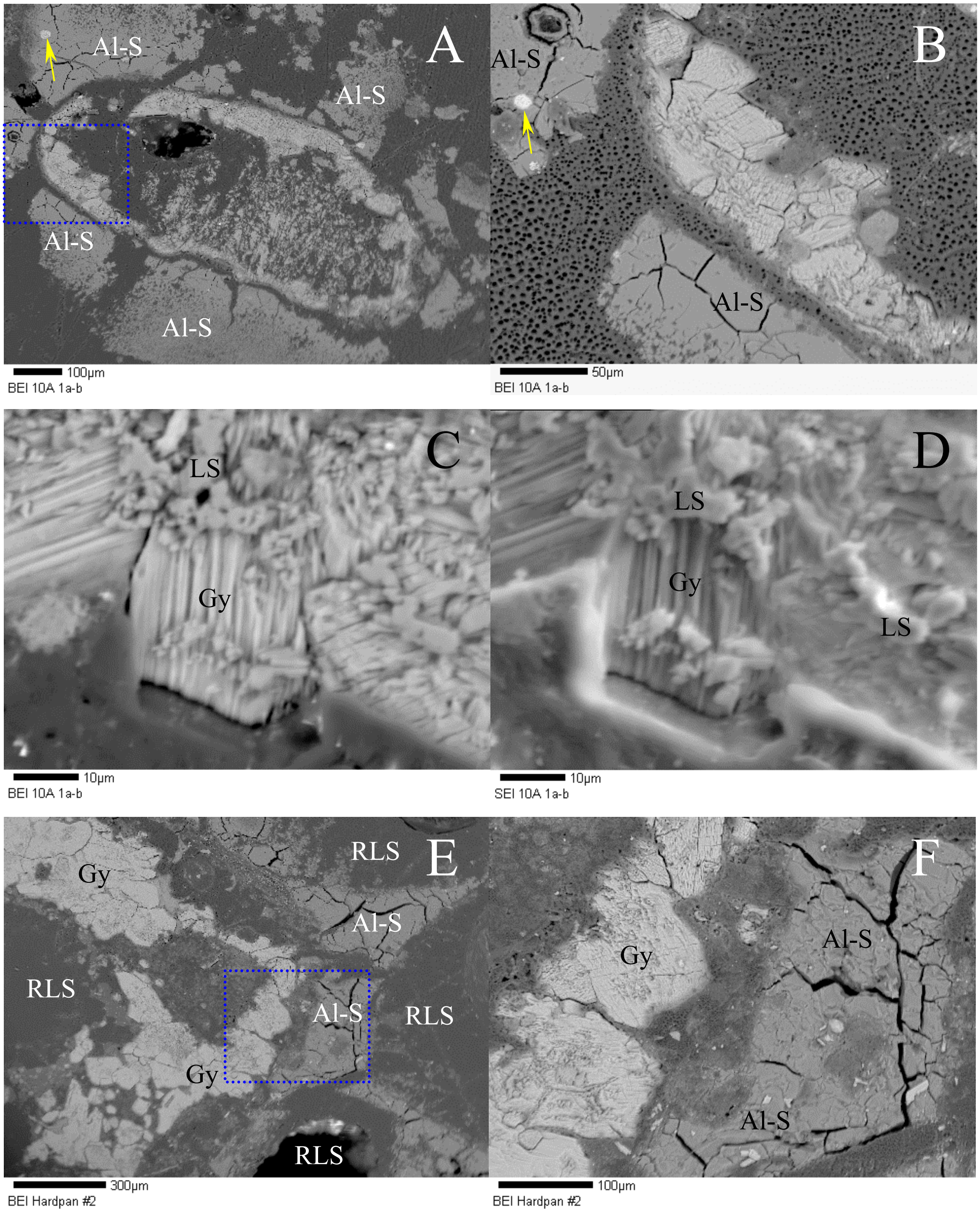
A
Al-S
Al-S
Al-S
Al-S
100µm
BEI 10A 1a-b
B
Al-S
Al-S
50µm
BEI 10A 1a-b
C
LS
Gy
10µm
BEI 10A 1a-b
D
LS
Gy
LS
10µm
SEI 10A 1a-b
E
Gy
RLS
Al-S
RLS
Al-S
RLS
Gy
RLS
300µm
BEI Hardpan #2
F
Gy
Al-S
Al-S
100µm
BEI Hardpan #2

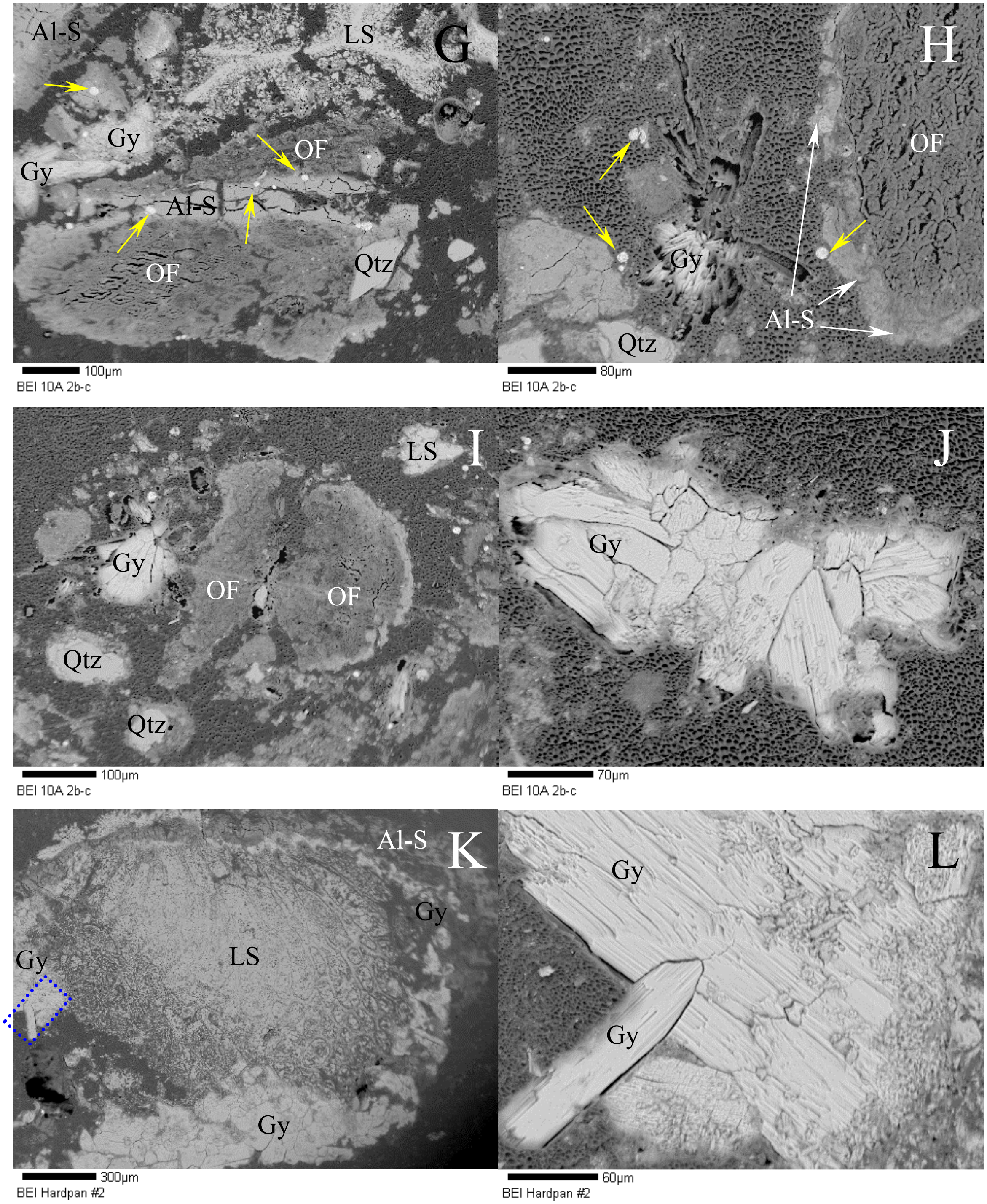
Al-S
LS
G
Gy
Gy
OF
Al-S
OF
Qtz
100µm
BEI 10A 2b-c
H
OF
Gy
Al-S
Qtz
80µm
BEI 10A 2b-c
LS
I
Gy
OF
OF
Qtz
Qtz
100µm
BEI 10A 2b-c
J
Gy
70µm
BEI 10A 2b-c
Al-S
K
Gy
Gy
LS
Gy
300µm
BEI Hardpan #2
Gy
L
Gy
60µm
BEI Hardpan #2

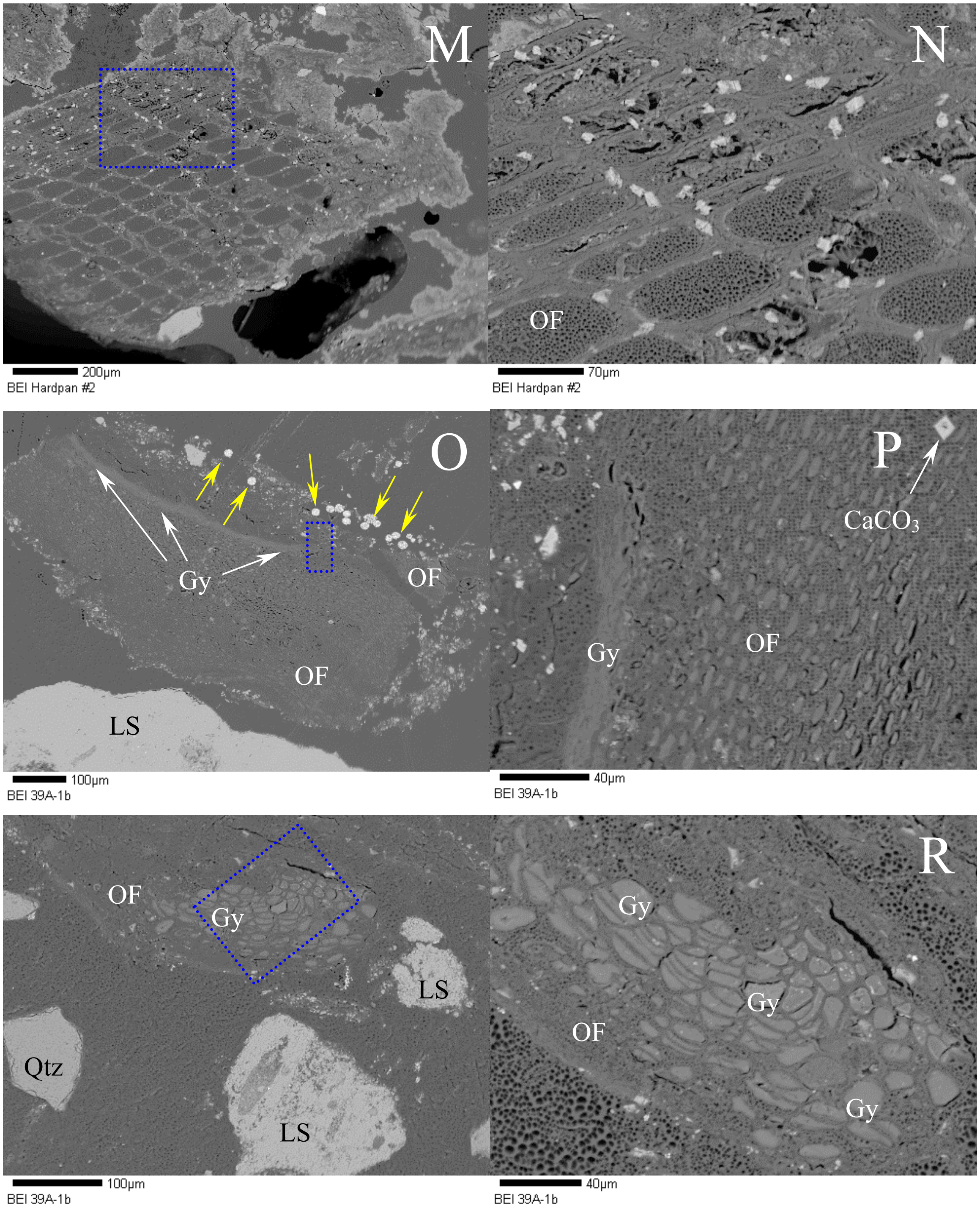
M
200µm
BEI Hardpan #2
N
OF
70µm
BEI Hardpan #2
O
Gy
OF
OF
LS
100µm
BEI 39A-1b
P
CaCO$_3$
Gy
OF
40µm
BEI 39A-1b
OF
Gy
LS
Qtz
LS
100µm
BEI 39A-1b
R
Gy
Gy
OF
Gy
40µm
BEI 39A-1b

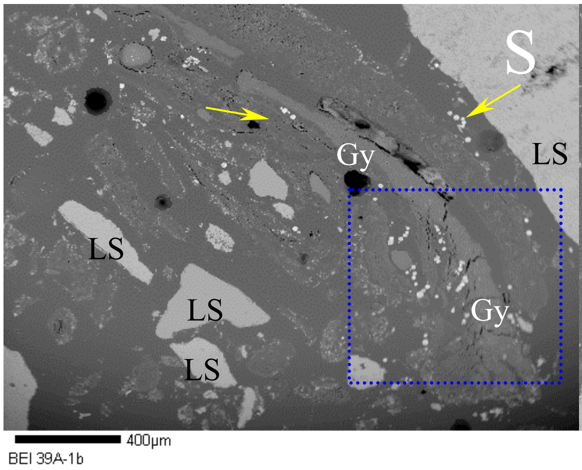
S
Gy
LS
LS
LS
LS
Gy
400µm
BEI 39A-1b

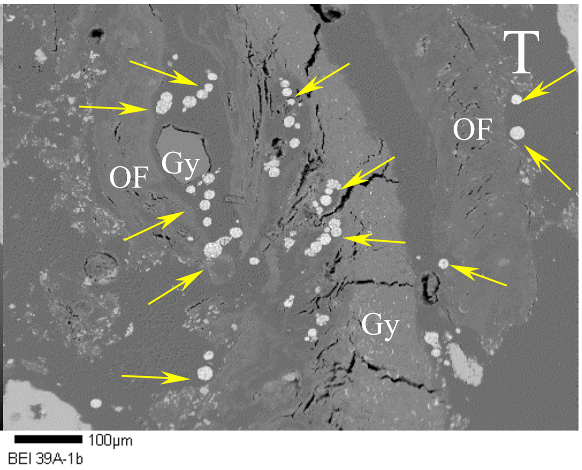
T
OF
OF
Gy
Gy
100µm
BEI 39A-1b

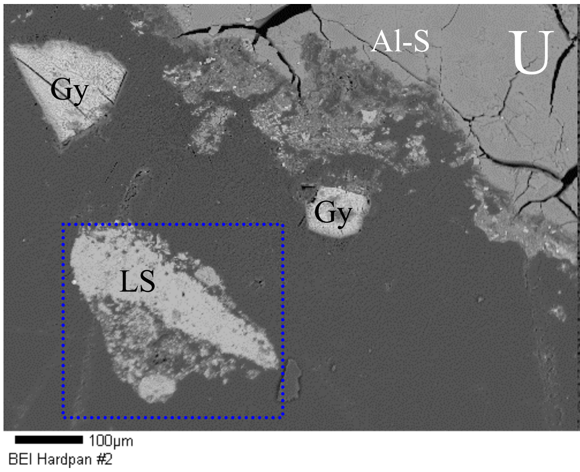
U
Al-S
Gy
Gy
LS
100µm
BEI Hardpan #2

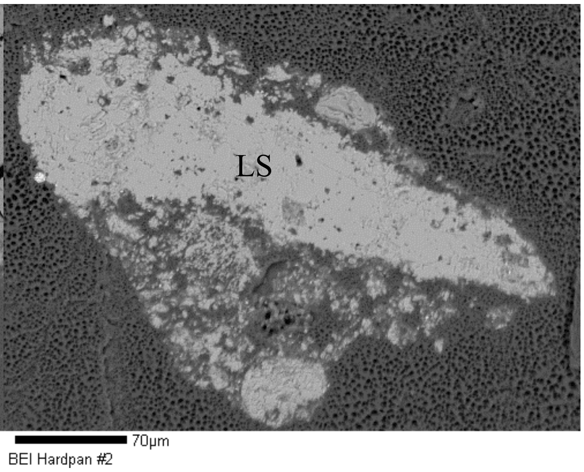
LS
70µm
BEI Hardpan #2

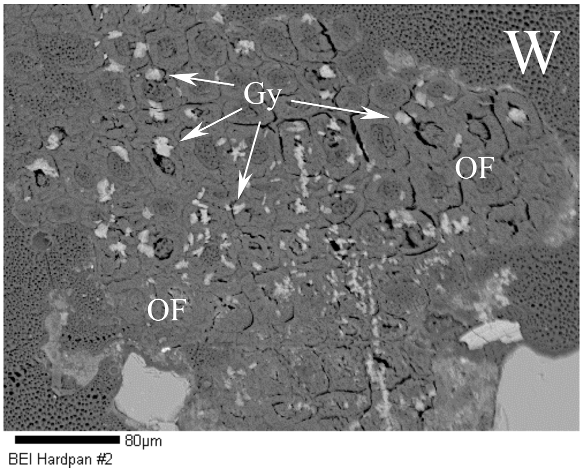
W
Gy
OF
OF
80µm
BEI Hardpan #2

Figure D.5. Electron microprobe images of the lower transitional zone. (A) Pristine limestone grain. (B) Pristine limestone with a small bright Fe, Ca-rich grain near the center (blue arrow), possibly iron-bearing carbonate. (C) Pristine limestone with a small bright Cu-rich (minor sulfur) grain at the top left (blue arrow). (D) Embayment in pristine limestone grain. (E) Pristine limestone grain with associated apatite. (F) Close-up of blue rectangular box shown in (E). (G) Pristine limestone. (H) Close-up of blue rectangular box shown in (G).

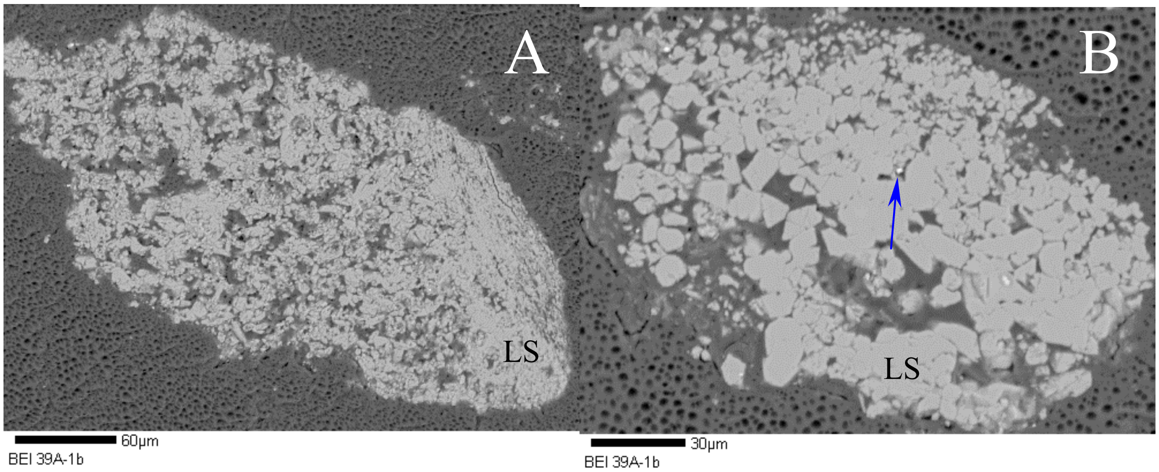

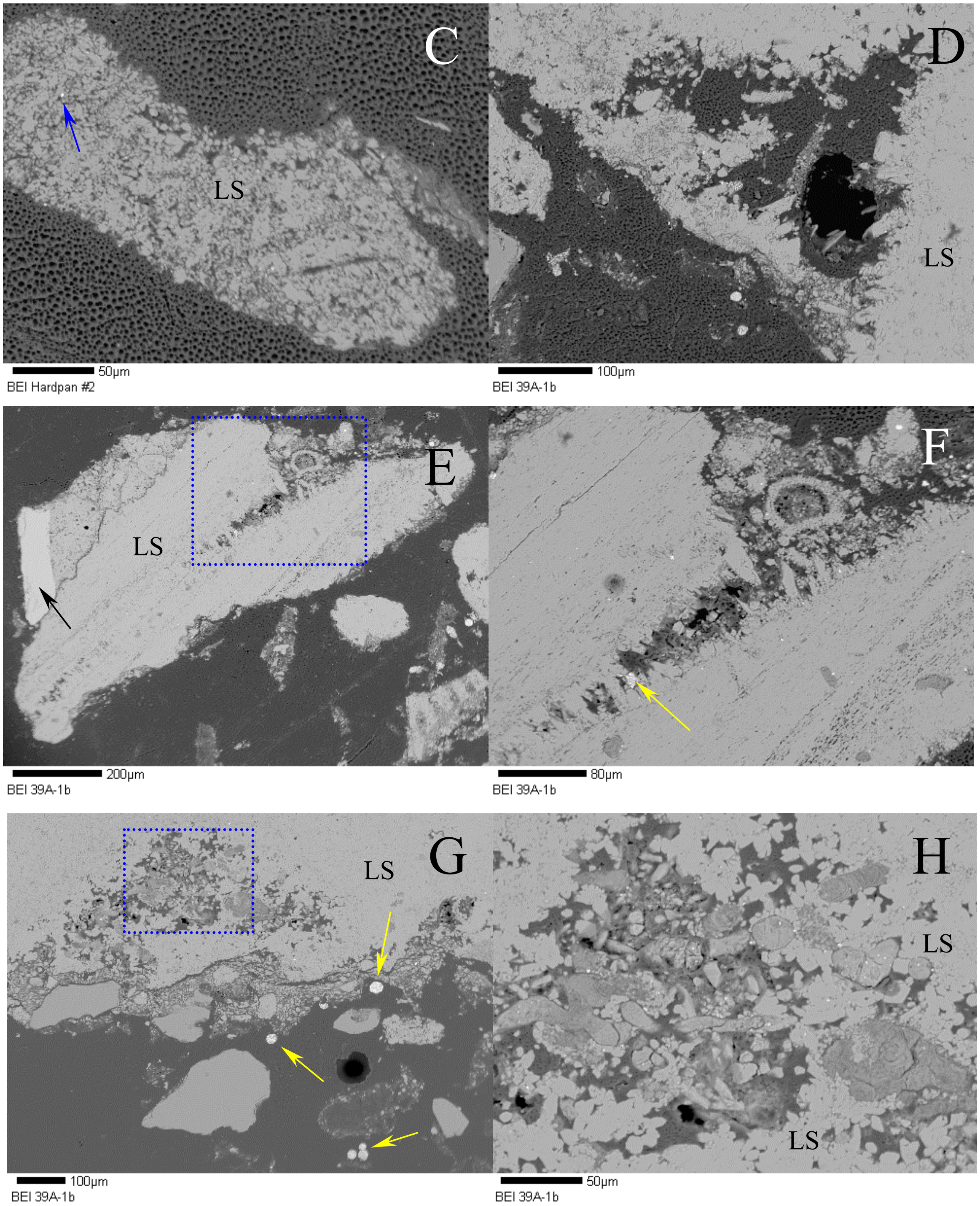
C
LS
50µm
BEI Hardpan #2
D
LS
100µm
BEI 39A-1b
E
LS
200µm
BEI 39A-1b
F
80µm
BEI 39A-1b
G
LS
100µm
BEI 39A-1b
H
LS
LS
50µm
BEI 39A-1b

Figure D.6. Miscellaneous electron microprobe images of the transitional zone. (A) Limestone grain with pyrite precipitated in fractures. Smooth areas are just $CaCO_3$, while the rounded, pocked areas are a mix of $CaCO_3$ and SiO_2. Two pyrite framboids are also present. (B) Cluster of framboidal pyrite embedded in a band of aluminum hydroxysulfate. (C) Quartz grain with an overgrowth patch of aluminum hydroxysulfate containing a high silica content. (D) Close-up of blue rectangular box in (C) showing a cluster of framboidal pyrite. (E) Fractured quartz grain with pyrite filling the fractures. (F) Quartz grain with pyrite precipitated within fractures. (G) Organic fragment outlined by aluminum hydroxysulfate and filled with clusters of rounded (framboidal?) pyrite. Also several patches of KCl are present. (H) Organic fragment rimmed by pyrite framboids. (I) Organic fragment with pyrite grains and limestone. (J) Close-up of blue rectangular box in (I) showing limestone fossil and associated spheres of pyrite.

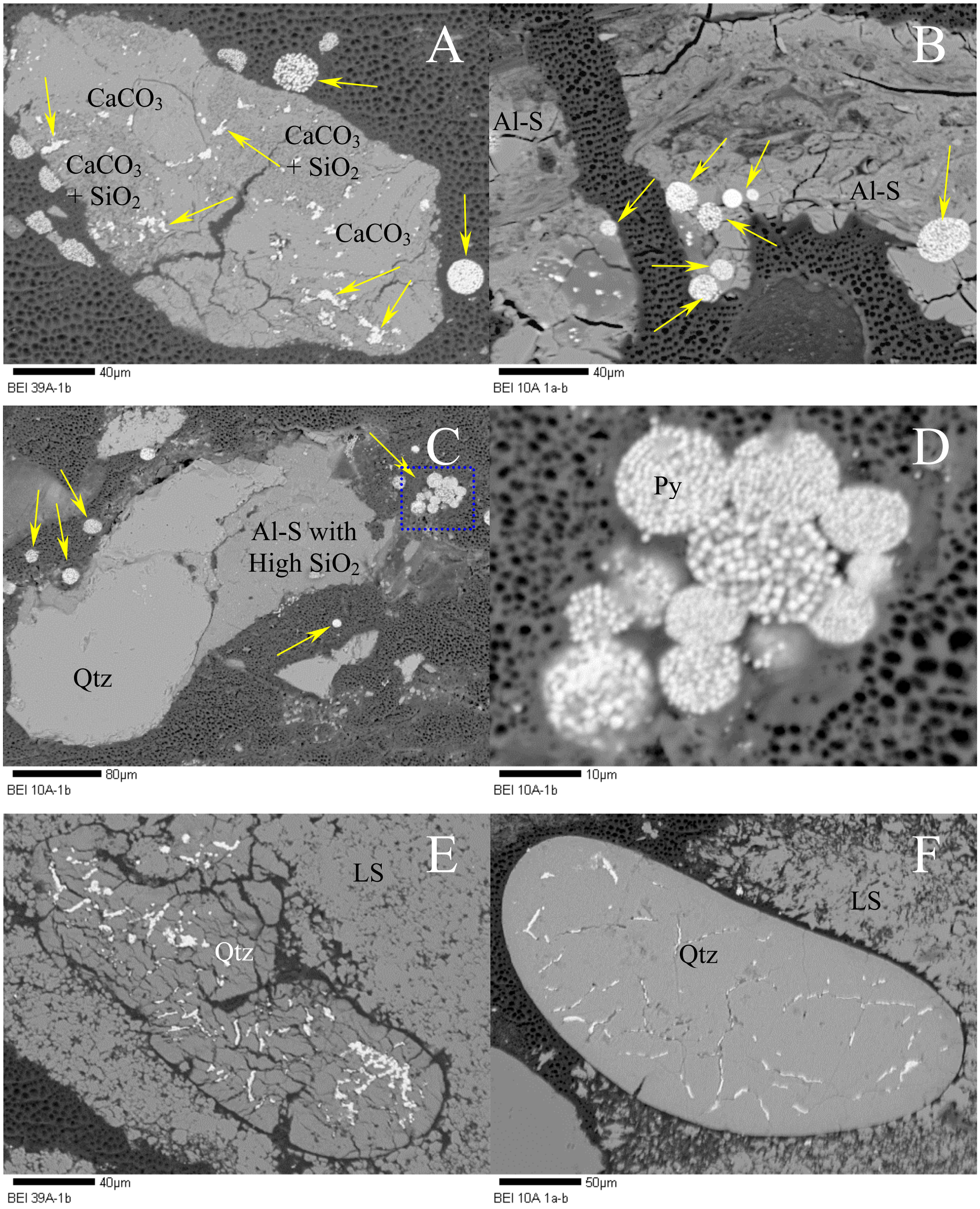
A
CaCO$_3$
CaCO$_3$ + SiO$_2$
CaCO$_3$ + SiO$_2$
CaCO$_3$
40μm
BEI 39A-1b
B
Al-S
Al-S
40μm
BEI 10A 1a-b
C
Al-S with High SiO$_2$
Qtz
80μm
BEI 10A-1b
D
Py
10μm
BEI 10A-1b
E
LS
Qtz
40μm
BEI 39A-1b
F
LS
Qtz
50μm
BEI 10A 1a-b

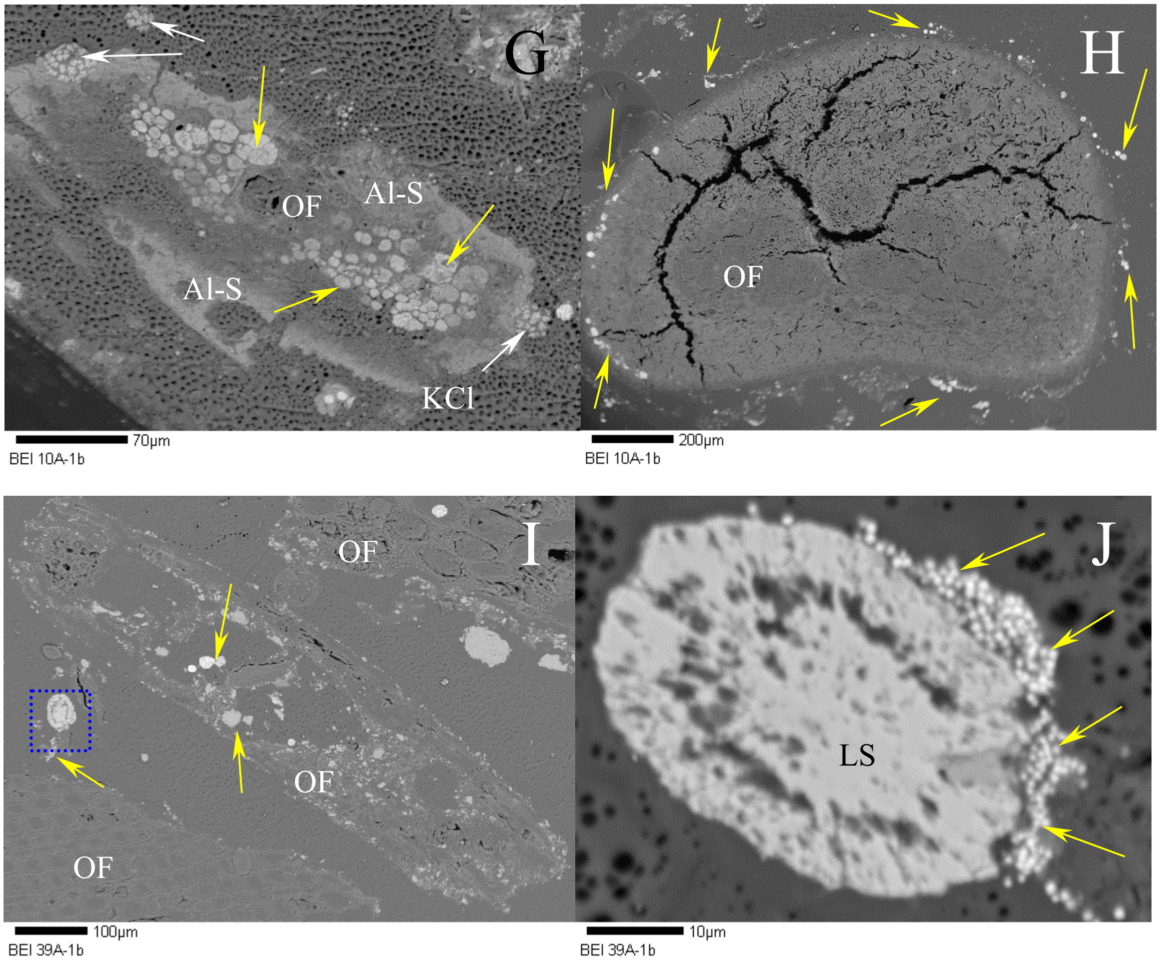
G
OF
Al-S
Al-S
KCl
70µm
BEI 10A-1b
H
OF
200µm
BEI 10A-1b
I
OF
OF
OF
100µm
BEI 39A-1b
J
LS
10µm
BEI 39A-1b

Figure D.7. Electron microprobe images of the sulfide zone. (A) Organic fragment with fine-grained pristine limestone and pyrite framboids clustered along the surface. (B) Overview of the sulfide zone showing distribution of pyrite framboids. (C) Individual spheroids and framboids of pyrite adjacent to limestone grains. (D) Limestone grain with overgrowth (green arrows) of an iron-rich phase (Fe-carbonate?) and a quartz inclusion which in turn contains pyrite inclusions. (E) Limestone fragment with bright iron-rich grain (Fe-carbonate?) on the outer edge (green arrow). (F) Aluminum hydroxysulfate containing elevated calcium and silica. (G) Organic fragment rimmed by fine-grained limestone similar to the initial substrate. (H) Aluminum hydroxysulfate and framboidal pyrite. (I) Pyrite in organic fragment. (J) Close-up of blue rectangular box in (I) showing pyrite framboids.

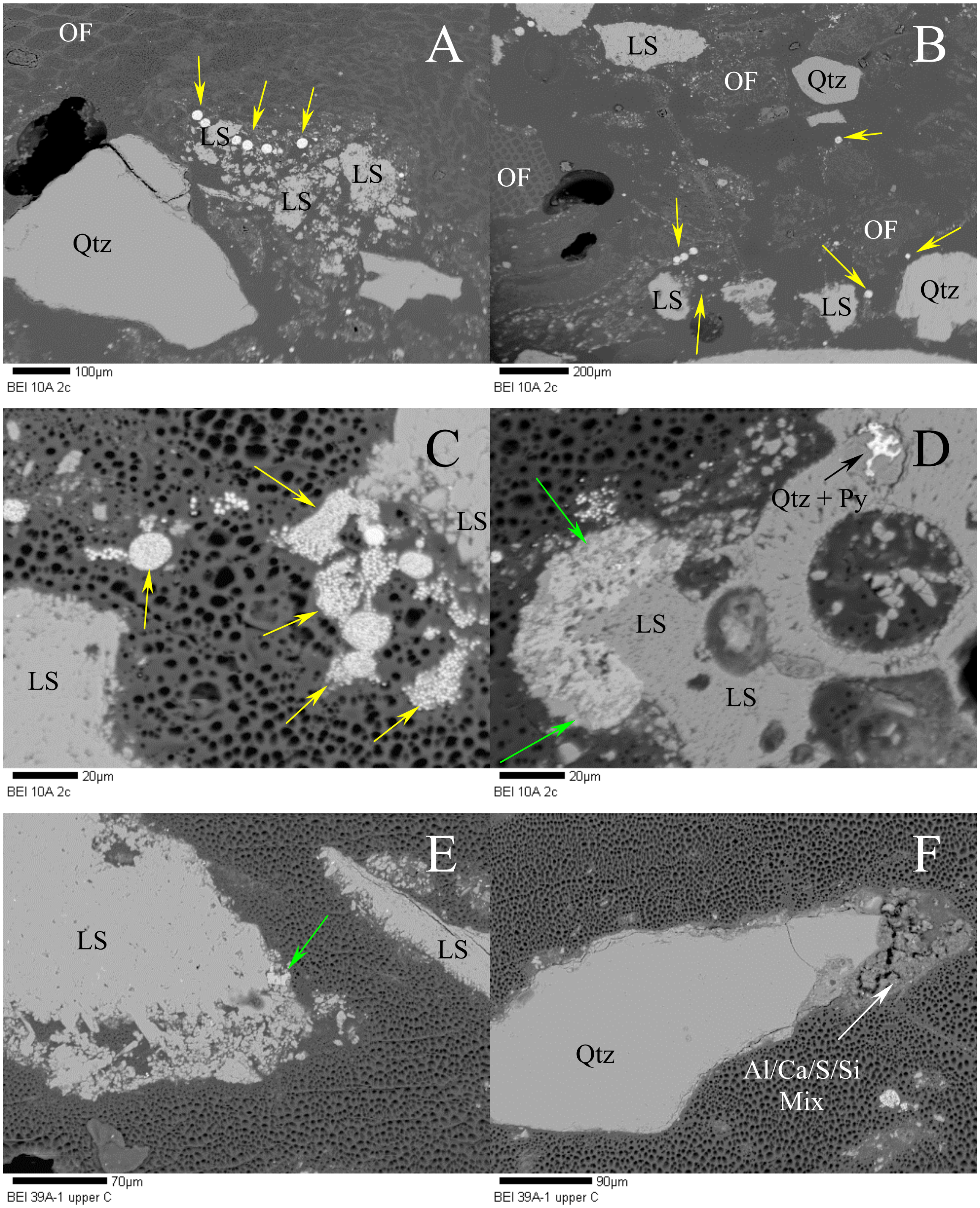
A
OF
LS
LS
LS
Qtz
100μm
BEI 10A 2c
B
LS
OF
Qtz
OF
OF
LS
LS
Qtz
200μm
BEI 10A 2c
C
LS
LS
20μm
BEI 10A 2c
D
Qtz + Py
LS
LS
20μm
BEI 10A 2c
E
LS
LS
70μm
BEI 39A-1 upper C
F
Qtz
Al/Ca/S/Si
Mix
90μm
BEI 39A-1 upper C

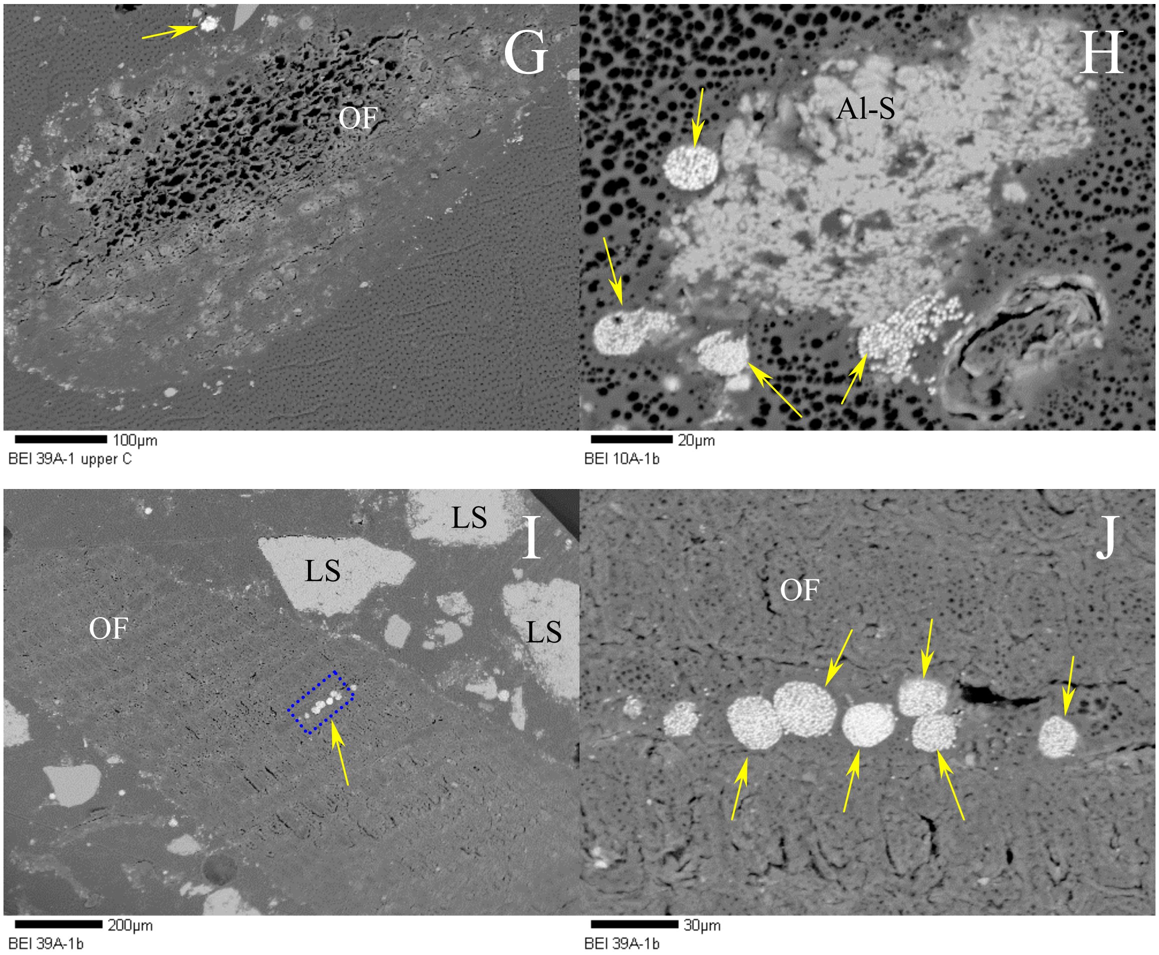
G
OF
100µm
BEI 39A-1 upper C
H
Al-S
20µm
BEI 10A-1b
I
LS
LS
LS
OF
200µm
BEI 39A-1b
J
OF
30µm
BEI 39A-1b

APPENDIX E

ENUMERATION OF SULFATE- AND IRON-REDUCING BACTERIA BY MOST PROBABLE NUMBER METHOD

Sulfate- and iron-reducing microorganisms were enumerated using the most probable number method. Core samples of the organic substrate were collect in June and November 2000 concomitant with the core samples reported in Chapters 2 – 4 from tanks 30A and 36A (see Fig. E.1 for sampling diagram). Sodium – Ammonium Acetate was added to four of the eight tanks (2A, 24A, 30A, 39A) beginning on July 26th, 2000. The June samples therefore provide baseline data for changes in bacterial populations following the acetate addition. Tank 36A is the control. In addition to the samples taken from tanks 30A and 36A in November 2000, single cores were taken from tanks 10A, 39A, and 44A.

Glass core tubes were used to prevent oxidation. The cores were extruded in an anaerobic environment on a sterile tray and cut in half lengthwise employing aseptic technique. Samples for MPN analyses were taken from the center of the core. Three grams of core material were added to 27 grams of sterile 0.1 M Sodium Pyrophosphate (pH 7.0) and shaken for 12 hours in a cool environment (~15°C). After twelve hours the solution was sonicated in a cooled water bath. Aliquots were then transferred to MPN tubes through serial dilution.

The media used in the MPN tubes for enumerating sulfate-reducing microorganisms was prepared following the general recipe given in Widdel and Bak

(1992) for a defined multipurpose medium. For 2 L of basal media, 2 mL of the following stock solutions from Widdel and Bak (1992) were added: nonchelated trace element mix, selenite-tungstate solution, vitamin mix, thiamine solution, vitamin B_{12} solution, and dithionite solution. Additionally, 60 mL of 1.0 M bicarbonate solution, 10 mL of yeast extract (0.5g/L), 0.1 g cysteine, 8 mL of either acetate or lactate (final concentration of 15 mM), and an iron nail were added. The tubes were sealed anaerobically and autoclaved. Positive growth was determined if the nail turned black. If the nail remained clean, then the sample was negative of growth.

The media used in the MPN tubes for enumerating iron-reducing microorganisms was modified from the sulfate-reduction media. The basal media was similar, except sulfate was omitted. Similar to the media for sulfate-reducing bacteria, for 2 L of basal iron-reducing media, 2 mL of the following stock solutions were added: nonchelated trace element mix, selenite-tungstate solution, vitamin mix, thiamine solution, and vitamin B_{12} solution. Additionally, 60 mL of 1.0 M bicarbonate solution, 5 mL of reductant (ascorbic acid/thioglycolate mix), 140 mL ferrihydrite solution, 6 mL of both acetate and lactate (final concentration of 20 mM of carbon). The tubes were sealed anaerobically and autoclaved. Growth was determined based on color change. When the media turned dark brown the tube was considered positive for growth of iron reduction. No magnetite was detected in any of the tubes. The MPN was calculated using a basic computer program code (Koch, 1994). Fig. E.2 gives the computer code. At the bottom of the computer code there is a link leading to three spreadsheets containing the calculated MPN values.

Fig. E.1. Plan view of core sampling location for Tanks 30A and 36A

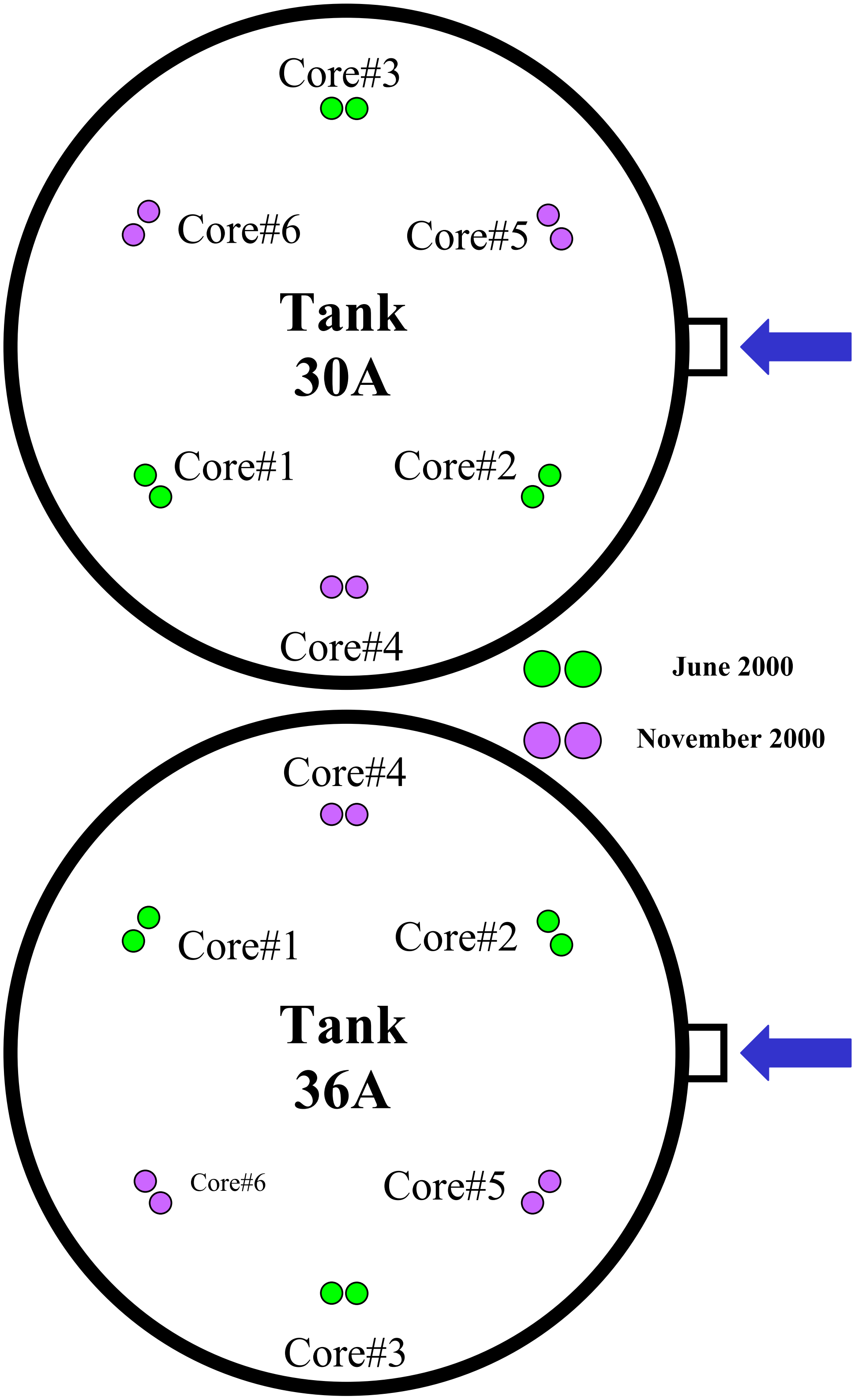

Fig. E.2. Basic computer code for calculating MPN

```
00010 'MPN, Robert C. Thomas, 6/20/01
00020 DIM D(15,5):TV=0:DEFSNG A-Z:CLS
00030 INPUT "DILUTION FACTOR TO TEST SOLUTION ";DIL
00040 INPUT "NUMBER OF LEVELS TESTED ";I
00050 PRINT "VOLUME, # OF TUBES, # WITH GROWTH"
00060 FOR J=1 TO I:INPUT V,N,G
00070 IF J=1 THEN NN=N
00080 D(J,1)=J:D(J,2)=V:D(J,3)=N:D(J,4)=G
00090 IF D(J,3)=0 THEN D(J,3)=NN
00100 TV=TV+D(J,2)*D(J,3)
00110 NEXT J
00120 X1=.001:X2=.8
00130 X=X1
00140 GOSUB 340
00150 Y1=Z
00160 X=X2
00170 GOSUB 340
00180 Y2=Z
00190 X=X2-(X2-X1)*Y2/(Y2-Y1)
00200 GOSUB 340
00210 Y=Z:PRINT X;Y
00220 IF ABS (Z)<.0001 THEN 270
00230 IF Y*Y2>0 THEN 260
00240 X1=X2:Y1=Y2
00250 X2=X:Y2=Y:GOTO 190
00260 Y1=Y1/2:GOTO 250
00270 PRINT:PRINT "VOLUME, # OF TUBES, # WITH GROWTH"
00280 FOR J=1 TO I:PRINT D(J,2),D(J,3),D(J,4)
00290 NEXT J
00300 PRINT
00310 PRINT "MOST PROBABLE NUMBER =";X
00320 PRINT "ORIGINAL TITER =";X*DIL
00330 END
00340 SUMMATION SUBROUTINE
00350 ZZ=0
00360 FOR J=1 TO I
00370 ZZ=ZZ+D(J,2)*D(J,4)/(1-EXP(-X*D(J,2)))
00380 NEXT J
00390 Z=ZZ-TV
00400 RETURN
```

CLICK HERE FOR SPREADSHEET WITH MPN CALCULATIONS

Tank 30A, Core 1, Oxide Zone

June 2000

SRB Lactate

●	●	●	●	○	○	○	○	○	○	1
●	●	●	●	●	○	○	○	○	○	
●	●	●	●	○	○	○	○	○	○	
●	●	●	●	○	○	○	○	○	○	4
10^{2}	10^{3}	10^{4}	10^{5}	10^{6}	10^{7}	10^{8}	10^{9}	10^{10}	10^{11}	

SRB Acetate

●	●	●	●	●	●	○	○	○	○	1
●	●	●	●	●	○	○	○	○	○	
●	●	●	●	●	○	○	○	○	○	
●	●	●	●	●	○	○	○	○	○	4
10^{2}	10^{3}	10^{4}	10^{5}	10^{6}	10^{7}	10^{8}	10^{9}	10^{10}	10^{11}	

SRB Prop/Butyr

●	●	●	●	●	●	○	○	○	○
●	●	●	●	●	●	○	○	○	○
10^{2}	10^{3}	10^{4}	10^{5}	10^{6}	10^{7}	10^{8}	10^{9}	10^{10}	10^{11}

Tank 30A, Core 1, Transitional Zone

June 2000

SRB Lactate

10^2	10^3	10^4	10^5	10^6	10^7	10^8	10^9	10^{10}	10^{11}	
●	●	●	●	○	○	○	○	○	○	1
●	●	●	●	●	○	○	○	○	○	↓
●	●	●	●	○	○	○	○	○	○	
●	●	●	●	●	●	○	○	○	○	4

SRB Acetate

10^2	10^3	10^4	10^5	10^6	10^7	10^8	10^9	10^{10}	10^{11}	
●	●	●	●	○	○	○	○	○	○	1
●	●	●	●	○	●	○	○	○	○	↓
●	●	●	●	◍	○	○	○	○	○	
●	●	●	●	○	○	○	○	○	○	4

SRB Prop/Butyr

10^2	10^3	10^4	10^5	10^6	10^7	10^8	10^9	10^{10}	10^{11}
●	●	●	●	●	●	●	●	○	○
●	●	●	●	●	○	○	○	○	○

Tank 30A, Core 1, Sulfide Zone
June 2000

SRB Lactate

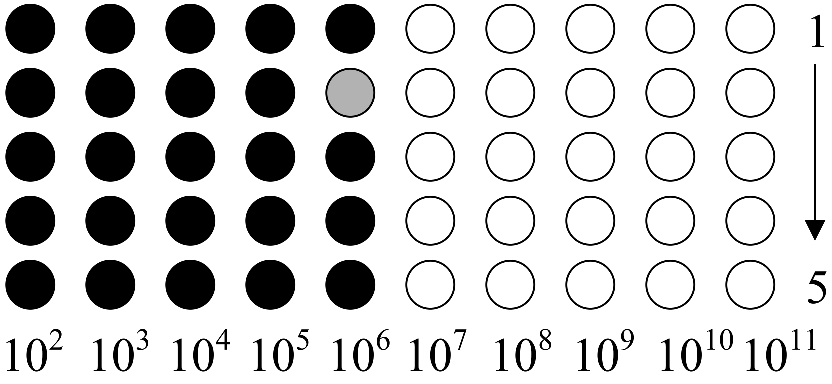

SRB Acetate

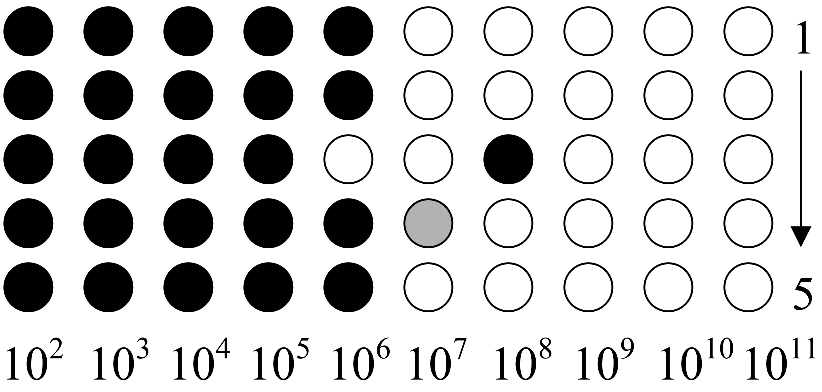

SRB Prop/Butyr

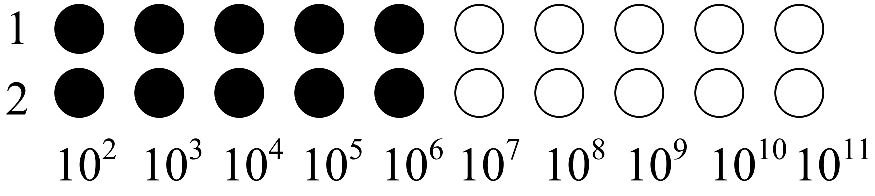

Tank 30A, Core 2, Oxide Zone

June 2000

No Data

Tank 30A, Core 2, Transitional Zone

June 2000

No Data

Tank 30A, Core 2, Sulfide Zone

June 2000

No Data

Tank 30A, Core 3, Oxide Zone
June 2000

No Data

Tank 30A, Core 3, Transitional Zone
June 2000

No Data

Tank 30A, Core 3, Sulfide Zone
June 2000

No Data

Tank 36A, Core 1, Oxide Zone

June 2000

No Data

Tank 36A, Core 1, Transitional Zone

June 2000

No Data

Tank 36A, Core 1, Sulfide Zone

June 2000

No Data

Tank 36A, Core 2, Oxide Zone
June 2000

No Data

Tank 36A, Core 2, Transitional Zone
June 2000

No Data

Tank 36A, Core 2, Sulfide Zone
June 2000

No Data

Tank 36A, Core 3, Oxide Zone

June 2000

No Data

Tank 36A, Core 3, Transitional Zone

June 2000

No Data

Tank 36A, Core 3, Sulfide Zone

June 2000

SRB Lactate

●	●	●	●	●	○	○	○	○	○	1
●	●	●	●	●	○	○	○	○	○	↓
●	●	●	●	●	○	○	○	○	○	↓
●	●	●	●	●	○	○	○	○	○	4
10^2	10^3	10^4	10^5	10^6	10^7	10^8	10^9	10^{10}	10^{11}	

SRB Acetate

●	●	●	●	●	○	○	○	○	○	1
●	●	●	●	●	○	○	○	○	○	↓
●	●	●	●	●	○	○	○	○	○	↓
●	●	●	●	○	○	○	○	○	○	4
10^2	10^3	10^4	10^5	10^6	10^7	10^8	10^9	10^{10}	10^{11}	

SRB Prop/Butyr

●	●	●	●	●	●	●	○	○	○
●	●	●	●	●	○	●	○	○	○
10^2	10^3	10^4	10^5	10^6	10^7	10^8	10^9	10^{10}	10^{11}

Tank 30A, Core 4, Oxide Zone
November 2000

SRB Lactate

●	●	●	●	●	●	○	○	○	○
●	●	●	●	●	●	●	○	○	○
●	●	●	●	●	●	○	○	○	○
●	●	●	●	●	●	●	○	○	○
10^2	10^3	10^4	10^5	10^6	10^7	10^8	10^9	10^{10}	10^{11}

SRB Acetate

●	●	●	●	●	●	○	○	○	○
●	●	●	●	●	●	○	○	○	○
●	●	●	●	●	●	●	○	○	○
●	●	●	●	●	●	●	○	○	○
10^2	10^3	10^4	10^5	10^6	10^7	10^8	10^9	10^{10}	10^{11}

Fe Reducing

●	●	●	●	●	●	○	●	○	○
●	●	●	●	●	●	○	○	○	○
●	●	●	●	●	○	○	○	○	○
●	●	●	●	●	●	○	○	○	○
10^2	10^3	10^4	10^5	10^6	10^7	10^8	10^9	10^{10}	10^{11}

Tank 30A, Core 4, Transitional Zone
November 2000

SRB Lactate

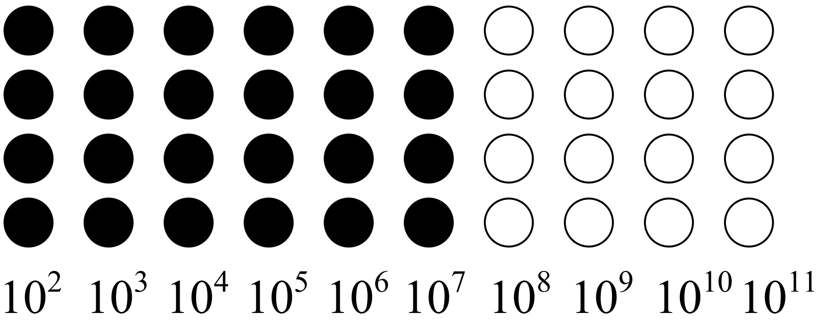

SRB Acetate

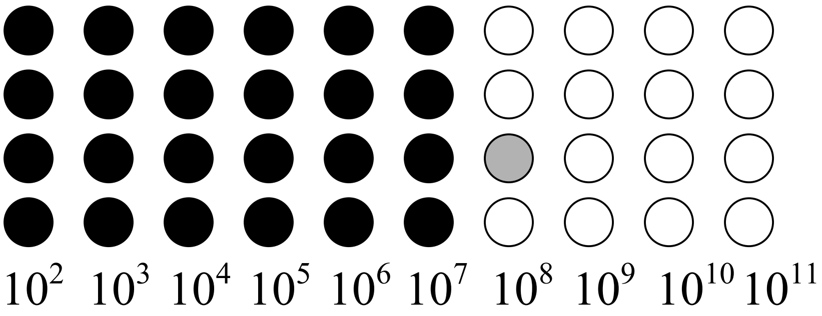

Fe Reducing

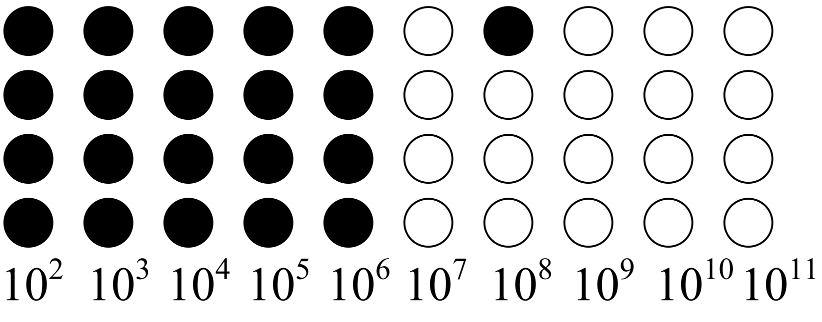

Tank 30A, Core 4, Sulfide Zone
November 2000

SRB Lactate

●	●	●	●	●	●	○	○	○	○
●	●	●	●	●	○	○	●	○	○
●	●	●	●	●	●	○	○	○	○
●	●	●	●	●	●	○	○	○	○
10^2	10^3	10^4	10^5	10^6	10^7	10^8	10^9	10^{10}	10^{11}

SRB Acetate

●	●	●	●	●	●	○	○	○	○
●	●	●	●	●	●	○	○	○	○
●	●	●	●	●	●	○	○	○	○
●	●	●	●	●	●	○	○	○	○
10^2	10^3	10^4	10^5	10^6	10^7	10^8	10^9	10^{10}	10^{11}

Tank 30A, Core 5, Oxide Zone
November 2000

SRB Lactate

●	●	●	●	●	●	○	○	○	○
●	●	●	●	●	○	○	○	○	○
●	●	●	●	●	●	○	○	○	○
●	●	●	●	●	●	○	○	○	○
10^{2}	10^{3}	10^{4}	10^{5}	10^{6}	10^{7}	10^{8}	10^{9}	10^{10}	10^{11}

SRB Acetate

●	●	●	●	●	○	○	○	○	○
●	●	●	●	●	○	○	○	○	○
●	●	●	●	●	○	○	○	○	○
●	●	●	●	●	●	○	○	○	○
10^{2}	10^{3}	10^{4}	10^{5}	10^{6}	10^{7}	10^{8}	10^{9}	10^{10}	10^{11}

Fe Reducing

●	●	●	●	●	●	○	○	○	○
●	●	●	●	●	○	○	○	○	○
●	●	●	●	●	●	○	○	○	○
●	●	●	●	●	●	○	○	○	○
10^{2}	10^{3}	10^{4}	10^{5}	10^{6}	10^{7}	10^{8}	10^{9}	10^{10}	10^{11}

Tank 30A, Core 5, Transitional Zone
November 2000

SRB Lactate

●	●	●	●	●	●	○	○	○	○
●	●	●	●	●	●	○	○	○	○
●	●	●	●	●	●	○	○	○	○
●	●	●	●	●	●	○	○	○	○
10^2	10^3	10^4	10^5	10^6	10^7	10^8	10^9	10^{10}	10^{11}

SRB Acetate

●	●	●	●	●	●	○	○	○	○
●	●	●	●	●	●	○	○	○	○
●	●	●	●	●	○	○	○	○	○
●	●	●	●	●	○	○	○	○	○
10^2	10^3	10^4	10^5	10^6	10^7	10^8	10^9	10^{10}	10^{11}

Fe Reducing

●	●	●	●	●	●	○	○	○	○
●	●	●	●	●	○	○	○	○	○
●	●	●	●	○	○	○	○	○	○
●	●	●	●	●	○	○	○	○	○
10^2	10^3	10^4	10^5	10^6	10^7	10^8	10^9	10^{10}	10^{11}

Tank 30A, Core 5, Sulfide Zone
November 2000

SRB Lactate

●	●	●	●	●	●	○	○	○	○
●	●	●	●	●	●	○	○	○	○
●	●	●	●	●	●	○	○	○	○
●	●	●	●	●	◐	●	○	○	○
10^2	10^3	10^4	10^5	10^6	10^7	10^8	10^9	10^{10}	10^{11}

SRB Acetate

●	●	●	●	●	●	○	●	○	○
●	●	●	●	●	●	●	○	○	○
●	●	●	●	●	●	○	○	○	○
●	●	●	●	●	●	●	○	○	○
10^2	10^3	10^4	10^5	10^6	10^7	10^8	10^9	10^{10}	10^{11}

Tank 30A, Core 6, Oxide Zone

November 2000

SRB Lactate

10^2	10^3	10^4	10^5	10^6	10^7	10^8	10^9	10^{10}	10^{11}
●	●	●	●	●	●	●	○	○	○
●	●	●	●	●	●	○	○	○	○
●	●	●	●	●	●	○	○	○	○
●	●	●	●	●	●	○	○	○	○

SRB Acetate

10^2	10^3	10^4	10^5	10^6	10^7	10^8	10^9	10^{10}	10^{11}
●	●	●	●	●	●	◍	○	○	○
●	●	●	●	●	●	○	○	○	○
●	●	●	●	●	●	○	○	○	○
●	●	●	●	●	●	○	○	○	○

Fe Reducing

10^2	10^3	10^4	10^5	10^6	10^7	10^8	10^9	10^{10}	10^{11}
●	●	●	●	●	●	○	○	○	○
●	●	●	●	●	●	○	○	○	○
●	●	●	●	●	○	○	○	○	○
●	●	●	●	●	●	○	○	○	○

Tank 30A, Core 6, Transitional Zone
November 2000

SRB Lactate

●	●	●	●	●	●	○	○	○	○
●	●	●	●	●	○	○	○	○	○
●	●	●	●	●	●	○	○	○	○
●	●	●	●	●	●	●	○	○	○
10^2	10^3	10^4	10^5	10^6	10^7	10^8	10^9	10^{10}	10^{11}

SRB Acetate

●	●	●	●	●	●	○	○	○	○
●	●	●	●	●	●	○	○	○	○
●	●	●	●	●	●	○	○	○	○
●	●	●	●	●	○	●	○	○	○
10^2	10^3	10^4	10^5	10^6	10^7	10^8	10^9	10^{10}	10^{11}

Tank 30A, Core 6, Sulfide Zone
November 2000

SRB Lactate

10^2	10^3	10^4	10^5	10^6	10^7	10^8	10^9	10^{10}	10^{11}
●	●	●	●	●	●	○	○	○	○
●	●	●	●	●	●	○	○	○	○
●	●	●	●	●	●	○	○	○	○
●	●	●	●	●	●	●	○	○	○

SRB Acetate

10^2	10^3	10^4	10^5	10^6	10^7	10^8	10^9	10^{10}	10^{11}
●	●	●	●	●	●	○	○	○	○
●	●	●	●	●	●	●	○	○	○
●	●	●	●	●	●	●	○	○	○
●	●	●	●	●	●	○	○	○	○

Tank 36A, Core 4, Oxide Zone

November 2000

SRB Lactate

●	●	●	●	●	○	○	○	○	○
●	●	●	●	●	○	○	○	○	○
●	●	●	●	●	●	○	○	○	○
●	●	●	●	●	●	○	○	○	○
10^2	10^3	10^4	10^5	10^6	10^7	10^8	10^9	10^{10}	10^{11}

SRB Acetate

●	●	●	●	○	○	○	○	○	○
●	●	●	●	○	●	○	○	○	○
●	●	●	●	●	●	○	○	○	○
●	●	●	●	○	○	○	○	○	○
10^2	10^3	10^4	10^5	10^6	10^7	10^8	10^9	10^{10}	10^{11}

Fe Reducing

●	●	●	●	○	○	○	○	○	○
●	●	○	●	○	○	○	○	○	○
●	●	●	●	○	○	○	○	○	○
●	●	●	●	○	○	○	○	○	○
10^2	10^3	10^4	10^5	10^6	10^7	10^8	10^9	10^{10}	10^{11}

Tank 36A, Core 4, Transitional Zone

November 2000

SRB Lactate

●	●	●	●	●	●	○	○	○	○
●	●	●	●	●	○	○	○	○	○
●	●	●	●	●	○	○	○	○	○
●	●	●	●	●	○	●	○	○	○
10^2	10^3	10^4	10^5	10^6	10^7	10^8	10^9	10^{10}	10^{11}

SRB Acetate

●	●	●	○	○	○	○	○	○	○
●	○	○	●	●	●	○	●	○	○
●	●	●	●	●	●	○	○	○	○
●	●	●	●	●	○	○	○	○	○
10^2	10^3	10^4	10^5	10^6	10^7	10^8	10^9	10^{10}	10^{11}

Fe Reducing

●	●	●	●	●	○	○	○	○	○
●	●	●	●	●	○	○	○	○	○
●	●	●	●	●	○	○	○	○	○
●	●	●	●	●	○	○	○	○	○
10^2	10^3	10^4	10^5	10^6	10^7	10^8	10^9	10^{10}	10^{11}

Tank 36A, Core 4, Sulfide Zone
November 2000

SRB Lactate

●	●	●	●	●	●	○	○	○	○
●	●	●	●	●	●	○	○	○	○
●	●	●	●	●	●	○	○	○	○
●	●	●	●	●	●	●	○	○	○
10^2	10^3	10^4	10^5	10^6	10^7	10^8	10^9	10^{10}	10^{11}

SRB Acetate

●	●	●	●	●	●	○	○	○	○
●	●	●	●	●	●	○	○	○	○
●	●	●	●	●	●	●	○	○	○
●	●	●	●	●	●	○	○	○	○
10^2	10^3	10^4	10^5	10^6	10^7	10^8	10^9	10^{10}	10^{11}

Tank 36A, Core 5, Oxide Zone

November 2000

SRB Lactate

●	●	●	●	○	○	○	○	○	○
●	●	●	●	●	○	○	○	○	○
●	●	●	●	○	○	○	○	○	○
●	●	●	●	●	○	○	○	○	○
10^2	10^3	10^4	10^5	10^6	10^7	10^8	10^9	10^{10}	10^{11}

SRB Acetate

●	●	●	●	○	○	○	○	○	○
●	●	●	●	○	●	○	○	○	○
●	●	●	●	●	○	○	○	○	○
●	●	●	●	●	○	○	○	○	○
10^2	10^3	10^4	10^5	10^6	10^7	10^8	10^9	10^{10}	10^{11}

Fe Reducing

●	●	●	○	○	○	○	○	○	○
●	●	○	●	○	○	○	○	○	○
●	●	●	○	○	○	○	○	○	○
●	●	●	○	○	○	○	○	○	○
10^2	10^3	10^4	10^5	10^6	10^7	10^8	10^9	10^{10}	10^{11}

Tank 36A, Core 5, Transitional Zone
November 2000

SRB Lactate

●	●	●	●	●	○	○	○	○	○
●	●	●	●	●	●	●	○	○	○
●	●	●	●	●	●	○	○	○	○
●	●	●	●	●	●	○	○	○	○
10^2	10^3	10^4	10^5	10^6	10^7	10^8	10^9	10^{10}	10^{11}

SRB Acetate

●	●	●	●	●	●	○	○	○	○
●	●	●	●	●	●	○	○	○	○
●	●	●	●	●	●	○	○	○	○
●	●	●	●	●	○	○	○	○	○
10^2	10^3	10^4	10^5	10^6	10^7	10^8	10^9	10^{10}	10^{11}

Fe Reducing

●	●	●	○	○	○	○	○	○	○
●	●	●	●	○	○	○	○	○	○
●	●	●	●	○	○	○	○	○	○
●	●	●	●	●	○	○	○	○	○
10^2	10^3	10^4	10^5	10^6	10^7	10^8	10^9	10^{10}	10^{11}

Tank 36A, Core 5, Sulfide Zone
November 2000

SRB Lactate

●	●	●	●	●	●	○	○	○	○
●	●	●	●	●	●	○	○	○	○
●	●	●	●	●	●	○	○	○	○
●	●	●	●	●	○	○	○	○	○
10^2	10^3	10^4	10^5	10^6	10^7	10^8	10^9	10^{10}	10^{11}

SRB Acetate

●	●	●	●	●	●	○	○	○	○
●	●	●	●	●	●	○	○	○	○
●	●	●	●	●	●	●	○	○	○
●	●	●	●	●	●	●	○	○	○
10^2	10^3	10^4	10^5	10^6	10^7	10^8	10^9	10^{10}	10^{11}

Tank 36A, Core 6, Oxide Zone

November 2000

SRB Lactate

●	●	●	●	●	●	○	○	○	○
●	●	●	●	●	○	○	○	○	○
●	●	●	●	●	○	○	○	○	○
●	●	●	●	●	○	○	○	○	○
10^2	10^3	10^4	10^5	10^6	10^7	10^8	10^9	10^{10}	10^{11}

SRB Acetate

●	●	●	●	●	○	○	○	○	○
●	●	●	●	●	○	○	○	○	○
●	●	●	●	●	○	○	○	○	○
●	●	●	●	●	○	○	○	○	○
10^2	10^3	10^4	10^5	10^6	10^7	10^8	10^9	10^{10}	10^{11}

Fe Reducing

●	●	●	●	○	○	○	○	○	○
●	●	●	●	●	○	○	○	○	○
●	●	●	●	○	○	○	○	○	○
●	●	●	●	●	○	○	○	○	○
10^2	10^3	10^4	10^5	10^6	10^7	10^8	10^9	10^{10}	10^{11}

Tank 36A, Core 6, Transitional Zone
November 2000

SRB Lactate

●	●	●	●	●	●	○	○	○	○
●	●	●	●	●	○	○	○	○	○
●	●	●	●	●	●	○	○	○	○
●	●	●	●	●	●	○	○	○	○
10^2	10^3	10^4	10^5	10^6	10^7	10^8	10^9	10^{10}	10^{11}

SRB Acetate

●	●	●	●	●	●	○	○	○	○
●	●	●	●	●	○	●	○	○	○
●	●	●	●	●	●	○	○	○	○
●	●	●	●	●	○	○	○	○	○
10^2	10^3	10^4	10^5	10^6	10^7	10^8	10^9	10^{10}	10^{11}

Fe Reducing

●	●	●	●	○	○	○	○	○	○
●	●	●	●	○	○	○	○	○	○
●	●	●	●	●	○	○	○	○	○
●	●	●	●	●	○	○	○	○	○
10^2	10^3	10^4	10^5	10^6	10^7	10^8	10^9	10^{10}	10^{11}

Tank 36A, Core 6, Sulfide Zone

November 2000

SRB Lactate

●	●	●	●	●	●	○	●	○	○
●	●	●	●	●	○	○	○	○	○
●	●	●	●	●	●	○	○	○	○
●	●	●	●	●	●	○	○	○	○
10^2	10^3	10^4	10^5	10^6	10^7	10^8	10^9	10^{10}	10^{11}

SRB Acetate

●	●	●	●	●	●	●	○	○	○
●	●	●	●	●	●	○	○	○	○
●	●	●	●	●	●	○	○	○	○
●	●	●	●	●	○	○	○	○	○
10^2	10^3	10^4	10^5	10^6	10^7	10^8	10^9	10^{10}	10^{11}

Tank 10A, Core 2, Oxide Zone
November 2000

SRB Lactate

●	●	●	●	●	○	○	○	○	○
●	●	●	●	○	○	○	○	○	○
●	●	●	○	○	○	○	○	○	○
●	●	●	●	○	○	○	○	○	○
10^2	10^3	10^4	10^5	10^6	10^7	10^8	10^9	10^{10}	10^{11}

SRB Acetate

●	●	●	●	●	○	○	○	○	○
●	●	●	●	●	○	●	○	○	○
●	●	●	●	○	○	○	○	○	○
●	●	●	●	○	○	○	○	○	○
10^2	10^3	10^4	10^5	10^6	10^7	10^8	10^9	10^{10}	10^{11}

Tank 10A, Core 2, Transitional Zone
November 2000

SRB Lactate

10^2	10^3	10^4	10^5	10^6	10^7	10^8	10^9	10^{10}	10^{11}
●	●	●	●	●	○	○	○	○	○
●	●	●	●	●	○	○	○	○	○
●	●	●	●	●	○	○	○	○	○
●	●	●	●	●	○	○	○	○	○

SRB Acetate

10^2	10^3	10^4	10^5	10^6	10^7	10^8	10^9	10^{10}	10^{11}
●	●	●	●	●	○	○	○	○	○
●	●	●	●	●	○	○	○	○	○
●	●	●	●	●	●	○	○	○	○
●	●	●	●	●	○	○	○	○	○

Tank 10A, Core 2, Sulfide Zone
November 2000

SRB Lactate

●	●	●	●	●	●	○	○	○	○
●	●	●	●	●	●	○	○	○	○
●	●	●	●	●	●	○	○	○	○
●	●	●	●	●	●	○	○	○	○
10^2	10^3	10^4	10^5	10^6	10^7	10^8	10^9	10^{10}	10^{11}

SRB Acetate

●	●	●	●	●	●	○	○	○	○
●	●	●	●	●	●	○	○	○	○
●	●	●	●	●	●	●	○	○	○
●	●	●	●	●	●	●	○	○	○
10^2	10^3	10^4	10^5	10^6	10^7	10^8	10^9	10^{10}	10^{11}

Tank 39A, Core 1, Oxide Zone
November 2000

SRB Lactate

10^2	10^3	10^4	10^5	10^6	10^7	10^8	10^9	10^{10}	10^{11}
●	●	●	●	●	●	○	○	○	○
●	●	●	●	●	●	○	○	○	○
●	●	●	●	●	●	○	○	○	○
●	●	●	●	●	○	○	○	○	○

SRB Acetate

10^2	10^3	10^4	10^5	10^6	10^7	10^8	10^9	10^{10}	10^{11}
●	●	●	●	●	○	○	○	○	○
●	●	●	●	●	○	○	○	○	○
●	●	●	●	●	●	○	○	○	○
●	●	●	●	●	●	○	○	○	○

Fe Reducing

10^2	10^3	10^4	10^5	10^6	10^7	10^8	10^9	10^{10}	10^{11}
●	●	●	●	●	○	○	○	○	○
●	●	●	●	●	○	○	○	○	○
●	●	●	●	○	○	○	○	○	○
●	●	●	●	●	○	○	○	○	○

Tank 39A, Core 1, Transitional Zone
November 2000

SRB Lactate

●	●	●	●	●	●	○	○	○	○
●	●	●	●	●	●	●	○	○	○
●	●	●	●	●	●	○	○	○	○
●	●	●	●	●	●	●	○	○	○
10^2	10^3	10^4	10^5	10^6	10^7	10^8	10^9	10^{10}	10^{11}

SRB Acetate

●	●	●	●	●	●	○	○	○	○
●	●	●	●	●	●	○	○	○	○
●	●	●	●	●	●	○	○	○	○
●	●	●	●	●	●	○	○	○	○
10^2	10^3	10^4	10^5	10^6	10^7	10^8	10^9	10^{10}	10^{11}

Tank 39A, Core 1, Sulfide Zone
November 2000

SRB Lactate

●	●	●	●	●	●	○	○	○	○
●	●	●	●	●	●	●	○	○	○
●	●	●	●	●	●	○	○	○	○
●	●	●	●	●	●	●	○	○	○
10^2	10^3	10^4	10^5	10^6	10^7	10^8	10^9	10^{10}	10^{11}

SRB Acetate

●	●	●	●	●	●	○	○	○	○
●	●	●	●	●	●	○	○	○	○
●	●	●	●	●	●	○	○	○	○
●	●	●	●	●	●	○	○	○	○
10^2	10^3	10^4	10^5	10^6	10^7	10^8	10^9	10^{10}	10^{11}

Tank 44A, Core 3, Oxide Zone

November 2000

SRB Lactate

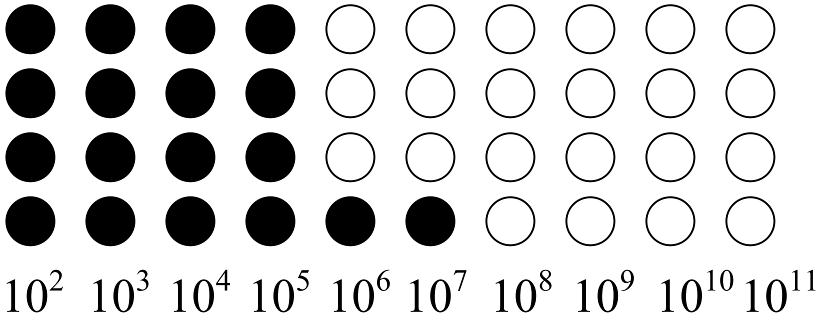

SRB Acetate

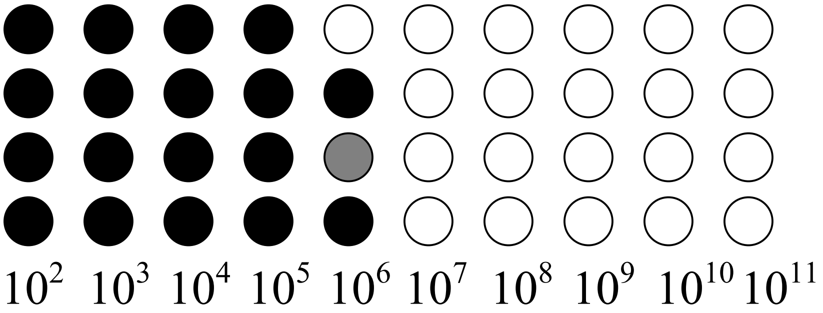

Fe Reducing

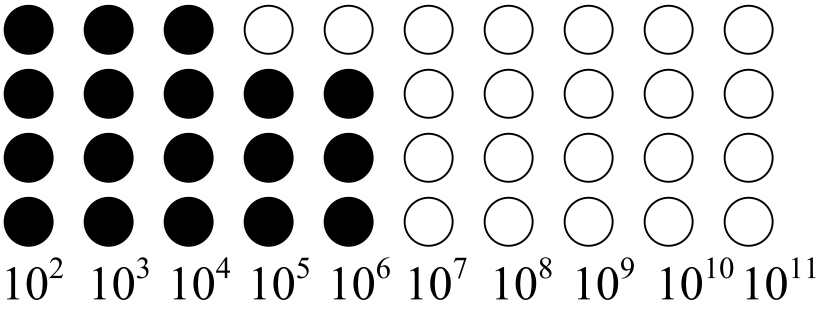

Tank 44A, Core 3, Transitional Zone
November 2000

SRB Lactate

●	●	●	●	○	○	○	○	○	○
●	●	●	●	●	○	○	○	○	○
●	●	●	●	●	○	◐	○	○	○
●	●	●	●	●	○	○	○	○	○
10^2	10^3	10^4	10^5	10^6	10^7	10^8	10^9	10^{10}	10^{11}

SRB Acetate

●	●	●	●	●	●	○	○	○	○
●	●	●	●	●	○	○	○	○	○
●	●	●	●	●	○	○	○	○	○
●	●	●	●	●	●	○	○	○	○
10^2	10^3	10^4	10^5	10^6	10^7	10^8	10^9	10^{10}	10^{11}

Fe Reducing

●	●	●	●	●	●	○	●	○	○
●	●	●	●	●	○	○	○	○	○
●	●	●	●	●	●	○	○	○	○
●	●	●	●	●	●	●	○	○	○
10^2	10^3	10^4	10^5	10^6	10^7	10^8	10^9	10^{10}	10^{11}

Tank 44A, Core 3, Sulfide Zone

November 2000

SRB Lactate

10^2	10^3	10^4	10^5	10^6	10^7	10^8	10^9	10^{10}	10^{11}
●	●	●	●	●	○	○	○	○	○
●	●	●	●	●	●	○	○	○	○
●	●	●	●	●	●	○	○	○	○
●	●	●	●	●	●	○	○	○	○

SRB Acetate

10^2	10^3	10^4	10^5	10^6	10^7	10^8	10^9	10^{10}	10^{11}
●	●	●	●	●	●	○	○	○	○
●	●	●	●	●	●	○	○	○	○
●	●	●	●	●	●	○	○	○	○
●	●	●	●	●	●	○	○	○	○